

2011

Impact Damage Resistance And Tolerance Of Polymer Nano-Fiber Interleaved Composite Laminates

Paul Kwaku Akangah

North Carolina Agricultural and Technical State University

Follow this and additional works at: <https://digital.library.ncat.edu/dissertations>

Recommended Citation

Akangah, Paul Kwaku, "Impact Damage Resistance And Tolerance Of Polymer Nano-Fiber Interleaved Composite Laminates" (2011). *Dissertations*. 26.

<https://digital.library.ncat.edu/dissertations/26>

This Dissertation is brought to you for free and open access by the Electronic Theses and Dissertations at Aggie Digital Collections and Scholarship. It has been accepted for inclusion in Dissertations by an authorized administrator of Aggie Digital Collections and Scholarship. For more information, please contact iyanna@ncat.edu.

IMPACT DAMAGE RESISTANCE AND TOLERANCE OF
POLYMER NANO-FIBER INTERLEAVED
COMPOSITE LAMINATES

by

Paul Kwaku Akangah

A dissertation submitted to the graduate faculty
in partial fulfillment of the requirements for the degree of
DOCTOR OF PHILOSOPHY

Department: Mechanical Engineering
Major: Mechanical Engineering
Major Professor: Dr. Kunigal Shivakumar

North Carolina A&T State University
Greensboro, North Carolina
2011

ABSTRACT

Akangah, Paul Kwaku. IMPACT DAMAGE RESISTANCE AND TOLERANCE OF POLYMER NANO-FIBER INTERLEAVED COMPOSITE LAMINATES. (**Major Professor, Dr. Kunigal Shivakumar**). North Carolina Agricultural and Technical State University.

The primary limitation of fiber reinforced composite laminates is their poor interlaminar strength and fracture toughness that result in poor impact damage resistance and tolerance. A number of methods have been tried to address this limitation. These methods are limited by factors such as increase in cost, weight, or loss of in-plane properties. A promising approach which does not degrade the in-plane properties is interleaving. Thermoplastic particle interleaving has been applied to reinforce laminates but the primary concern of in-plane properties degradation has not been addressed. Polymer nano-fiber interleaving was investigated in this dissertation as an alternative approach to particle interleaving. The concept showed promise because of the very high surface area to volume ratio and high strain to fracture of the interleaving Nylon-66 nano-fibers.

The objectives of the work were to determine the relationship between the electric field and the polymer flow-rate, to improve the electrospinning process, to assess low-velocity impact damage resistance and tolerance, and to compare the performance of the base laminate to the interleaved laminate. An electrospinning set-up with a collector current management technique was developed to match the electric field to the flow-rate. Twenty-four ply quasi-isotropic base and interleaved AS4/3501-6 composite laminates were produced. Interleaving was achieved with 0.7 g/m² nano-fabric. The impacted

specimens were retested in compression. The results showed that interleaving increased the threshold impact height and force by 26% and 13%, respectively. At 4.0 J threshold impact energy, residual compression strength was 40% for the base and 45% for the interleaved laminates.

School of Graduate Studies
North Carolina Agricultural and Technical State University

This is to certify that the Doctoral Dissertation of

Paul Kwaku Akangah

has met the dissertation requirements of
North Carolina Agricultural and Technical State University

Greensboro, North Carolina
2011

Approved by:

Dr. Kunigal Shivakumar
Major Professor

Dr. Sameer A. Hamoush
Committee Member

Dr. Samuel P. Owusu-Ofori
Committee Member

Dr. Shih-Liang Wang
Committee Member

Dr. Samuel P. Owusu-Ofori
Department Chairperson

Dr. Sanjiv Sarin
Associate Vice Chancellor for
Research and Graduate Dean

DEDICATION

I dedicate this success to my late father, Mr. Martin Sai Akangah, who imbued in me the spirit of hard work and compassion.

BIOGRAPHICAL SKETCH

Paul Akangah was born in Accra, Ghana to Mr. Martin Akangah and Madam Victoria Hounghlah. He received his Bachelor's degree in Mechanical Engineering from the Kwame Nkrumah University of Science and Technology (KNUST), Kumasi, Ghana, in 1993. He obtained his M.Sc degree in Mechanical Engineering from the Norwegian University of Science and Technology, Trondheim, Norway, in 1998. He was first employed at Nestle Ghana Ltd, as a Technical/Management Trainee and later promoted to Assistant Industrial Engineer. At Nestle, he was responsible for energy and utility monitoring, and capacity planning.

From 2002 to 2004, he was an instructor at the Arcada Polytechnic, Espoo, Finland. He received another M.Sc degree from the Royal Institute of Technology (KTH) in Energy Engineering in 2005. From 2004 to 2006, he was an instructor at his alma mater, KNUST as well as a part-time Instructor at the Regional Maritime University (RMU) in Accra, Ghana.

He enrolled in the Department of Mechanical Engineering Ph.D. program at the North Carolina Agricultural and Technical State University in 2006. His research is in the area of polymer nano-fiber interleaving and its effect on the impact damage resistance and tolerance of carbon/epoxy composite laminates.

ACKNOWLEDGMENTS

First and foremost, I would like to thank my supervisor, Dr. Kunigal Shivakumar, who provided me with guidance, support and encouragement throughout my study. Acknowledgments are also extended to my committee members, Dr. Samuel Owusu-Ofori, Dr. Shih-Liang Wang and Dr. Sameer A. Hamoush for reviewing my work and offering many useful recommendations.

I am very grateful to the Center for Composite Materials Research (CCMR) at the North Carolina A & T State University (NC A&T SU) and the Department of Mechanical Engineering for the opportunity to enroll in this program. I am indebted to the following funding agencies; U.S. Army Research Laboratory-Micro Autonomous Systems and Technology, Office of Naval Research, U.S. Army Research Office, and NASA URC for their financial and technical assistance. Thanks also to the CCMR Staff, especially, Mr. Mathew Sharpe, Laboratory Manager, Dr. Shivalingappa Lingaiah, Mr. John Skujins, Prof. Robert Sadler and Mr. Jesse Chambers-an engineering graduate of NCAT and currently with Bechtel Marine Propulsions Corporation, for various assistance in completing this work. I also like to thank my fellow graduate students, especially, Anthony Cunningham, ABSM Talucdher Rupan, Ebony Adams, Mohammed Mynul and Mohammed Ali for their support.

My heartfelt appreciation to Mr. Kwame Akangah and Mrs. Monique Fagla, who encouraged and motivated me to fight on when all hope, seemed to be lost. A special thanks to my childhood friend, Mr. Eric Fiafor, for his continual friendship. To my wife Hermione and my sons Russell and Victor for their love. To God, be the Glory!

TABLE OF CONTENTS

LIST OF FIGURES	xii
LIST OF TABLES	xviii
LIST OF SYMBOLS	xix
CHAPTER 1. INTRODUCTION	1
1.1 Background.....	1
1.1.1 Angle-ply Laminates.....	4
1.1.2 Cross-ply Laminates	7
1.2 Methods to Prevent Edge Delaminations.....	10
1.3 Literature Review on Low Velocity Impact Characterization.....	13
1.3.1 Basic Impact Mechanics	13
1.3.2 Important Accomplishments in Impact Mechanics	14
1.3.3 Test Standards for Impact and Compression After Impact Tests	20
1.4 Methods to Enhance Impact Damage Resistance and Tolerance	22
1.4.1 Matrix Toughening Method.....	22
1.4.2 Through-the-thickness Reinforcement Method	23
1.4.3 Interleaving Method.....	24
1.5 Limitations of Current Methods.....	28
1.6 The Polymer Nano-fiber Interleaved Concept.....	29
1.7 Goals and Objectives	30
1.8 Scope	31

CHAPTER 2. ELECTROSPINNING PROCESS AND IMPROVEMENTS	32
2.1 Introduction.....	32
2.2 Electrospinning at CCMR.....	32
2.2.1 Stationary Flat Plate Collector	32
2.2.2 Rotating Drum Set-up.....	33
2.2.3 Multi-nozzle Electrospinning Set-up	34
2.2.4 X-Traversing Electrospinning Set-up	35
2.3 Development of Improved Electrospinning.....	36
2.3.1 Electro-Mechanism of Electrospinning	36
2.3.2 Implementation of Collector Current Management System	38
2.3.2.1 Materials and Methods.....	39
2.3.2.2 Experiment I: Determination of Operating Diagram using the Method of Shin et al	41
2.3.2.3 Results and Discussion (Experiment I).....	41
2.3.2.4 Experiment II: Determination of Operating Diagram using the Method of Yan & Gevelber.....	44
2.3.2.5 Results and Discussion (Experiment II)	45
2.3.2.6 SEM Analysis to Determine Fiber Morphology.....	47
2.3.2.7 Generalization of Results	48
2.4 Size Scale-up and Description of Equipment	48
2.5 Results of Performance Evaluation.....	52
2.5.1 Processing Parameter Selection	52
2.5.2 SEM Analysis	53

2.5.3	Electrospinning Yield	55
2.6	Summary	58
CHAPTER 3. LAMINATES FABRICATION AND SPECIMENS PREPARATION ..		60
3.1	Introduction.....	60
3.2	Material Systems.....	60
3.3	Fabrication of Base and Interleaved Laminates.....	62
3.3.1	Prepreg Cutting Process.....	63
3.3.2	Stacking and Debulking.....	63
3.3.3	Molding.....	65
3.3.3.1	Mold Preparation	65
3.3.3.2	Bagging.....	65
3.3.3.3	Autoclave Process.....	68
3.4	Structural Diagnostics Inc (SDI) C-Scan of Laminates	70
3.4.1	C-Scan Test.....	70
3.4.2	Results.....	71
3.5	Preparation of Test Specimens.....	73
3.5.1	Machining	73
3.5.2	Specimens Drying.....	74
3.5.3	Test Specimen Dimensions.....	75
3.6	Summary	77
CHAPTER 4. LOW VELOCITY IMPACT ASSESSMENT OF INTERLEAVED LAMINATES.....		78
4.1	Introduction.....	78

4.2	Impact Analysis of Dynatup	78
4.2.1	Description of Test Set-up	78
4.2.2	Rigid Body Mechanics of Impact	81
4.2.3	Deformation Mechanics after Impact	82
4.2.4	Energy Analysis of the Impact.....	82
4.2.5	Single Degree of Freedom (SDOF) Analysis of Plate and Impactor.....	83
4.3	Test Matrix.....	85
4.4	Impact Test.....	87
4.5	Test Results and Discussion.....	88
4.5.1	Damage Analysis	88
4.5.1.1	Visual Analysis	88
4.5.1.2	Indentation Depth.....	89
4.5.1.3	Damage Analysis by C-Scan	92
4.5.2	Impact Response of Undamaged Laminate	98
4.5.3	Impact Response of Damaged Laminate	100
4.5.3.1	Critical Force	100
4.5.3.2	Damage Progression	103
4.5.3.3	Critical Energy	105
4.5.3.4	Contact Duration.....	108
4.6	Summary	110
CHAPTER 5. COMPRESSION AFTER IMPACT (CAI) TEST		112
5.1	Introduction.....	112

5.2	Test Specimen.....	112
5.3	Test Apparatus	113
5.4	Testing	115
5.5	Results and Discussion	119
5.5.1	Visual Inspection	119
5.5.2	Residual Compressive Strength and Discussion.....	121
5.5.3	Plots.....	123
5.4	Summary	125
CHAPTER 6. CONCLUSIONS AND RECOMMENDATIONS FOR FUTURE WORK.....		127
6.1	Summary.....	127
6.1.1	Electrospinning.....	127
6.1.2	Impact Study	128
6.1.3	Compression After Impact Test Results	129
6.2	Conclusions.....	129
6.3	Recommendations for Future Work.....	130
6.3.1	Free-surface Electrospinning	130
6.3.2	Functionalization of Nano-fibers	130
6.3.3	Determination of Effective Nano-fabric Diameter and Areal Density	131
REFERENCES		132
APPENDIX A. CHARACTERIZATION OF COMPRESSIVE PROPERTIES OF TEST LAMINATES		138

APPENDIX B. DAMAGE ASSESSMENT OF IMPACT TEST BASED ON VISUAL INSPECTION.....	139
APPENDIX C. C-SCAN RESULTS	143
APPENDIX D. SUMMARY OF IMPACT TEST DATA	148
APPENDIX E. IMPACT RESPONSE PLOTS FOR BASE SPECIMENS.....	150
APPENDIX F. IMPACT RESPONSE PLOTS FOR INTERLEAVED SPECIMENS.....	164

LIST OF FIGURES

FIGURES	PAGE
1.1. High interlaminar stresses due to load-path discontinuities	1
1.2. Types of matrix cracks in impacted laminate. (a) Shear and (b) Tensile cracks	2
1.3. Basic delamination modes in composite laminates. (a) Mode-I (tension), (b) Mode-II (shearing) and (c) Mode-III (tearing).....	3
1.4. Effect of ply orientation on in-plane Poisson ratio and shear coupling coefficient	4
1.5. Angle-ply laminate under tensile axial stress	5
1.6. Shear deformation of individual plies in an angle-ply laminate	5
1.7. Interlaminar and in-plane shear stresses in an angle-ply laminate	6
1.8. State of interlaminar and in-plane shear stresses in an angle-ply laminate	7
1.9. Variation of normalized interlaminar shear stress as function of ply angle in angle ply laminate	7
1.10. Cross-ply laminate under axial tensile stress	8
1.11. Transverse deformation of individual plies in cross-ply laminate.....	8
1.12. State of interlaminar shear stress in cross-ply laminate.....	9
1.13. (a) Free-body diagram of a cross-ply laminate, (b) Interlaminar normal and (c) Shear stress shear in cross-ply laminate	10
1.14. Through thickness distributions of edge interlaminar normal stress as a function of stacking sequence.....	10
1.15. Schematic of edge cap to prevent edge delamination.....	11
1.16. Principle of critical ply termination	12
1.17. Improved TDOF spring-mass model	15
1.18. Types of impact response.....	15

1.19.	Typical failure types in laminated composite plate	17
1.20.	Schematic and microscopic photographic cross-section of T800H/3900-2	26
1.21.	Schematic and Scanning Electron Microscope (SEM) micrograph of UT500/111/ionomer laminate.....	27
1.22.	Toughening mechanisms for (a) conventional interleaved CFRP and (b) Ionomer-interleaved Carbon/Epoxy	27
1.23.	Nano-fiber interleaved Concept.....	29
2.1.	Stationary collector electrospinning apparatus. (a) Schematic diagram and (b) Photograph of apparatus.....	33
2.2.	Rotating drum electrospinning apparatus. (a) Schematic and (b) Photograph of apparatus.....	34
2.3.	Two-needle rotating drum electrospinning set-up. (a) Schematic and (b) Photograph of set-up	35
2.4.	X-traversing needle electrospinning set-up. (a) Schematic and (b) Photograph of apparatus.....	36
2.5.	Actual electromechanics of fiber formation. (a) Photograph and (b) Schematic of whipping instability.....	37
2.6.	Relationship between collector current and fiber morphology. (a) Collector current regimes, and (b) Corresponding fiber morphology	37
2.7.	Various electrospinning process regimes. (a) Flow-rate (Q) greater than dynamic jet flow-rate (Q_{jet}); (b) Flow-rate (Q) equals to dynamic jet flow-rate (Q_{jet}), and (c) Flow-rate (Q) less than dynamic jet flow-rate (Q_{jet}).....	38
2.8.	Electrospinning with collector current management system to improve spinning. Demonstration on a stationary collector. (a) Schematic and (b) The experimental set-up	39
2.9.	Collector current management system components	40
2.10.	Plot of collector current, I , versus electric field, E^* , for Nylon-66 (12wt% concentration) showing all three repeated tests at 0.4 ml/hr	42
2.11.	Plot of averaged current, I , versus electric field, E^* , for Nylon-66 (12wt% concentration) at 0.4 ml/hr	43

2.12.	Plot of average collector current, I , versus electric field, E^* , for Nylon-66 (12 wt% concentration) solution. The insert shows idealized $I-E^*$ curve	43
2.13.	Plot of critical electric field versus flow-rate Q using the method of Shin et al	44
2.14.	Plot of critical electric field versus flow-rate Q using the method proposed by Yan & Gevelber	46
2.15.	Comparison of both methods for determining operating diagram.....	46
2.16.	SEM micrograph of fiber morphology obtained at 0.4 ml/hr at (a) ~ 15k and (b) 40k resolutions.....	47
2.17.	Photograph of rotating drum electrospinning system.....	49
2.18.	Electrospinning set-up during spinning operation. Velmex Xslide and humidifier clearly seen in the background.....	50
2.19.	Schematic of two needle rotating drum electrospinning system	51
2.20.	SEM micrograph of nano-fabrics showing beads (circled). (a) Original system, and (b) New and improved system (example 1)	53
2.21.	SEM micrographs of nano-fabric at 50k resolution. (a) Original system with fiber diameter range 85-180 nm and (b) New and improved system with fiber diameter range 60-125 nm (example 1).....	54
2.22.	SEM micrographs of nano-fabric made by the new and improved system at $V = 26$ kV, $D = 15$ cm (example 2). (a) Micrograph at 3k resolution, and (b) Micrograph at 50k resolution	54
2.23.	Removal of electrospun nano-fabric from rotating drum. (a) Schematic of cutting line and (b) Schematic of cut nano-fabric	55
2.24.	Determination of number of sample, for a reliability of 82% and a confidence level (C) of 95%	56
2.25.	Distribution of areal density along length of rotating drum	57
3.1.	SEM micrograph of nano-fibers used for interleaving.....	61
3.2.	Schematic of base laminate layout.....	62
3.3.	Schematic of interleaved laminate layout.....	62

3.4.	Prepreg cutting from a roll for 0/+ 45/90 layers; example of -45° ply	63
3.5.	Debulking of prepreg layers.....	64
3.6.	Debulked prepreg prior to bagging.....	66
3.7.	Cowl plate mounting for uniform thickness and breather yarns for evacuating gases.....	66
3.8.	Prepared preform ready for autoclave.....	67
3.9.	Mounting of laminate into autoclave and instrumentation	68
3.10.	Specimen time, temperature and pressure cure cycle for autoclave process	69
3.11.	Completed laminate prior to trimming	69
3.12.	SDI ultrasonic c-scan equipment	70
3.13.	Through-thickness c-scanning of the laminate	71
3.14.	C-scan image of base laminates. (a) Laminate # 1 and (b) Laminate # 2.....	72
3.15.	C-scanned images of interleaved laminates. (a) Laminate # P1 and (b) Laminate # P2	73
3.16.	(a) Laminate layout, (b) Test specimen and (c) specimen layout.....	74
3.17.	Drying cycle of c-scanned test specimens	75
3.18.	Thickness measurement of a test specimen	76
4.1.	Photograph of the Dynatup Model 8250 Impact Testing System and data acquisition system.....	79
4.2.	Analysis of impact test.....	80
4.3.	Spring-mass models for impact deformation mechanics. (a) Schematic of specimen deformation, (b) Complete and (c) SDOF models	84
4.4.	Photograph of drop tower impact test fixture	87
4.5.	Schematic of clamped test specimen. (a) Plan and (b) Sectioned view.....	88
4.6.	Indentation depth measurement. (a) Schematic and (b) Photograph of set-up.....	89
4.7.	Indentation depth versus impact height	92

4.8.	Structural Diagnostics Inc (SDI) c-scan equipment for the measurement of damage area.....	93
4.9.	C-scan images for base and interleaved specimens impacted at $H = 64$ mm and their corresponding damage areas	94
4.10.	Damage area versus impact height for the present study.....	95
4.11.	Damage area versus impact height for the preliminary study.....	95
4.12.	Damage area versus impact force for the present study	97
4.13.	Damage area versus impact force for the preliminary study	97
4.14.	Typical Impact force-time response of undamaged test specimen at impact height of 64 mm ($E_0 = 3.21$ J).....	98
4.15.	Impact force-displacement response of undamaged interleaved laminate at impact height of 64 mm ($E_0 = 3.35$ J)	99
4.16.	Impact force-displacement response of undamaged test specimen at impact height of 64 mm ($E_0 = 3.21$ J).....	99
4.17.	Impact force-displacement response of undamaged interleaved laminate at impact height of 64 mm ($E_0 = 3.35$ J)	100
4.18.	Typical impact force-time response of a damaged base laminate at impact height of 89 mm ($E_0 = 4.65$ J).....	101
4.19.	Impact force-time response of a damaged interleaved laminate at impact height of 89 mm ($E_0 = 4.53$ J).....	101
4.20.	Impact force-time response of base laminate showing failure progression	104
4.21.	Impact force-time response of interleaved laminate showing failure progression	104
4.22.	Critical force versus impact height	105
4.23.	Typical energy response for inelastic impact event.....	106
4.24.	Graphical method for the determination of critical impact energy, E_c	107
4.25.	Critical energy versus impact height.....	107
4.26.	Contact duration versus impact height.....	110

5.1.	Compression After Impact (a) Schematic of test fixture and (b) Photograph of test fixture	113
5.2.	Details of clamping and strain gages location. Gages #4 and 3 located behind gages #1 and #2 (dimensions in mm).....	114
5.3.	Typical compressive stress versus displacement at $H = 57$ mm.....	117
5.4.	Compressive stress versus displacement response of impact damaged base laminates for low impact heights.....	117
5.5.	Compressive stress versus displacement response of impact damaged base laminates for high impact heights	118
5.6.	Compressive stress versus displacement response of impact damaged interleaved laminates for low impact heights	118
5.7.	Compressive stress versus displacement response of impact damaged interleaved laminates for high impact heights	119
5.8.	Failure modes of base laminates. (a) Edge-crushing failure and (b) failure at the impacted site	120
5.9.	Failure modes of interleaved laminates. (a) Edge-crushing failure and (b) Failure at the impacted site.....	120
5.10.	Edge view of a CAI test specimen (base).....	120
5.11.	Edge view of a CAI test specimen (interleaved)	121
5.12.	Compression failure strength of base laminate.....	124
5.13.	Compression failure strength of interleaved laminate	124
5.14.	Compressive residual strength ratio versus impact height and energy	125

LIST OF TABLES

TABLES	PAGE
1.1. Boeing BSS 7260 Standard.....	21
2.1. Experimental results to determine the onset of whipping instability.....	45
2.2. Processing parameters for original and present method.....	52
2.3. Summary of physical properties of electrospun nano-fibers.....	58
3.1. List of specimen dimensions.....	76
4.1. Impact test matrix.....	86
4.2. Damage assessment of laminate back-face.....	90
4.3. Indentation depth results for base and interleaved laminates.....	91
4.4. Maximum and critical force for base and interleaved laminates.....	102
4.5. Contact durations for base and interleaved laminates.....	109
5.1. Percentage bending strain of base and interleaved test laminates.....	115
5.2. Residual compressive strength and failure modes for base laminates.....	122
5.3. Residual compressive strength and failure modes for interleaved laminates.....	122

LIST OF SYMBOLS

σ_z	Interlaminar normal stress, MPa
τ_{xz}, τ_{yz}	Interlaminar shear stress, MPa
$\bar{\sigma}_x$	Average axial tensile stress, MPa
σ_x	Axial tensile stress, MPa
ν_{xy}, ν	In-plane Poisson ratio, Laminate's Poisson ratio
$\alpha, \alpha_o, \alpha_m$	Static indentation depth, permanent static indentation depth left upon unloading, static indentation depth corresponding to the force P_m , mm
\forall	Taylor cone volume, mm ³
a	Acceleration of impactor, m/s ²
A	Semi major axis length, mm
A_0	Constant in critical electric field power-law equation, $A_0 = 2$
b	Width of laminate, mm
B	Semi minor axis length, mm
C	Confidence level, mainly 95% for engineering applications
c	Empirical constant in spring-mass-dashpot (SMD) model
CAI	Compression After Impact
C_E	Ratio of impact energy to specimen thickness, 6.7 J/mm
$CFRP$	Carbon Fiber Reinforced Polymer
C_L	Unidirectional delaminated ply strip length, mm
$CNTs$	Carbon Nano Tubes
COR	Coefficient of restitution
$CSIPAP$	Composite Structure Impact Assessment Program
C_W	Unidirectional delaminated ply strip width, mm
d	Indentation depth, mm
dof	Degree of freedom
D	Distance between tip of the syringe needle and collector, mm
D^*	Flexural rigidity, Nm

D_a	Damage area, mm ²
D_L	Axial distance between two needles oriented at right angle to each other
$E, E_0, E_T, E_a, E(t)$	Impact, maximum, dissipated, threshold impact and instantaneous energies, J
E^*, E_c^*	Average electric field; average critical electric field, kV/cm
E_{loss}	Energy losses during acceleration of the impactor, J
E_p	Equivalent in-plane modulus of the laminate, GPa
E_{xx}	Longitudinal in-plane modulus, GPa
E_{yy}	Transverse in-plane modulus, GPa
F_{IC}	Ultimate compressive residual strength, MPa
F_y, F_z	Force in y and z directions, N
g	Acceleration due to gravity, 9.81 m/s ²
$G_I, G_{II}, G_{III}, G_{IIC}$	Mode-I, II, III and critical strain energy release rates, J/m ²
h	Laminate thickness, mm
H, H_T	Impact height, threshold impact height, mm
I	Collector current, μ A
IFT	Interlaminar fracture toughness
k	Exponent in critical electric field power-law equation, $k = 2.5 - 3.0$
k_b, k_m, k_s, k_c, k_0	Bending stiffness, membrane stiffness, shear stiffness, contact stiffness, pristine bending stiffness of the laminate, N/m
k_{bs}	Effective stiffness due to bending and shear, N/m
L	Length of rotating drum collector, mm
L_T	Needle traverse distance, mm
M	Mass of impactor, kg
MAV	Micro Air Vehicle
M_p	Mass of test section of the laminate plate, kg
$MSDOF$	Modified single degree of freedom system
M_x	Moment about the x-axis, Nm
N	Number of repeated ply blocks in (-45/90/-45/0) _{NS}
n	Empirical constant in spring-mass-dashpot (SMD) model

n^*	Number of delaminations
NN	Number of randomly selected samples
$P, P_m, P_c, P(t)$	Contact force, contact force where unloading begins, critical force, instantaneous force, kN
Q	Polymer flow-rate, ml/hr
Q_{jet}	Dynamic jet flow-rate, ml/hr
R	Radius of rotating drum collector, mm
R_c	Reliability at confidence level, C
R^*	Collector current management resistance, $1\text{ M}\Omega$
R_c	Reliability factor in the determination of sample sizes
R_p	Resistance of the electrospinning space, Ω
$S.D$	Standard deviation
$SDOF$	Single Degree of Freedom
SEM	Scanning Electron Microscope
SMD	Spring-Mass-Dashpot
t	Time, s
T_d	Contact duration of the damaged laminate, ms
T_0	Contact duration of the undamaged laminate, ms
$TDOF$	Two Degree of Freedom
V, V_s	Applied voltage, spinning voltage, kV
$V_0, V_c, V_r, V(t)$	Initial impact velocity, critical velocity, rebound velocity, instantaneous velocity, m/s
V_T	Drum linear velocity, 1.5 m/s used in this study
W	Out-of-plane displacement, mm
Y	Electrospun nano-fiber yield, g/hr

CHAPTER 1

INTRODUCTION

1.1 Background

Advanced composite materials have desirable properties such as high-stiffness, high-strength and low-density when compared to conventional monolithic materials and are, therefore, used in applications where both high stiffness-to-weight and strength-to-weight ratios are desirable. The primary limitation of composite laminates is their poor interlaminar strength and fracture toughness that reduces impact damage resistance and tolerance because of delaminations (O'Brien, 1990; Sela & Ishai, 1989). Interlaminar stresses develop in composite laminates due to mismatch of ply orientation and anisotropic, mechanical and thermal properties. As a result of stress concentration, high interlaminar stresses occur at the free edges, at structural load-path discontinuities such as bonded joints, bolted joints, notches, ply drop-offs (O'Brien, 1984) as shown in Figure 1.1.

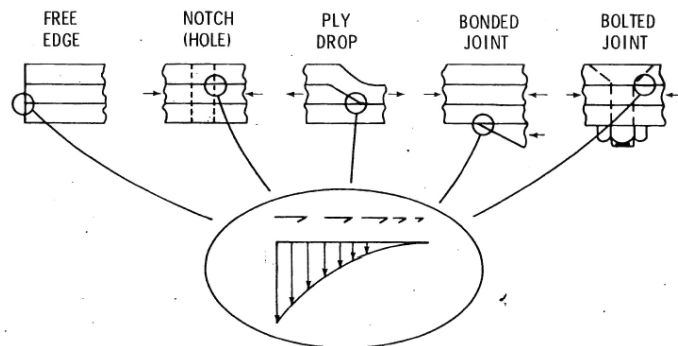


Figure 1.1. High interlaminar stresses due to load-path discontinuities (O'Brien, 1984)

High interlaminar stresses also occur in the vicinity of damage due to low-velocity impacts on composite structures (Chan, 1991; Pagano, 1989; Salpekar, O'Brien, & Shivakumar, 1996). Such high stresses combined with weak interlaminar properties cause delamination in composite laminates and degradation of the compressive strength of the laminate. Interlaminar stresses are out-of-plane stresses and can be classified as interlaminar normal stress, σ_z , and interlaminar shear stresses, τ_{xz} and τ_{yz} . During low-velocity impact, two types of matrix cracks are commonly formed. These are shear and tensile cracks and are illustrated in Figure 1.2 (Abrate, 1998).

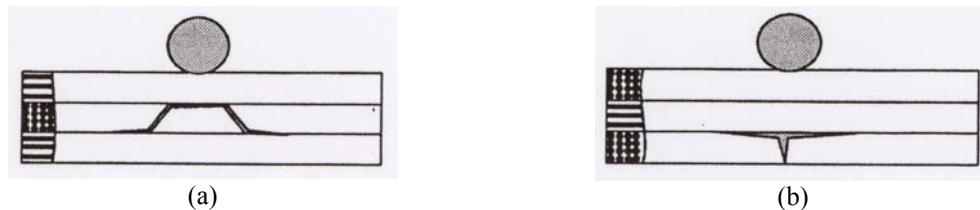


Figure 1.2. Types of matrix cracks in impacted laminate. (a) Shear and (b) Tensile cracks (Abrate, 1998)

Out-of-plane shear stress due to bending of the laminate during the impact event creates shear cracks. Tensile cracks occur when in-plane normal stresses exceed the transverse tensile strength of the ply. These cracks propagate into the interface between the adjacent layers and high interlaminar stresses are created due to stress concentrations. When these stresses exceed the laminate's interlaminar strength, delaminations are created (Salpekar et al, 1996). The three basic delamination modes are shown in Figure 1.3 (Daniel & Ishai, 2005).

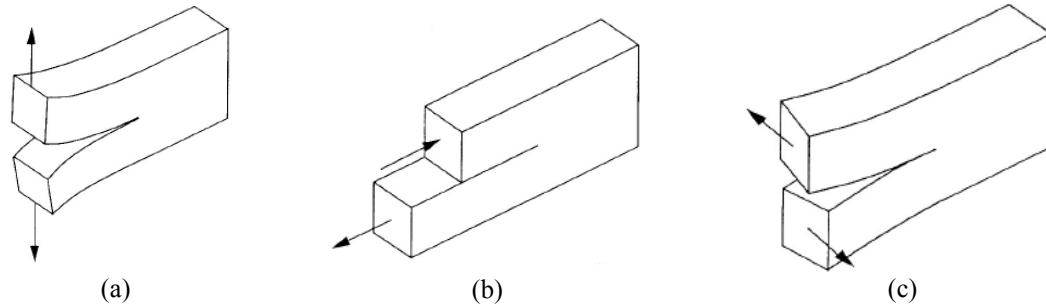


Figure 1.3. Basic delamination modes in composite laminates. (a) Mode-I (tension), (b) Mode-II (shearing) and (c) Mode-III (tearing) (Daniel & Ishai, 2005)

Mode-I delamination is caused by normal tensile interlaminar stress, σ_z , and this stress tends to separate one ply from the other while mode-II delamination is caused by interlaminar shear stresses which cause one ply to slide over the other. Mode-III is a tearing mode caused by out-of-plane shear stress. Chan (1991) suggested that whereas the initiation of delamination was characterized by mode-I delamination (G_I), its growth rate was characterized by the total strain-energy release rate, G_T . However, Davies, Zhang, Zhou & Watson (1994) suggested that delamination initiation was due to mode-II shear-propagation. The magnitude of Poisson ratio and shear coupling coefficient mismatch between plies depend on the ply orientation (fiber angle) between any consecutive plies. Therefore, the laminate's stacking sequence determines the type of interlaminar stresses created in the laminate (Daniel & Ishai, 2005; Jones, 1999). The stacking sequence describes the distribution of ply orientation through the laminate thickness. Figure 1.4 (Daniel & Ishai, 2005) shows the variation of in-plane Poisson ratio, ν_{xy} , and shear coupling coefficient, η_{xs} , as a function of ply orientation.

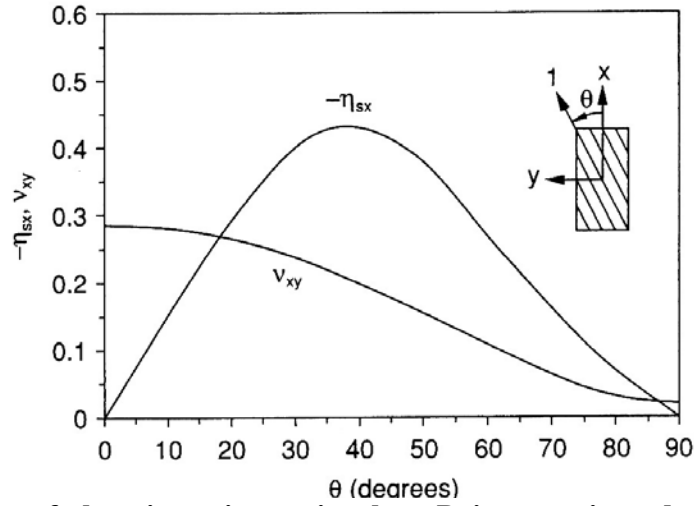


Figure 1.4. Effect of ply orientation on in-plane Poisson ratio and shear coupling coefficient (Daniel & Ishai, 2005)

1.1.1 Angle-ply Laminates

Consider an angle-ply laminate with the stacking sequence $(\pm\theta)_s$ and loaded in tension by an average axial stress, $\bar{\sigma}_x$, as shown in Figure 1.5. When each ply in the laminate is subjected to the same axial stress $\sigma_x = \bar{\sigma}_x$, the deformation of the $(\pm\theta)$ individual angle-ply in the laminate will be different and as a result of shear coupling, each ply will undergo shear deformation as shown in Figure 1.6 (Daniel & Ishai, 2005). However, when perfectly bonded together, their shear deformation would cancel out due to shear transfer mechanism the between layers. This shear transfer mechanism between layers is illustrated in Figure 1.7. The interlaminar shear stress, τ_{xz} , acts on each ply in equal magnitude but in opposite directions and they cancel out when the plies are bonded together. The interlaminar shear stress, τ_{xz} , starts from zero to a maximum value at the free-edge.

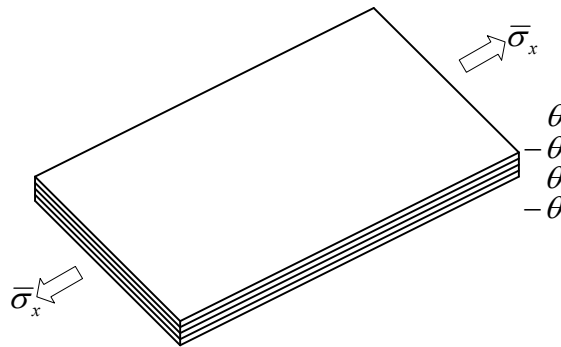


Figure 1.5. Angle-ply laminate under tensile axial stress

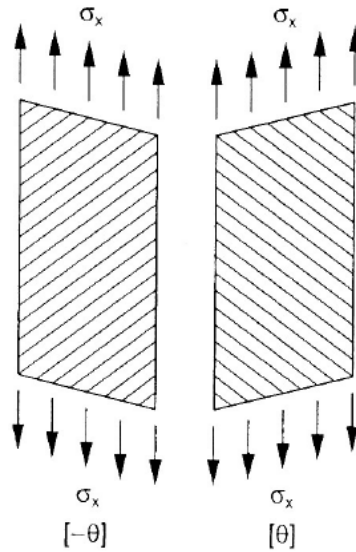


Figure 1.6. Shear deformation of individual plies in an angle-ply laminate (Daniel & Ishai, 2005)

If shear coupling is zero, then under zero shear deformation the moment due to interlaminar shear stress, τ_{xz} , must balance the moment due to in-plane shear stress, τ_{xy} , as given in Equation (1.1).

$$\tau_{xz} dx dy 2y = \tau_{xy} dy dz 2x \quad (1.1)$$

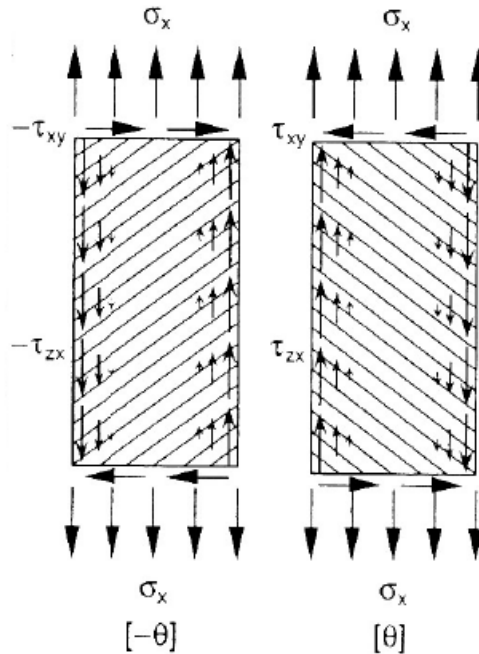


Figure 1.7. Interlaminar and in-plane shear stresses in an angle-ply laminate (Daniel & Ishai, 2005)

The in-plane shear stress, τ_{xy} , is constant for most part of the width of the laminate and drops to zero at the free edges. As a result, the interlaminar shear stress, τ_{xz} , exists at the interface of each ply as shown Figure 1.8 (Daniel & Ishai, 2005) and acts in opposite direction on each ply. The existence of this shear stress tends to cause mode-II interlaminar delamination. The magnitude and direction of the interlaminar shear stress manifesting at the interface depend on the ply orientation in the $(\pm\theta)$ laminate as shown in Figure 1.9 (Daniel & Ishai, 2005). As the ply fiber angle varies from 0° to 90° , the interlaminar stress also varies, with maximum tensile stress occurring at about 30° and minimum compressive stress occurring at about 70° . Therefore, depending on the ply orientation, interlaminar delamination may be enhanced or delayed.

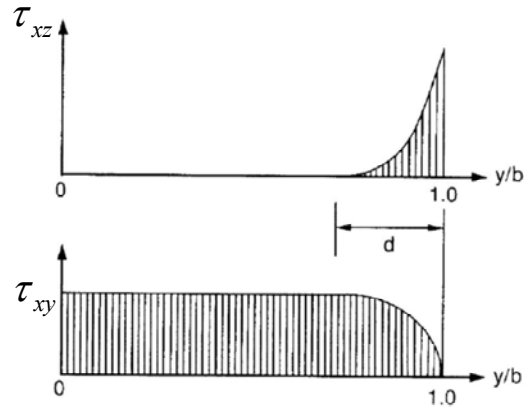


Figure 1.8. State of interlaminar and in-plane shear stresses in an angle-ply laminate (Daniel & Ishai, 2005)

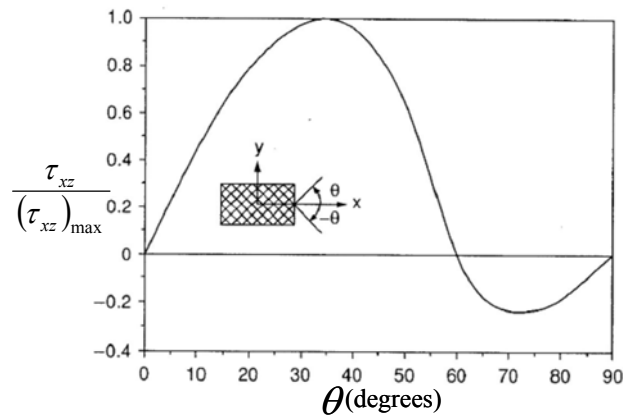


Figure 1.9. Variation of normalized interlaminar shear stress as function of ply angle in angle ply laminate (Daniel & Ishai, 2005)

1.1.2 Cross-ply Laminates

Consider the deformation of a cross-ply laminate with $(0/90)_S$ stacking sequence and subjected to average axial tensile stress, $\bar{\sigma}_x$, as shown in Figure 1.10. When the individual plies deform independently, they experience different axial stresses such that their axial deformation are the same but transverse deformations are different due to

Poisson ratio mismatch as shown in Figure 1.11 (Daniel & Ishai, 2005). When the plies are bonded together, their transverse deformations and strains become equal and therefore the interlaminar shear stress, τ_{yz} , must be zero at the free edges. As a result, the 0° ply must be in tension and the 90° ply must be in compression as shown in Figure 1.12 (Daniel & Ishai, 2005).

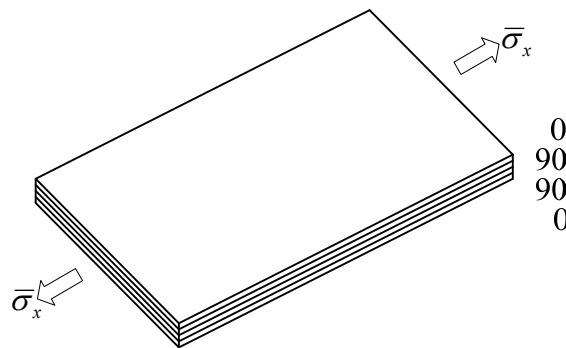


Figure 1.10. Cross-ply laminate under axial tensile stress

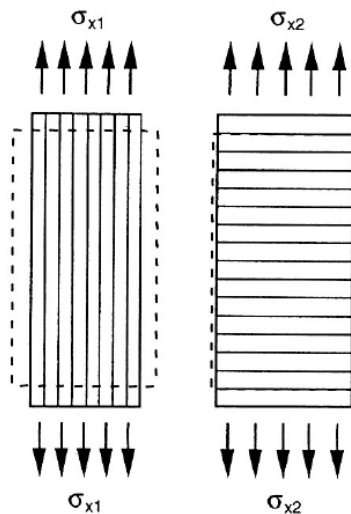


Figure 1.11. Transverse deformation of individual plies in cross-ply laminate (Daniel & Ishai, 2005)

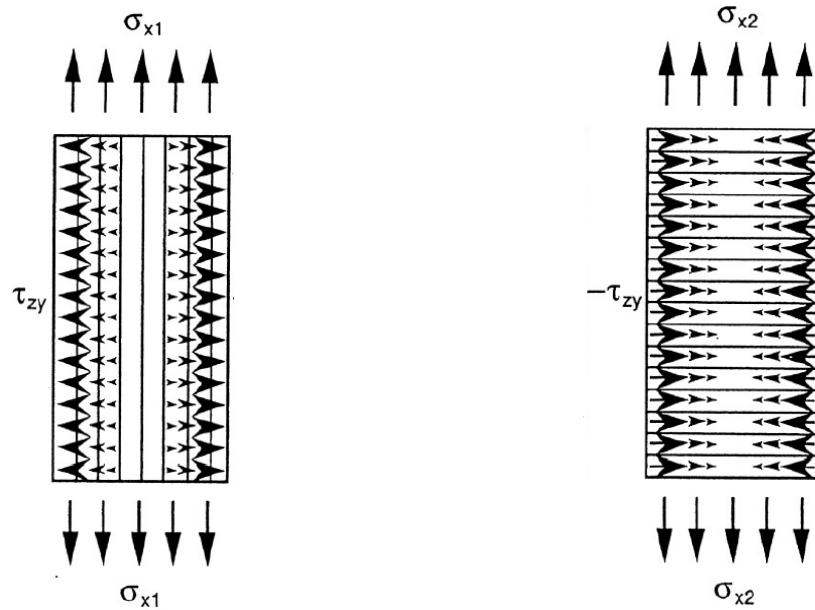


Figure 1.12. State of interlaminar shear stress in cross-ply laminate (Daniel & Ishai, 2005)

Consider the free body diagram of an element of the 0° ply near the free edge of a cross-ply laminate shown in Figure 1.13(a) (Daniel & Ishai, 2005). The distribution of the interlaminar stresses is shown in Figures 1.13(b) and (c) (Daniel & Ishai, 2005). The interlaminar shear stress, τ_{yz} , varies along the width of the laminate and to maintain equilibrium, interlaminar normal stress must exist between the plies. Pagano & Pipes (1999) postulated the distribution of this interlaminar normal stress and this is shown in Figure 1.13(b). Under these conditions, there exists a very large interlaminar normal stress that has the tendency to cause edge delamination (Daniel & Ishai, 2005). This stress is also affected by the stacking sequence as shown in Figure 1.14 (Daniel & Ishai, 2005). The mid-plane of $(15/45/-45/-15)_S$ does not experience edge delamination but interlaminar delamination.

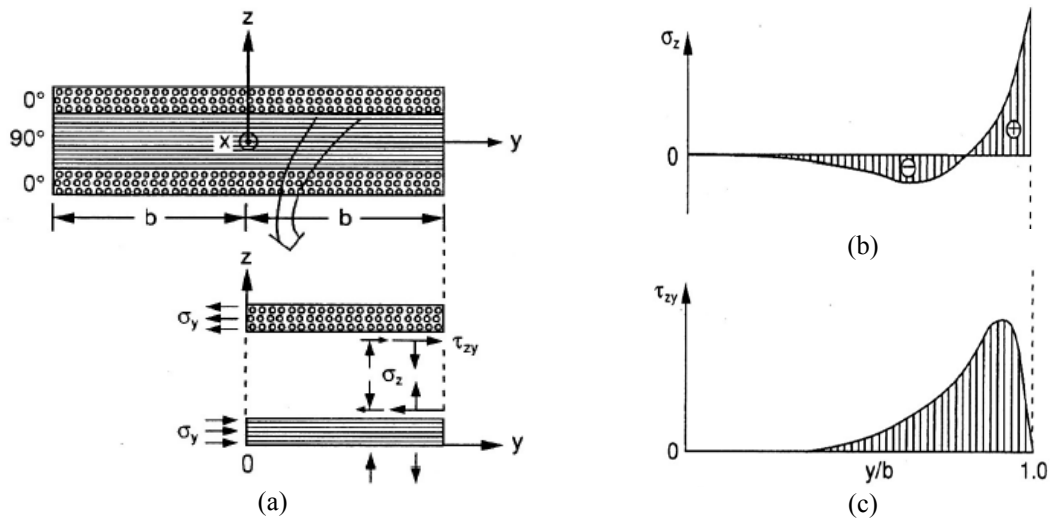


Figure 1.13. (a) Free-body diagram of a cross-ply laminate, (b) Interlaminar normal and (c) Shear stress shear in cross-ply laminate (Daniel & Ishai, 2005)

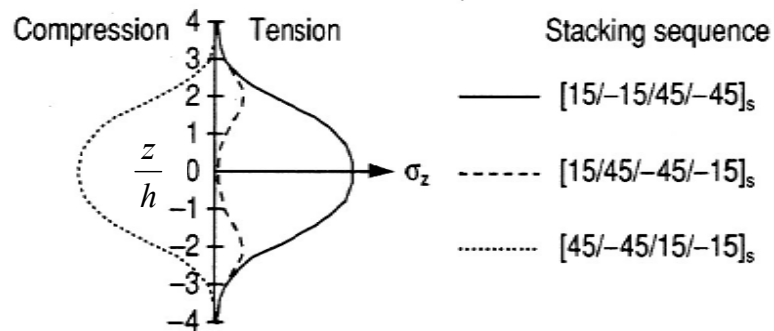


Figure 1.14. Through thickness distributions of edge interlaminar normal stress as a function of stacking sequence (Daniel & Ishai, 2005)

1.2 Methods to Prevent Edge Delaminations

Material property mismatch between adjacent plies is responsible for delamination initiation and the presence of uninterrupted load path aids in its growth (Chan, 1991; Sun & Chu, 1991). Delamination failure at a laminate's free edge is

dominated by two major modes: opening mode delamination (Howard, Gossard & Jones, 1989; Sun & Chu, 1991) and shear-dominated failure (Sun & Chu, 1991). Over the years, researchers have developed many useful techniques to reinforce Carbon-fiber reinforced polymer (CFRP) laminate edge and thus prevent edge delamination. Some of these techniques are edge cap reinforcement, notched edges, interleaving and critical ply termination (Browning & Schwartz, 1986; Chan & Ochoa, 1989; Chan, 1991; Odagiri, Muraki, & Tobukuro, 1988; Pagano & Pipes, 1971). Howard et al (1989) investigated the use of U-shaped caps in preventing edge delaminations. These were made from a single layer of Kevlar-49 impregnated with epoxy resin. Kim (1983) also investigated the use of edge-cap in preventing edge delaminations. The edge-cap was made of fiberglass and adhesive, wrapped over the edge of the laminate as shown in Figure 1.15. Both researchers concluded that static and fatigue laminate strengths are improved by capping the laminate's free-edge.

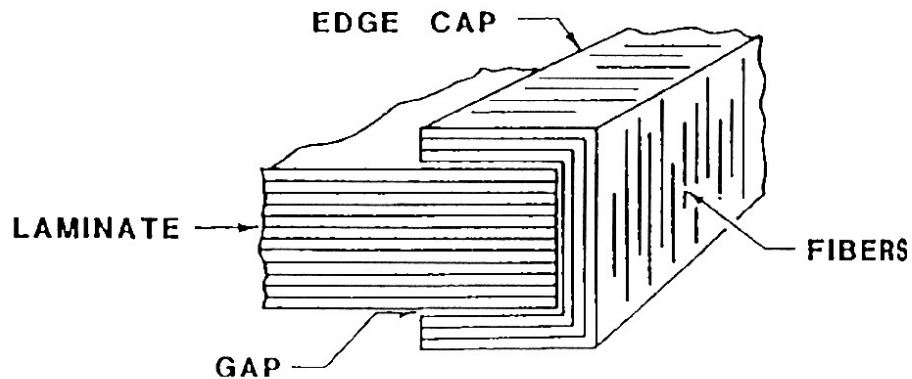


Figure 1.15. Schematic of edge cap to prevent edge delamination (Kim, 1983)

Since delamination growth is promoted by the presence of uninterrupted load paths, Sun & Chu (1991) suggested the use of notches along the edges of the laminates to prevent edge delamination and increase laminate strength. The notches interrupt the load paths to the laminate's free-edges and therefore improve the laminate's interlaminar strength. To minimize the local stress concentration created by the notches, the researchers carefully sized the notch diameter and pitch. X-ray radiographs taken just before failure of the laminates showed that delamination failure was initiated at 470 and 620 kN/m in the unnotched and notched laminates, respectively.

Critical ply termination is another method that uses the idea of load path interruption to improve the laminate strength. In this method, by terminating certain critical plies before they reach the free-edge, interlaminar stresses are reduced and edge delamination is therefore prevented resulting in improved laminate strength and fatigue life (Chan, 1991; Sun & Chu, 1991). The principle of critical ply termination is shown in Figure 1.16 (Chan, 1991).

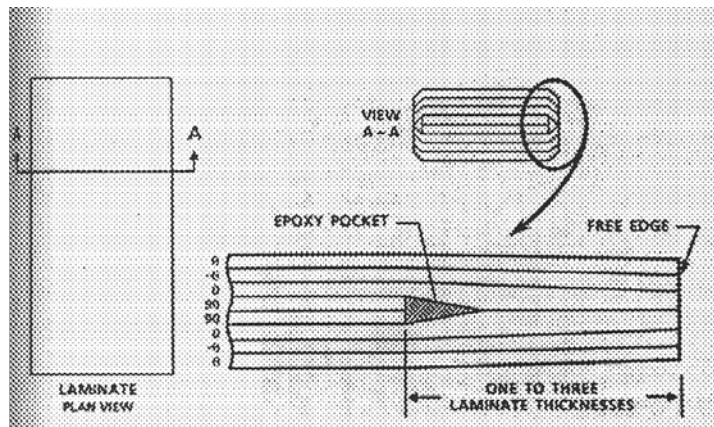


Figure 1.16. Principle of critical ply termination (Chan, 1991)

1.3 Literature Review on Low Velocity Impact Characterization

1.3.1 Basic Impact Mechanics

The Hertz contact law defines a relation between indentation and deformation (Timenshenko, 1913). This has been extended to low velocity impact problems by many researchers by neglecting vibrations produced by the collision (Greszczuk, 1982; Karas, 1339; Lee, 1941; Preston & Cook, 1975; Shivakumar, Elber, & Illg, 1985a). The Hertz law is given by:

$$P = k_c \alpha^{3/2} \quad (1.2)$$

where P is the indentation (contact) force, α the indentation deformation and k_c is the contact stiffness whose value depends on the material and geometric properties of the target and the indenter. When permanent indentation occurs at low loading levels, the contact law for the unloading phase is given in Equation (1.3) (Abrate, 1998; Tan & Sun, 1985).

$$P = P_m \left(\frac{\alpha - \alpha_0}{\alpha_m - \alpha_0} \right)^q \quad (1.3)$$

where P_m is the contact force where unloading begins, α_m is the static indentation corresponding to the force P_m , α_0 is the permanent static indentation during the unloading cycle, and q is an exponent that is determined experimentally. Lee (1941) modified the Hertz contact law to predict the contact deformation, contact force and the flexural deformation of the target structure. Preston & Cook (1975), and Greszczuk (1982) used the modified Hertz law to calculate the contact force during impact.

1.3.2 Important Accomplishments in Impact Mechanics

Shivakumar et al (1985a) suggested that the impact force predicted by the Hertz method tends to be overly conservative while the modified Hertz method underestimates the force because both methods neglect the large deformation and transverse shear deformation of the target. To address these deficiencies, they developed the energy-balance and the two-degree of freedom (TDOF) spring-mass models. The energy model predicts the impact force while the TDOF spring-mass model predicts the complete force-time response during impact on a circular composite laminate. Using the principle conservation of total potential energy and expressing contact energy in terms of the Hertz law, the energy-balance model is given by Equation (1.4) (Shivakumar et al, 1985a).

$$MV_0^2 = k_{bs}w^2 + \frac{k_m w^4}{2} + \frac{4}{5} \left[\frac{(k_{bs}w + k_m w^3)^5}{n^2} \right]^{1/3} \quad (1.4)$$

where M is the mass of the impactor, V_0 is the impact velocity, w is the plate deflection, k_{bs} is the effective stiffness due to bending and shear, k_m is the membrane stiffness. Closed form solutions for bending and membrane stiffness for centrally loaded circular composite plate of various boundary conditions were given by Shivakumar et al (1985a). The spring-mass model was characterized by four springs representing bending (k_b), shear (k_s), membrane (k_m) and contact (k_c) rigidities as shown in Figure 1.17 (Shivakumar et al, 1985a). When the impactor mass was greater than 3.5 times the effective mass of the plate ($M > 3.5M_p$), the TDOF spring-mass system reduced to single degree-of-freedom (SDOF) spring-mass system (Shivakumar et al, 1985a).

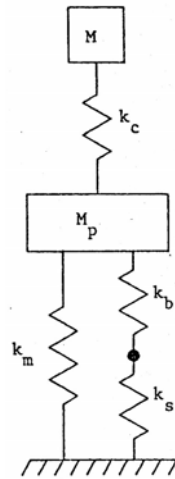


Figure 1.17. Improved TDOF spring-mass model (Shivakumar et al, 1985a)

Olsson (2000) and Davies & Olsson (2004) reviewed different types of elastic impact response in which the type of structural response is controlled by the impactor-to-plate-mass ratio and not by impact velocity. These studies suggested that structural response type can be classified into response dominated by dilatational waves, response dominated by flexural waves, and finally, quasi-static response. These responses are shown in Figure 1.18 (Olsson, 2000).

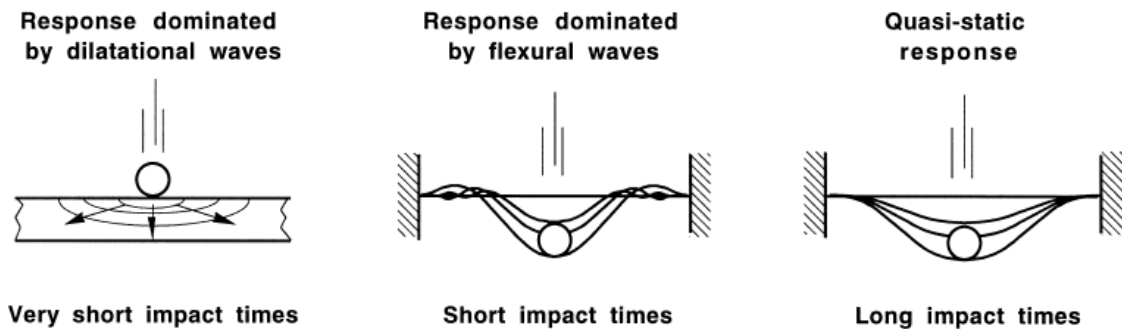
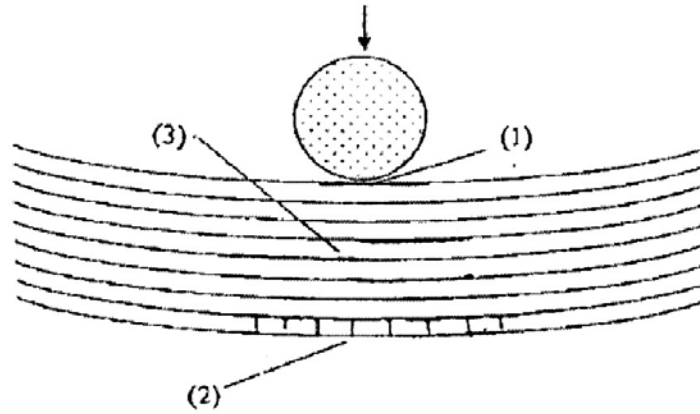


Figure 1.18. Types of impact response (Olsson, 2000)

Since the target structure responds differently depending on the impactor-to-plate-mass ratio, Olsson (2000) suggested that the impactor mass must be greater than two times the laminate mass, i.e. $M/M_p \geq 2$. Feraboli (2006a) on the other hand, suggested that for large-mass impact event, $M/M_p \geq 10$ and recommended $M/M_p = 10$ to 20 . Davies & Olsson (2004) studied the impact response of various types of laminated plates with varying degrees of impact damage. For the undamaged laminate, force and deflection time response for large-mass impact results in a bell shaped response. When membrane effect is present, large deflection results and as a result, pointed force-time response is manifested. In the case of fiber breakage, the force-time response has a capped appearance. Large mass impact response of laminated composite is governed by the interaction of local and global deflections and the induced stresses resulting from flexure and contact loads cause impact damage such as matrix cracks, delaminations and fiber breakage and typical failure types in impacted laminate plate are shown in Figure 1.19 (Davies & Olsson, 2004). Tensile failure occurs when the in-plane normal stresses exceed the transverse tensile strength of the ply (Abrate, 1998). This failure causes matrix cracks and delamination occurs where the cracks meet an interface (Davies, Hitchings & Zhang, 1999). Compressive failure is usually a point damage in nature and does not degrade the laminate's properties while shear-driven delaminations occur in the interior where strains are at a maximum. The major risk in internal delaminations in composites is a significant decrease in compression strength (Davies and Olsson, 2004).



- (1) Compressive failure
- (2) Tensile failure
- (3) Shear-driven delaminations

Figure 1.19. Typical failure types in laminated composite plate (Davies & Olsson, 2004)

Davies et al (1994) suggested that delamination initiation was always accompanied by sudden stiffness loss as a result of unstable crack growth governed by Mode-II shear propagation. They obtained the critical force required to initiate delamination and this critical force, P_c , is given in Equation (1.5).

$$P_c = \sqrt{\frac{8\pi^2 E_p h^3}{9(1-\nu^2)} G_{IIc}} \quad (1.5)$$

where E_p is the equivalent in-plane modulus of the laminate, h is the laminate thickness, ν is the equivalent Poisson ratio and G_{IIc} is the mode-II critical strain energy release rate. Equation (1.5) is based on the assumption that the damage and strains are axisymmetrical (Davies et al, 1999). Equation (1.5) can be re-formulated using the effective rigidity

defined by; $D^* = \frac{E_p h^3}{12(1-\nu^2)}$. The P_c equation reduces to:

$$P_c = \pi \sqrt{\frac{32}{3} D^* G_{IIc}} \quad (1.6)$$

Suemasu & Majima (1996) re-formulated Equation (1.6) in another form by introducing a variable n^* as the number of delaminations. This is presented in Equation (1.7).

$$P_c = \pi \sqrt{\frac{32 D^* G_{IIc}}{(n^* + 2)}} \quad (1.7)$$

When $n^* = 1$, Equation (1.7) gives the same result as Equation (1.5) or Equation (1.6). Equations (1.5), (1.6) and (1.7) are valid for small deflections where membrane deflections are negligible (Davies & Olsson, 2004). Where large deflections are present, the critical force must be corrected for the extra force carried by the membrane as these forces do not contribute to the delamination growth (Davies & Olsson, 2004; Olsson, 2001). In addition, the critical force depends on the lamina properties, stacking sequence and laminate thickness (Zhang, Hounslow, & Grassi, 2006).

A major limitation of simple single-degree-of-freedom (SDOF) models is that they are only applicable to elastic impact events and not at the onset and propagation of damage. To extend the validity of the SDOF model to include the onset and propagation of damage in the inelastic region, Feraboli (2006b) developed three modified SDOF (MSDOF) models. The three models developed were Damage Stiffness (K_D), Dissipated Energy (E_D) and Spring-Mass-Dashpot (SMD) Models. The maximum forces predicted by these models are valid only for quasi-static impacts and when membrane effects are negligible.

While the Damage Stiffness model underestimates the maximum force during inelastic impact event, the Dissipated Energy Model overestimates the maximum force during inelastic impact event. The Spring-Mass-Dashpot (SMD) Model given by Equation (1.8), however, approximates very well, the maximum impact force during inelastic impact event. The parameters n and c are determined empirically (Feraboli, 2006b). By choosing the appropriate values for n and c , elastic and inelastic impact events can be modeled.

$$P_{\max}(t) = \frac{1}{2} \left(-cV^n(t) + \sqrt{c^2V^{2n}(t) + 8k_0E(t)} \right) \quad (1.8)$$

Delfose & Poursartip (1997), Feraboli, Ireland, & Kedward (2004), and Feraboli & Kedward (2004) suggested the use of impact force to describe damage resistance (onset of damage) and impact energy to describe damage tolerance (extent of damage). Impact damage resistance is defined as how well composite structure resists impact damage due to foreign body impact (Christoforou, 2001). Damage tolerance refers to the ability of the structure to sustain design loads after damage (Christoforou, 2001; Herup, 1996). By reviewing literature, Feraboli & Kedward (2004) identified critical impact energy as an important parameter in defining impact events. Critical energy is defined the impact energy corresponding to the critical impact force. For any impact event, the critical force and energy are independent of the impact force in the inelastic impact region (Feraboli & Kedward, 2004).

Feraboli & Kedward (2006) pioneered the concept of Composite Structure Impact Assessment Program (CSIPAP) that uses multi-parameter approach to gain deep insight into the impact response of composite structures. The approach uses five fundamental

plots to completely describe the impact event. These plots are the maximum and critical force versus impact energy; the critical and dissipated energy versus impact energy; contact duration versus impact energy; the coefficient of restitution (COR) versus impact energy and, the ratio of contact duration versus impact energy. The COR plot indicates the effective structural stiffness while the normalized contact duration plot describes the residual stiffness of the structure. In CSIPAP program, testing is done in three sequential parts, in the first part, elastic tests are performed to record pristine parameters such as contact duration and COR, in the second part, a series of inelastic tests are performed to record critical and maximum forces, critical and dissipated energy, COR, and contact durations. In the third part, a second elastic test on damaged specimens is conducted to record the post-failure contact duration of the specimen. Repeated impact test (elastic, inelastic and then followed by another elastic test) was first proposed by Lifshitz, Gov, & Gandelsman (1995). By analyzing the impact event by these five plots, it is possible to compare impact test results across different test programs and the method has the advantage of bridging the impact response of a laminate to its damage resistance and tolerance (Feraboli & Kedward, 2006).

1.3.3 Test Standards for Impact and Compression After Impact Tests

Some of the commonly used compressions after impact (CAI) test methods are the National Aeronautics and Space Administration (NASA), Boeing, Pritchard Hogg and CRAG standards (Abrate, 1998). The Boeing standard defines impact and compression testing of composite laminates and details of the standard are summarized in Table 1.1 (Abrate, 1998; Fuoss, Straznický & Poon, 1998).

Table 1.1. Boeing BSS 7260 Standard

Parameter	Value
Specimen Specifications	
Specimen Thickness	4.0 to 5.0 mm
Specimen Size	101.6 mm x 152.2 mm
Stacking Sequence	(45/0/-45/90) _{NS}
Impact Test Specifications	
Tup Diameter	16 mm, hemispherical, hardened steel
Tup Mass	4.6 to 6.8 kg
Support	76.2 mm x 127 mm
Clamping Method	Clamped at four points, simply-supported mode
Loading	Central loading
No. of Test Specimens	5
Compression Test Specifications	
Loading	End loading
Loading Rate	0.5 mm/min
Clamping Method	Simply-supported
No. of Test Specimens	5
Impact Energy per unit thickness	6.7 J/mm

The Boeing Standard was adopted by American Society for Testing and Materials (ASTM) in May 2005 as the ASTM D7136 and ASTM D7137 Test Standards for Measuring the Damage Resistance of a Fiber-Reinforced Polymer Matrix Composite to a Drop-Weight Impact Event and Compressive Residual Strength Properties of Damaged Polymer Matrix Composite Plates, respectively (Instron, 2011). In these standards, damage resistance is quantified in terms of damage size and type of damage, and damage tolerance is measured by the residual compression strength of the damaged specimen.

1.4 Methods to Enhance Impact Damage Resistance and Tolerance

Methods to improve the interlaminar strength and fracture toughness for composite laminates can be broadly classified as materials improvement (high-strain fibers and tougher matrices) and laminate construction such as through-the-thickness reinforcements, interleaving (Aymerich, Pani, & Priolo, 2006a; Chan, 1991), stacking sequence, critical ply termination, discrete critical ply (Chan, 1991). Of these methods, through-the-thickness reinforcements and interleaving are suggested to be the most effective ways of improving delamination resistance caused by low-velocity impact damage (Chan, 1991). Kuboki, Jar, & Forest (2003) reported good correlation between mode-I delamination resistance and the critical force at the onset of impact damage. In another study, Hwang, Kwon, Lee, & Hwang (2000) reported that the critical strain energy release rate measured by low-velocity impact events is between the mode-I and mode-II critical strain energy release rates as measured by interlaminar fracture toughness test. Zheng (2007) and Davie et al (1994) also reported that, the growth of delaminations in laminated plates is driven primarily by interlaminar shear stresses.

1.4.1 Matrix Toughening Method

Matrix toughening approach uses tougher thermoset or thermoplastic matrices (Chan, 1991). This method improves the interlaminar fracture toughness but in-plane mechanical properties are sacrificed (Yokozeki et al, 2009). Review of the literature established that some important limitations of toughened matrices are that the relative increase in the fracture toughness of the bulk matrix is not readily transferable to the composite material and degradation of the hot/wet performance of the material leading to

its restricted applications in aerospace primary structures (Sela & Ishai, 1989).

1.4.2 Through-the-thickness Reinforcement Method

Z-pin technology is a through-the-thickness reinforcement method that uses short, fine pins made of high stiffness, high strength materials such as titanium alloy, steel; or fibrous carbon composite with a diameter between 0.2-1.0 mm that are inserted through prepreg, dry preform or foam cores (Mouritz, 2007). Cartié, Troulis, & Partridge (2006) studied the interlaminar fracture toughness of z-pinned reinforced CFRP. Results showed that z-pinning technique did not improve resistance to delamination initiation. However, interlaminar fracture toughness increases with increasing areal density of z-pins. Zhang et al (2006) studied the effects of z-pining on low-velocity impact and compression-after-impact response of CFRP. According to their results, z-pinning reduces damaged area by 64% and increases residual strength by 45%. However, z-pinning causes reduction in the critical impact force. Mouritz (2007) found that while z-pinning increases the delamination toughness, in-plane mechanical properties are degraded and the extent of degradation is dependent on z-pin areal density.

Aymerich, Pani, & Priolo, (2006a & 2006b) investigated the effect of stitching on the impact resistance of cross-ply Carbon/Epoxy laminates. The researchers concluded that stitching does not prevent the initiation and growth of delaminations, but it does however reduce the delamination area (Aymerich, 2006a). In another study, Aymerich et al (2006b) concluded that the performance of the stitched laminate depends on how well the base laminate performs under impact event. In addition, they found that stitching is most effective when the impact force is above critical and delamination is fully

developed in the laminate. Mouritz (2003) examined various impact data on stitched laminates involving low velocity and ballistic impacts and determined that stitching improved impact delamination resistance only when delamination cracks were above a threshold value of 15 mm.

1.4.3 Interleaving Method

Interleaving is a method of improving the interlaminar fracture toughness of a composite laminate by inserting a thin, discrete layer of particles or film of tough material system between the prepreg's layers (Masters, 1989). The main idea of interleaving is to toughen the matrix interface and consequently, the interlaminar and transverse strengths of the laminate are improved (Chan, 1991). In a review by Sela & Ishai (1989), they suggested the use of selective interleaving where interlayer toughening is applied only to the critical areas prone to delamination such as holes, ply drops etc. Selective toughening is important because particle or film interleaving add significantly to the weight of the laminate and for mode-I and mode-II delamination, the effective adhesive thickness is about 0.1 mm. In addition to the increased weight of interlayer material, poor adhesion between the interlayer material and the prepreg layer could result in catastrophic failure (Stevanovic, 2001).

Akangah, Lingaiah, & Shivakumar (2010) and Shivakumar et al (2009) researched the use of Nylon-66 nano-fabric interleaving. Shivakumar et al (2009) first suggested the idea as a consequence of making toughened and ultra light weight membrane for artificial dragonfly wings using electrospinning. In the preliminary impact study, nano-fibers with diameters ranging from 75–250 nm were made using 12 wt%

concentration Nylon-66 solutions. The areal density of the fabric ranged from 1.6 to 2.0 g/m². This represented between 1.0 and 1.4% of the areal density of AS4/3501-6 prepreg, which is 150 g/m². Akangah et al (2010) made sixteen ply quasi-isotropic test specimens with dimensions 76.2 mm x 76.2 mm. The specimens were impact-tested using a cantilever beam with end-mass and instrumented with accelerometer to measure the impact force. The base and interleaved laminates had a thickness of 2.13 and 2.18 mm, respectively. The impactor was a spherical steel ball with a diameter of 12.7 mm attached to the end-mass. The test section was circular with a diameter of 50.8 mm and boundary condition was assumed to be clamped all around for analysis purposes. The impactor-laminate test section mass ratio was 8. The results showed that interleaving increased the laminate thickness marginally, increased the critical force by 60% and reduced the damage growth rate by more than one half with respect to impact height and force. As a result of the marginal increase in the interleaved laminate's thickness, interleaving will not significantly degrade the laminate's in-plane properties.

An example of particle interleaving is the toughened T800H/3900-2 composite material, which is the first advanced composite material to be certified for aeronautics applications (Hojo et al, 2006). This material system uses a thermosetting resin and contains tough and fine amorphous polyamide particles with a high glass transition temperature dispersed in the base thermosetting resin. A schematic and microscopic photographic cross-section of the material is shown in Figure 1.20 (Hojo et al, 2006). A major drawback of the T800H/3900-2 material system is the increased laminate thickness (~20%), leading to the degradation of in-plane mechanical properties and strength (~15–

20%) (Shivakumar et al, 2009; Takeda, Kobayashi, Ogihara, & Kobayashi, 1999) and the reduction of the glass transition temperature from 195 to 145 °C (Shivakumar et al, 2009). Despite the excellent mode-II interlaminar toughness of T800H/3900-2, the mode-I fracture toughness decreases with increasing crack length (Hojo et al, 2006). This drawback is remedied by using a novel ionomer based thermoplastic resin as the interlayer material. Results for both mode-I and mode-II loading show a steady increase in fracture toughness with increasing interlayer thickness. Figure 1.21 (Matsuda et al, 1999) shows the schematic and microscopic photograph of the Toho Rayon UT500/111/ionomer prepreg.

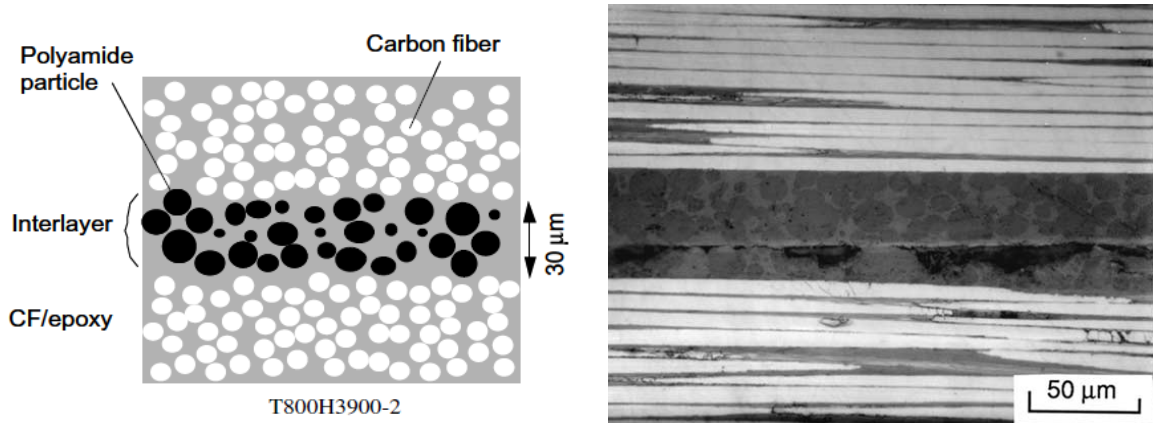


Figure 1.20. Schematic and microscopic photographic cross-section of T800H/3900-2 (Hojo et al, 2006)

It can be observed that the ionomer extends into the fiber epoxy region. The toughening principle is shown Figure 1.22. But, the major issue of increased laminate thickness remained unresolved. In a conventional interleaved CFRP, the toughened

region is limited to the resin-rich layer between any two adjacent layers as shown in Figure 1.22(a). When a crack path deviates from the toughened region, it can be arrested only by the fibers and as a result, the fracture toughness decreased. In the ionomer-interleaved Carbon/Epoxy laminate, because its thickness extends into the fiber-epoxy region, crack path-deviation does not degrade the fracture toughness (Figure 1.22(b)). This is considered a unique advantage of using ionomer interleaving.

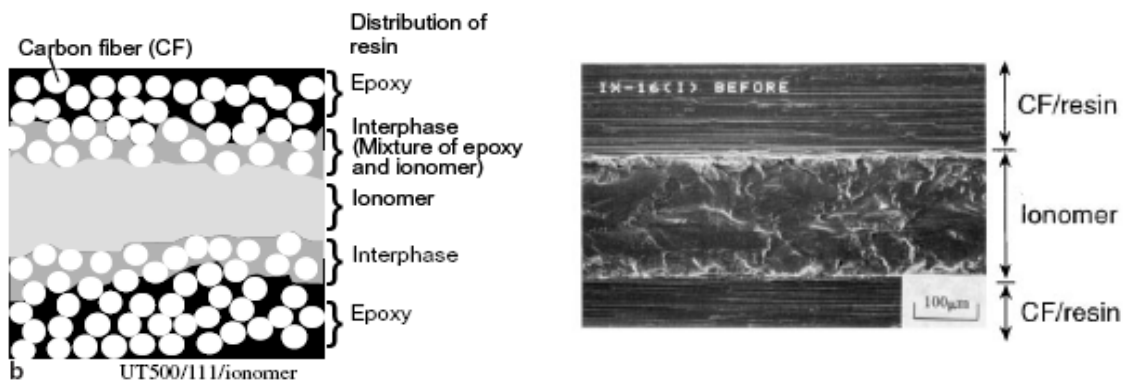


Figure 1.21. Schematic and Scanning Electron Microscope (SEM) micrograph of UT500/111/ionomer laminate (Matsuda et al, 1999)

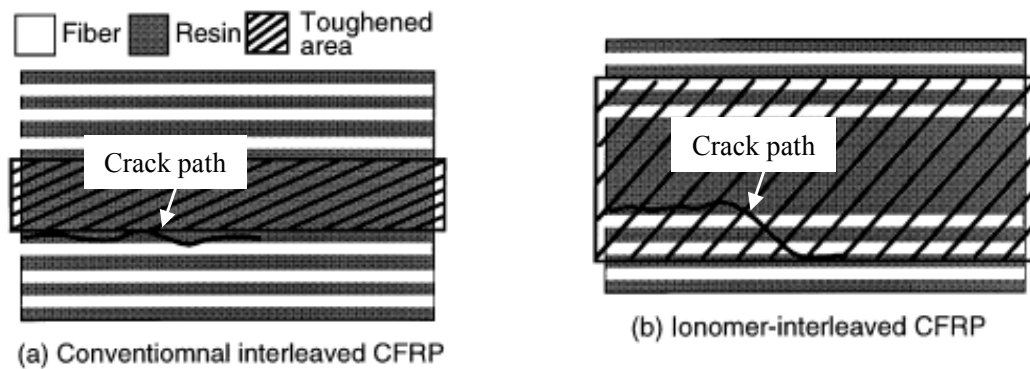


Figure 1.22. Toughening mechanisms for (a) conventional interleaved CFRP and (b) Ionomer-interleaved Carbon/Epoxy (Matsuda et al, 1999)

1.5 Limitations of Current Methods

Many limitations plague the existing methods of improving impact delamination resistance and tolerance. These drawbacks are currently limiting the applications of carbon/epoxy composite laminates and must be seriously addressed. A major drawback of matrix toughening is the adverse effect of hot/wet performance degradation of the composite material leading to increased water pick-up and limited applications in primary structures (Sela & Ishai, 1989). Although, many methods have been successfully used to toughened matrices, improvements in toughening the bulk matrix material are not transferable to the composite material (Masters, 1989; Sela & Ishai, 1989).

A key restriction of the particle or film interleaving and through-the-thickness reinforcement, such as stitching and z-pinning, methods is the loss of in-plane mechanical properties of the laminate because of the increased laminate thickness after interleaving. A number of issues currently plague the manufacturing and use of z-pin technology. These include manufacturing, tooling and labor costs. Other issues such as testing the durability of z-pins under realistic aerospace environment are needed before the technology can be used to its full potential in aerospace applications (Mouritz, 2007). Z-pinning techniques changes the morphology of composite laminates by introducing defects such as resin-rich pockets near the z-pins, high fiber weaving regions etc (Steeves & Fleck, 2006). These defects are capable of introducing complex failure regimes and must be studied in detail. Laminate stitching involves very complicated manufacturing process; the process is also labor intensive involving sophisticated equipment. In addition, stitching is effective only when delamination cracks have developed to a

threshold value of 15 mm or more. A technique that appears to improve impact resistance and tolerance without unduly increasing manufacturing and labor cost and no degradation of in-plane properties is polymer nano-fiber interleaving. This method is pursued in this research.

1.6 The Polymer Nano-fiber Interleaved Concept

The T800H/3900-2 prepreg and its successor, the Toho Rayon UT500/111 are excellent material systems but the bulky interleaved thickness results in loss of in-plane mechanical properties, increased weight and lower glass transition temperature. Any effective solution must significantly reduce the interleaved thickness so that, in-plane mechanical properties are not significantly affected. The concept illustrated in Figure 1.23 is a polymer nano-fiber interleaved for a quasi-isotropic laminate, with stacking sequence $(-45/90/45/0)_{3S}$.

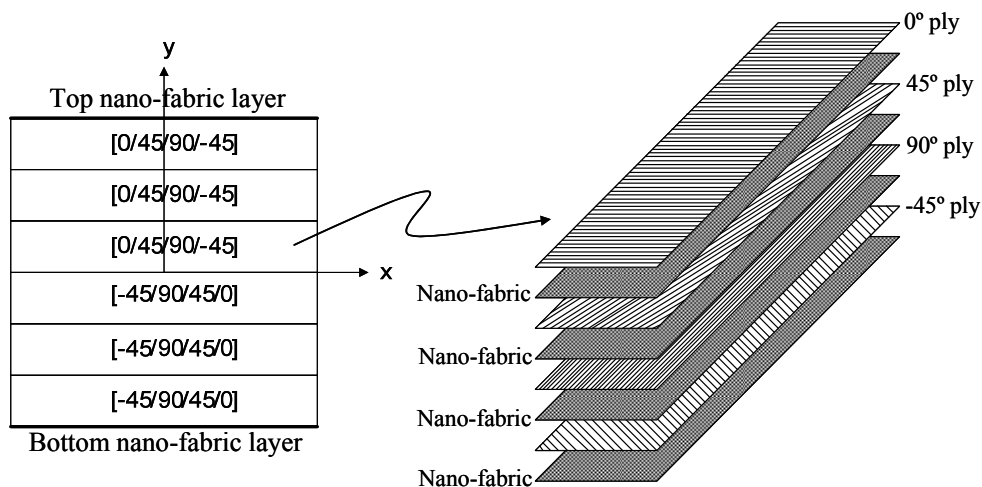


Figure 1.23. Nano-fiber interleaved Concept

The figure shows the complete stacking sequence and a one-sixth block of stacking sequence for the interleaved laminate. Polymer nano-fibers were produced by electrospinning, a method which has been used in the medical field for over six decades. The interleaving material must have excellent adhesion with the base or parent material and must also exhibit high strain to fracture behavior. The proposed concept uses the method of polymer nano-fiber interleaving. The material for making nano-fibers is Nylon-66 and nano-fibers are produced by electrospinning. Nano-fibers have a high specific surface area and a high aspect ratio. Nylon-66 has excellent adhesion to epoxy matrix and high strain to fracture. In this proposed concept, a thin layer of polymer nano-fabric is inserted between plies of composite laminate prepregs. In addition, a layer polymer nano-fabric is appended to the top and bottom of the laminate.

1.7 Goals and Objectives

Because of the desirable qualities of thermoplastic polymer nano-fibers such as very high surface area to mass ratio, excellent ductility and good adhesion with epoxy, it is anticipated that a small amount (1-2 wt%) would offer high impact damage resistance and tolerance. The goals of this research are to determine the relationship between the polymer flow-rate and the electric field, to determine the effect of polymer nano-fiber interleaving on the impact damage resistance and tolerance of AS4/3501-6 composite laminates produced by interleaving. The specific objectives are:

1. To design, build and demonstrate an efficient and automatically controlled electrospinning set-up,
2. To assess the low-velocity impact damage resistance of interleaved quasi-

- isotropic laminates and compare it with the base (non-interleaved) laminates, and,
3. To assess the impact damage tolerance of both the base and the interleaved laminates using compression after impact (CAI) test.

1.8 Scope

This dissertation is in six chapters. Chapter One presents the background to the problem and identifies some key drawbacks of the current methods. It also explains the concept that is expected to address the weaknesses identified and set the scope of the research work. Chapter Two explains the evolution of electrospinning at the Center for Composite Materials Research (CCMR) at the North Carolina A & T State University (NC A&T SU) and the development of a new and improved electrospinning apparatus. A collector-current management approach was used in characterizing the electrospinning process. Chapter Three explains the fabrication of the base and interleaved laminates and the preparation of the test specimens. Non-destructive techniques are used in assessing the external and internal defects of the laminate. Impact testing is presented in Chapter Four. The test specimens and the test matrix are described and the impact testing procedure explained and includes the precautions taken. The results, analysis and discussions are also presented in chapter Four. Chapter Five describes the Compression-after-impact (CAI) test to assess the damage tolerance, the results of the CAI tests and the discussion of the results. Finally, the conclusions and the recommendations are given in Chapter Six along with the suggestions for further work.

CHAPTER 2

ELECTROSPINNING PROCESS AND IMPROVEMENTS

2.1 Introduction

Electrospinning is a technique for spinning polymer nano-fibers in the range of 10 nm to 10 μ m using electrostatic force. The concept was conceived in the medical field and recently found attractive in many fields including polymer composites. This Chapter presents a history of electrospinning developments at the Center for Composite Materials Research (CCMR) at the North Carolina A & T State University (NC A&T SU).

2.2 Electrospinning at CCMR

2.2.1 Stationary Flat Plate Collector

The first basic electrospinning system developed at CCMR in 2004 had a syringe with a needle and a stationary flat plate collector. This basic design was tested and nano-fabrics were prepared for micro-air vehicles (MAV) as part of the Ultra Light Weight Materials Program funded by US Army's ARO MURI. The schematic and photograph of the basic set-up is shown in Figure 2.1. In this design, the syringe pump was mounted on a screw controlled laboratory jack platform and the distance between the collector and needle, D , adjusted by turning the screw. The needle was connected to a high positive DC voltage source and the collector was connected to ground potential. Non-uniform areal density of the fabric limited the application of this basic design.

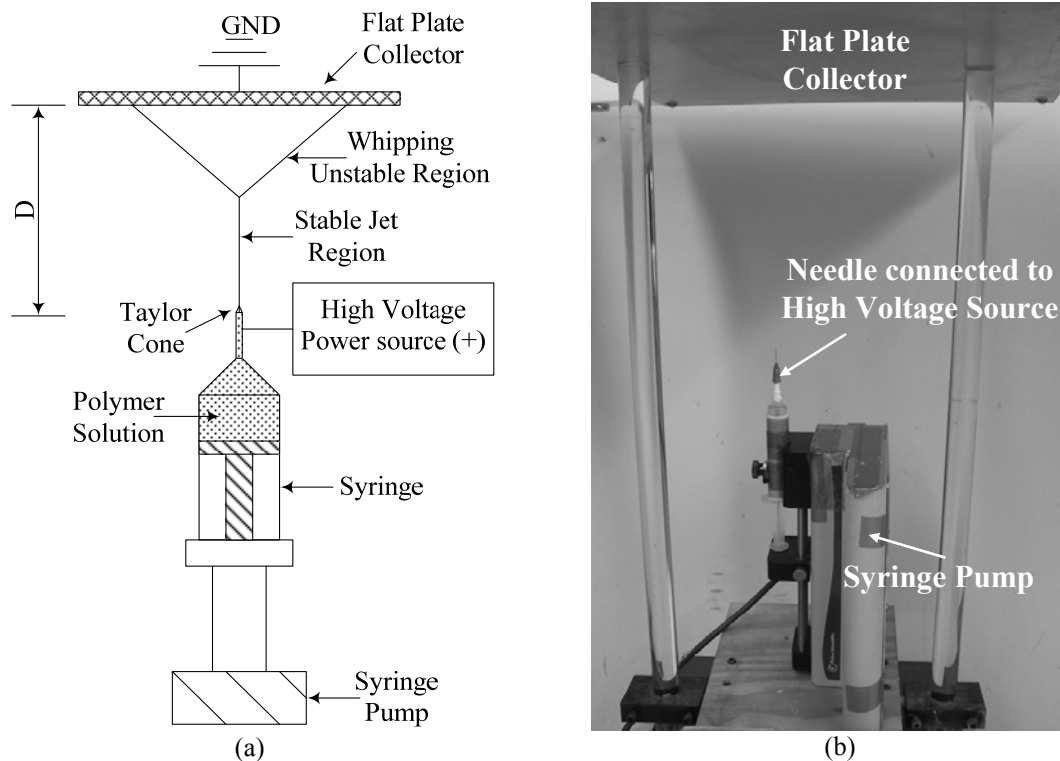


Figure 2.1. Stationary collector electrospinning apparatus. (a) Schematic diagram and (b) Photograph of apparatus

2.2.2 Rotating Drum Set-up

In this design, the stationary plate was replaced by a rotating drum to fabricate continuous fabric. The drum speed was controlled by a pneumatic motor. Some of the major problems of this design were difficulty in maintaining constant rotational speed and preventing fibers from depositing on surfaces other than the drum even when the drum was maintained at a negative voltage and non-uniformity of areal density of the fabric. The schematic and photograph of the rotating drum system is shown in Figures 2.2(a) and (b), respectively (Lingaiah, Shivakumar, Sadler, & Sharpe, 2008).

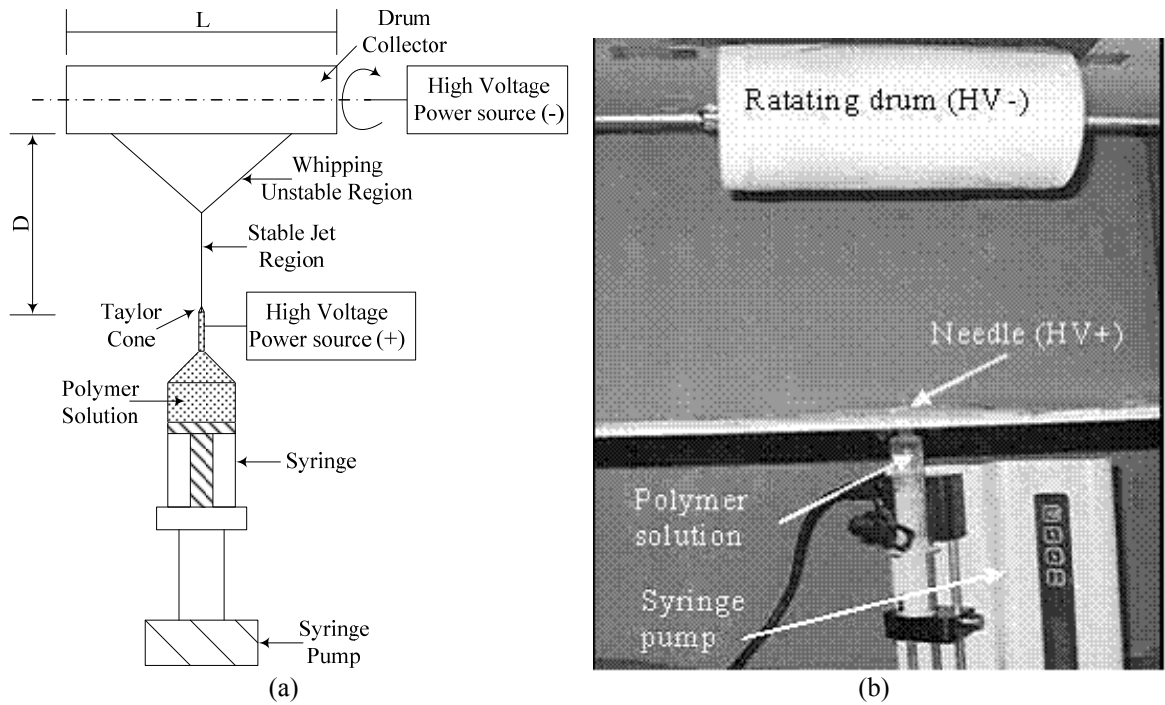


Figure 2.2. Rotating drum electrospinning apparatus. (a) Schematic and (b) Photograph of apparatus (Lingaiah et al, 2008)

2.2.3 Multi-nozzle Electrospinning Set-up

In an attempt to solve the non-uniform areal density of the nano-fabric produced, a multi-nozzle apparatus was developed. It consisted of between two needles to as many needles as needed. The needles are separated by axial distance, D_L , and angular angle (90° for a two needle system). By carefully manipulating the distance D_L between the needles, a limited control of the uniform areal density was achieved. However, a greater number of nozzles and a special arrangement were required to achieve acceptable uniformity. This arrangement was complex. The schematic and photograph of the apparatus is shown in Figures 2.3(a) and (b), respectively (Lingaiah et al, 2008).

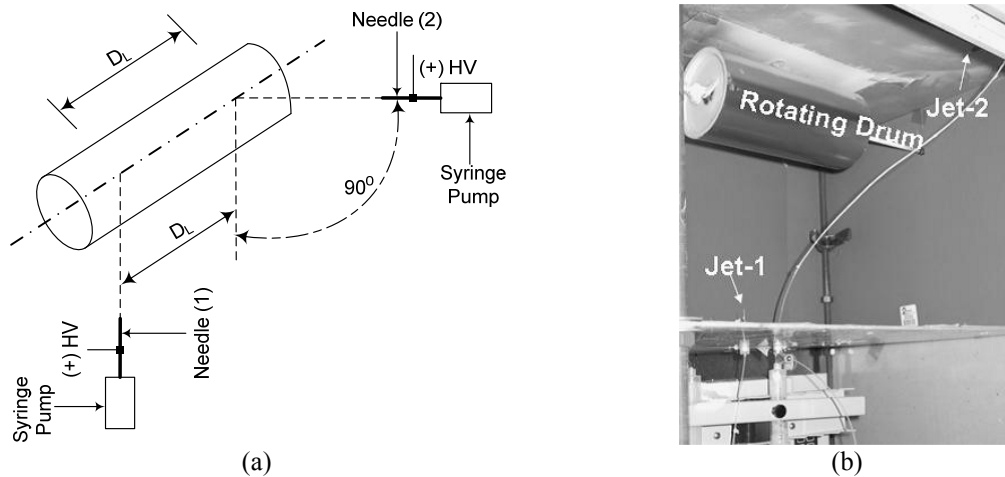


Figure 2.3. Two-needle rotating drum electrospinning set-up. (a) Schematic and (b) Photograph of set-up (Lingaiah et al, 2008)

2.2.4 X-Traversing Electrospinning Set-up

The uniform areal density drawback was practically resolved by using X-traverse mechanism where the needle mounted on this mechanism traversed along the length of the drum. In this design, the pneumatic motor was replaced by a variable speed DC stepper motor. This greatly improved the drum speed control and facilitated the studying of the effect of drum speed on fiber morphology and orientation. The effects of various traverse speeds were also studied. The set-up is shown in Figure 2.4. The key concern of matching flow-rate to electric field remained a major challenge. Repeated electrospinning and SEM imaging were required to adjust the electric field to a predetermined flow-rate. To eliminate this repeated process and to match flow-rate to the electric field, recent studies (Munir, Iskandar, & Khairurrijal, 2008, 2009; Samatham & Kim, 2006; Shin, 2000; Shin, Hohman, Brenner, & Rutledge, 2001; Theron, Zussman & Yarin, 2004; Yan & Gevelber, 2010) were applied to develop an improved electrospinning system.

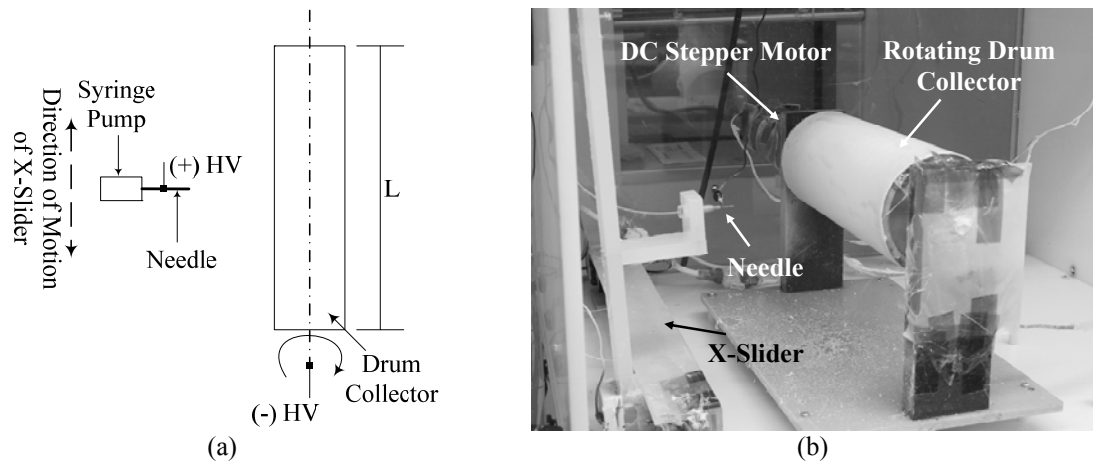


Figure 2.4. X-traversing needle electrospinning set-up. (a) Schematic and (b) Photograph of apparatus

2.3 Development of Improved Electrospinning

2.3.1 Electro-Mechanism of Electrospinning

The electrospinning process balances three forces; the electric field force, the polymer surface tension and the viscoelastic force of the polymer. The jet formed at the tip of the nozzle is of a millimeter-scale while the fiber deposited on the collector is of a nanometer-scale order. Initially, it was thought that splitting of the jet as it traveled from the nozzle to the collector was responsible for the size reduction. However, advanced photographic techniques have shown that whipping jet is responsible for the fiber size reduction as shown in Figure 2.5 (Reneker & Yarin, 2008). For any electric field strength, E^* , there exist a flow-rate, Q , required to maintain a steady Taylor cone (Samatham & Kim, 2006; Theron, et al, 2004). Using this concept, Samatham & Kim (2006) were able to correlate the fiber morphology with the collector current. Figure 2.6 shows this correlation.

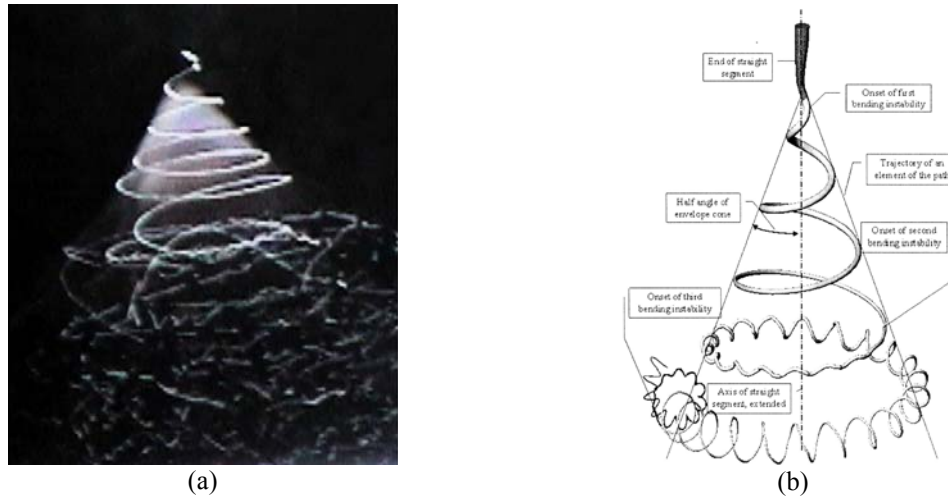


Figure 2.5. Actual electromechanics of fiber formation. (a) Photograph and (b) Schematic of whipping instability (Reneker & Yarin, 2008)

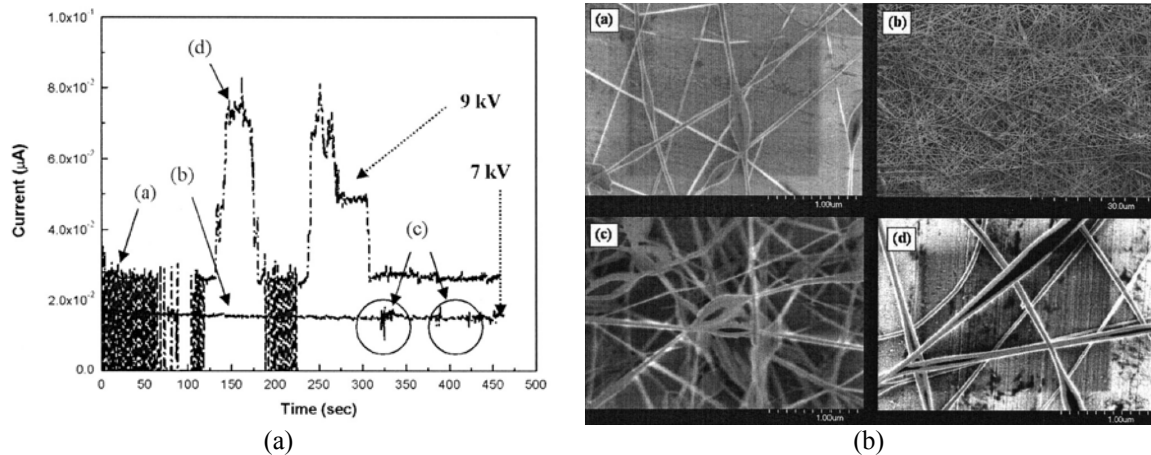


Figure 2.6. Relationship between collector current and fiber morphology. (a) Collector current regimes, and (b) Corresponding fiber morphology (Samatham & Kim, 2006)

Shin et al (2001) demonstrated that whipping instability was initiated when the instantaneous collector current, I , against electric field, E^* , curve changed from linear to non-linear. Yan & Gevelber (2010) showed that the normalized variance of the collector

current, I , was minimized when flow-rate, Q , matched the dynamic jet flow-rate, Q_{jet} , and at this stage, whipping instability was initiated as shown in Figure 2.7.

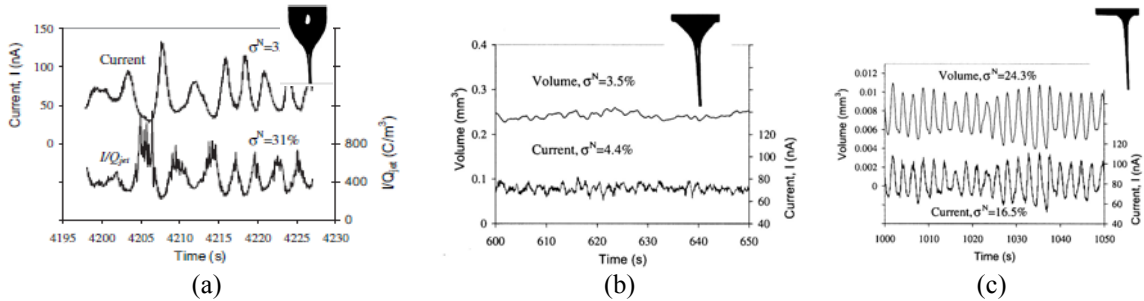


Figure 2.7. Various electrospinning process regimes. (a) Flow-rate (Q) greater than dynamic jet flow-rate (Q_{jet}); (b) Flow-rate (Q) equals to dynamic jet flow-rate (Q_{jet}), and (c) Flow-rate (Q) less than dynamic jet flow-rate (Q_{jet}) (Yan & Gevelber, 2010)

Collector Current is the control variable for controlling the fiber diameter and its uniformity and it depends on the spinning voltage and on environmental parameters such as humidity, temperature and solution properties (Munir et al, 2009). Changes in these parameters result in different collector current profile and as a result, changes in the fiber diameter and morphology. Also, improper mixing of the polymer solution results in the variation of viscosity within the solution and consequently, the fluctuation in the collector current and the poor fiber morphology.

2.3.2 Implementation of Collector Current Management System

To match the electric field to the flow-rate for electrospinning, the collector current management method was used. This involved the following objectives: (a) to develop a model of the relationship between collector current, I , and electric field, E^* , for

various flow-rates, Q ; (b) to determine the onset of whipping instability at various flow rates, Q ; and finally, (c) to determine the operating diagram for the electrospinning process for only the whipping instability part.

2.3.2.1 Materials and Methods

The electrospinning set-up was a flat plate collector that was instrumented with the collector current management system as shown in Figure 2.8. A schematic of the collector current management system is enclosed in broken lines as shown in Figure 2.8. A photograph of the system is shown in Figure 2.9. The electrospinning set-up used 30 gauge needles with an inner diameter of 0.1524 mm (0.006 in), outer diameter of 0.3048 mm (0.012 in) and a length of 12.7 mm (0.5 in). A polymer solution was prepared using Nylon-66 crystals supplied by DuPont Company (Zytel 101, MW = 20,000 g/mol) and a 90% formic acid and chloroform were obtained from Aldrich Co.

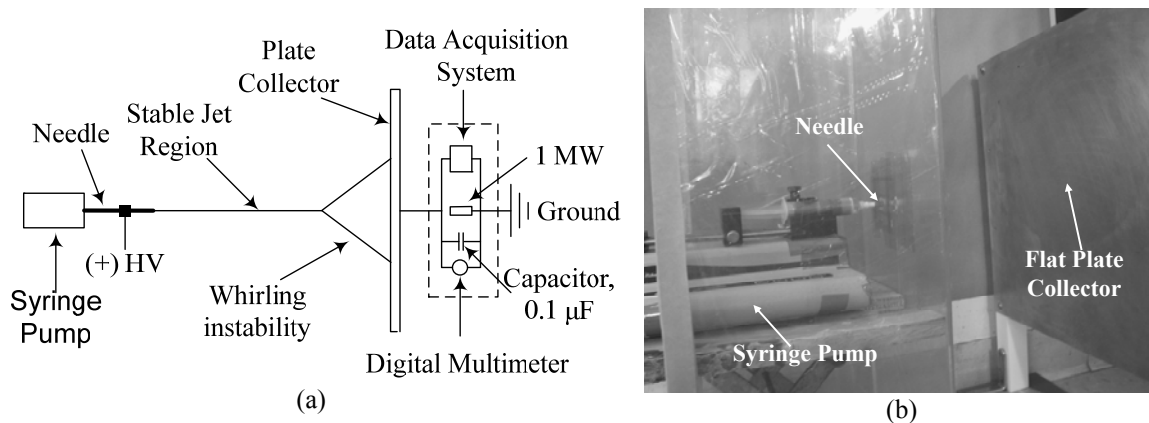


Figure 2.8. Electrospinning with collector current management system to improve spinning. Demonstration on a stationary collector. (a) Schematic and (b) The experimental set-up

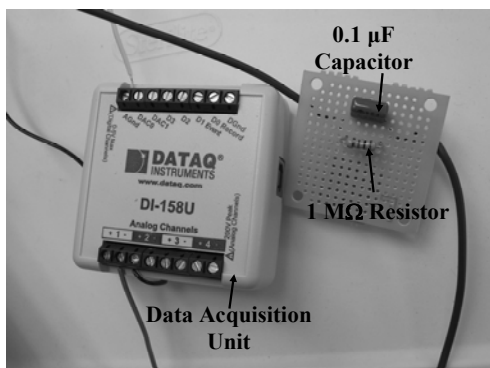


Figure 2.9. Collector current management system components

A 40 g polymer solution with 12 wt% concentration was prepared by dissolving a measured weight of Nylon-66 crystals in a mixture of 90% formic acid and chloroform in a weight ratio of 75/25, respectively. The resulting solution was transferred to a 10 cc syringe fitted with the a 30 gauge needle. Efficient electrospinning requires the solution to be adequately mixed. This was achieved by vigorously mixing the solution using a pneumatic mixer and evacuating the trapped air bubbles in a vacuum chamber maintained at -85 kPa (-25 in-Hg) for 5 minutes. The conductivity and viscosity of the resulting solution were measured using Russell RL060C portable conductivity meter and Brookfield DV-II+ Pro instrument, respectively. The needle was maintained at a high positive potential, which was generated using a high voltage generator of the type FC40R3 with a maximum voltage of 40 kV from Glassman High Voltage Inc. The collector was connected to ground through a 1.0 MΩ resistor and 0.1μF capacitor across which a Digital Multimeter and a USB DI-148U DAQ data acquisition unit were connected. The function of the capacitor is to filter out the 50 Hz signal of the power supply network.

2.3.2.2 Experiment I: Determination of Operating Diagram using the Method of Shin et al (2001)

Electrospinning occurs in an electric field between 1.0-2.0 kV/cm (Yamashitaa, Miyakeb, Higashiyamab, & Tanakaa, 2010). Based on an average electric field of 2.0 kV/cm and a voltage of 36 kV, a stand-off distance of 18 cm was calculated. Tests were conducted with a flow-rate in the range of 0.3-0.9 ml/hr based on previous work (Akangah et al, 2010) using a flat plate collector and the voltage was varied from 9 to 36 kV in steps of 1.8 kV. For each flow-rate, Q , three collector voltage measurements were recorded and the average was calculated. The average collector voltages acquired by the collector current management system were converted into collector currents using Ohm's Law.

2.3.2.3 Results and Discussion (Experiment I)

This study determined the relationship between the collector current, I , and the electric field, E^* , determined the critical electric field for each flow-rate and developed an operating diagram for the range of flow-rate under investigation. Preparation of the polymer solution resulted in a negligible solvent lost of about 0.12% and the average conductivity and viscosity was found to be 2.28 mS and 327 cP, respectively. Figure 2.10 is a plot of the collector current versus the electric field for all three calculated currents for the flow-rate of 0.4 ml/hr. The average values are plotted in Figure 2.11. This study found that the curves were divided into linear and non-linear parts as observed by Shin et al (2001). The researchers established that whipping instability begun when the slope of the curve changed from linear to nonlinear. For the case of a flow-rate of 0.4 ml/hr, the two regions were approximated by straight lines as shown Figure 2.11. At the intersection

of these lines, the critical electric field was obtained by dropping a vertical line from the point of intersection to the electric field axis and reading the value of the electric field and this was found to be approximately 1.5 kV/cm for the 0.4 ml/hr flow-rate. Figure 2.12 shows the average collector currents for the range of flow-rates investigated. Critical electric fields, E_c^* , at the start of whipping for each flow-rate were extracted and plotted as a function of the flow-rate (Q) as shown in Figure 2.13. The figure describes the operating diagram of the electrospinning process in the whipping instability regime using the method of Shin et al (2001). The best fit to the data was a power curve in the form $E_c^* = 2Q^{0.3}$. The critical electric field describes by this equation is the minimum field for efficient electrospinning. To ensure that no beads are formed, it is recommended to operate above this minimum value. At flow-rates above 0.7 ml/hr, no discernible Taylor cone was formed at the maximum value of the high voltage generator.

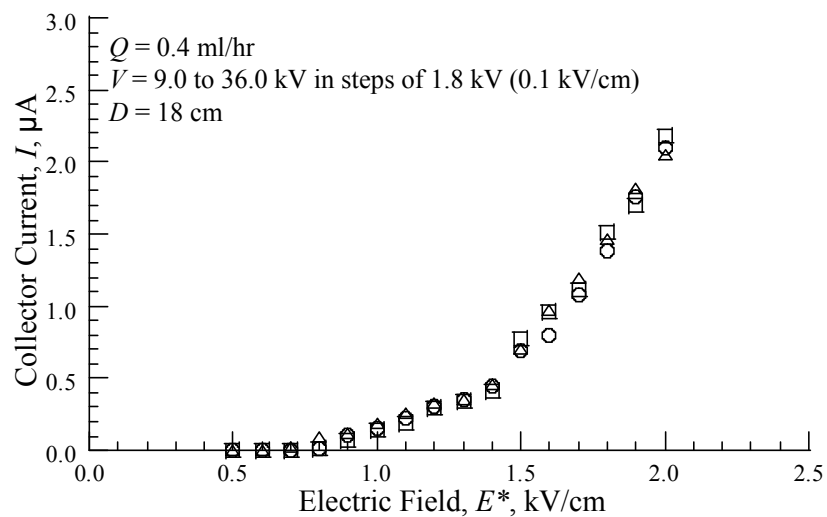


Figure 2.10. Plot of collector current, I , versus electric field, E^* , for Nylon-66 (12 wt% concentration) showing all three repeated tests at 0.4 ml/hr

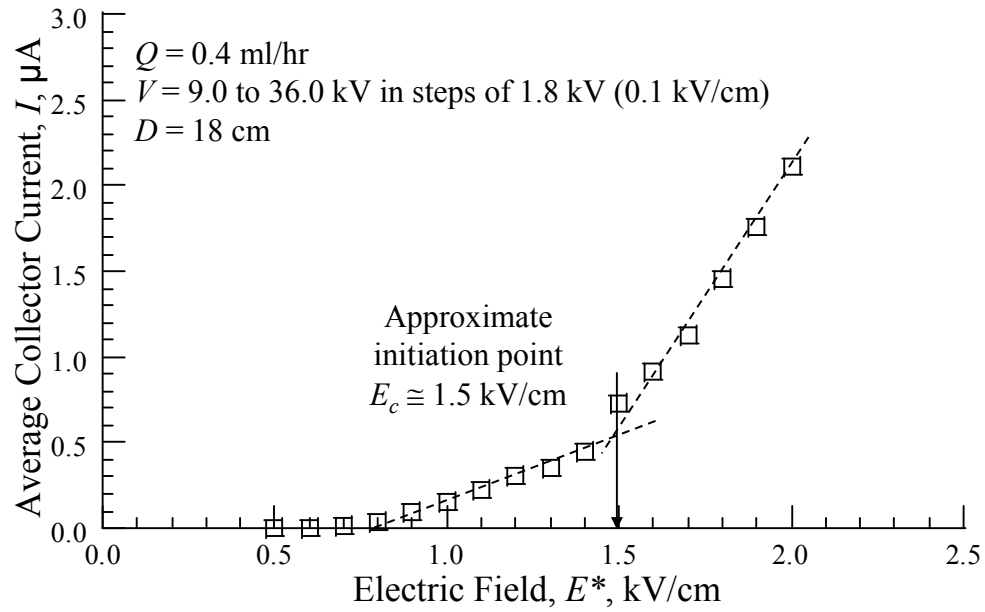


Figure 2.11. Plot of averaged current, I , versus electric field, E^* , for Nylon-66 (12 wt% concentration) at 0.4 ml/hr

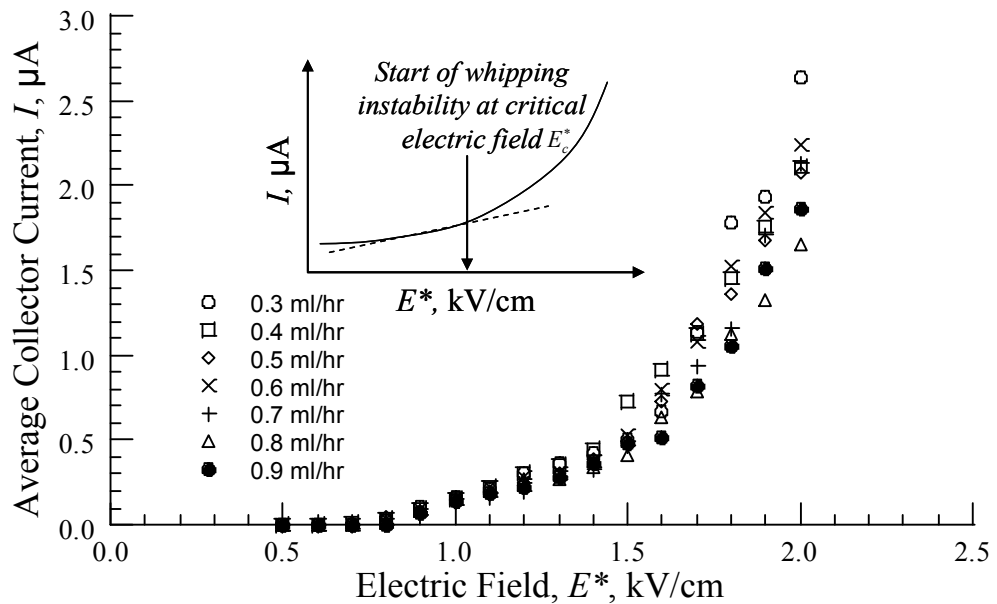


Figure 2.12. Plot of average collector current, I , versus electric field, E^* , for Nylon-66 (12 wt% concentration) solution. The insert shows idealized I - E^* curve

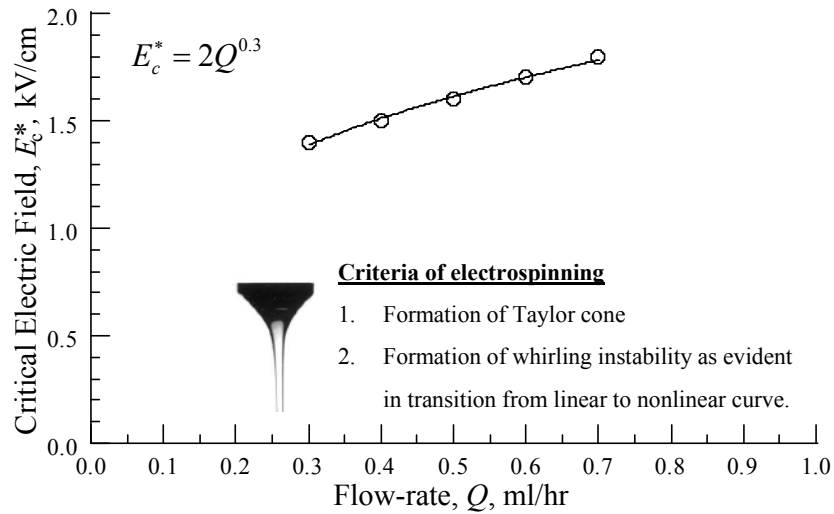


Figure 2.13. Plot of critical electric field versus flow-rate Q using the method of Shin et al (2001)

2.3.2.4 Experiment II: Determination of Operating Diagram using the Method of Yan & Gevelber (2010)

In this experiment, 0.3-0.7 ml/hr flow-rates were selected and the fibers were electrospun using the same flat plate electrospinning set-up shown in Figure 2.8. At the start of the experiment, a flow rate of 0.3 ml/hr was chosen and the voltage was varied from 9 to 36 kV in steps of 1.8 kV. At each voltage, the collector voltages, V_s , were acquired using the data acquisition unit connected to a PC by sampling the data at the rate of 10 Hz. Data were collected for a period of two minutes and during this period, a total of 1,200 data points were collected at each spinning voltage. Data were collected for the range of flow-rate under investigation. The experiments were repeated for two additional times at each flow-rate.

For each flow-rate, Q , the collector current standard deviation at each voltage from 9 to 36 kV was calculated for the 1,200 data points. The voltages corresponding to

the least collector current standard deviations at each flow-rate were the critical spinning voltages. The critical electric field was obtained by dividing the critical voltage by the distance, D .

2.3.2.5 Results and Discussion (Experiment II)

A total of fifteen critical spinning electric field results were obtained and recorded in Table 2.1. The operating diagram for the whipping instability part of the electrospinning process is shown in Figure 2.14 and the best fit to the experimental data is a power law curve with the form $E_c^* = 2Q^{0.25}$. Comparing both methods as in Figure 2.15, it can be seen that there are some differences between the two methods, although, both results are described by power law equations.

Table 2.1. Experimental results to determine the onset of whipping instability

Flow Rate, Q , ml/hr	Critical Spinning Voltage, V_c , kV	Critical Electric Field, $E_c^* = \frac{V_c}{D}$, kV/cm
0.3	28.8	1.51
	28.6	1.50
	28.2	1.50
0.4	32.4	1.68
	31.8	1.64
	32.4	1.68
0.5	32.0	1.70
	31.6	1.73
	32.0	1.69
0.6	33.2	1.82
	33.8	1.79
	32.6	1.81
0.7	35.0	1.87
	35.0	1.87
	34.4	1.89

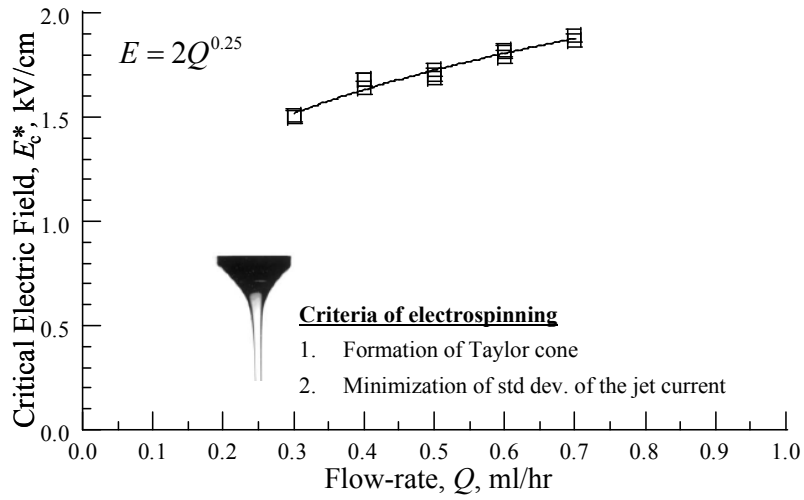


Figure 2.14. Plot of critical electric field versus flow-rate Q using the method proposed by Yan & Gevelber (2010)

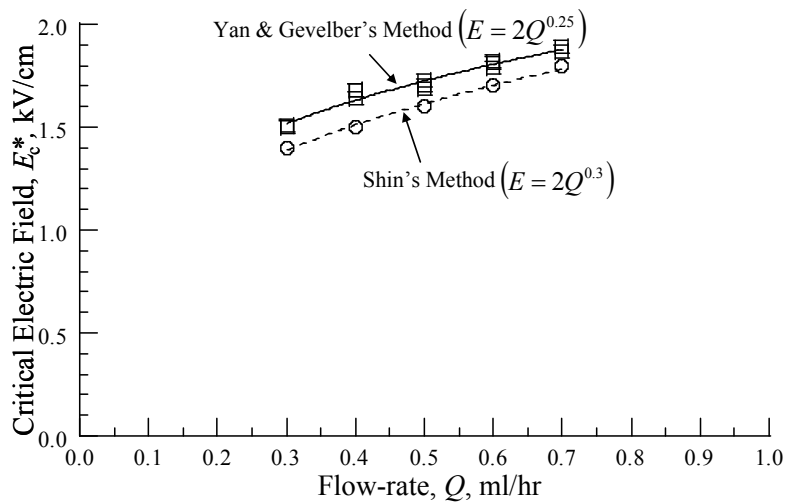


Figure 2.15. Comparison of both methods for determining operating diagram

The reference environmental conditions under which these tests were conducted were within the range, 24 ± 2 °C and $50 \pm 5\%$, for temperature and relative humidity, respectively. These conditions were not optimized because it was outside the scope of

this present work. However, as environmental conditions could affect the morphology of the fibers and in extreme cases (high RH%), fibers may not be formed at all (De Vrieze et al, 2009). It is important to determine these optimum values for the electrospinning of Nylon-66 12 wt% solution.

2.3.2.6 SEM Analysis to Determine Fiber Morphology

SEM analysis was used to determine the effect of matching the flow-rate to the electric field on the fiber morphology. Two square fabrics measuring approximately 5 mm were cut from each specimen to represent the left and right fabrics. A total of ten such specimens were cut. Each specimen was mounted on specimen stub and held in place with a carbon tape. The specimens were first coated with Au/Pd film for 200 seconds using Desk IV Vacuum Sputter System prior to SEM analysis. SEM equipment type FEI XL30 was used for this analysis. Image-J software was used to analyze the SEM images and the typical results are showed in Figure 2.16 for 0.4 ml/hr flow-rate.

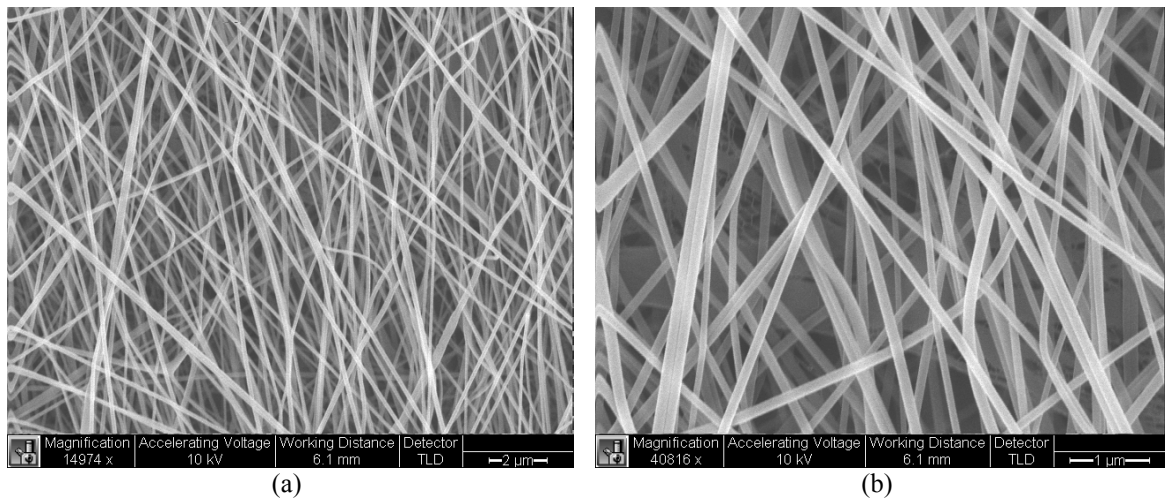


Figure 2.16. SEM micrograph of fiber morphology obtained at 0.4 ml/hr at (a) ~ 15k and (b) 40k resolutions

The results showed that the minimum fiber diameters occurred at 0.4 ml/hr flow-rate with the fiber diameters ranging from 80 to 160 nm. Therefore, the best possible electrospinning parameters were 0.4 ml/hr flow-rate; 12 wt% concentration of Nylon-66; 30 gauge needle (0.1524 mm inner diameter) and an average electric field of 1.67 kV/cm. Figure 2.16 showed the SEM micrograph at a flow-rate of 0.4 ml/hr.

2.3.2.7 Generalization of Results

The general form of the equation can be cast in the form, $E_c^* = A_0 Q^k$, where for Nylon-66 (12 wt%), $A_0 = 2$ and $k = 0.25-0.30$. Different polymers will have different A_0 constants and depending on the conductivity and viscosity of the solution, the index will be different. Accurate determination of these constants depends on the method used. Since the transition from the linear to the non-linear form occurs over a wide range (Shin, 2000), accurately determining these constants using Shin's method can be difficult. The method proposed by Yan & Gevelber (2010) had a better fidelity. A major disadvantage with this method is the need for a starting critical electric field around which to conduct the experiment. In the absence of such an approximate electric field, the data may become massive and perhaps unyielding. The approach adopted here was to use Shin's method to get that approximate value and refine it using Yan & Gevelber's method.

2.4 Size Scale-up and Description of Equipment

A large drum size was required to make nano-fabric for the large laminate size needed. Previous work on electrospinning (Lingaiah et al, 2008) using rotating drum of radius of 57 mm (2.25 in) and a rotating speed of 250 rpm (corresponding to a linear

speed of 1.5 m/s) resulted in random fibers with diameters ranging from 75 to 250 nm, for a single-nozzle electrospinning set-up. In this present study, the drum had a radius of 146 mm (5.75 in). Since approximately the same linear speed was desired, the linear speeds were matched and the rotating speed for the scaled-up system was found to be 98 rpm.

Figure 2.17 shows the photograph of the scaled-up rotating drum electrospinning system. The enclosure measured 914 mm x 1,220 mm x 1,830 mm (36 in x 48 in x 72 in) and was assembled using aluminum TSLOTS. The electrospinning apparatus was equipped with a 250 CFM high efficiency filter system. This was connected to a variable AC transformer to regulate the motor speed and the air-flow velocity in the chamber. At the other end was an extraction tube connected to an extraction hood where the harmful polymer solution vapors were safely extracted from the chamber. The system was equipped with two KDS 100 syringe pump that were independently controlled.

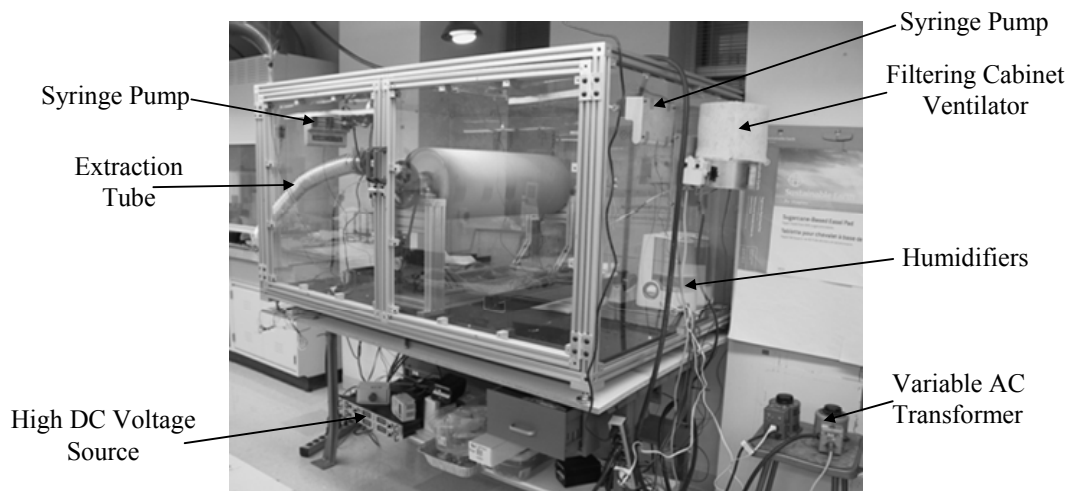


Figure 2.17. Photograph of rotating drum electrospinning system

Each syringe pump was equipped with a 10 ml syringe fitted with 30 gauge needle that was maintained at a high positive DC voltage and independently powered using Glassman's High Voltage Power supply of the type FX40R3 with maximum reversible voltage of 40 kV. Each needle was mounted on a Teflon pole driven by a Velmex Xslide XN10-0300-E2-21 equipped with a Vexta Type 23T1 single shaft stepper motor which was controlled by a VXM-1J step motor controller. The traverse speed of the Xslides was programmed to be 12 mm/s (0.47 in/s) and the Xslides were started while they were in opposite directions so that they were always out-of-phase. Two humidifiers were mounted inside the enclosure to maintain humidity, especially during the winter period. At full capacity, the steam mass flow-rate was measured to be about 0.3 kg/hr. Figure 2.18 clearly shows the Xslide and the humidifiers in the background.

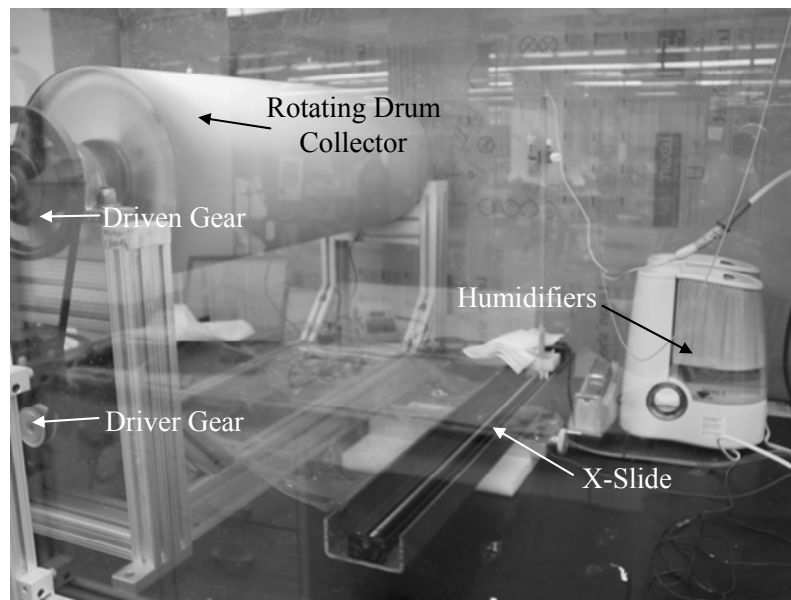


Figure 2.18. Electrospinning set-up during spinning operation. Velmex Xslide and humidifier clearly seen in the background

The chamber environmental conditions were monitored by means of an electronic sensor and outputted on a computer screen using USB connection. The drum was mounted on a TSLOT stand and connected to a motor by means of a 4:1 reduction gear driven by a toothed belt to avoid slippage. The drum motor was controlled by a BFL6200A-5 brushless speed control system to regulate the drum speed. The drum collector was connected to a 1.0 M Ω resistor and 0.1 μ F capacitor across which a data acquisition unit was connected. The data acquisition system was a USB DI-148U USB DAQ unit and the collector voltage was monitored using PC based software that was supplied with the DAQ unit. Figure 2.19 shows the schematic of the rotating drum electrospinning set-up, with two spinning systems, instrumented with the collector current management system. This setup was used to validate the characterization experiment and also to fabricate the nano-fabric for interleaving.

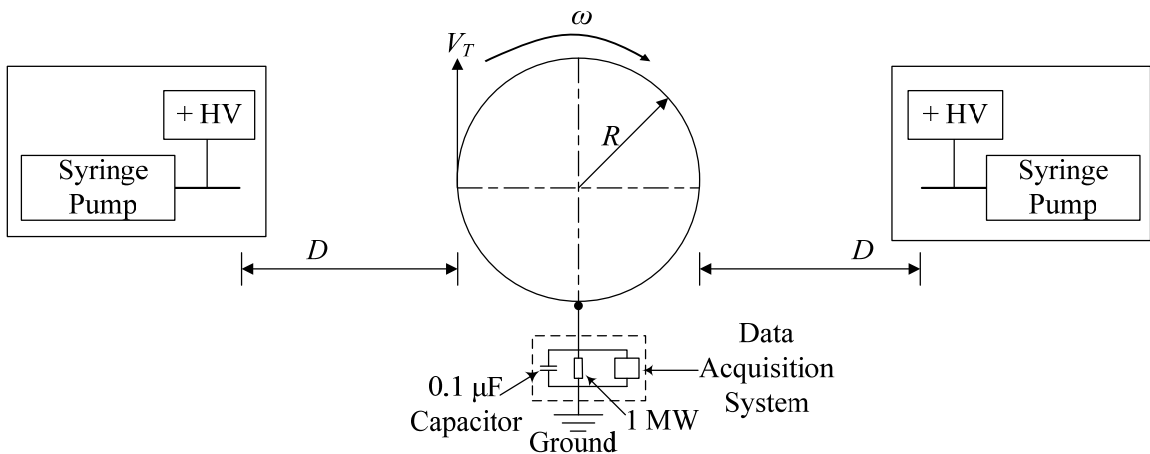


Figure 2.19. Schematic of two needle rotating drum electrospinning system

2.5 Results of Performance Evaluation

2.5.1 Processing Parameter Selection

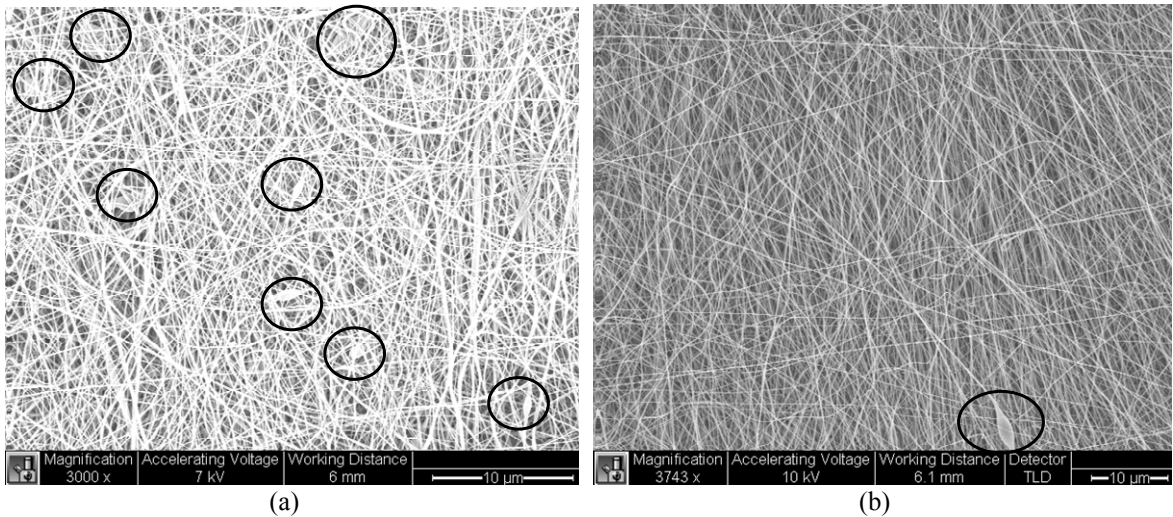
To determine the performance of the new and improved drums electrospinning system, the nano-fibers were produced based on the parameters identified in section 2.3. The performance matrices were the number of beads, electrospinning yield, fiber diameter and range. These metrics were compared to that of the original drum electrospinning system. The parameters used in making the nano-fibers are tabulated in Table 2.2. In the example 2, the distance was fixed at 15 cm. An electric field step size of 0.1 kV/cm was chosen to correspond to a spinning voltage step size of 1.5 kV. Starting from a voltage of 20 kV, the spinning voltage was varied until a spinning voltage of 26 kV, the critical spinning voltage, was reached. This resulted in a critical electric field of 1.7 kV/cm. The nano-fibers made were analyzed using the SEM and the diameters were measured using Image-J software.

Table 2.2. Processing parameters for original and present method

Processing Parameters	Original Method (Lingaiah et al, 2008)	Present Method	
		Example 1	Example 2
Voltage, kV	30.0	36.0	26.0
Distance, cm	20.3	21.5	15.0
Critical Electric Field, kV/cm	-	1.7	1.7
Time, hours	2.0	4.0	4.0
Flow-rate, ml/hr	1.0	0.4	0.4
# of needles	1	2	2
Traverse Length, mm	305.0	762.0	762.0

2.5.2 SEM Analysis

Ten images were taken from each specimen at different resolutions ranging from 500 nm to 20 μm . For each specimen, the minimum and maximum fiber diameters were measured, using Image-J software. SEM results in Figures 2.20 and 2.21 show that the range of fiber diameters for the original method was 85-180 nm and for the new and improved system, the range was 60-125 nm. In addition, eight beads were detected in the fabric made by the original system but only one bead was detected in fabric made by the present study. Figure 2.22 shows the SEM micrograph for example 2. Three beads were observed and fiber diameters ranged from 70-130 nm.



**Figure 2.20. SEM micrograph of nano-fabrics showing beads (circled).
(a) Original system, and (b) New and improved system (example 1)**

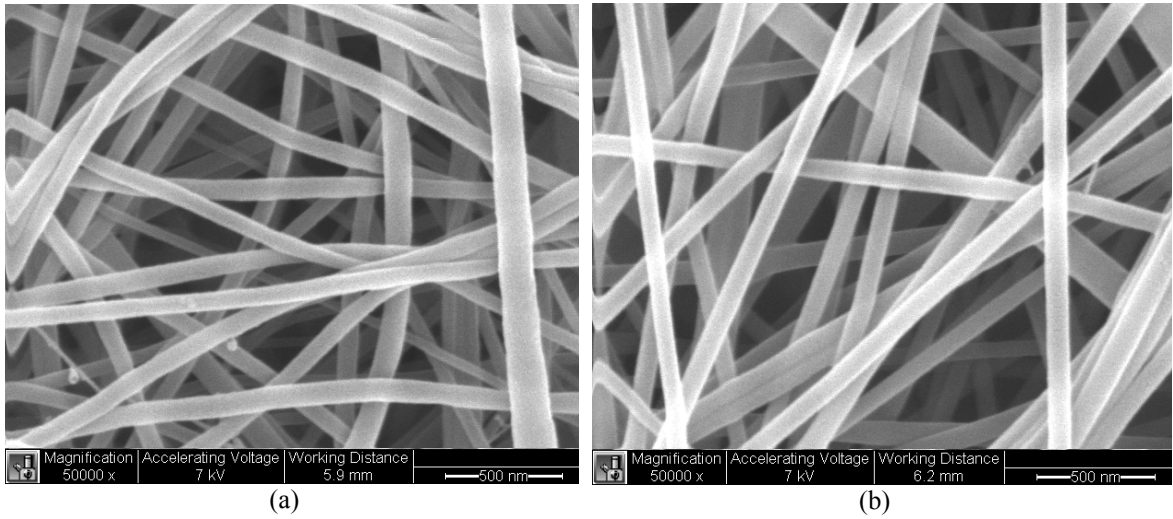


Figure 2.21. SEM micrographs of nano-fabric at 50k resolution. (a) Original system with fiber diameter range 85-180 nm and (b) New and improved system with fiber diameter range 60-125 nm (example 1)

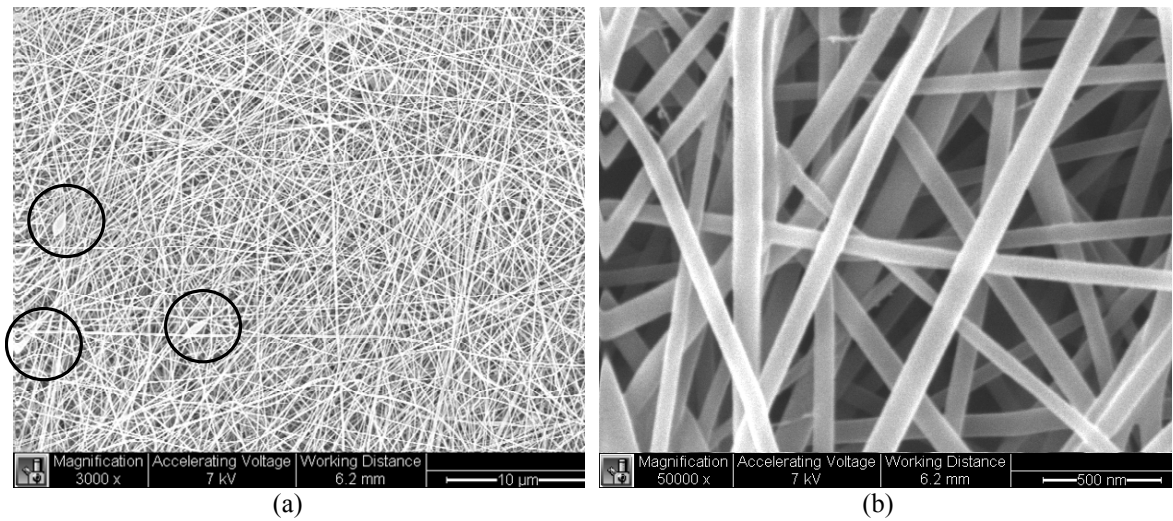


Figure 2.22. SEM micrographs of nano-fabric made by the new and improved system at $V = 26$ kV, $D = 15$ cm (example 2). (a) Micrograph at 3k resolution, and (b) Micrograph at 50k resolution

2.5.3 Electrospinning Yield

To calculate the yield, the areal density of the fabric was first determined. The schematic of peeling off the nano-fabric from the drum and strip dimensions are shown in Figure 2.23. The sample size for areal density determination is calculated using Equation (2.1) (Lipson & Sheth, 1973).

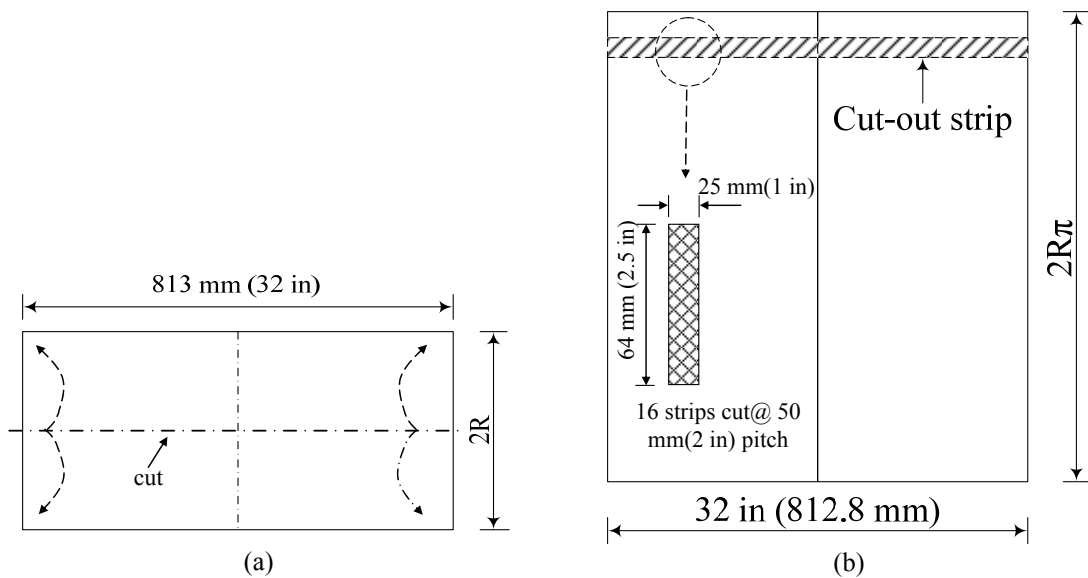


Figure 2.23. Removal of electrospun nano-fabric from rotating drum. (a) Schematic of cutting line and (b) Schematic of cut nano-fabric

$$R_c = (1 - C)^{1/(NN+1)} \quad (2.1)$$

where R_c is the reliability at confidence level C and NN is the sample size. For most engineering applications, $C = 0.95$. A plot of R_c versus NN is shown in Figure 2.24. At a reliability of 0.82, 16 sample size of strips was chosen. Sixteen strips of 25.4 mm (1.0 in) in width and 64 mm (2.5 in) in height were cut from randomly selected fabric. A pitch

distance of 51 mm (2 in) was maintained between the centerlines of consecutive strips.

The areal density is calculated using Equations (2.2).

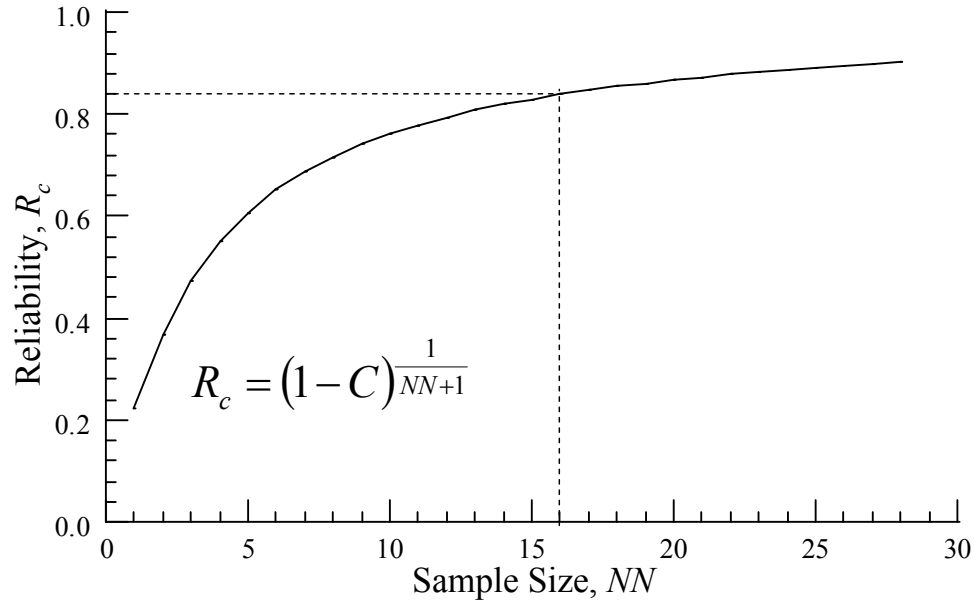


Figure 2.24. Determination of number of sample, for a reliability of 82% and a confidence level (C) of 95%

$$\text{Areal density (g/m}^2\text{)} = \frac{\text{Weight of fabric (g)}}{\text{Length (m) x Width (m)}} \quad (2.2)$$

The mass of the fabric in grams was determined by cutting and weighing a sample strip measuring *width* of 25 mm (1.0 in) and *length* of 64 mm (2.5 in) from randomly selected fabrics. The sample average areal density distribution along the length of the rotating drum is shown in Figure 2.25.

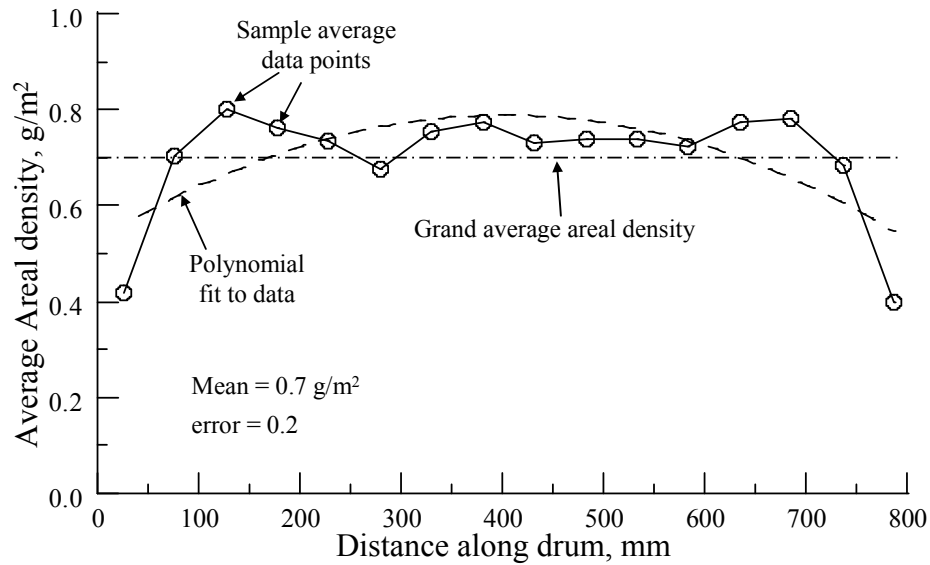


Figure 2.25. Distribution of areal density along length of rotating drum

A curve was drawn through the sample average data points and polynomial curve was fitted to the sample average data points. The grand average areal density and standard deviation (S.D) of the nano-fabrics were calculated based on the average data points of the strips and found to be 0.7 g/m^2 and 0.1 , respectively. The experimental error is equal to $\text{S.D} * t_{\frac{\alpha}{2}, \nu-1}$. Where $t_{\frac{\alpha}{2}}$ is the two-tail student t distribution, $(1-\alpha)$ is the confidence interval and ν is the degree of freedom (dof). At a confidence co-efficient of 95% and 16 dof, experimental error = 0.2 . Summary of the results are tabulated in Table 2.3.

The electrospinning yield is given by Equation (2.3).

$$Y = \frac{\text{Areal Density} * \text{Area}}{\# \text{Needles} * \text{hr}} \left[\frac{\text{g}}{\text{hr}} \right] \quad (2.3)$$

where *areal density* is the grand average areal density, g/m^2 ; *area* is the nano-fabric surface area ($2\pi RL_T$), m^2 ; *#needles* is the number of needles used for electrospinning; *hr* is the electrospinning duration measured in hours; L_T is the traverse length and R is the drum radius.

Table 2.3. Summary of physical properties of electrospun nano-fibers

Results	Original Method (Lingaiah, et al, 2008)	Present Method	
		Example 1	Example 2
Areal Density, g/m^2	0.96	0.70	0.85
Yield, Y , g/hr	0.05	0.06	0.07
Diameter Range, nm	85-180	60-125	70-130
# of Beads	8	1	3

2.6 Summary

A collector current management system that matched the flow to the electric field was implemented and the operating diagram for the electrospinning of Nylon-66 was developed. The critical electric field ranged from 1.6 to 1.7 kV/cm and the minimum electrospinning distance was obtained to be 21.5 cm at a flow-rate of 0.4 ml/hr . A scaled-up rotating drum electrospinning system was designed, built and its operations were verified. The performance of the original system was compared to the one developed in this study. Fiber diameters of the fabric from the original and present system ranged from 85 to 180 nm and from 65 to 125, respectively. The number of beads reduced from 8 to 1. The average areal density for the original and present study was 0.96 and 0.70 g/m^2 , respectively. Based on this areal density, the electrospinning throughput was respectively,

0.05 and 0.06 g/h for the original and present study. Optimization of the electrospinning environmental conditions was outside the scope of this work. However, the temperature was maintained within the stated range of: 24 ± 2 °C and the relative humidity range was: $50 \pm 5\%$.

CHAPTER 3

LAMINATES FABRICATION AND SPECIMENS PREPARATION

3.1 Introduction

This chapter describes the fabrication of the laminates and the preparation of specimens for impact and subsequent compression after impact (CAI) tests. The autoclave method and the prepreg supplier's recommended specifications were used to fabricate laminate panels. A number of precautions were taken to ensure safety, proper ply orientation and stacking sequence of the laminate. The laminate quality was visually inspected, c-scanned, and the thickness was measured. The laminates were carefully cut into test specimens of required size.

3.2 Material Systems

Aerospace grade AS4/3501-6 prepreg supplied by Hexcel Composites was chosen for this work. The material was supplied as a roll of prepreg tape of epoxy matrix (3501-6) reinforced with continuous unidirectional carbon fibers (AS4). The roll measured 1,230 mm (48.5 in) in width and was stored in a freezer at a temperature of -23 °C (-10 °F). It was thawed overnight at room temperature in a plastic bag before cutting them into 355 mm x 762 mm (14 in x 30 in) sized plies with orientations of -45°, 90°, 45°, and 0° with respect to fiber directions..

The electrospinning parameters identified in Chapter 2 were used to make the nano-fabric sheets. The parameters used in electrospinning were, a flow-rate of 0.4 ml/hr,

12 wt% concentration, gauge 30 needle with inner diameter of 0.1524 mm (0.006 in), and an average critical electric field ranging from 1.6 to 1.7 kV/cm. The range of environmental parameters maintained in the chamber during electrospinning was relative humidity between 45 and 55% and temperature between 22 and 26 °C. The rotating drum collector linear speed was set at 1.5 m/s. In all, 38 pieces fabrics were made. An SEM micrograph of the nano-fabric used for interleaving is shown in Figure 3.1.

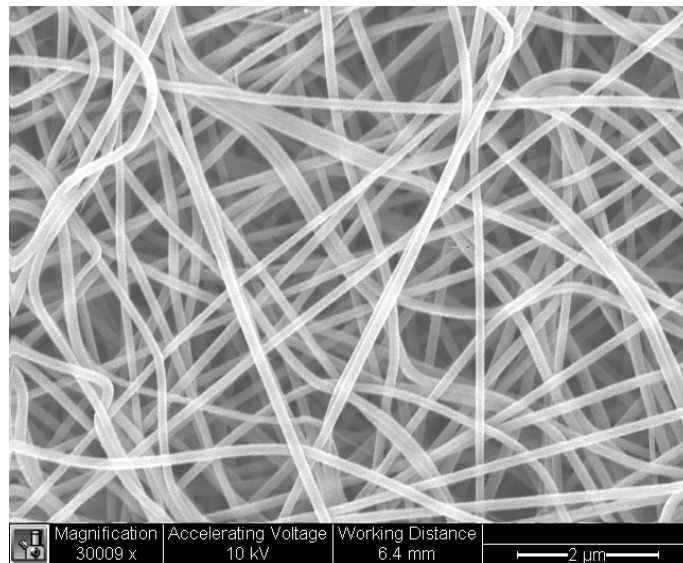


Figure 3.1. SEM micrograph of nano-fibers used for interleaving

The complete stacking sequence of the laminate with a one-sixth block are shown in Figures 3.2 and 3.3 for both the base and interleaved laminates, respectively. The interleaved laminates were made by placing one layer of nano-fabric in between two consecutive prepreg layers. In addition, a layer of nano-fabric was also placed on the top and bottom of the laminate.

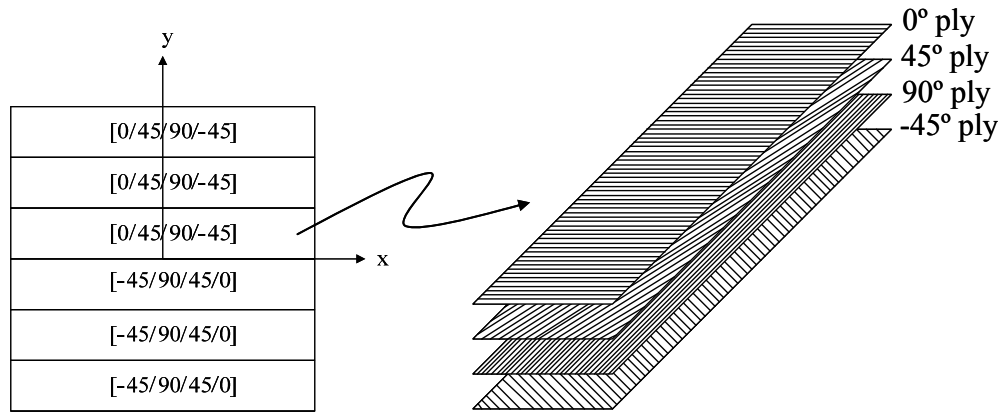


Figure 3.2. Schematic of base laminate layout

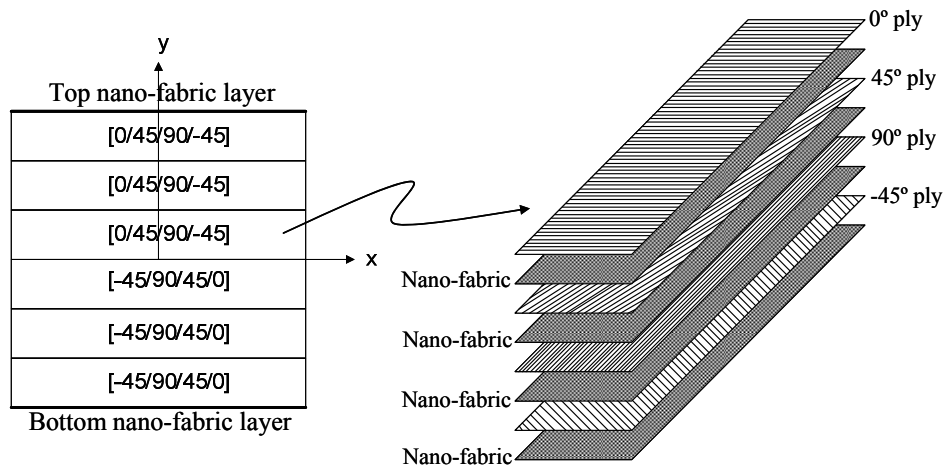


Figure 3.3. Schematic of interleaved laminate layout

3.3 Fabrication of Base and Interleaved Laminates

Fabrication of quasi-isotropic laminate consisted of the following procedures: prepreg cutting, stacking, debulking, and molding. Each of these steps is explained below. Most of the processes are similar for both the base and the interleaved laminates.

3.3.1 Prepreg Cutting Process

To ensure proper control of fiber alignment, a plastic triangle template was used to align a previously prepared rectangular plastic template on the prepreg as shown in Figure 3.4. This rectangular template measuring 325 x 762 mm was used to cut the plies for the laminate. Figure 3.4 shows how -45° ply is cut using this procedure. In total, 128 plies were cut consisting of 32 plies each for 0° , 45° , -45° and 90° ply orientations.

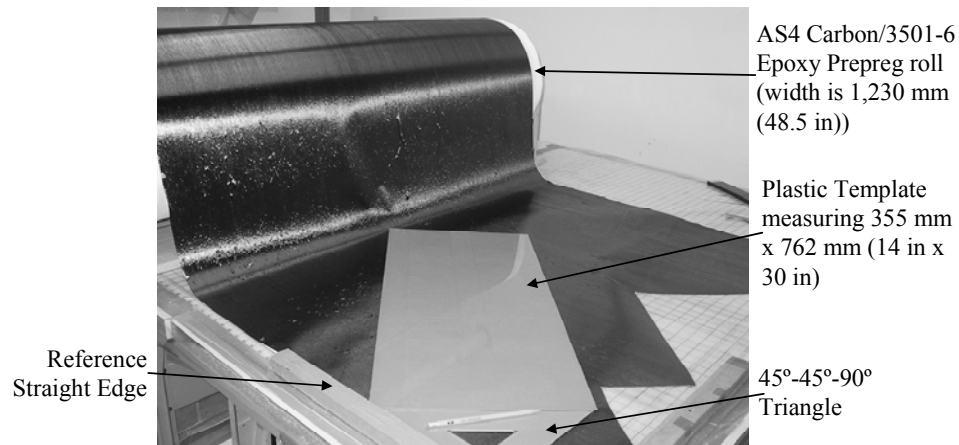


Figure 3.4. Prepreg cutting from a roll for $0/\pm 45/90$ layers; example of -45° ply

3.3.2 Stacking and Debulking

Prepregs were stacked as explained in Section 3.2. The debulking procedure was performed as follows. Prior to debulking, a mold was prepared. A suitable-sized bottom Teflon sheet was secured to the previously cleaned surface of the mold. A double-sided tape was applied along the top and bottom length-wise of the reference straight edge. The reference edge was then aligned with the edge of the bottom Teflon film allowing about 12.7 mm (0.5 in) space between the edge of the tape and the perimeter of the mold. A

silicon rubber dam was installed over the mold's vacuum port with a double-sided tape. A double thick pad of polyester breather was secured in place with flash tape to cover the hole in the rubber dam and a suitable-sized Teflon sheet was attached to the breather. A mastic sealant tape was applied to the perimeter of the mold plate and away from the bottom Teflon film. The purpose of the Teflon film was to aid in the evacuation of air from the prepreg layers. After removing the backing paper from the mastic sealant tape, a suitable sized bagging film was gently tacked to the top of the exposed mastic sealant tape and trimmed.

The previously stacked prepreg was placed between the two Teflon films and pressed against a reference straight edge. After sealing the bagging film, a vacuum was applied and the prepreg layers debulked until the vacuum stabilized at about 101.6 kPa (30 in-Hg) for two minutes. The picture in Figure 3.5 shows the debulked prepreg layers.

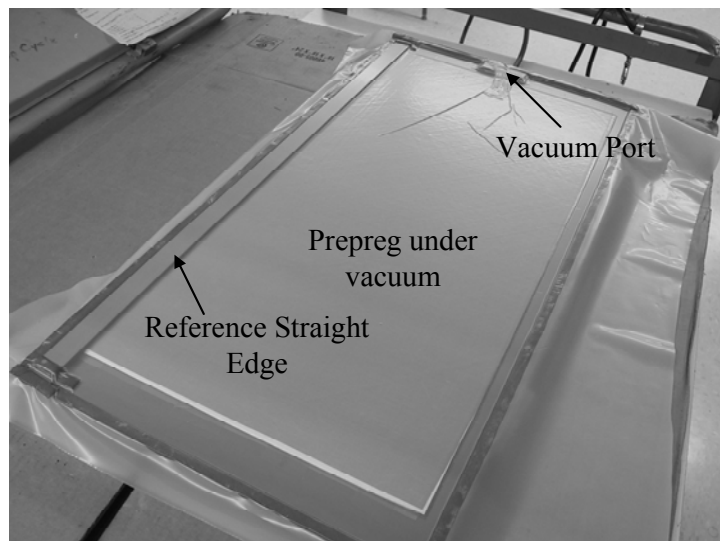


Figure 3.5. Debulking of prepreg layers

3.3.3 Molding

The debulked prepreg was then prepared for molding. The process consisted of mold preparation, bagging, and molding.

3.3.3.1 Mold Preparation

A 6.35 mm x 432 mm x 876 mm (0.25 in x 17 in x 34.5 in) flat steel mold plate was used for making the laminate. The mold was cleaned using laboratory alcohol. Two coats of mold flash were applied taking care to allow the first coat to flash off before applying the second coat. A double-sided flash tape was applied around the perimeter of the mold allowing about 12.7 mm (0.5 in) space between the edge of the tape and the perimeter of the mold. A suitably-sized release film was applied and trimmed to cover the double-sided tape on the mold surface. This was the bottom release film. A reference straight edge, previously treated with mold release solution, had flash tape wrapped around it to prevent the resin from sticking to it. A double-sided tape was placed along the top and bottom length-wise of the reference straight edge. The reference edge was then aligned with the edge of the bottom release film.

3.3.3.2 Bagging

The debulked prepreg reference edge was placed firmly against the side of the reference straight edge and on top of the bottom release film as shown in Figure 3.6. Precautions were taken to prevent contaminating the prepreg during this process. Two breather yarns of 7781 E-Glass were applied across the ends of the preform after which a top release film was applied to cover the preform, the double-sided tape and the straight reference edge. Two coats of mold release were applied to a previously cleaned 20 gauge

steel cowl plate. The cowl plate was applied on top of the release film making sure that it was aligned against the side of the reference straight edge and taking care not to puncture the film. Pieces of the flash tape were used to secure the plate in place. The breather yarns were then folded over the cowl plate and held in place by pieces of the flash tape as shown in Figure 3.7.

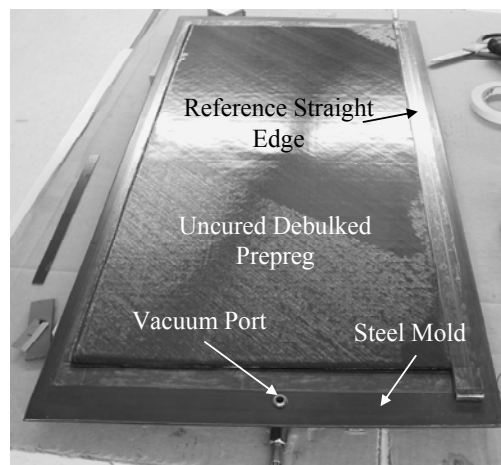


Figure 3.6. Debulked prepreg prior to bagging

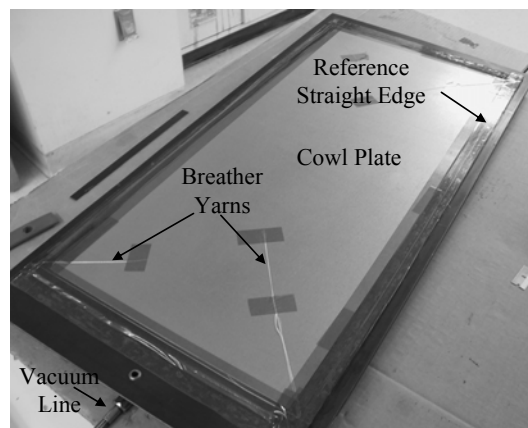


Figure 3.7. Cowl plate mounting for uniform thickness and breather yarns for evacuating gases

A silicon rubber dam was installed over the mold's vacuum port with double-sided tape. A double thick pad of polyester breather was secured into place with the flash tape to cover the hole in the rubber dam. Mastic sealant tape was applied around the perimeter of the mold plate and away from the bottom release film. A suitably-sized polyester breather was cut and applied to the top of the cowl plate and upper release film. After removing the backing paper from the mastic sealant tape, a suitably-sized bagging film was gently tacked to the top of the exposed mastic sealant tape and trimmed. The bagged preform was vacuum tested by closing the 3-way valve between the mold and the vacuum pump and noting the rate of vacuum leak. The vacuum leak rate should not exceed 3.4 kPa/min (1.0 in-Hg/min). Figure 3.8 shows the vacuum tested bagged preform ready for the autoclave process.

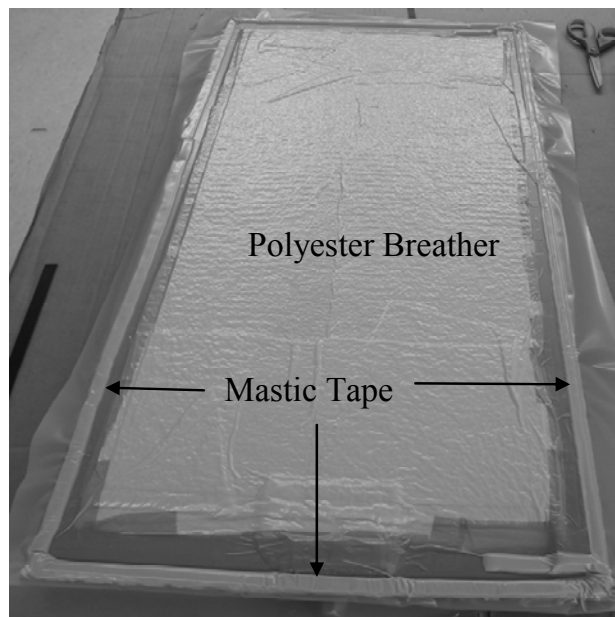


Figure 3.8. Prepared preform ready for autoclave

3.3.3.3 Autoclave Process

The bagged preformed sitting on the mold was inserted into the autoclave chamber as shown in Figure 3.9 and the autoclave's vacuum line attached to the mold's vacuum port. The autoclave's vacuum pump was turned on and a leak check performed again. When the result was found to be satisfactory, the autoclave door was closed and bolted with the recommended torque of 240 Nm (250 ft-lb).

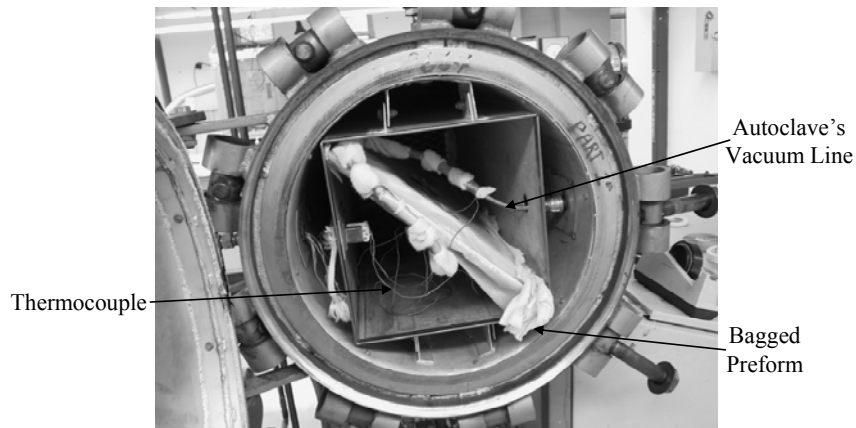


Figure 3.9. Mounting of laminate into autoclave and instrumentation

Nitrogen gas pressure was applied to the autoclave chamber and the appropriate process cycle initiated. As the temperature increased, the resin viscosity decreased rapidly and resin chemical reaction began. At the end of the temperature hold at 177 °C (350 °F), resin viscosity was at a minimum and the applied pressure squeezed out the excess resin. The pressure was held constant throughout the cure cycle so that the resin cured and turned into a glassy state. At the end of this cycle, the autoclave power was

turned off and the pressure and temperature were allowed to drop ambient conditions (atmospheric pressure and 38 °C (100°F) temperature). Figure 3.10 illustrated the time, temperature, pressure and vacuum of the autoclave cycle. The picture of a resulting laminate is shown in Figure 3.11.

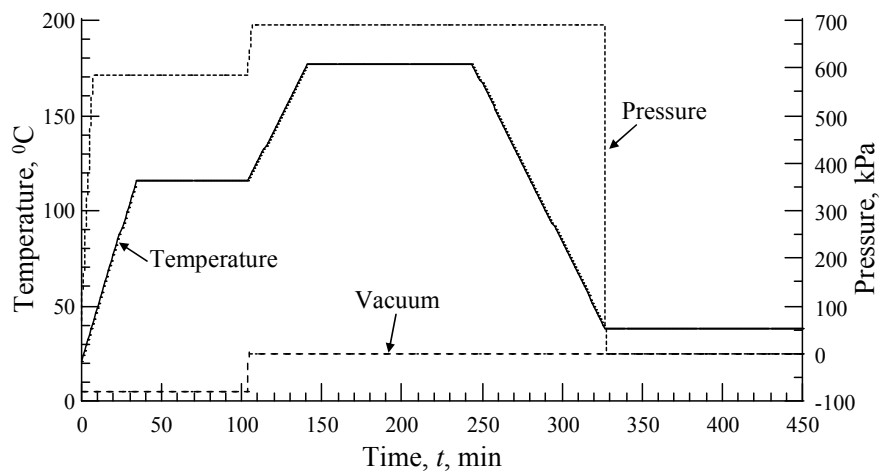


Figure 3.10. Specimen time, temperature and pressure cure cycle for autoclave process

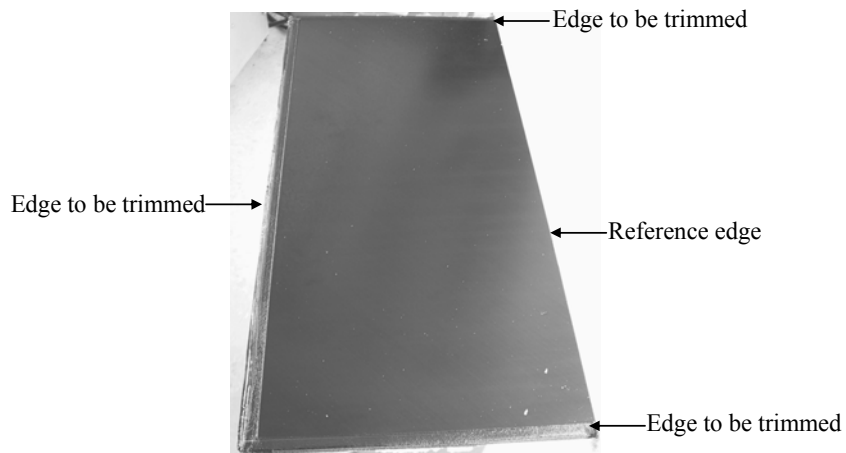


Figure 3.11. Completed laminate prior to trimming

3.4 Structural Diagnostics Inc (SDI) C-Scan of Laminates

Ultrasonic waves are high frequency sound waves that vibrate at a frequency above 20 kHz. During a c-scan operation, a transducer transforms a voltage pulse into an ultrasonic pulse. These pulses are transmitted through the test specimen thickness in either pulse-echo or through transmission mode. Through transmission mode was used in this work. In this mode, two transducers were used to represent a pulser and a receiver, which respectively transmits and receives visuals. Figure 3.12 shows the SDI c-scan equipment used for this work.

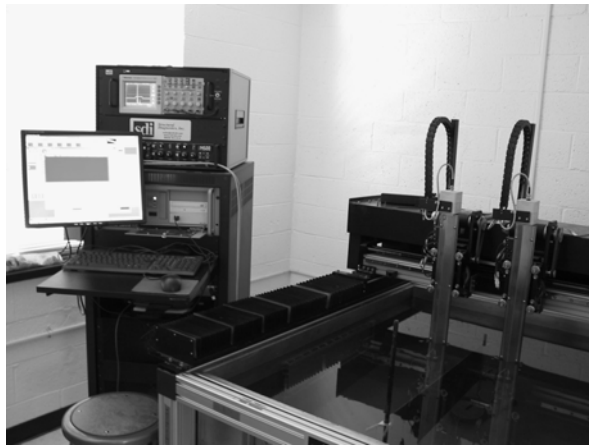


Figure 3.12. SDI ultrasonic c-scan equipment

3.4.1 C-Scan Test

Prior to the c-scan, the test laminates were visually inspected for any surface flaws and defects. The two focused transducers with diameters of 12.7 mm (0.5 in) and frequency of 5 MHz are manufactured by DuPont. The following amplifier and machine

settings were used for laminate c-scan tests: 30% gain, 42 dB attenuation, scan speed of 63.5 mm/s (2.5 in/s) and scan index of 0.75 mm (0.030 in). Using these settings, the laminates were c-scanned for delamination defects to ensure that they are satisfactory. Figure 3.13 shows the testing of a laminate for internal defects. The SDI WinScan software is a data acquisition package used for the acquiring and analyzing the scanned data.

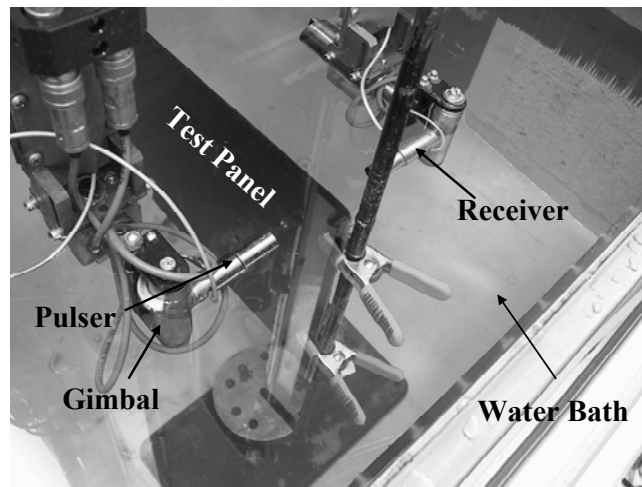


Figure 3.13. Through-thickness c-scanning of the laminate

3.4.2 Results

The c-scan results for both the base and the interleaved test laminates are shown in Figures 3.14 and 3.15, respectively. Ten color codes and their corresponding signal attenuation ranges are shown in both figures. The red color code corresponding to signal attenuation between 90–100% represents essentially no flaw in the specimen. The lower the signal attenuation range, the higher the damage detected in the laminate. The blue

color code represents the most flawed area in the laminate. The images show that both the base and the interleaved test laminates were damage-free. The edges of the test laminates showed signal transmission within the range of 0-10%. This low value was due to trapped air between the clamps and the laminate along the edges. After the c-scan, the laminates were immediately cut into test specimens using water lubricated diamond tipped saw and the specimens were dried and stored in desiccator to avoid moisture absorption. The specimens were wiped clean with a cloth before the drying process.

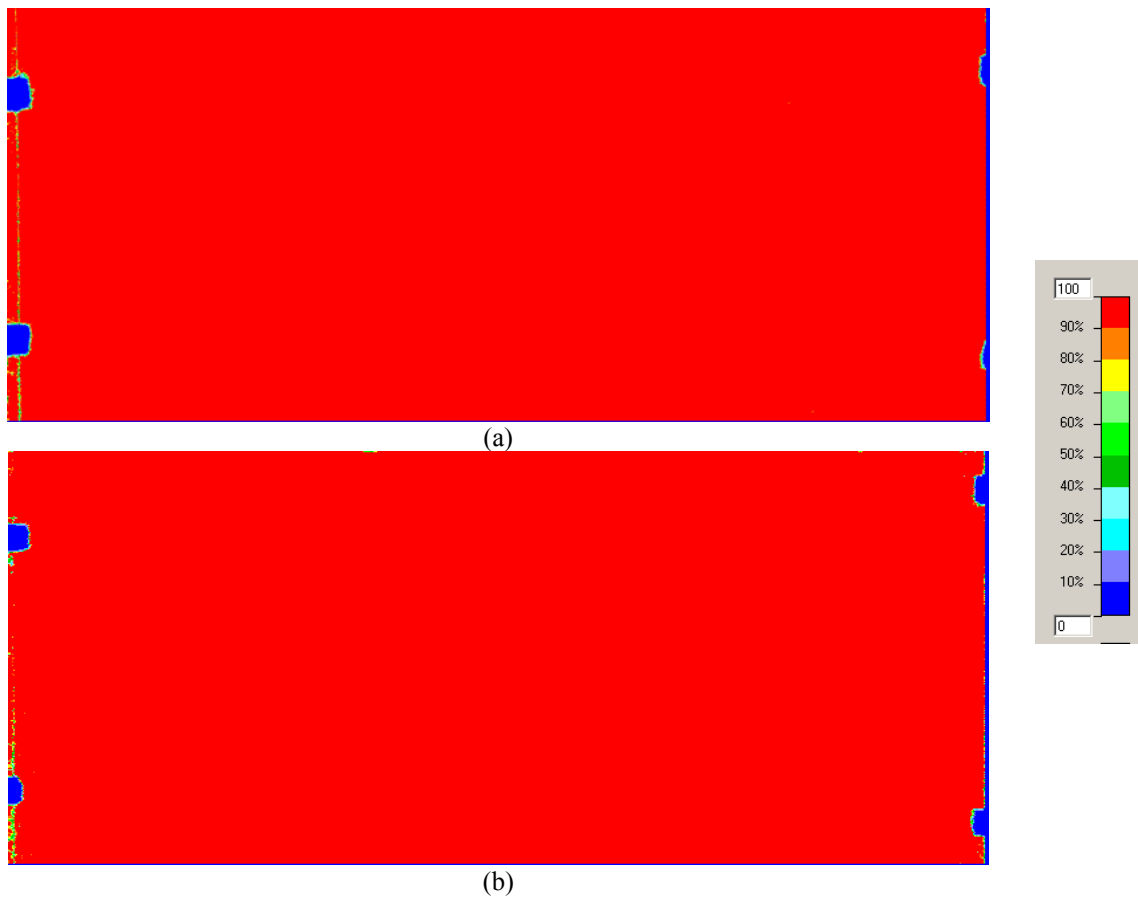


Figure 3.14. C-scan image of base laminates. (a) Laminate # 1 and (b) Laminate # 2

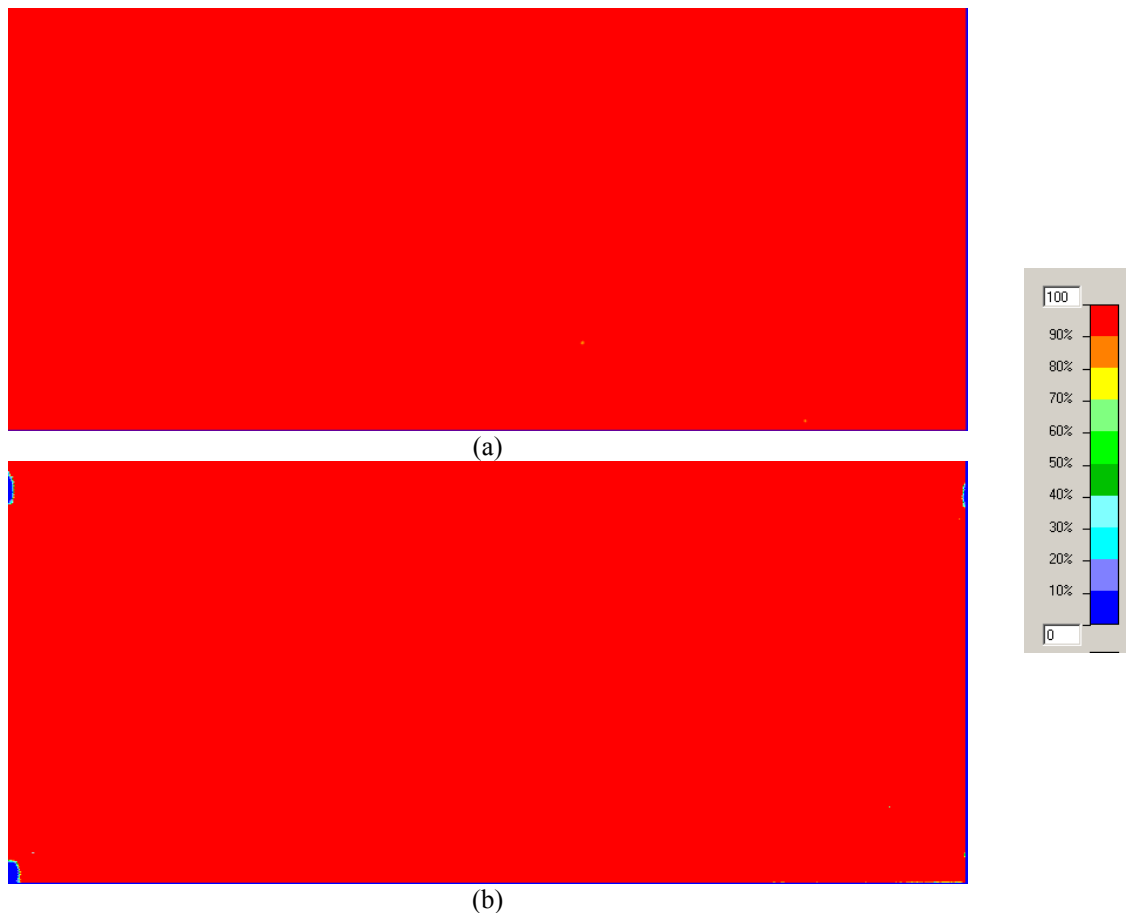


Figure 3.15. C-scanned images of interleaved laminates. (a) Laminate # *P1* and (b) Laminate # *P2*

3.5 Preparation of Test Specimens

3.5.1 Machining

The seven laminates, each measuring 356 mm x 762 mm (14 in x 30 in), were machined into a total of seventy test specimens (forty-two base and twenty-eight interleaved test specimens) measuring 102 mm x 152 mm (4 in x 6 in) using the reference edge for locating the laminate. Figure 3.16 shows laminate layout, test specimen and specimen configuration.

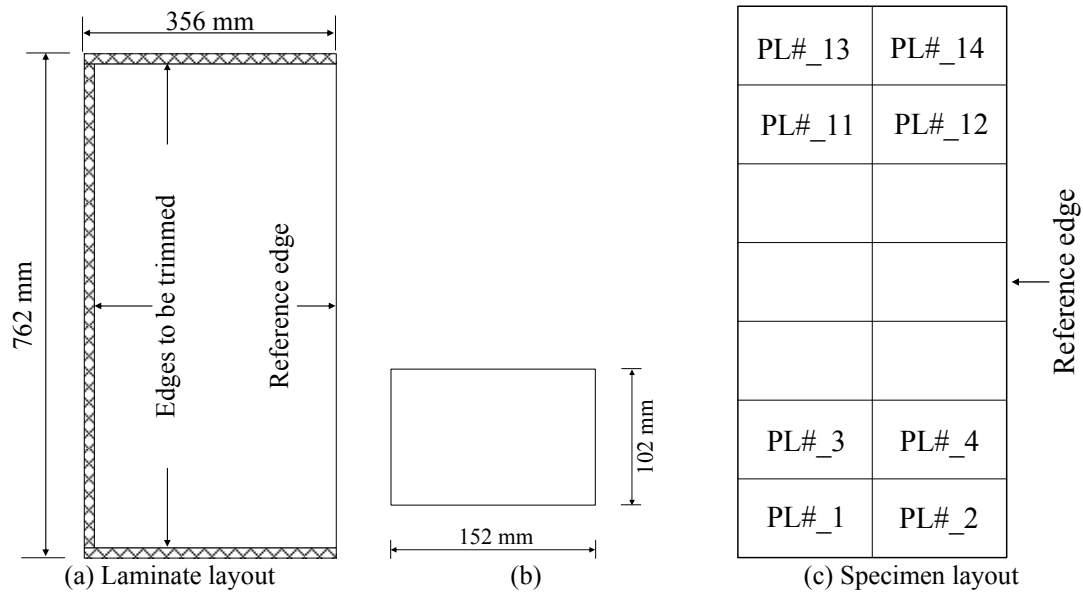


Figure 3.16. (a) Laminate layout, (b) Test specimen and (c) specimen layout

Specimens were designated as $PL\#_specimen\#$, where $PL\#$ is 1, 2, and 3 for base laminates and $P1$ and $P2$ for interleaved laminates. For the base laminate, the first number indicated the laminate number. For the interleaved laminate, the letter P indicated the fact that the laminate was interleaved and the number after the letter P indicated the laminate number.

3.5.2 Specimens Drying

Specimen drying was necessary after machining to drive out water from the specimens before subsequent tests could be performed. The drying cycle was controlled to prevent thermal stress build up in the specimen. The drying temperature was ramped up to 60 °C from ambient temperature over 12 hours and was maintained for another 24 hours and then ramped down to the ambient temperature in 12 hours as shown in Figure 3.17. Total drying duration per cycles was about 48 hours.

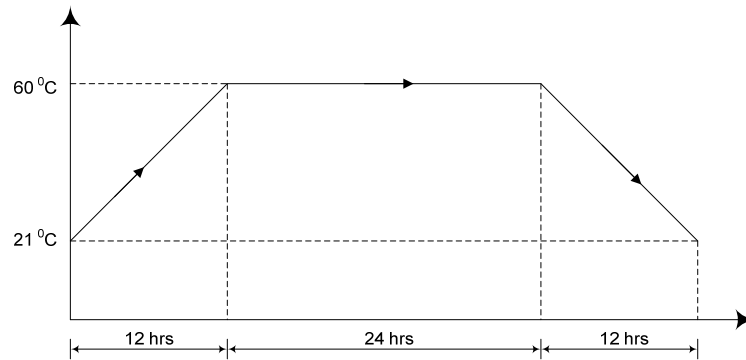


Figure 3.17. Drying cycle of c-scanned test specimens

3.5.3 Test Specimen Dimensions

Using a confidence level of 0.95 and reliability of 0.90 (Lipson & Sheth, 1973), 32 specimens were randomly sampled for thickness measurement. A Mitutoyo micrometer with a flat anvil face was used for thickness measurement. The thickness, h , was measured at four locations in the proposed area of impact (ASTM, 2008). Figure 3.18 shows the thickness of a test specimen being measured. The width and length of test specimens were measured using IP 54 Fowler Digital Vernier Caliper. The average results are tabulated in Table 3.1. The base laminate thickness ranged from 4.10 to 4.18 mm while the interleaved laminate thickness ranged from 4.11 to 4.18 mm. The average thickness and S.D for the base and interleaved laminates are 4.14 mm and 0.023; and 4.15 mm and 0.023, respectively. At confidence level of 95% and degree of freedom for the base and the interleaved of 18 and 14, respectively, the experimental error was calculated to be 0.05. From the results, there was no significant difference in the average thickness of base and interleaved laminates. The specimens were stored in a dessicator until impact testing was performed.

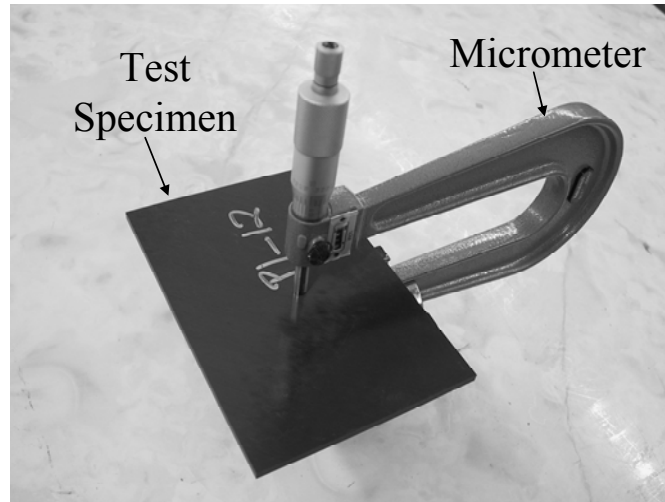


Figure 3.18. Thickness measurement of a test specimen

Table 3.1. List of specimen dimensions

Base Specimens				Interleaved Specimens			
ID#	Length, <i>l</i> , mm	Width, <i>w</i> , mm	Thickness, <i>h</i> , mm	ID#	Length, <i>l</i> , mm	Width, <i>w</i> , mm	Thickness, <i>h</i> , mm
1_14	152.71	102.06	4.16	P2_12	152.78	102.04	4.16
1_3	152.30	102.25	4.14	P2_5	152.49	101.48	4.17
1_8	152.00	101.83	4.10	P2_3	152.90	102.08	4.17
1_9	152.10	101.42	4.18	P1_5	152.27	101.29	4.18
2_11	152.74	101.50	4.16	P1_2	152.72	101.55	4.16
1_1	152.32	101.34	4.15	P2_6	152.84	101.27	4.13
2_4	152.85	101.97	4.14	P1_12	152.04	101.98	4.14
2_9	152.42	101.37	4.17	P1_6	152.34	101.32	4.18
1_6	153.04	102.02	4.12	P2_8	152.68	102.11	4.17
2_5	152.43	102.19	4.13	P1_14	152.76	101.28	4.18
2_8	152.64	101.50	4.10	P2_2	152.08	101.77	4.12
1_7	152.15	101.32	4.14	P2_10	152.10	101.65	4.11
1_11	152.65	102.16	4.12	P1_4	152.47	101.80	4.14
1_12	152.15	101.94	4.15	P1_10	152.62	102.12	4.17
3_11	151.72	101.83	4.16				
3_1	153.51	101.69	4.15				
3_9	153.11	101.88	4.17				
3_12	153.21	101.45	4.11				
Ave.	152.6	101.8	4.14 (0.05)*		152.5	101.7	4.15(0.05)*

*experimental error

3.6 Summary

A total of 5 laminates were made, three base and two interleaved laminates. The laminates measured 356 mm x 762 mm (14 in x 30 in). The laminates were visually inspected for external damage and c-scanned to assess the internal flaws and were found to be satisfactory. Fourteen test specimens were machined from each laminate using a diamond-tipped saw. The machining process was water lubricated to ensure dimensional accuracy and to prevent delamination. Random sampling was used to determine the average thickness of the base and interleaved laminates and was found to be 4.14 and 4.15 mm, respectively. The specimens were dried and stored in a dessicator until required for impact testing.

CHAPTER 4

LOW VELOCITY IMPACT ASSESSMENT OF INTERLEAVED LAMINATES

4.1 Introduction

Impact damage resistance of a structure is how well the structure survives low-velocity impact damage and this is measured in terms of impact the force or energy. This chapter investigates the impact damage resistance of a twenty-four ply quasi-isotropic base and interleaved laminates. Impact testing was performed according to ASTM D7136/D7136-07 Standard. Damage was inflicted to the specimens using drop weight tower with impactor mass of 5.41 kg having a hemispherical tup with a diameter of 25 mm. The data acquisition system stored the entire impact event and created the impact force-time, impact force-deflection, and energy-time history curves. The impact height ranged from 54 to 254 mm and the corresponding velocities ranged from 1.03 to 2.22 m/s. The indentation depth was measured after impact, the specimens were visually inspected for fiber breakage, and the damage area was assessed using c-scan.

4.2 Impact Analysis of Dynatup

4.2.1 Description of Test Set-up

A series of low velocity impact tests were performed using Instron's Dynatup Model 8250 Impact Testing System which was equipped with a pneumatic rebound brake system to prevent multiple strikes and a variable weight crosshead arrangement. The system was also equipped with instrumentation to measure the velocity just before impact

and a load transducer mounted in the impactor to measure the impact force as a function of time. The high-speed data acquisition system has the capability of storing the entire impact event and producing the impact force-time, impact force-deflection, and energy-time history curves. A photograph of the Dynatup Impact Testing System is shown in Figure 4.1.



Figure 4.1. Photograph of the Dynatup Model 8250 Impact Testing System and data acquisition system

The drop tower can be operated in a gravity or in a forced velocity mode. In the forced velocity mode, a compressed spring is used to achieve higher impact velocities and energies. In this work, the gravity mode was used for all impact tests. To perform the

impact test at repeated heights, the pneumatic hoist system automatically transports the cross-head weight to the pre-determined height after testing. Formulation of the physical problem was based on the mathematical model shown in Figure 4.2.

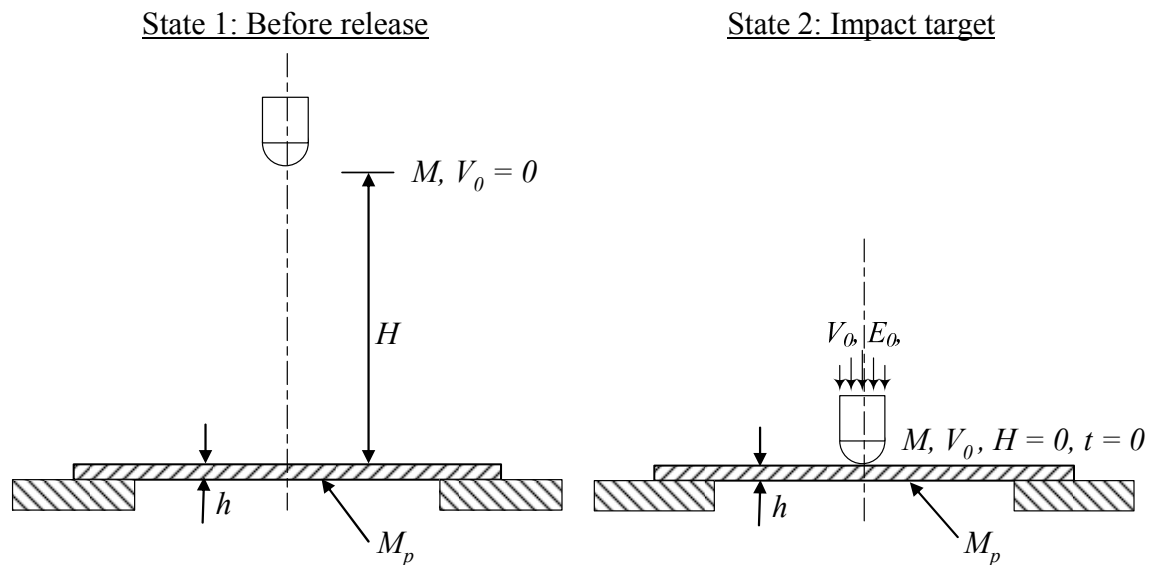


Figure 4.2. Analysis of impact test

The impact process consisted of two distinct states. In the first state, the impactor, consisting of the tub and the cross-head, was raised to the preset impact height, H . The total mass of the impactor was M . At this state, the velocity of the impactor was zero and the potential energy was MgH . After releasing the impactor, it was accelerated by gravity and just before striking the target (laminare) at time $t = 0$, the velocity was $V(0) = V_0$. This velocity was obtained by equating the potential energy to the kinetic energy of the impactor, assuming no loss of energy during the event. The second state was the contact

deformation of the target as energy was transferred from the impactor to the target. The impactor was constrained to strike the target at the center of the rectangular test section of mass M_p . After impact, the pneumatic rebound brake arrested the impactor preventing multiple strikes on the target. The impact event data were captured by the PC using the data acquisition system.

The basic parameters of the impact mechanics are the mass of the impactor (M), the impact height (H), the target type (base versus interleaved), the target thickness (h), the mass of the laminate test section (M_p), the impact velocity (V_0) at the instant of impact at $t = 0$, the impact duration (T_d), and the instantaneous velocity ($V(t)$) which describes the velocity-time response during the impact event. The impact mechanics consists of two events: (a) rigid body motion mechanics of the impactor before impact, and (b) deformation mechanics of the target after impact.

4.2.2 Rigid Body Mechanics of Impact

From the principle of conservation of energy and assuming the energy lost during the acceleration of the impactor is negligible, we obtain;

$$MgH = \frac{MV_0^2}{2} \quad (4.1)$$

where, H is the impact height, g is the acceleration due to gravity, 9.81 m/s^2 , M is the mass of the impactor, and V_0 is the velocity of the impactor at the instant of impact. By re-arranging the terms, impact velocity, V_0 , is:

$$V_0 = \sqrt{2gH} \quad (4.2)$$

4.2.3 Deformation Mechanics after Impact

The motion of the impactor is described by Equation 4.3 or 4.4. The force transducer mounted in the impactor measures the de-acceleration of the impactor after making contact with the target. Re-arranging and integrating Equation (4.4), the instantaneous velocity, $V(t)$, given by Equation (4.5) is obtained.

$$P(t) = Ma(t) \quad (4.3)$$

$$P(t) = M \frac{dV(t)}{dt} \quad (4.4)$$

$$V(t) = V_0 - \frac{1}{M} \int_0^t P(t) dt \quad (4.5)$$

where V_0 is the impact velocity at $t = 0$, which is given by Equation 4.2. After making impact with the target, the impactor and the target move together. As the impact is at the center of the plate, the central deflection of the plate, $W(t)$, can be obtained by integrating Equation 4.5 which results in Equation 4.6 for a plate that was stationary before impact.

$$W(t) = \int_0^t \left[V_0 - \frac{1}{M} \int_0^t P(t) dt \right] dt \quad (4.6)$$

4.2.4 Energy Analysis of the Impact

The impactor potential energy is converted to kinetic energy as the impactor travels along the rail. During impact with the target, the kinetic energy of the impactor deforms the target and work is done on the target, which is equal to the strain energy of the laminate. The maximum impact energy transferred by the impactor to the laminate is stored as elastic energy, $E_{elastic}$, and dissipated energy, E_a . That is:

$$E_0 = \frac{1}{2}MV_0^2 = E_{elastic} + E_a \quad (4.7)$$

The elastic energy, $E_{elastic}$, released by the target is used to accelerate the impactor with a rebound velocity, V_r . The dissipated energy is the sum of energy used in creating damage in the laminate. The energy dissipated by the target in the form of vibration and heat and, by the impact setup in the form of inelastic behavior of the impactor and support (Delfosse & Poursartip, 1997; Shivakumar, Elber, & Illg, 1985b) can be calculated by considering the impact and rebound velocity or by considering the area under the force-displacement curve. The rebound velocity is the reverse velocity of the impactor at $P(t) = 0$.

$$E_a = \frac{1}{2}M(V_0^2 - V_r^2) = \int_0^{T_d} P(t)W(t)dt \quad (4.8)$$

where V_r is the rebound velocity of the impactor in m/s, T_d is the contact duration for the damaged specimen in ms. The instantaneous energy transferred from the impactor to the target is given by:

$$E(t) = \frac{1}{2}MV_0^2 - \frac{1}{2}MV^2(t) \quad (4.9)$$

4.2.5 Single Degree of Freedom (SDOF) Analysis of Plate and Impactor

Figure 4.3 (a) shows the schematic of the specimen deformation during impact. The complete spring-mass model shown in Figure 4.3(b) represents the analytical model of the deformation mechanics. In this model, the springs k_c , k_m , k_b and k_s represent the contact, membrane, bending and shear stiffness, respectively, as previously explained in reference (Shivakumar et al, 1985a & 1985b).

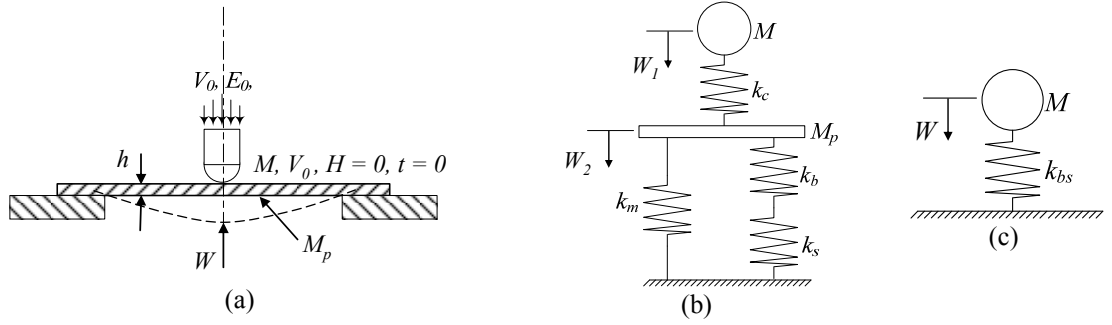


Figure 4.3. Spring-mass models for impact deformation mechanics. (a) Schematic of specimen deformation, (b) Complete and (c) SDOF models

Geometric nonlinearities and indentation can be neglected when there is no damage in the specimen after the impact event and the complete model reduces to the single-degree-of-freedom (SDOF) model shown in Figure 4.3(c) for analysis of the impact event (Abrate, 1998). In the SDOF model, the target is represented by the combined bending-shear spring with stiffness, k_{bs} . The equation of motion for the SDOF model is given by:

$$M\ddot{W} + k_{bs}W = 0 \quad (4.10)$$

The assumed general solution to the free undamped system in Equation 4.10 can be found in any text book on dynamics. Solving for the deflection, W , and using the initial conditions; $V(0) = V_0$ and $W(0) = 0$, give the solution as;

$$W(t) = \frac{V_0}{\omega} \sin \omega t \quad (4.11)$$

where $\omega = \sqrt{\frac{k_{bs}}{M}}$ is the frequency in radians. The force-time response is given by;

$$P(t) = V_0 (k_{bs} M)^{0.5} \sin\left(\frac{\pi t}{T_0}\right) \quad (4.12)$$

where $T_0 = \frac{\pi}{\omega} = \pi \sqrt{\frac{M}{k_{bs}}}$ is the contact duration for the undamaged laminate. For the undamaged plate, the central deflection, $W(t)$, and force, $P(t)$, and impact duration, T_0 , matches the experimental data. The pristine stiffness, k_{bs} , can be found from the initial slope of the force versus displacement curve or using computational tool such as ANSYS.

4.3 Test Matrix

The impact test matrix is shown in Table 4.1. The impact height ranged from 57 to 254 mm and two or three specimens were impact-tested at each height. The impact height and their corresponding specimens' designation are shown in the table. The maximum impact height to produce significant delaminations and fiber rupture in the laminate is given in Reference (ASTM, 2008) and stated in Equation (4.14):

$$H = \frac{C_E h}{Mg} \quad (4.14)$$

where $C_E = 6.7 \text{ J/mm}$ is a constant for fiber-reinforced polymer matrix composite such as Carbon/Epoxy material, $M = 5.41 \text{ kg}$ is the mass of the impactor, $h = 4.14 \text{ mm}$ is the plate thickness and $g = 9.81 \text{ m/s}^2$ is the acceleration due to gravity. Solving, the impact height was obtained as $H = 523 \text{ mm}$. A value of 550 mm was chosen in order to ensure that significant damage was occurred in the laminate. Preliminary impact testing showed that the minimum height to conveniently perform an impact test was 57 mm (2.25 in) and for impact heights greater than 254 mm (10 in), the extent of damage interacted with the

boundary of the test fixture. Based on these limitations, impact height range of 57 to 254 mm was chosen.

Table 4.1. Impact test matrix

Impact Height, H , mm	Test Specimen ID #	
	Base Laminate*	Interleaved Laminate*
57	3_3	P2_10
	3_12	P1_1
	-	P1_7
64	3_4	P1_14
	3_10	P2_9
	-	P2_14
76	3_8	P1_2
		P1_6
		P2_1
83	3_14	P2_12
	1_3	P1_10
	-	P1_11
89	3_11	P1_5
	1_14	P1_13
	-	P2_3
102	3_6	P2_4
	3_7	P2_7
	2_7	P1_4
127	1_10	-
	2_10	-
	2_12	-
152	3_13	P2_6
	3_5	P2_8
	2_9	P2_5
254	3_9	P1_3
	1_6	P1_8
	1_7	P1_9

*Average mass of laminate test section, M_p , = 0.0641 kg. Mass of impactor, M , = 5.41 kg

4.4 Impact Test

Low velocity impact tests were conducted using ASTM Standard D 7136/ D 7136M-07 (ASTM, 2008). The test fixture is shown in Figure 4.4. The drop tower impact test machine had a hemispherical hardened steel tup with diameter of 25.4 mm (1.0 in). The impact test section measured 76 mm x 127 mm (3 in x 5 in) and its mass was calculated to be approximately 0.0641 kg using AS4/3501-6 material properties (Daniel & Ishai, 2005). The mass of the impactor was 5.41 kg and the ratio of impactor to laminate mass was approximately 84. Therefore, the laminate mass was neglected in this analysis. The specimen was secured by four rubber tipped clamps and was assumed to be simply-supported for the analysis (Delfosse & Poursartip, 1997). A sketch of a test specimen secured by four clamps is shown in Figure 4.5. To perform an impact test, the test specimen was placed on a rigid steel frame with 76 mm x 127 mm (3 in x 5 in) rectangular cut-out and centered over the cut-out by means of the three guiding pins. It was held in place by four adjustable rubber-tipped toggle clamps.

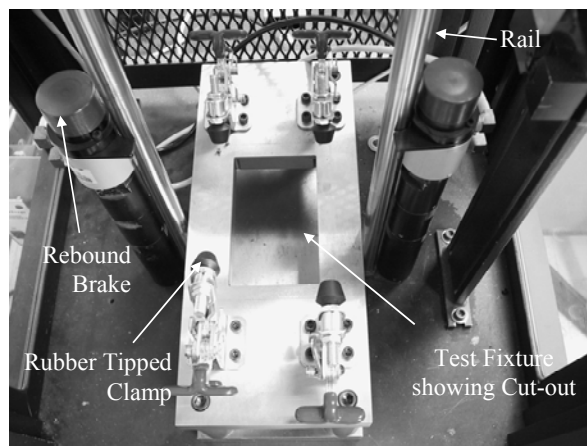


Figure 4.4. Photograph of drop tower impact test fixture

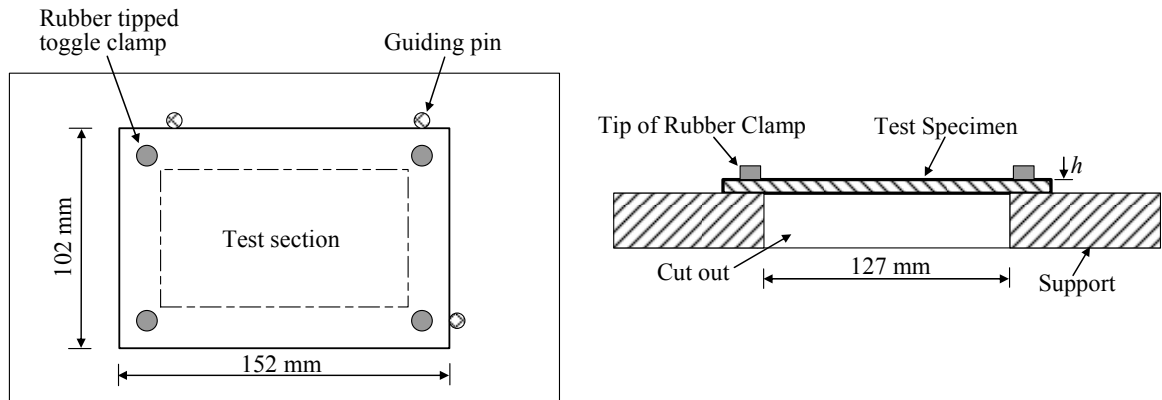


Figure 4.5. Schematic of clamped test specimen. (a) Plan and (b) Sectioned view

Each toggle clamp was configured to exert a minimum of 1.1 kN on the test specimen. The impact height was set by measuring the vertical distance between the tip of the impactor and the top surface of the clamped specimen. After properly centering and clamping the specimen, the impactor was released from a pre-set height. After traveling this distance and striking the specimen, the pneumatic rebound brake was automatically activated to prevent multiple strikes. The pneumatic hoist system repositioned the impactor to the previously set height. Each specimen was visually inspected for back-face damage and the indentation depth was measured.

4.5 Test Results and Discussion

4.5.1 Damage Analysis

4.5.1.1 Visual Analysis

After impact testing, test specimens were visually inspected for the extent of the damage. The back-face damage geometry was recorded and if fiber breakage occurred, then the crack length (C_L) and width (C_W) were recorded. Visual observation of the back

face damage demonstrated that first fiber cracks were observed at impact height of 89 mm for the base laminate and 152 mm for the interleaved laminate. The detailed results are tabulated in Appendix B. Partial results are presented in Table 4.2.

4.5.1.2 Indentation Depth

After documenting the back-face damage, the indentation depth was measured and recorded using a dial indicator with 0.025 mm (0.001 in) accuracy and 3.0 mm (0.125 in) diameter ball. Figure 4.6 shows indentation depth measurement of a test specimen. Summary of the indentation depth results for both the base and the interleaved laminates are shown in Table 4.3. These are plotted in Figure 4.7. It can be seen that interleaving significantly delayed the occurrence of indentation. In addition, at any given impact height the indentation depth for the base laminate is consistently higher than that of the interleaved laminate.

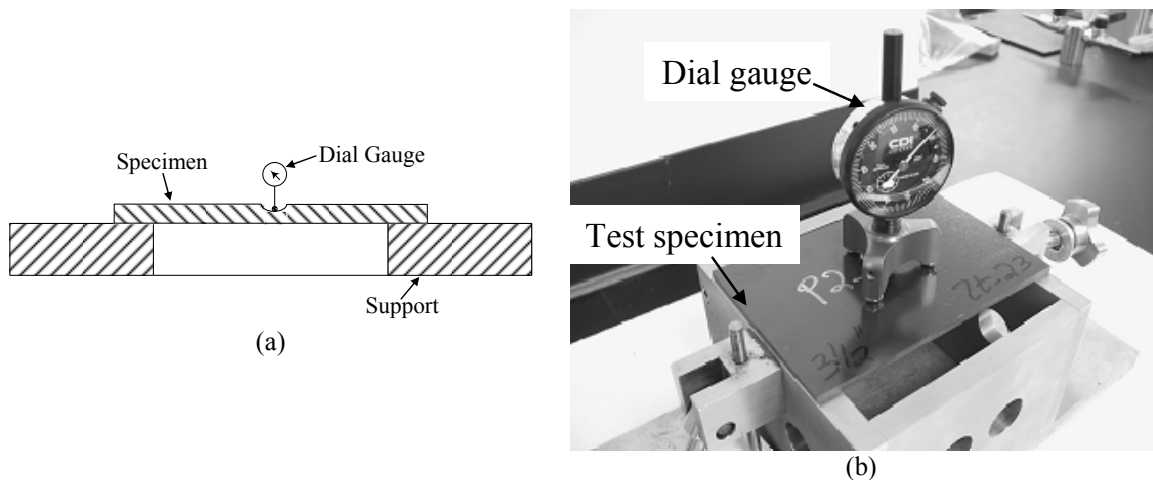


Figure 4.6. Indentation depth measurement. (a) Schematic and (b) Photograph of set-up

Table 4.2. Damage assessment of laminate back-face

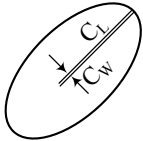
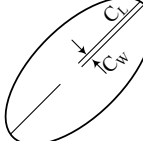
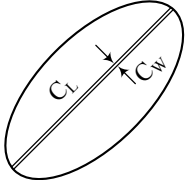
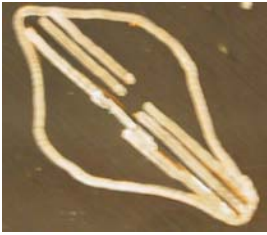
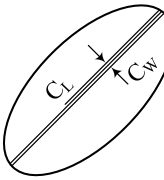
Base Laminate		Interleaved Laminate			
Impact Height, <i>H</i> , mm	Back-face		Impact Height, <i>H</i> , mm	Back-face	
	Photograph	Schematic		Photograph	Schematic
83		 Elliptical Delamination, No Visible Cracks $2A = 18.5$; $2B = 14$	102		 Elliptical Delamination, No Visible Cracks $2A = 17.5$; $2B = 15$
89		 Elliptical Delamination, Multiple Cracks, C_L $= 10$; $C_W = 5$ $2A = 23.5$; $2B = 14$	152		 Elliptical Delamination, Multiple Cracks, C_L $= 15$, $C_W = 5$ $2A = 22$; $2B = 20$
102		 Elliptical Delamination, Multiple Cracks, C_L $= 2A$; $C_W = 7$ $2A = 28$; $2B = 16$	254		 Elliptical Delamination, Multiple Cracks, C_L $= 2A$, $C_W = 8$ $2A = 42$; $2B = 18.5$

Table 4.3. Indentation depth results for base and interleaved laminates

Impact Height, H , mm	Base Laminate		Interleaved Laminate	
	Test Specimen ID #	Indentation Depth, d , mm	Test Specimen ID #	Indentation Depth, d , mm
57	3_3	0.000	P2_10	0.000
	3_12	0.025	P1_1	0.000
			P1_7	0.000
64	3_4	0.102	P1_14	0.000
	3_10	0.102	P2_9	0.000
			P2_14	0.000
76	3_8	0.102	P1_2	0.000
			P1_6	0.000
			P2_1	0.000
83	3_14	0.102	P2_12	0.076
	1_3	-	P1_10	0.000
			P1_11	0.000
89	3_11	0.102	P1_5	0.102
	1_14		P1_13	0.076
			P2_3	0.076
102	3_6	0.127	P2_4	0.102
	3_7	0.127	P2_7	0.127
	2_7		P1_4	0.127
152	3_13	0.178	P2_6	0.152
	3_5	0.152	P2_8	0.152
	2_9	--	P2_5	0.152
254	3_9	0.216	P1_3	0.203
	1_6		P1_8	0.203
	1_7		P1_9	0.178

The damage onset impact height for indentation is 65 mm for the base laminate and 82 mm for the interleaved laminate. Gao, Jiao, Lu, & Ning (2007) observed that thermoplastic particle interleaving sustained higher indentation depths than the base laminate but this was not observed in this study. The high indentation depths may be attributed to the increased thickness of the thermoplastic interleaved laminate. In this study, the high contact stresses could have been absorbed by the nano-fabric on the

surface of the laminate, resulting in the indentation depth of the interleaved laminate being lower than the base laminate.

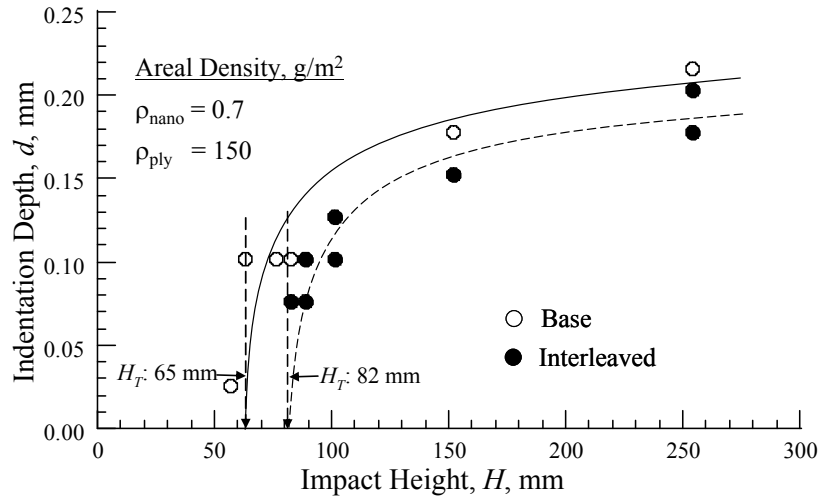


Figure 4.7. Indentation depth versus impact height

4.5.1.3 Damage Analysis by C-Scan

Structural Diagnostics Inc (SDI) ultrasonic C-Scan equipment was used for assessing internal damage in the test specimens. Figure 4.8 shows the SDI C-Scan equipment used for the c-scan test. Through-thickness method, employing two 12.7 mm (0.5 in) 5 MHz focused transducers manufactured by DuPont, was used for the c-scan test. The SDI ultrasonic c-scan operation was completely controlled by SDI MasterScan software. The following amplifier and machine settings for specimen c-scan tests were set using the MasterScan software: 30% gain, 42 dB attenuation, scan speed of 30.5 mm/s (1.2 in/s), scan index of 0.2 mm (0.008 in). The extent of the damage in the test specimen

measured by the c-scan is proportional to the extent of signal attenuation from the pulser to the receiver. The higher the signal attenuation, the larger the extent of the damage sustained in the test specimen. This damage area was measured using the SDI WinScan software, a data acquisition and analysis software. After the c-scan test, the specimens were dried in an oven using the method described in Chapter 3 and then stored in a desiccator until tested in compression. Typical c-scan images for the base and the interleaved test specimens are shown in Figure 4.9. At the impact height ($H = 64$ mm) the base laminates developed large damage areas than the interleaved laminates. The damage area of the base laminates were predominately in the range 0-10%, indicating significant damage compared to the to the damage area of the interleaved laminates. The rest of images are presented in Appendix C and the results of the damaged areas are tabulated in Appendix D along with other impact data. In the preliminary study, the damaged area was calculated by approximating the geometry of the area to be elliptical.

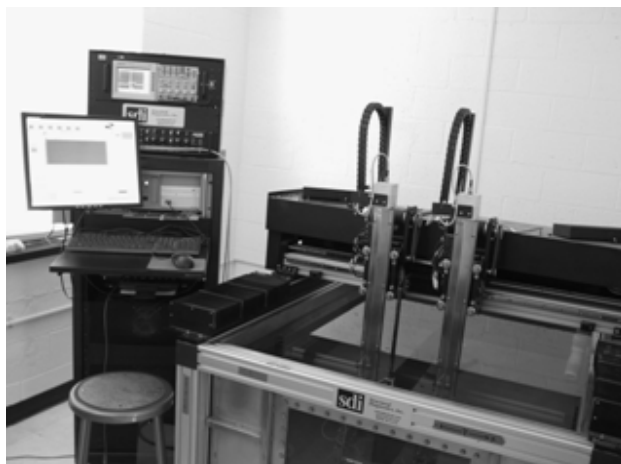


Figure 4.8. Structural Diagnostics Inc (SDI) c-scan equipment for the measurement of damage area

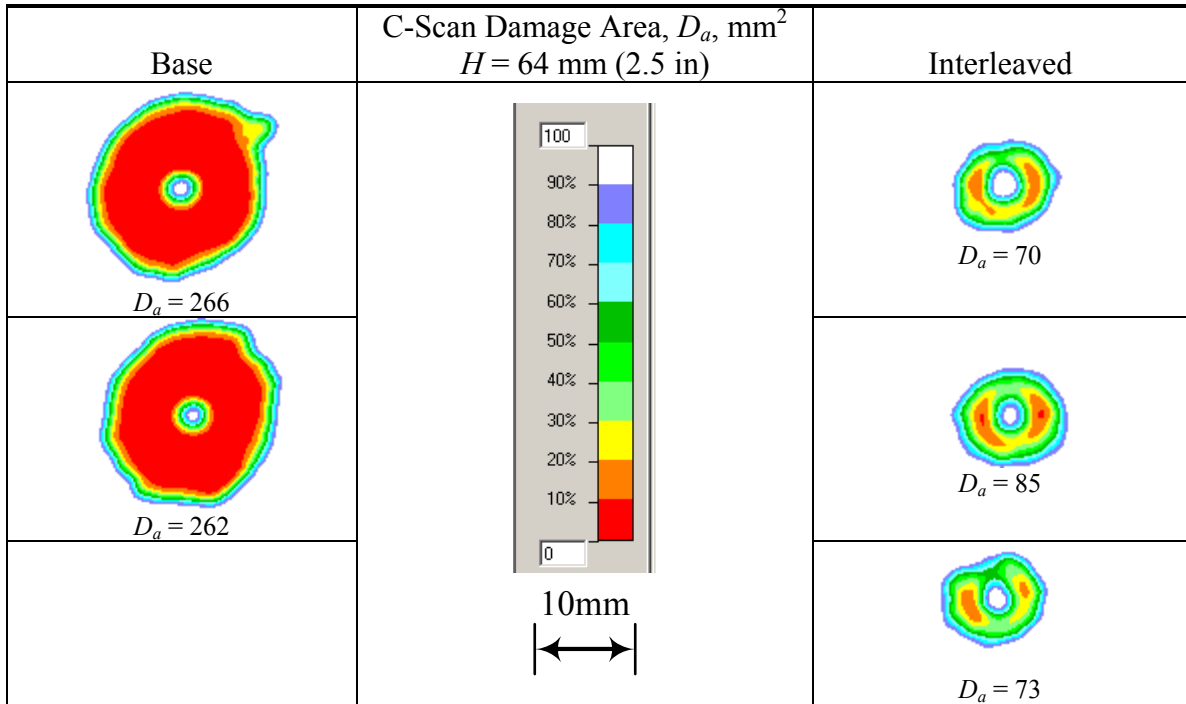


Figure 4.9. C-scan images for base and interleaved specimens impacted at $H = 64$ mm and their corresponding damage areas

Figures 4.10 and 4.11 show the damaged area versus impact height for both the base and the interleaved laminates for the present and preliminary studies. The threshold impact height (H_T) for the base and interleaved laminates are 65 and 82 mm, respectively. These values are the same as the heights obtained at the onset of indentation in Figure 4.7. The present study also show that the damaged growth rates with respect to the impact height for the base and the interleaved laminates are 2.10 and 2.14 mm²/mm, respectively. In the preliminary study (Akangah et al, 2010), the threshold impact height increased from 38.1 to 50.8 mm as a result of interleaving with 1.8 g/m² nano-fabric as shown in Figure 4.11.

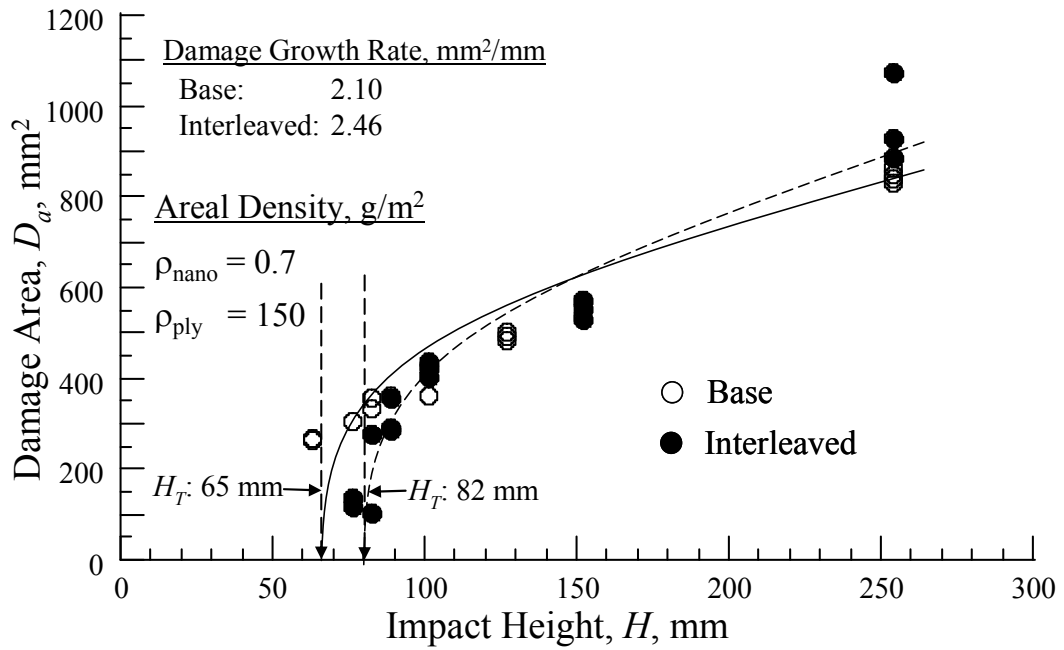


Figure 4.10. Damage area versus impact height for the present study

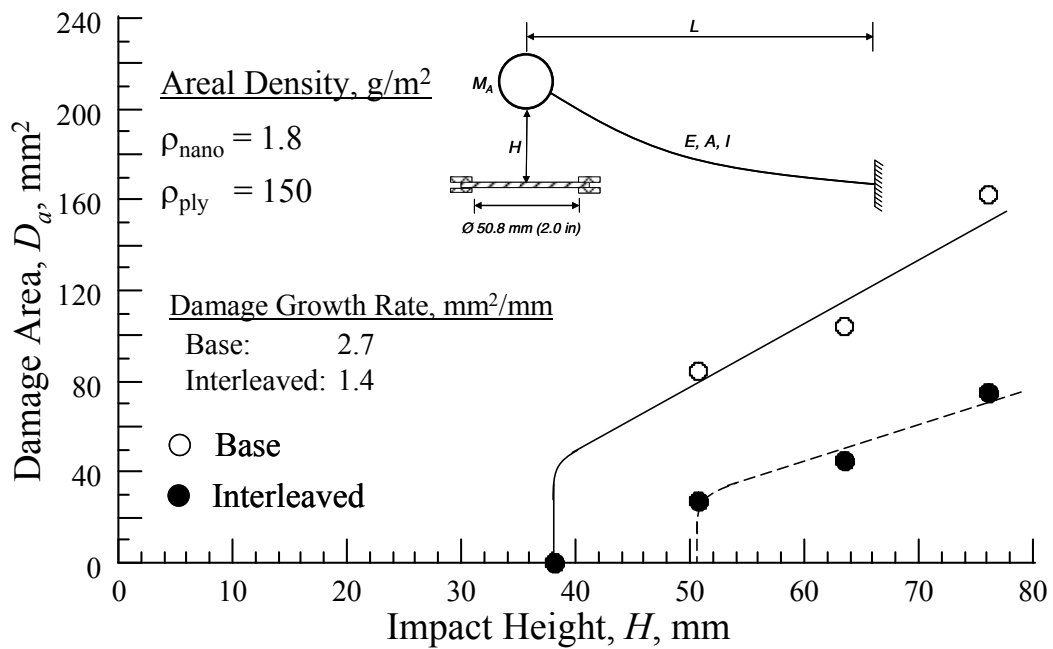


Figure 4.11. Damage area versus impact height for the preliminary study (Akangah et al, 2010)

Figures 4.12 and 4.13 show the damaged area versus impact force for the present and preliminary studies, respectively. The present research results show that the damaged growth rate with respect to impact force for the base laminate is $113 \text{ mm}^2/\text{kN}$ and that for the interleaved laminate is $157 \text{ mm}^2/\text{kN}$. However, the preliminary results show that the damaged growth rate with respect to impact force for the base laminate is $140 \text{ mm}^2/\text{kN}$ and for the interleaved laminate is $60 \text{ mm}^2/\text{kN}$.

The impact damage growth rate for the interleaved laminate was reduced by nearly one-half with respect to impact height and reduced by more than one-half with respect to impact force by interleaving with nano-fabric sheet with areal density of 1.8 g/m^2 . In the present study, there were no significant differences in the damage growth rates for the base and interleaved laminates. Gao et al (2007) identified the interleaving toughening mechanism as: geometrical effect of the interlayer, crack path deflection and crack tip shielding. These toughening modes were not adequately brought to bear because of the low areal density of the nano-fabric used in this study. Comparing the preliminary results with the present one suggests that there is a need to understand the effect of varying nano-fiber areal density on the impact damage resistance and tolerance of carbon/epoxy laminates. The difficulty in making large nano-fabric sheets with appreciable areal density using needle electrospinning method also suggests the need for increasing the electrospun nanofiber through-put.

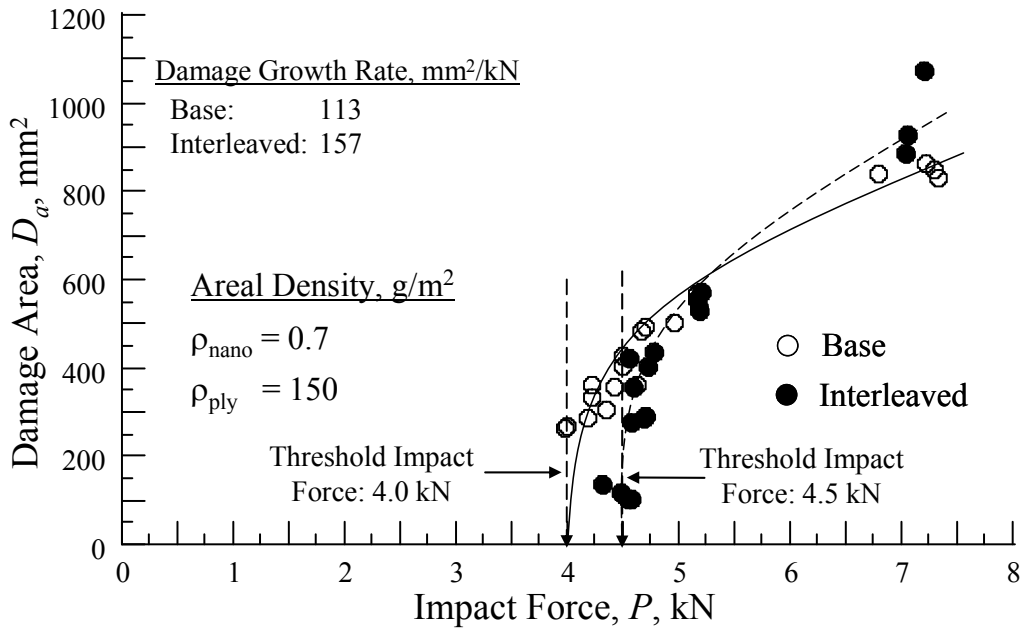


Figure 4.12. Damage area versus impact force for the present study

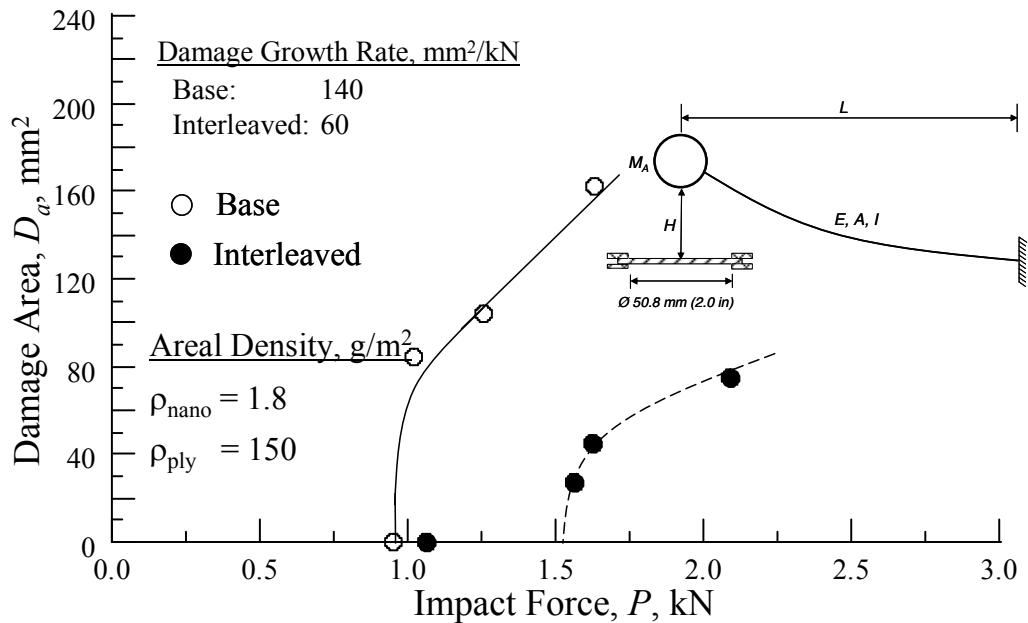


Figure 4.13. Damage area versus impact force for the preliminary study (Akangah et al 2010)

4.5.2 Impact Response of Undamaged Laminate

Figures 4.14 and 4.15 show a typical impact force-time response curve for base and interleaved laminates impacted at 3.21 and 3.35 J, respectively. The impact force-time response of the laminates shows a nice smooth sinusoidal response, which is a characteristic of undamaged laminates. The loading and unloading curves for the base and interleaved laminates at the corresponding impact event are shown in Figure 4.16 and 4.17, respectively. There is no hysteresis in the loading and unloading portions of the impact force-displacement curves indicating no energy loss and no significant laminate stiffness loss during the impact. The pristine stiffness of the laminate, k_0 , was calculated by taking the initial slope of the force versus displacement curve as shown in Figure 4.16. This was found to be 2.5 kN/mm and this result is validated using ANSYS analysis.

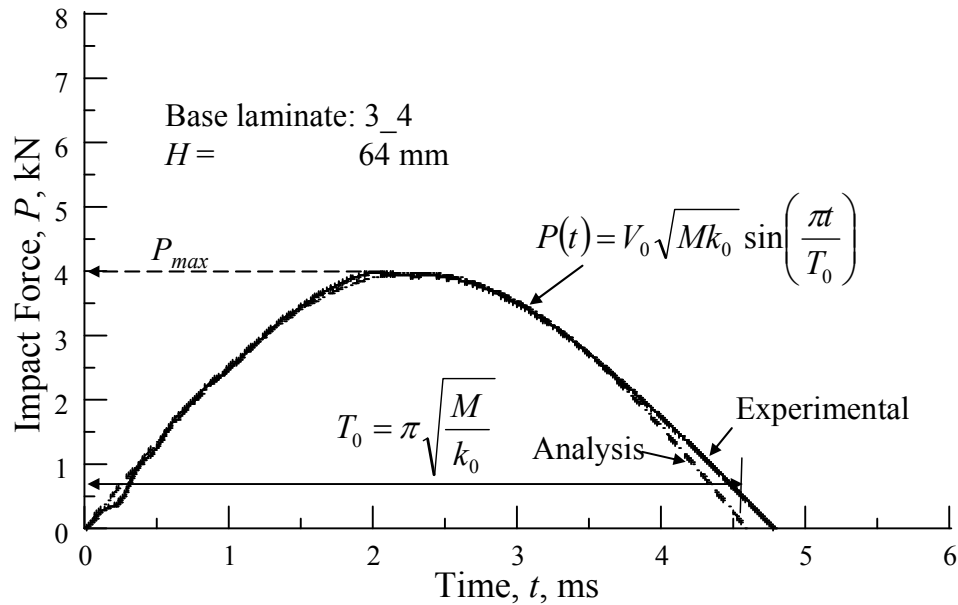


Figure 4.14. Typical Impact force-time response of undamaged test specimen at impact height of 64 mm ($E_0 = 3.21$ J)

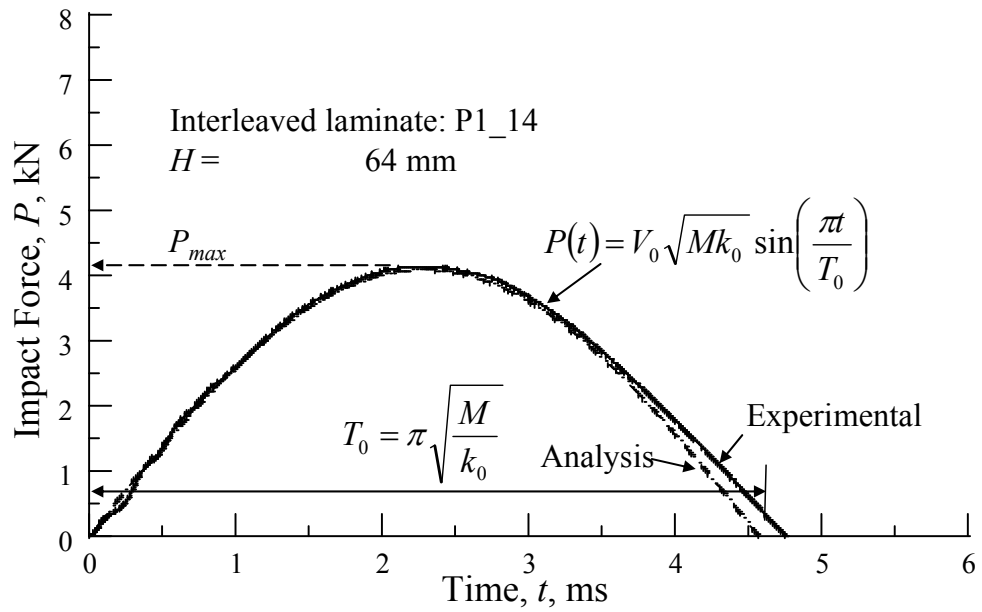


Figure 4.15. Impact force-displacement response of undamaged interleaved laminate at impact height of 64 mm ($E_0 = 3.35$ J)

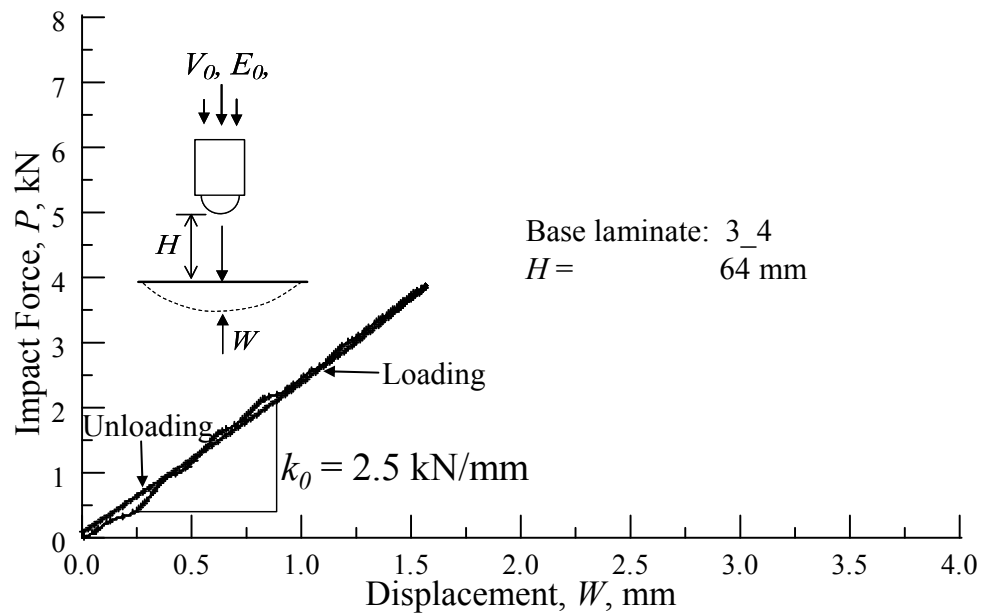


Figure 4.16. Impact force-displacement response of undamaged test specimen at impact height of 64 mm ($E_0 = 3.21$ J)

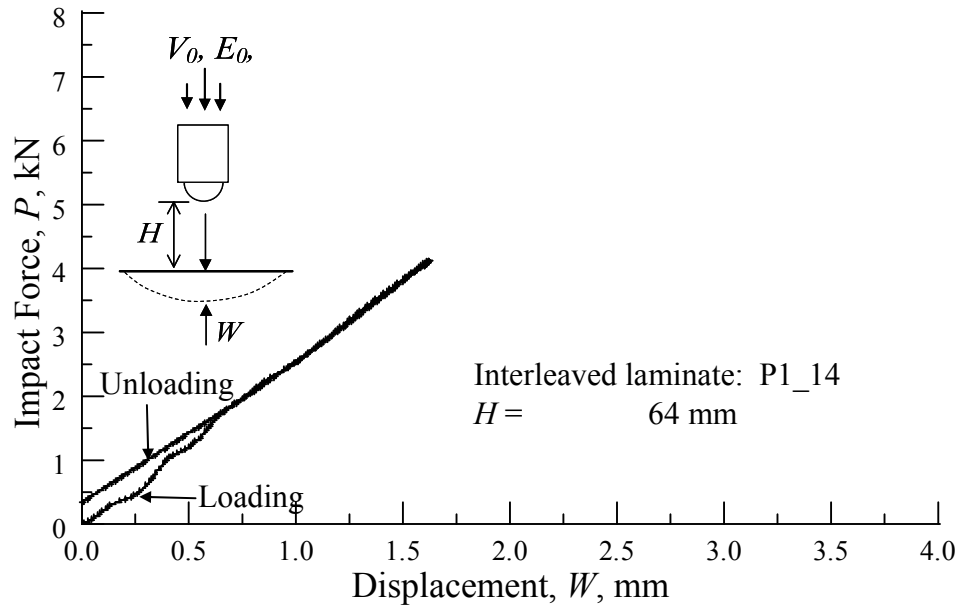


Figure 4.17. Impact force-displacement response of undamaged interleaved laminate at impact height of 64 mm ($E_0 = 3.35$ J)

4.5.3 Impact Response of Damaged Laminate

4.5.3.1 Critical Force

For inelastic impact event, the impact-force response of the test laminate is not smooth. This is an indication of damage. There is a sudden load drop indicating sudden stiffness change due to damage initiation (Schoeppner & Abrate, 2000). Figures 4.18 and 4.19 show the force-time response of the base and the interleaved laminates impacted at 4.65 and 4.53 J, respectively. The first load drop corresponds to the critical force and is caused by unstable delamination propagation (Kwon & Sankar, 1993). The critical force for inelastic impact event can be determined by superimposing the analytical elastic impact-time response onto the inelastic response as shown in Figure 4.19 and the critical forces at the corresponding impact height are tabulated in Table 4.4.

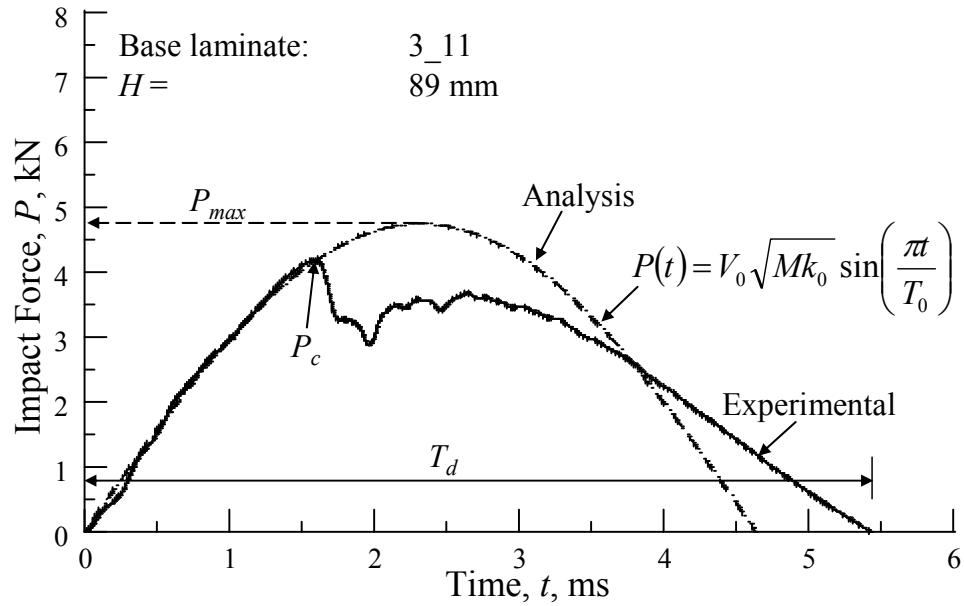


Figure 4.18. Typical impact force-time response of a damaged base laminate at impact height of 89 mm ($E_0 = 4.65$ J)

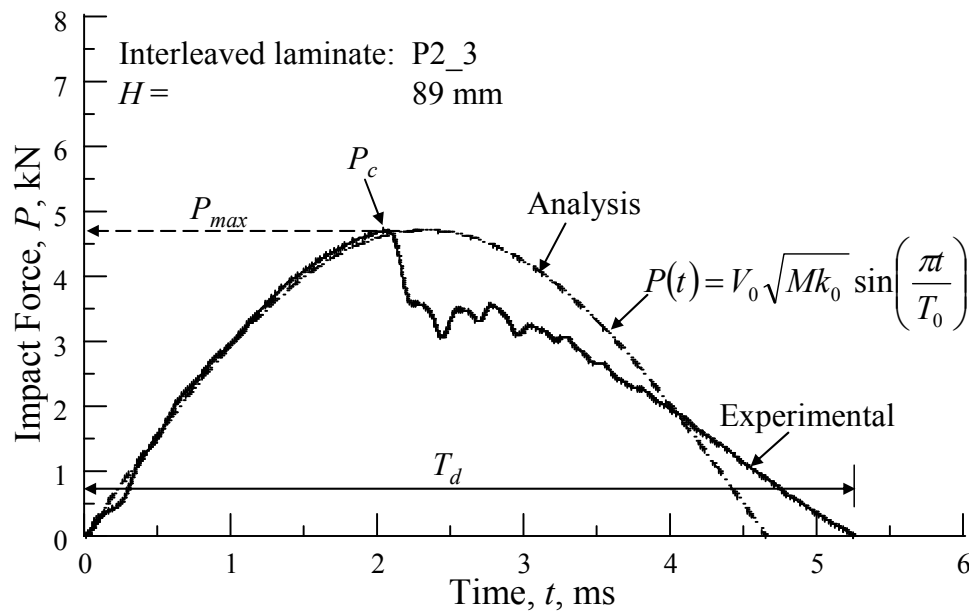


Figure 4.19. Impact force-time response of a damaged interleaved laminate at impact height of 89 mm ($E_0 = 4.53$ J)

Table 4.4. Maximum and critical force for base and interleaved laminates

Impact Height, H , mm	Base		Interleaved	
	Impact Force, kN		Impact Force, kN	
	Critical, P_c	Maximum, P_{max}	Critical, P_c	Maximum, P_{max}
57	--	3.980	--	3.930
	--	3.945	--	3.858
	--	--	--	3.980
64	4.091	4.091	--	4.138
	4.251	4.251	--	4.047
	--	--	--	4.074
76	4.344	4.344	--	4.369
			--	4.477
			--	4.315
83	4.231	4.231	4.571	4.571
	4.428	4.428	4.582	4.582
			--	4.533
89	4.179	4.179	4.678	4.678
	4.638	4.638	4.705	4.705
			4.589	4.589
102	4.508	4.508	4.717	4.717
	4.214	4.214	4.777	4.777
	4.498	4.498	4.555	4.555
127	4.909	4.958		
	4.533	4.697	--	--
	4.570	4.676		
152	4.416	5.189	4.631	5.204
	4.572	5.161	4.701	5.159
	4.934	5.048	4.672	5.188
254	4.235	7.329	4.850	7.031
	4.882	7.214	4.786	7.207
	4.840	7.292	4.831	7.056
	4.580	6.788	--	--
	4.5 (0.4)*		4.7 (0.2)*	

*experimental error

The analytical elastic response given by Equation (4.12) only describes the loading portion up to the first load drop of the impact response as shown in Figures 4.20 and 4.21 for base and interleaved laminates, respectively. After the first load drop, as

expected, the analytical curve moves away from the experimental curve and the load at this point is the critical load, P_c , and it describes the onset of matrix cracks and delamination during the impact event. From Table 4.4, the average critical force and standard deviation for the base and the interleaved laminates were listed as 4.5 kN (0.24) and 4.7 kN (0.09), respectively. At confidence level of 95% and degree of freedom for the base and the interleaved laminates of 18 and 12, respectively, the experimental error was calculated to be 0.4 for the base and 0.2 for the interleaved laminates.

4.5.3.2 Damage Progression

Figures 4.20 and 4.21 show the impact force response curves, for the base and interleaved laminates. The impact force response curves for the range of impact height tested, except for $H = 57$ mm, are shifted by 2 ms for the purpose of comparing the data and for clarity. For $H = 57$ and 64 mm for the base laminate, and for $H = 57, 64$ and 76 mm for the interleaved laminate, the impact force-time response curves have smooth sinusoidal response, which is a characteristic of the undamaged specimen. However, for $H = 76$ and 83 mm and greater, the impact force-time response curves are not smooth, which is an indication of damage to various degrees. The threshold points are represented by a closed circle and at these points, the curves experienced sudden load drop, representing the transition from undamaged to damage in the laminate. The associated force at these points is the critical force. The critical force versus impact height is plotted in Figure 4.22 for the base and the interleaved laminates. The average critical force for the base laminate is 4.5 kN and that for the interleaved laminate 4.7 kN.

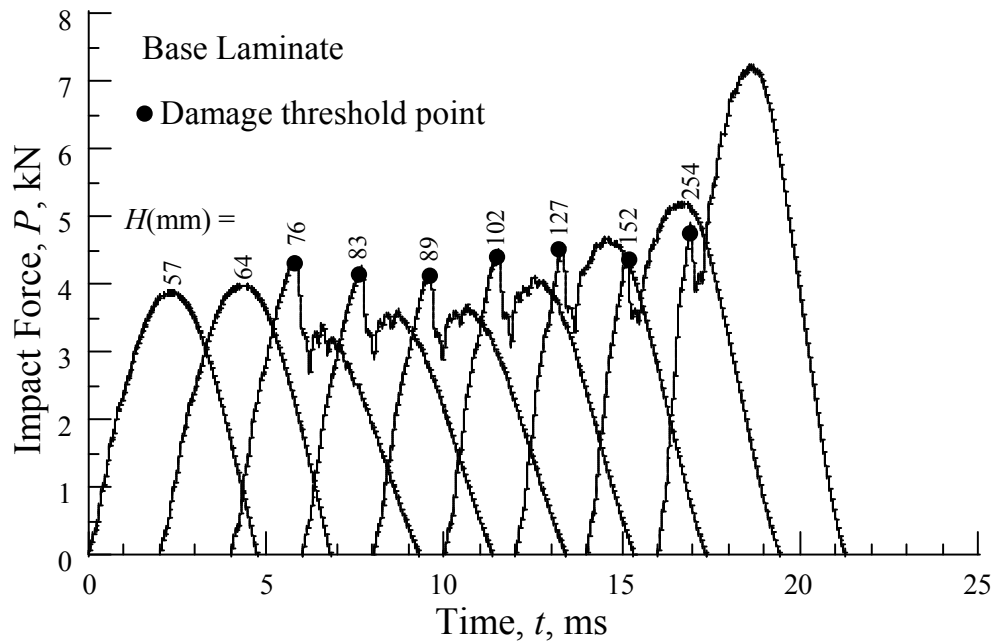


Figure 4.20. Impact force-time response of base laminate showing failure progression

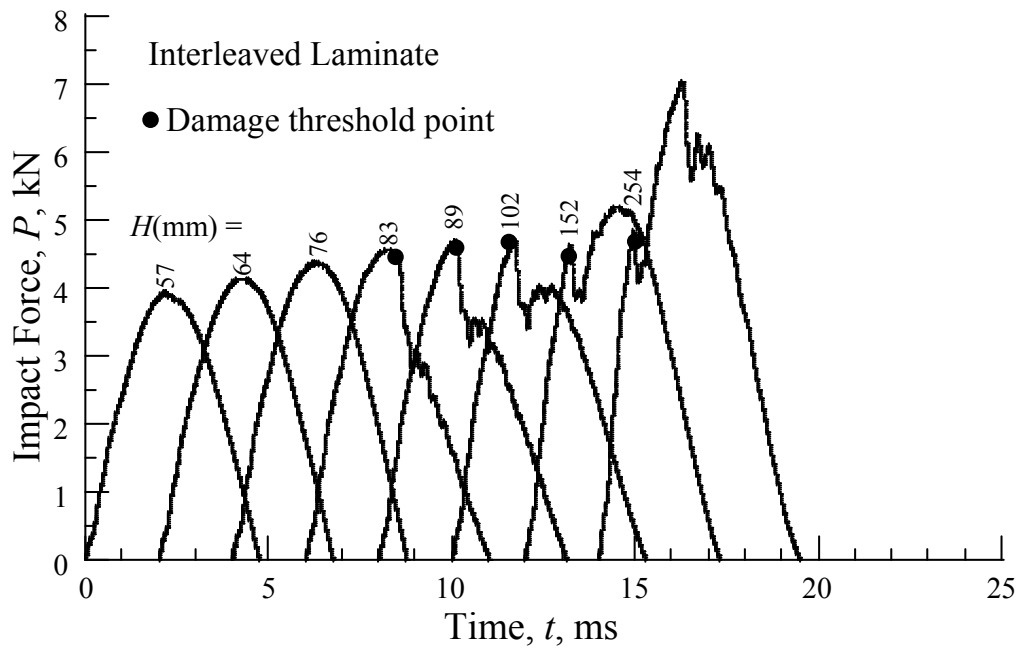


Figure 4.21. Impact force-time response of interleaved laminate showing failure progression

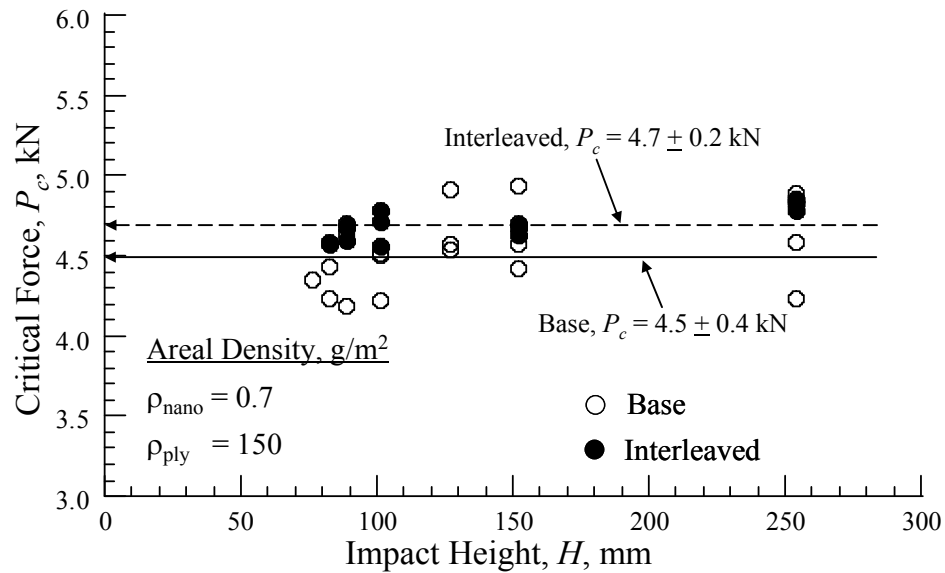


Figure 4.22. Critical force versus impact height

4.5.3.3 Critical Energy

A typical energy curve for inelastic impact event is shown in Figure 4.23. The maximum impact energy, E_0 , is the energy transferred by the impactor to the test specimen. The dissipated energy, E_a , is the energy that is not returned to the tup during the unloading phase and is the sum of energy used in creating damage in the target and dissipated through the target in the form of heat and vibrations. For elastic impact event, the dissipated energy is normally zero. Another important parameter is the critical energy (E_c), which is the energy at damage onset. Figure 4.24 explains the nomenclature of various terms used in the text and also shows the graphical method for the determination of the critical energy during inelastic impact event. The critical energy is the point on the energy curve that has the same instantaneous time as the critical force on the impact force history curve. The critical energy is a measure of the energy required for initiating

damage in the laminate. In elastic impact event, the critical energy does not exist, because no damage is created in the laminate due to impact. More detailed impact data for both base and interleaved specimens are tabulated in Appendix D, and plots for the base and the interleaved impact events are presented in Appendices E and F, respectively.

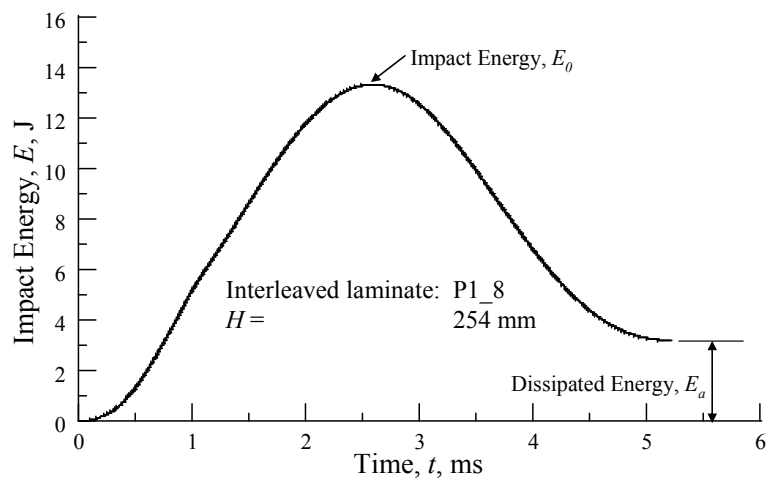


Figure 4.23. Typical energy response for inelastic impact event

Figure 4.25 shows the critical energy for the base and interleaved laminates. The areal density of a ply of AS4/3501-6 was 150 g/m^2 and a layer of nano-fabric used for interleaving was 0.7 g/m^2 . This represented about 0.47% of the composite ply's areal density. The average critical energy of the base laminate was 4.0 J and that of the interleaved laminate was 4.5 J. At 95% confidence level, the experimental data were within the range of 3.3 and 4.7 J for the base laminate and between 4.2 and 4.8 J for the interleaved laminate. Using the average data, interleaving represented an increase of 12.5% in the energy over the base laminate.

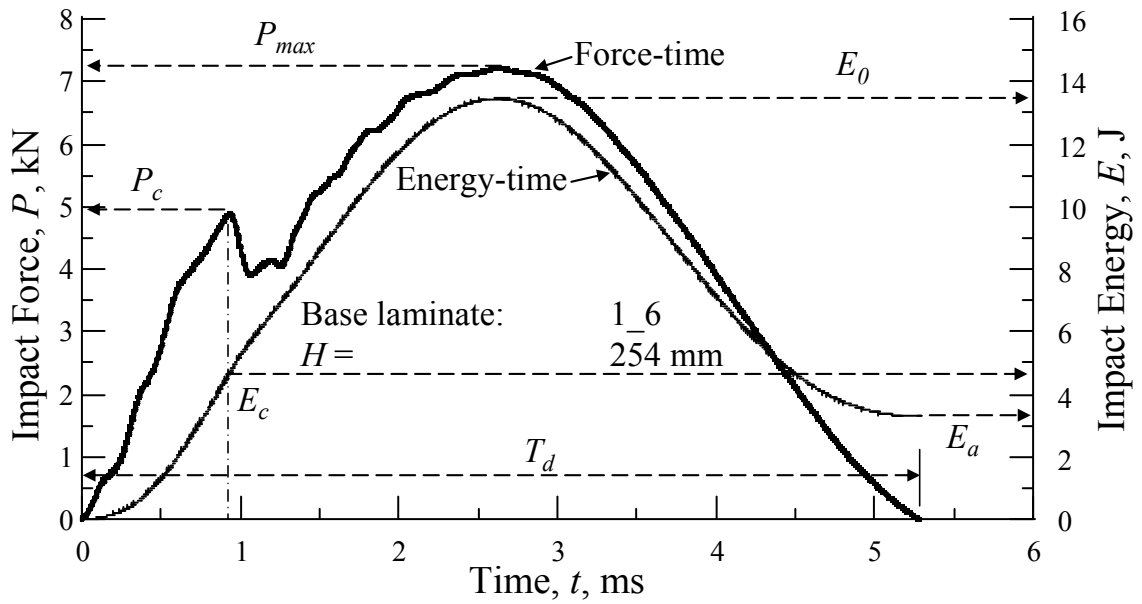


Figure 4.24. Graphical method for the determination of critical impact energy, E_c

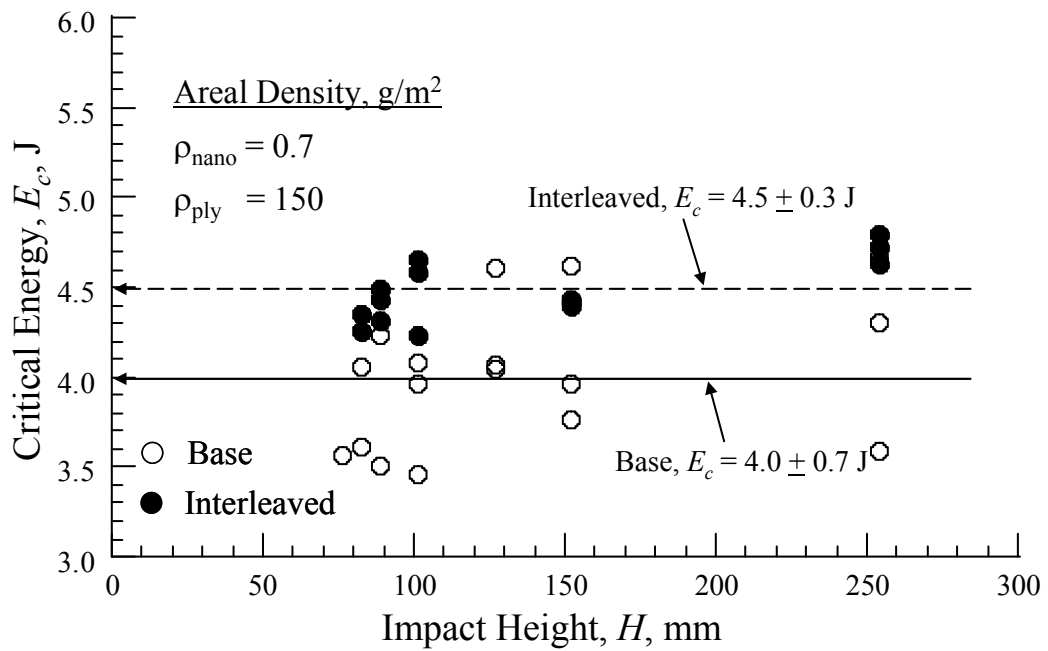


Figure 4.25. Critical energy versus impact height

The threshold impact force for base and interleaved laminates was lower than their respective critical force of 4.5 and 4.7 kN. The critical force was obtained from the impact force-time response and represented the force at damage onset at which stiffness changes can be detected (ASTM, 2008). The threshold force on the other hand, correlated to the damage area measured by the c-scan analysis to the impact force. These damages include matrix cracks which does not adversely degrade the stiffness of a plate. This explains the discrepancies between the critical and threshold forces. Using the threshold impact force, interleaving improved the impact resistance by only 13% when a 0.7 g/m² nano-fabric sheet was used, as against an increase from 1.0 to 1.6 kN when interleaved with 1.8 g/m² nano-fabric sheet. This represents an improvement of 60% (Akangah et al, 2010). Furthermore, the preliminary study showed that the impact damage growth rate reduced from 140 to 60 mm²/kN, representing a 57% improvement. This discrepancy could be due to the low fabric areal density used in this present study and the differences between the impactor–plate mass ratio (8 in the preliminary study as against 84 in the present study). Feraboli (2006a) recommended a ratio in the range of 10 to 20.

4.5.3.4 Contact Duration

The total contact duration (T_d) which is the time of the first mode of oscillation, was measured by considering the time elapse between two consecutive zero forces as previously shown in Figure 4.24. The contact duration for the base and interleaved laminates are listed in Table 4.5. For $H = 57$ and 64 mm for the base laminate, and for $H = 57, 64$ and 76 mm for the interleaved laminate, the average contact duration for the undamaged part was 4.78 ms for both laminates, indicating that contact duration was

unchanged during elastic impact events. However, for $H = 76$ and 83 mm and greater, the contact duration ranged from 5.3 to 5.5 ms for the base laminate and from 4.7 to 5.5 ms for the interleaved laminate.

Table 4.5. Contact durations for base and interleaved laminates

Height, H , mm	Duration, T_d , ms	
	Base	Interleaved
57	4.79	4.75
	4.74	4.82
	--	4.72
64	5.17	4.76
	5.08	4.77
	--	4.79
76	5.32	4.78
	--	4.72
	--	4.82
83	5.37	5.03
	5.29	4.74
	--	4.79
89	5.43	5.14
	5.36	5.09
	--	5.18
102	5.43	5.28
	5.40	5.29
	5.35	5.34
127	5.40	--
	5.39	--
	5.37	--
152	5.45	5.31
	5.47	5.33
	5.38	5.31
254	5.35	5.50
	5.28	5.21
	5.26	5.47
	5.48	--

The results from Table 4.5 are plotted in Figure 4.26 showing the contact duration versus impact height. For elastic impact regime, the average contact duration for both the base and the interleaved laminate was 4.78 ms. The threshold impact height for the base laminate was 65 mm and for the interleaved laminate was approximately 82 mm. This represented an increase of 26%. In the inelastic impact regime, the average contact duration for both the base and the interleaved laminates increased gradually, indicating increasing damage as impact height increased.

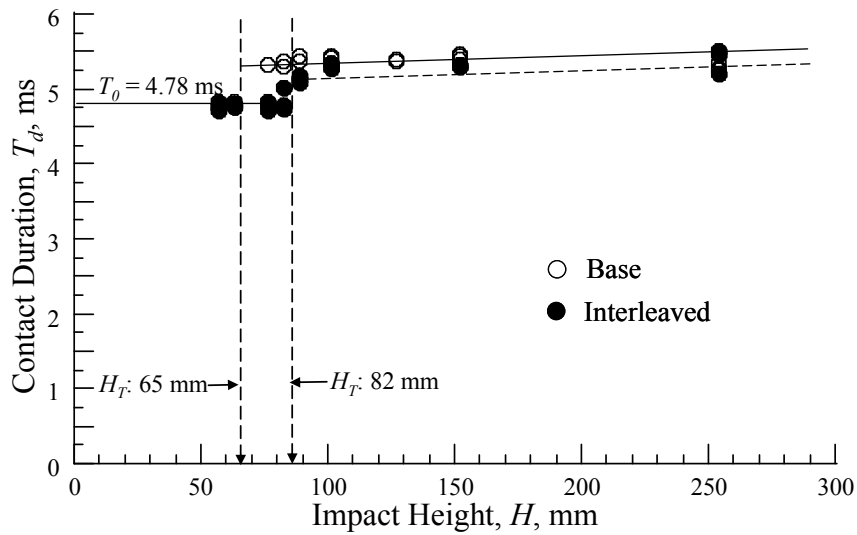


Figure 4.26. Contact duration versus impact height

4.6 Summary

Twenty-four ply quasi-isotropic composite laminates of the base and the interleaved AS4/3501-6 composite laminates with simply-supported arrangement were impact-tested to assess the improvements in impact damage resistance of these composite

specimens. The interleaved laminate was produced by electrospun Nylon 66 nano-fabric with areal density of 0.7 g/m^2 . The impact velocity ranged from 1.03 to 2.22 m/s and the height ranged from 54 to 254 mm. The impactor mass was 5.41 kg. The following observations were arrived at regarding the influence of interleaving on the impact damage resistance:

- The critical force increased from 4.5 to 4.7 kN by interleaving, representing an improvement of 4.4%.
- The critical energy increased from 4.0 to 4.5 J, which was an improvement of 12.6%.
- The threshold impact height, force and energy were approximately 65 mm, 4.0 kN and 3.0 J, respectively for the base specimen and 82 mm, 4.5 kN and 4.0 J, respectively for the interleaved specimen.
- Within the range of impact energies considered, the maximum impact forces for the interleaved specimen were greater than those of the base specimen, but the differences were gradually eroded at higher impact energies.
- Visual inspection showed that first fiber breakage occurred at the impact height of 89 for the base laminate and at 152 mm interleaved laminate, representing a 71% improvement.

CHAPTER 5

COMPRESSION AFTER IMPACT (CAI) TEST

5.1 Introduction

Damage tolerance of a structure is its ability to carry loads after sustaining damage. Presently, impact damage tolerance of a composite laminate is measured using the ASTM compression after impact (CAI) test. In this study, various degrees of damage were inflicted to the laminate by low-velocity impact as presented in Chapter Four. The residual compressive strengths of these laminates were determined using CAI test according to the ASTM D7137D/7137M-07 Standard. From these compression strengths, the damage tolerance and resistance to damage growth rates were obtained for the base and the polymer nano-fiber interleaved laminates.

5.2 Test Specimen

Impact damaged specimen tested in CAI are listed in Table 4.1. The damage ranged from barely visible indentation to extensive delamination to fiber breakage. The test specimen configuration is the same as that of the specimen used for impact testing, that is, 102 mm width, 152 mm length and about 4.14 mm thickness. Table 3.1 lists the dimensions of the test specimens. Prior to conducting the CAI test, the baseline compression strength of undamaged laminates was determined using ASTM D3410/D3410M-03 Standard. The details of the test and compression strengths are given in Appendix A. The average compressive strength, the standard deviation of the undamaged base laminate was 650 MPa (22) and that of the interleaved laminate was 620

MPa (31). At a confidence level of 95% and degree of freedom of 5, the experimental error was determined to be 60 for the undamaged base laminate and 80 for the undamaged interleaved laminate. The compressive strength of the undamaged laminate is the weighted average of the base and interleaved laminates and this was found to be 635 MPa.

5.3 Test Apparatus

The CAI test was originally developed by the Boeing Company and adapted by the ASTM D30 Sub-Committee (Instron, 2011). The details of the test and its limitations are given in the standard. A schematic and photograph of the test fixture are shown in Figure 5.1. The details of how the specimen was supported on the sides are shown in Figure 5.2.

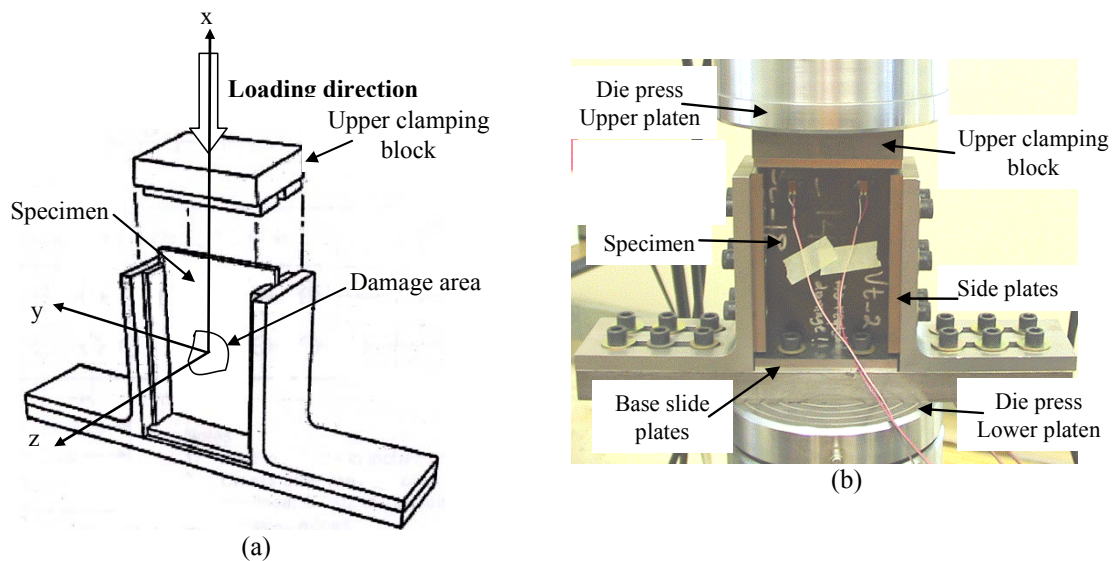


Figure 5.1. Compression After Impact (a) Schematic of test fixture and (b) Photograph of test fixture

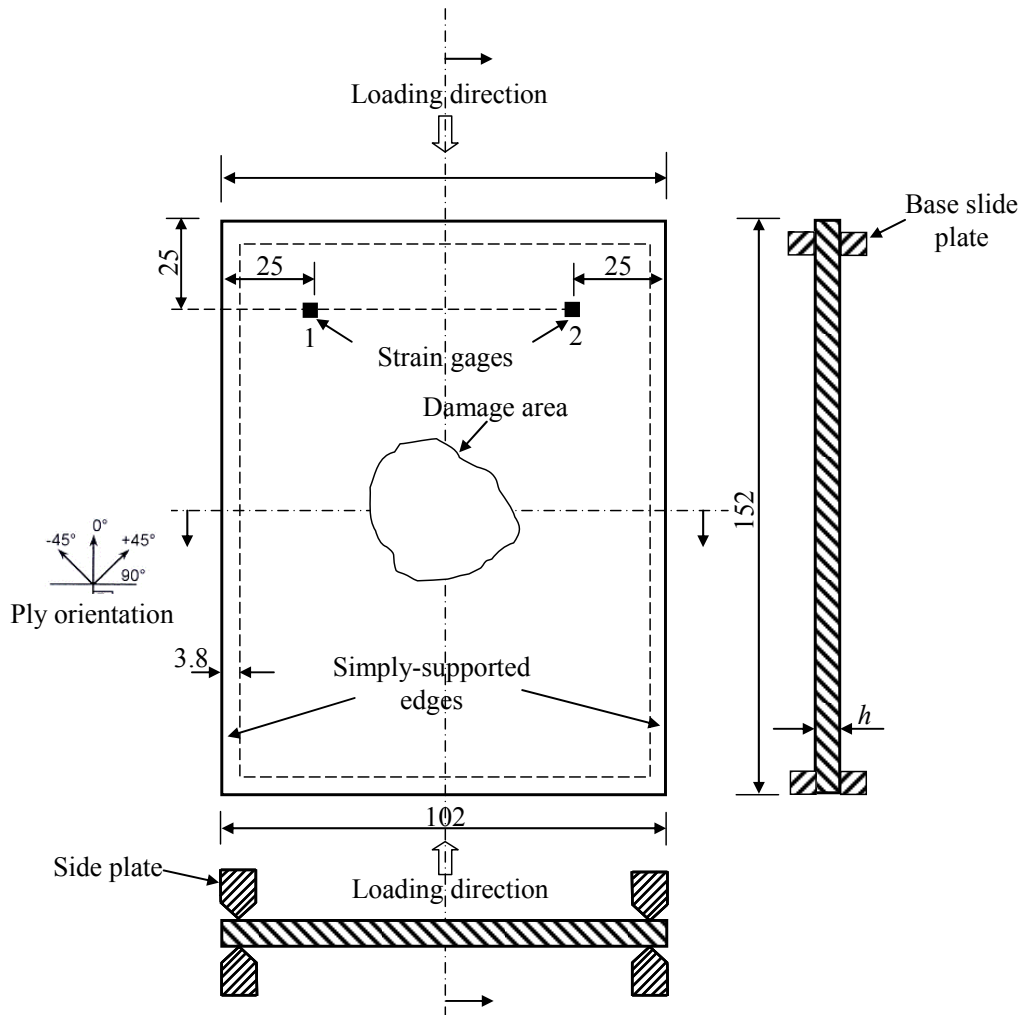


Figure 5.2. Details of clamping and strain gages location. Gages #4 and 3 located behind gages #1 and #2 (dimensions in mm)

The side plates are knife edged supports which restrain the out-of-plane bending due to buckling of the specimen during testing. The upper and bottom clamping blocks are designed to keep the specimen aligned and allowed it to undergo compressive deformation. The specimen is slightly taller than the fixture to accommodate compression deformation. The specimens were instrumented with four strain gages to measure the

bending and axial strains. The locations of strain gages were towards the upper end of the specimen on both the front and back faces and they are shown in Figure 5.2. Strain gages 1 and 2 are on the front faces and gages 3 and 4 are on the back faces of the specimen.

The average axial strain is given by $\varepsilon_a = \frac{\varepsilon_1 + \varepsilon_2 + \varepsilon_3 + \varepsilon_4}{4}$, and the bending strain is

given by $\varepsilon_b = \left| \frac{(\varepsilon_1 + \varepsilon_2) - (\varepsilon_3 + \varepsilon_4)}{4} \right|$. The percentage bending strain, $\frac{\varepsilon_b}{\varepsilon_a} \times 100$, at or near

the maximum applied load indicates out-of-plane bending. The maximum bending strains calculated for typical tests are listed in Table 5.1. These values are within the maximum bending strain of 10% allowed in the standard.

Table 5.1. Percentage bending strain of base and interleaved test laminates

Base				Interleaved			
ID#	ε_a	ε_b	$\frac{\varepsilon_b}{\varepsilon_a} \times 100\%$	ID#	ε_a	ε_b	$\frac{\varepsilon_b}{\varepsilon_a} \times 100\%$
1_14	7,934	351	4.4	P1_2	7,103	641	9.0
2_10	8,958	778	8.7	P1_14	11,393	741	6.5
1_5	13,034	795	6.1	P2_10	10,587	715	6.7

5.4 Testing

CAI tests were conducted using the MTS Universal Testing Machine. The impacted test specimen was mounted in the test fixture and aligned to prevent bending. The specimen was supported using the side and base plates, and these plates were initially secured by hand-tightening their respective screws. The upper block was gently

installed taking care not to damage the specimen. The fixture was placed gently on the lower platen of the test machine and aligned with the vertical axis of the machine. A compressive preload force of 450 N was applied to the upper block to guarantee that all loading surfaces were in contact. This compressive preload force was later reduced to 150 N, the fixture screws were tightened to the recommended torque of 7 Nm and the force and strain gage readings were re-zeroed. A displacement control method was used and the specimen was loaded at the rate of 0.02 mm/s. The force, cross-head displacement and strains were recorded at every 0.2 s until the specimen failed. From the load-displacement data, the maximum compression force (P_{max}) was extracted and used to calculate the residual compressive strength (F_{RC}).

$$F_{RC} = \frac{P_{max}}{wh} \quad (5.1)$$

where w and h are the width and thickness of the test specimen in mm, respectively.

During the testing, loud cracking sounds could be heard as a result of matrix cracking, fiber-matrix debonding, delamination and fiber breakage. After test, each specimen was visually inspected for the failure mode, area and location of failure. A typical stress- displacement of the cross-head is shown in Figure 5.3. The specimen failed immediately after the maximum load was reached. This maximum load was used to calculate the residual compressive strength (F_{RC}) of the laminate. Figures 5.4 to 5.7 show the compressive stress versus displacement for the base and the interleaved laminates. From the figures, it is observed that, the residual compressive strength decreases as the impact height increases.

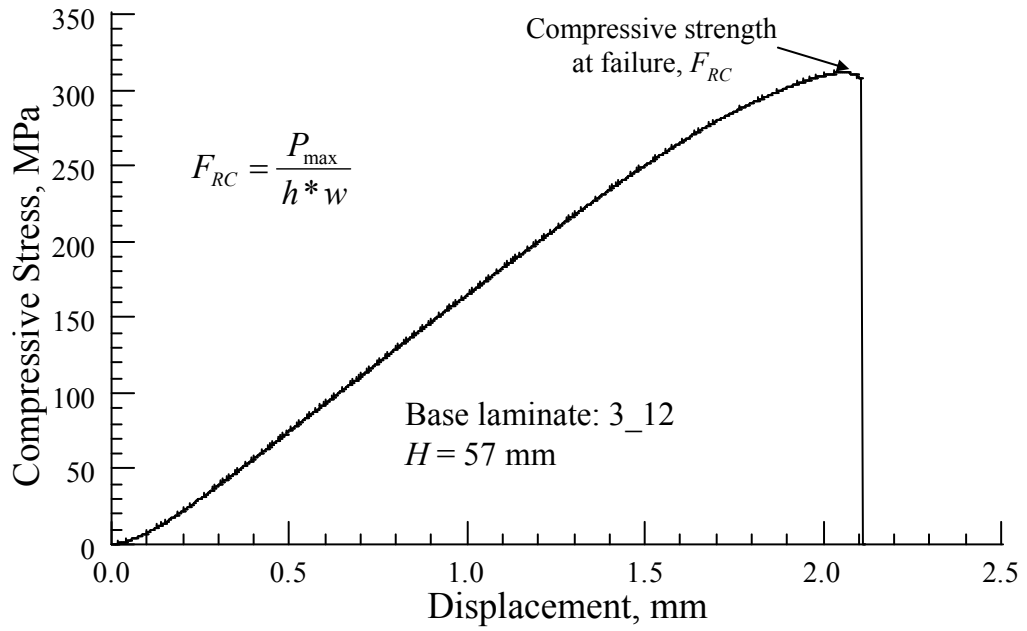


Figure 5.3. Typical compressive stress versus displacement at $H = 57$ mm

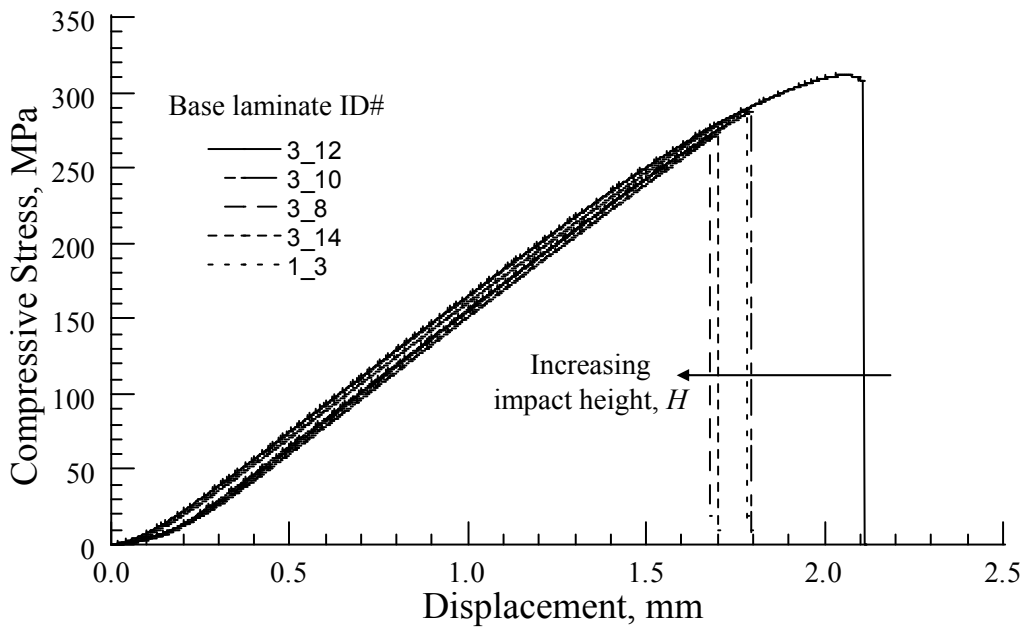


Figure 5.4. Compressive stress versus displacement response of impact damaged base laminates for low impact heights

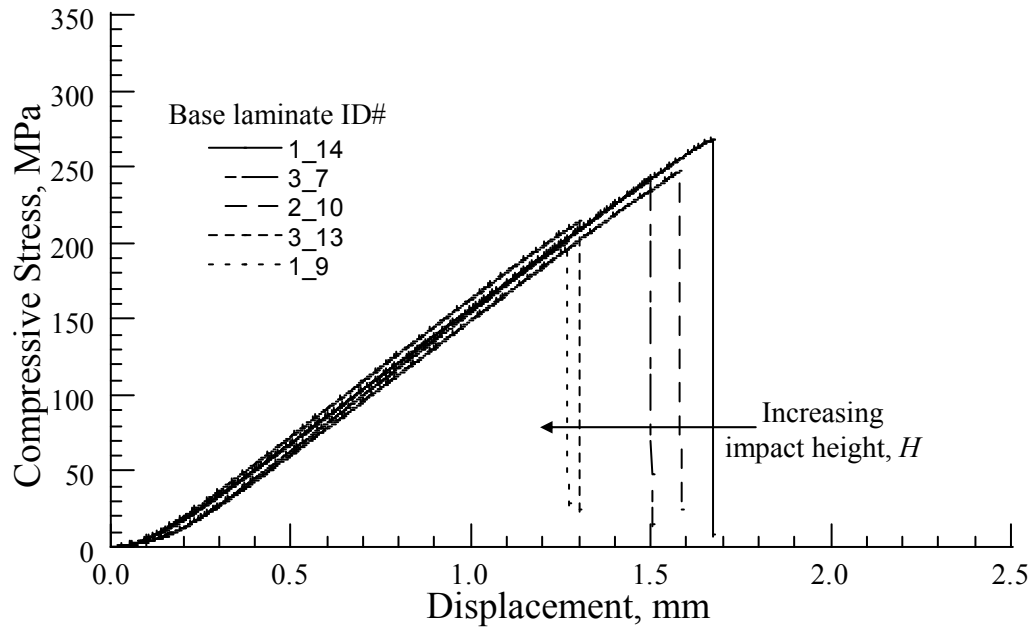


Figure 5.5. Compressive stress versus displacement response of impact damaged base laminates for high impact heights

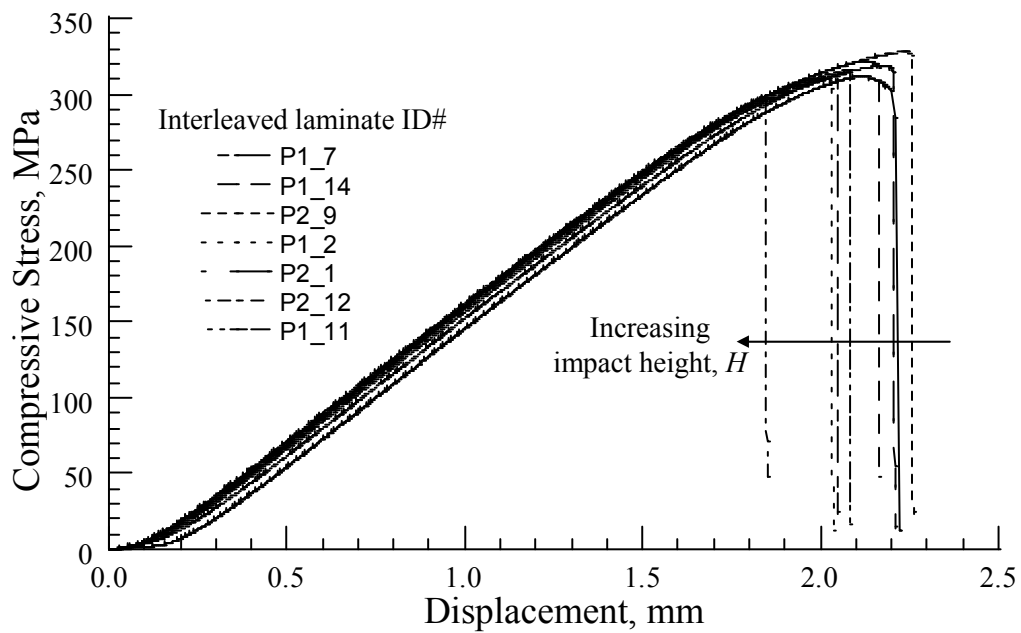


Figure 5.6. Compressive stress versus displacement response of impact damaged interleaved laminates for low impact heights

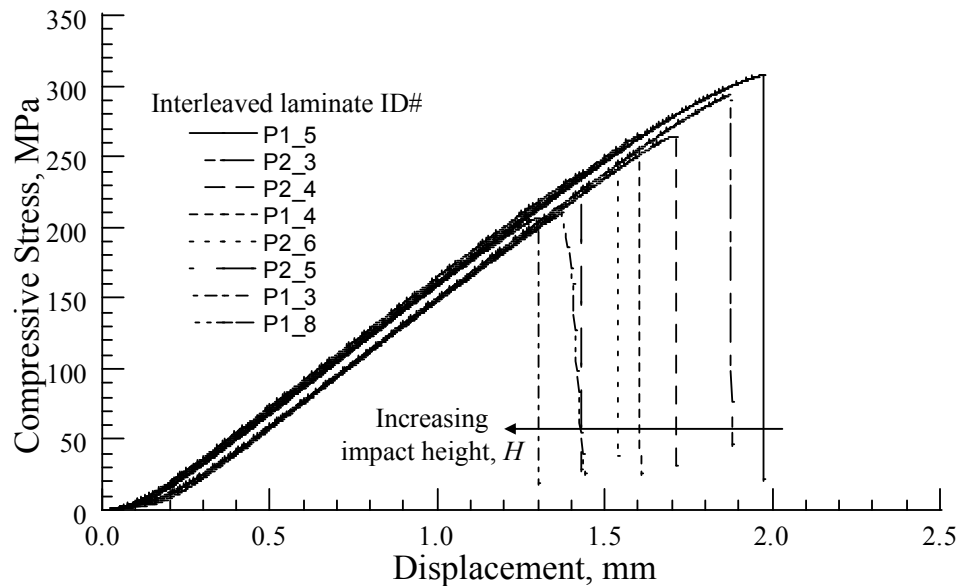


Figure 5.7. Compressive stress versus displacement response of impact damaged interleaved laminates for high impact heights

5.5 Results and Discussion

5.5.1 Visual Inspection

Visual inspection of the test specimen showed that compression failures can be classified into edge-crushing referred to as edge-failure and delamination across the width of the specimen at the impacted site referred to as failure at impact site. These failures are shown in Figure 5.8 for the base laminate and in Figure 5.9 for the interleaved laminate. Edge-crushing is not an intended failure mode, but occurred nevertheless because of the concentrated contact stresses. An edge view of the compression failure of the base laminate is shown in Figure 5.10 and that of the interleaved laminate is shown in Figure 5.11. Typical kink and shearing are seen for both laminates. These are photographs of laminates with specimen failure.

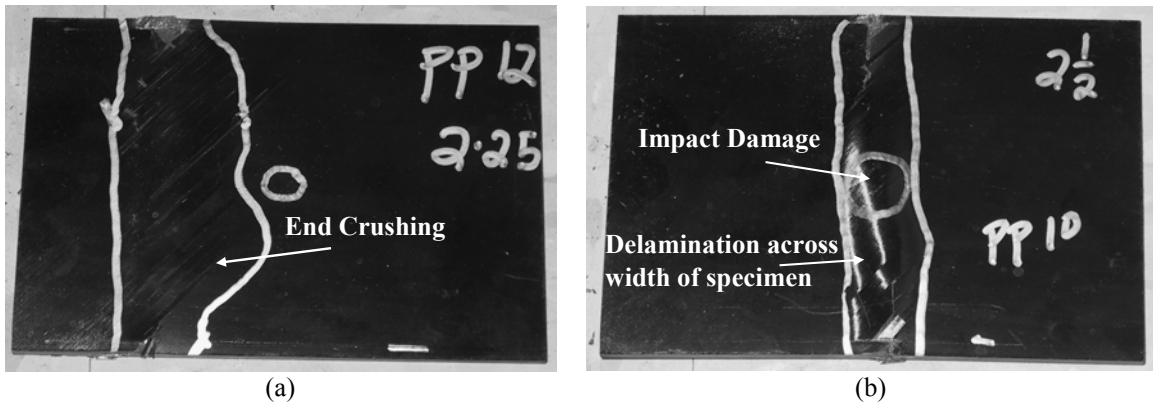


Figure 5.8. Failure modes of base laminates. (a) Edge-crushing failure and (b) failure at the impacted site



Figure 5.9. Failure modes of interleaved laminates. (a) Edge-crushing failure and (b) Failure at the impacted site

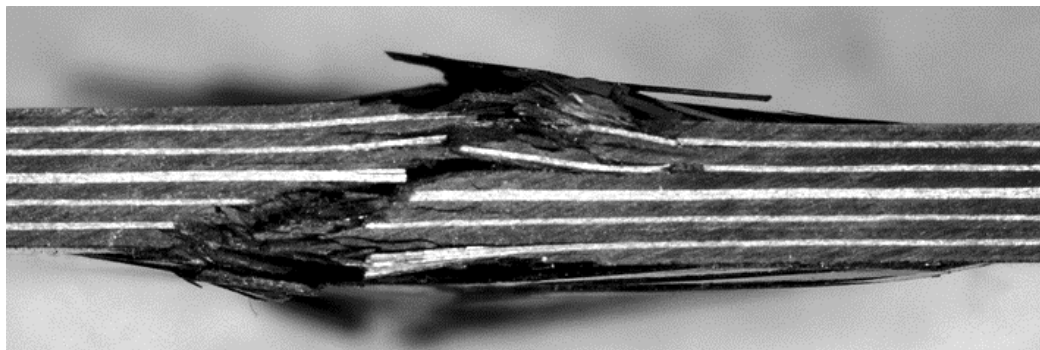


Figure 5.10. Edge view of a CAI test specimen (base)

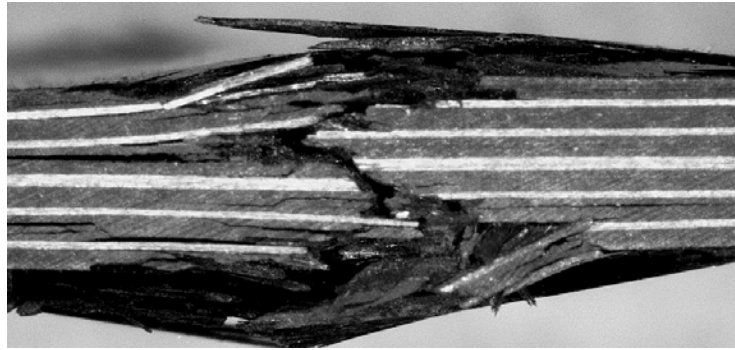


Figure 5.11. Edge view of a CAI test specimen (interleaved)

5.5.2 Residual Compressive Strength and Discussion

The impact height, residual compressive strength and impact energy of the base laminate is listed in Table 5.2 and those of the interleaved laminate are listed in Table 5.3. The average residual compression strength of the base and the interleaved laminates with edge-failure represented approximately one-half the compression strength of the undamaged laminate (635 MPa). At impact height of 76 mm, the residual strength of the base laminate was reduced by 57% of the undamaged laminate compressive strength. At impact height of 83 mm, the residual strength of the interleaved laminate had reduced by 53% of the undamaged laminate compressive strength. At the maximum impact height, $H = 254$ mm, the residual strengths of the base and the interleaved laminates were reduced to 32% and 33%, respectively. The results from the tables indicated that at the maximum impact height, the residual compressive strength is about one-third of the compressive strength of the undamaged laminate. This suggests that for large impact damage in a quasi-isotropic laminate, the minimum compressive strength is one-third of the undamaged laminate.

Table 5.2. Residual compressive strength and failure modes for base laminates

Impact Height, H , mm	Residual Compression		Failure Mode	Impact Energy, E_0 , J
	Strength, F_{RC} , MPa	Ratio, F_{RC}/F_{IC}^*		
57	311.5	0.49	Edge failure	2.93
64	287.6	0.45		3.41
76	271.3	0.43	Failure at impact site	4.10
83	273.4	0.42		4.43
	288.4	0.45		4.36
89	267.7	0.42		4.85
102	242.8	0.38		5.38
127	248.0	0.39		6.84
152	214.1	0.34		8.07
254	200.8	0.32		13.50

* F_{IC} = 635 MPa, compression strength of undamaged base and interleaved laminates

Table 5.3. Residual compressive strength and failure modes for interleaved laminates

Impact Height, H , mm	Residual Compressive		Failure Mode	Impact Energy, E_0 , J
	Strength, F_{RC} , MPa	Ratio, F_{RC}/F_{IC}^*		
57	311.8	0.49	Edge failure	2.94
	312.5	0.49		2.98
64	322.0	0.51		3.35
	328.0	0.52		3.34
76	310.4	0.49		3.93
	318.8	0.50		3.93
83	297.4	0.47	Failure at impact site	4.26
	316.1	0.50		4.15
89	307.8	0.48		4.60
	293.7	0.46		4.53
102	264.5	0.42		5.46
	265.8	0.42		5.39
152	253.1	0.40		8.06
	238.0	0.37		7.97
254	206.9	0.33	13.26	
	210.2	0.33	13.33	

* F_{IC} = 635 MPa, compression strength of undamaged base and interleaved laminates

Alternatively, large impact damage in laminates can be treated as open hole in a wide laminate to estimate the strength, because the stress concentration factor in an open hole in a quasi-isotropic laminate is three, meaning that the open-hole compressive strength is a third of the undamaged laminate.

5.5.3 Plots

The compression failure strengths of the base and interleaved laminates are shown in Figures 5.12 and 5.13, respectively. The open symbols indicate the experimental compression failure strength of laminates with edge failure. The closed symbols indicate the experimental compression failure strength of laminates with specimen failure at the impact site. The average edge failure strength for the base and interleaved laminates are respectively, 300 and 320 MPa. The difference between the two values can be considered negligible and it can be concluded that the edge failure strength are the same. This value is the weighted average and was calculated to be 315 MPa representing one-half the compressive strength of the undamaged laminate (635 MPa). The impact threshold height is approximately 65 for the base laminate and 80 mm for the interleaved laminate. This confirms the impact threshold height obtained from the impact test. The normalized residual compressive strength is plotted against impact height and energy and shown in Figure 5.14. The impact height and energy have linear correspondence and either one could be used in interpreting the plot. At about 3.0 J impact energy level, the residual compressive failure strength of the base laminate degraded by about 55% while the residual compressive strength of the interleaved laminate did not degrade.

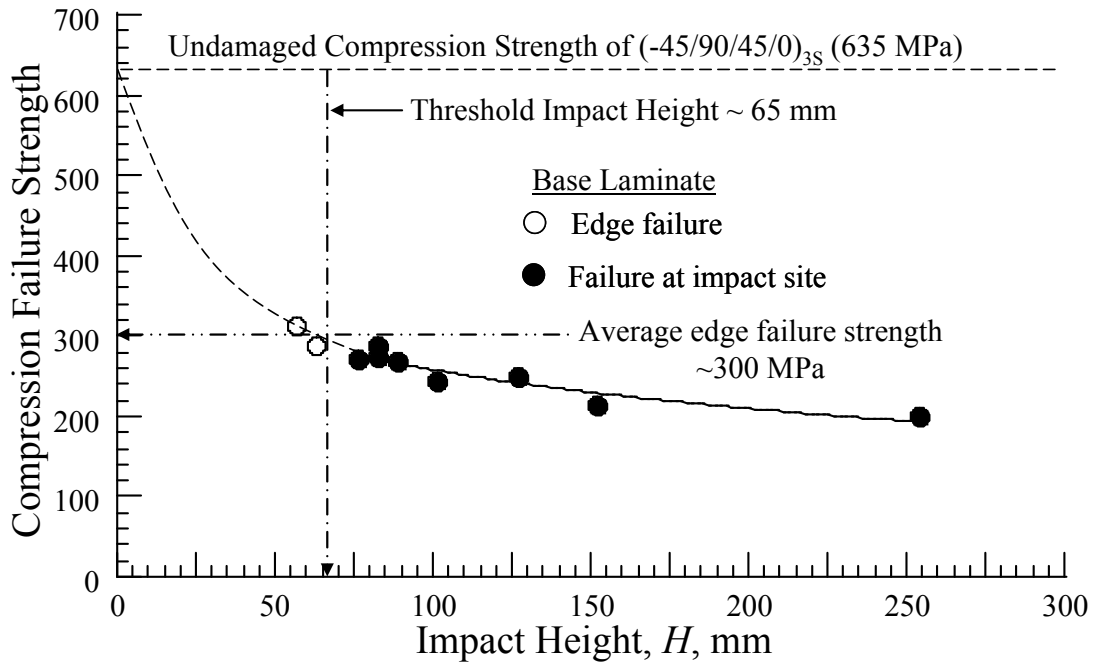


Figure 5.12. Compression failure strength of base laminate

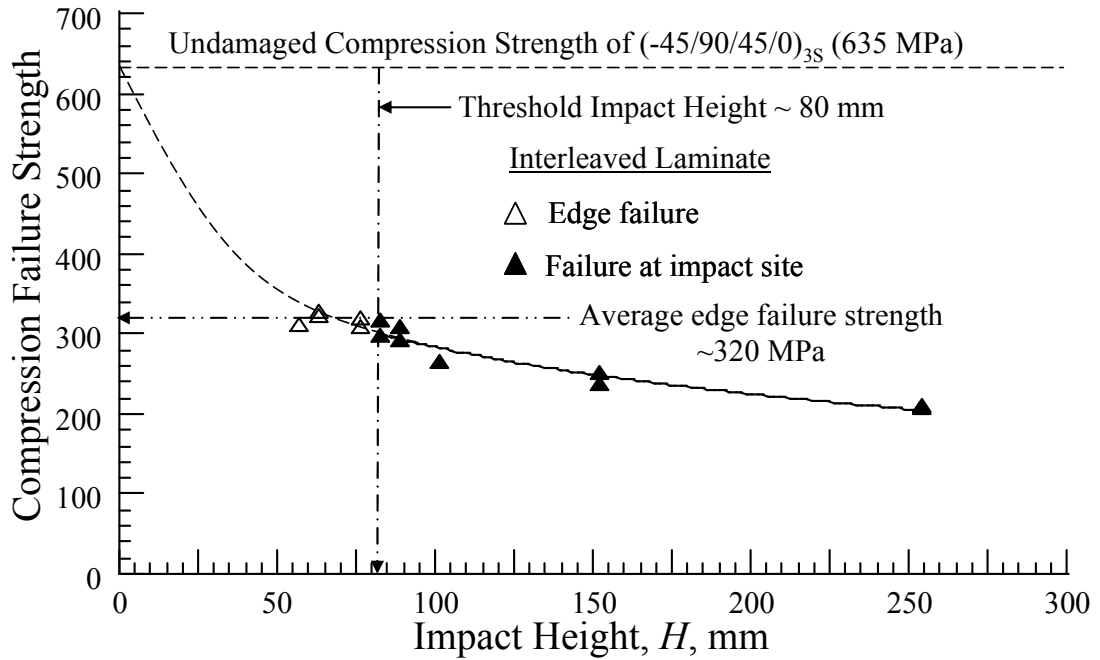


Figure 5.13. Compression failure strength of interleaved laminate

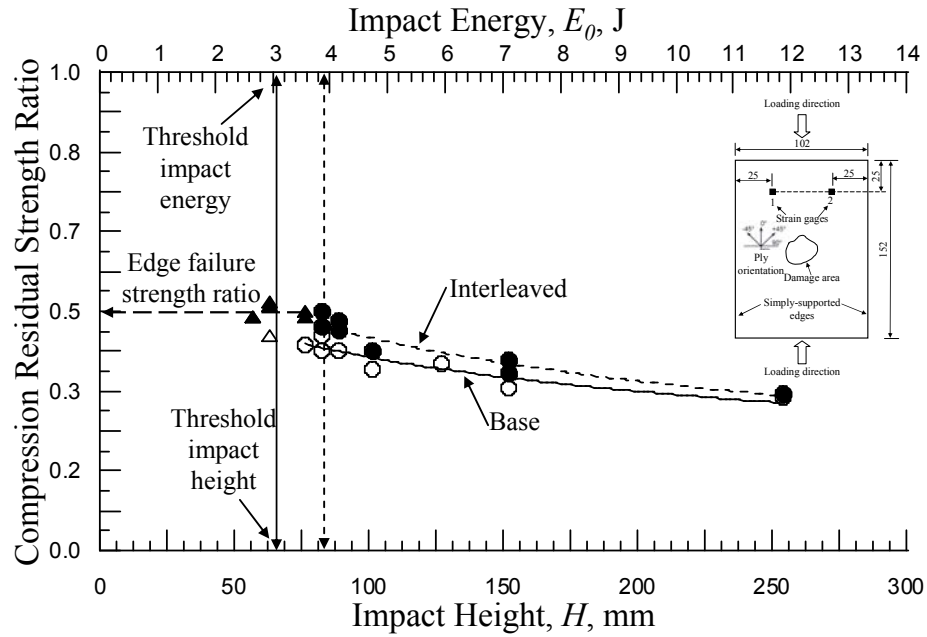


Figure 5.14. Compressive residual strength ratio versus impact height and energy

At about 4.0 J impact energy, the compression failure strength of the base and interleaved laminates degraded to 40% and 45%, respectively. For the range of impact energy investigated, the compression residual strength ratio of the interleaved laminate was consistently higher than that of the base laminate. Therefore, the interleaved laminate proved to be more impact damage tolerant than the base laminate.

5.4 Summary

The impact damage tolerant of a twenty-four ply quasi-isotropic interleaved composite laminate previously damaged by low-velocity impact test according was investigated. The composite laminate was interleaved by electrospun Nylon-66 nano-fabric with areal density of 0.7 g/m^2 . The impact velocity ranged from 1.03 to 2.22 m/s,

and the impact energy ranged from 3.0 to 13.5 J. The impactor mass was 5.41 kg. The impact tested specimen were compression tested to failure per ASTM Standard D7137D/7137M-07. The test results were within the guidelines of the ASTM standard.

The results led to the following conclusions:

- Edge failure occurred at 50% of the undamaged compression strength of the laminate. This was the same for both base and interleaved laminates.
- Threshold impact energy was 3.0 J for the base laminate and 4.0 J for the interleaved laminate.
- At 4.0 J threshold impact energy, the residual compression strength was 40% of the undamaged laminate for base laminate and 45% of the undamaged laminate for the interleaved laminate.

CHAPTER 6

CONCLUSIONS AND RECOMMENDATIONS FOR FUTURE WORK

6.1 Summary

The research presented in this dissertation has contributed to three areas:

1. Scaling of electrospinning to make large interleaved composite laminates,
2. Automated control of polymer flow for a given electric field and adjusting the distance between the tip of the syringe and the collector for a given polymer flow-rate by monitoring the collector voltage fluctuations, and
3. Introduction of a new concept of polymer nano-fiber interleaving to improve impact damage resistance and tolerance of the composite laminates. The damage resistance and tolerance were determined using weight impact tests and compression after impact studies.

6.1.1 Electrospinning

The original electrospinning had a circular drum collector and X-traverse syringe. The drum diameter and length were 114 mm (4.5 in) and 305 mm (12 in), respectively. This drum size was not suitable for making suitably-sized nano-fabric for specimens of the size recommended by ASTM. Therefore, the whole system was redesigned and fabricated to have drum diameter of 292 mm (11.5 in) and length of 813 mm (32 in). While building the new system, a collector monitoring system was introduced per the work many researchers. The resulting system was capable of spinning with single or dual syringes with X-traverse mechanism in preparing the nano-fabric of size 813 by 910 mm.

In this study, the fabricated nano-fabric had an average areal density of 0.7 g/m^2 which represented about 0.5% of the areal density of AS4/3501-6. This is small compared to the required ratio of 1 to 2%. However, the fabric was used to fabricate interleaved composites of twenty-four quasi-isotropic $(-45/90/45/0)_{3S}$ laminates. The nano-fabric was inserted between consecutive layers and placed on the surface of the top and bottom plies. The base laminate was also made to enable a comparison of the impact and damage tolerance performance.

6.1.2 Impact Study

The test specimen measured $102 \times 152 \text{ mm}$ ($4 \times 6 \text{ in}$) and the impact test section measured $76 \times 127 \text{ mm}$ ($3 \times 5 \text{ in}$). During the impact testing, the specimen support was assumed to be simply-supported. An impactor mass of 5.41 kg having hemispherical steel tup with a diameter of 25.4 mm (1.0 in) was used for the impact test. The impact energy ranged from 3.0 to 13.5 J . The results showed that the critical force for the base laminate was 4.5 kN and that for the interleaved laminate was 4.7 kN . The critical energy for the base and the interleaved laminates were 4.0 and 4.5 J , respectively. In the elastic impact regime, the contact durations for both test specimens were the same. The threshold impact height, force and energy for the base laminate were 65 mm , 4.0 kN , 3.0 J , respectively, and 82 mm and 4.5 kN , 4.0 J , respectively, for the interleaved laminate. The damaged growth rate with respect to impact force for the base laminate was $113 \text{ mm}^2/\text{kN}$ and $157 \text{ mm}^2/\text{kN}$ for the interleaved laminate. The damaged growth rate with respect to impact height was $2.10 \text{ mm}^2/\text{mm}$ for the base laminate and $2.46 \text{ mm}^2/\text{mm}$ for the interleaved laminate. Visual inspections showed that first fiber breakage occurred at the

impact heights of 89 mm and 152 mm for the base and the interleaved laminates, respectively.

6.1.3 Compression After Impact Test Results

All impacted test specimens were tested in compression to determine impact damage tolerance. CAI test results showed that the minimum impact energy to cause failure of the impact site was 3.0 J (or 65 mm impact height) for the base laminate whereas it was 4.0 J (or 80 mm impact height) for the interleaved laminate.

6.2 Conclusions

The effect of Nylon-66 nano-fiber interleaving on the impact damage resistance and tolerance of a twenty-four ply quasi-isotropic laminate was investigated. Interleaving did not significantly increase the thickness of the interleaved laminate. The impact height ranged from 57 to 254 mm and the impact velocity ranged from 1.03 to 2.22 m/s. All the impacted test specimens were tested in compression to failure. The following specific conclusions may be drawn from the results obtained in this work:

- By matching the electric field to the flow-rate, fiber morphology was improved, minimal and consistent fiber diameters were obtained, and electrospinning efficiency was improved by 20%.
- The impact damage resistance parameters improved by the following margins:
 - The critical force and energy increased by 5% and 13%, respectively.
 - The threshold impact height, force, and energy increased by 26%, 13% and 33%, respectively.

- The damage growth rate did not show any significant difference between the base and the interleaved laminates.
- The improvements in the impact damage tolerance parameters can be summarized as follows:
 - The compression strength of the undamaged laminate was 635 MPa.
 - The minimum energy to cause failure at the impact site increased by 25% improvement with respect to impact energy.
 - At high impact energies, both the base and the interleaved laminates degraded nearly to the same extent.

6.3 Recommendations for Future Work

6.3.1 Free-surface Electrospinning

There is the need to improve the electrospinning through-put. The free-surface electrospinning system presents a very viable method of increasing the through-put because the system does not use syringe pumps and needles. As a result, problems with needle clogging, uneven flow-rates would be eliminated. One significant drawback of the free-surface system is the large fiber diameter and the wide range between the minimum and maximum fiber diameters. The mechanical strength of the nano-fibers depends on fibers having high specific surface areas and high aspect ratios.

6.3.2 Functionalization of Nano-fibers

By adding a precursor to the polymer solution during electrospinning and subjecting the electrospun polymer nano-fibers to secondary treatment, the application of the functionalized polymer nano-fibers can be extended. Wang, Fu, & Li (2009) reported

the electrospinning of polymer nano-fibers with carbon nano-tubes as precursors to improve the mechanical properties of the nano-fibers. Although, no specific results in this study suggested poor adhesion of the nano-fibers with the epoxy resin, improvement to crack resistance may be achieved by surface treating the nano-fibers to improve adhesion.

6.3.3 Determination of Effective Nano-fabric Diameter and Areal Density

Goa et al (2007) identified the interleaving toughening mechanism as: geometrical effect of the interlayer, crack path deflection and crack tip shielding nano-fabric interleaving is by fiber bridging. Increasing the nano-fabric areal density and decreasing fiber diameter will enhance these mechanisms and therefore improved the interlaminar toughness. It is assumed that the dependence of interlaminar toughness on areal density will peak at some optimal areal density. The objective will be to find this optimal nano-fabric areal density. Zhang, Lin, & Wang (2010) reported that smaller fiber diameter led to stable crack growth and did not degrade the flexure property while, increased interleave thickness resulted in improved mode-I delamination toughness and degradation in flexure property. The smallest nano-fiber diameter that can be achieved depends very much on the type of electrospinning technology used and appropriate technology should be selected in any future work to achieve a nano-scale fiber diameter while increasing the nano-fiber through-put.

REFERENCES

- Abrate, S. (1998). *Impact on Composite Structures*. Cambridge: Cambridge University Press.
- Akangah, P., Lingaiah, S., & Shivakumar, K. (2010). Effect of Nylon-66 Nano-fiber Interleaving on Impact Damage Resistance of Epoxy/Carbon fiber Composite Laminates. *Composite Structures*, 92(6), 1432-1439.
- ASTM. (2008). Annual Book of ASTM Standards. *Standard Test Method or Measuring the Damage Resistance of a Fiber-Reinforced Polymer Matrix Composite to a Drop-Weight Impact Event, D 7136/D 7136M*. West Conshohocken, PA: ASTM Standards.
- Aymerich, F., Pani, C., & Priolo, P. (2006a). Damage Response of Stitched Cross-ply Laminates under Impact Loadings. *Engineering Fracture Mechanics*, 74(4), 500-514.
- Aymerich, F., Pani, C., & Priolo, P. (2006b). Effect of Stitching on the Low-velocity Impact Response of (03/903)s Graphite/Epoxy Laminates. *Composites Part A: Applied Science and Manufacturing*, 38(4), 1174-1182.
- Browning, C. E., & Schwartz, H. S. (1986). Delamination Resistant Composite Concepts. In Ed. J.M. Whitney (Ed.), *Composite Materials: Testing and Design, ASTM STP 893* (pp. 256-265). Philadelphia: American Society for Testing and Materials.
- Cartié, D. D. R., Troulis, M., & Partridge, I. K. (2006). Delamination of Z-pinned Carbon Fibre Reinforced Laminates. *Composites Science and Technology*, 66(6), 855-861.
- Chan, W. C., & Ochoa, O. O. (1989). Edge Delamination Resistance by a Critical Ply Termination. *Key Engineering Materials*, 37, 285-304.
- Chan, W.S. (1991). Design Approaches for Edge Delamination Resistance in Laminated Composites. *Jl. of Composites Technology & Research*, 14(2), 91-96.
- Christoforou, A. P. (2001). Impact Dynamics and Damage in Composite Structures. *Composite Structures*, 52(2), 181-188.
- Daniel, I. M., & Ishai, O. (2005). *Engineering Mechanics of Composite Materials*. NY: Oxford University Press.
- Davies, G. A. O., Hitchings, D., & Zhang, X. (1999). *Damage Tolerance to Low Velocity Impact of Laminated Composites*. Application of Damage Tolerance Principles for Improved Airworthiness of Rotorcraft, Corfu, Greece.

- Davies, G. A. O., & Olsson, R. (2004). Impact on Composite Structures. *Aeronautical Jl*, 108(1089), 541-563.
- Davies, G. A. O., Zhang, X., Zhou, G., & Watson, S. (1994). Numerical Modelling of Impact Damage. *Composites*, 25(5), 342-350.
- De Vrieze, S., Van Camp, T., Nelvig, A., Hagström, B., Westbroek, P., & De Clerck, K. (2009). The Effect of Temperature and Humidity on Electrospinning. *Journal of Materials Science*, 44(5), 1357-1362.
- Delfosse, D., & Poursartip, A. (1997). Energy-based Approach to Impact Damage in CFRP Laminates. *Composites Part A: Applied Science and Manufacturing*, 28(7), 647-655.
- Feraboli, P., & Kedward, K. T. (2004). Enhanced Evaluation of the Low-velocity Impact Response of Composite Plates. *AIAA Jl*, 42(10), 2143–2152.
- Feraboli, P. (2006a). Some Recommendations for the Characterization of the Impact Performance of Composite Panels by means of Drop Tower Impact Testing. *Journal of Aircraft*, 43(6), 1710-1718.
- Feraboli, P., & Kedward, K.T. (2006). A New Composite Structure Impact Performance Assessment Program. *Composites Science and Technology*, 66(10), 1336-1347.
- Feraboli, P. J., Ireland, D. R., & Kedward, K. T. (2004). *The role of Peak Force and Impact Energy in Low Velocity Impact Events*. 45th AIAA/ASME/ASCE/AHS/ASC Structures, Dynamics and Materials Conference, Palm Springs, CA.
- Feraboli, P. (2006b). Modified SDOF Models for Improved Representation of the Impact Response of Composite Plates. *Journal of Composite Materials*, 40(24), 2235-2255.
- Fuoss, E., Straznicky, P. V., & Poon, C. (1998). Effects of Stacking Sequence on the Impact Resistance in Composite Laminates -- Part 1: Parametric Study. *Composite Structures*, 41(1), 67-77.
- Gao, F., Jiao, G., Lu, Z., & Ning, R. (2007). Mode II Delamination and Damage Resistance of Carbon/Epoxy Composite Laminates Interleaved with Thermoplastic Particles. *Journal of Composite Materials*, 41(1), 111-123.
- Greszczuk, L. B. (1982). *Impact Dynamics*. NY: John Wiley.
- Herup, E. J. (1996). *Low-velocity Impact on Composite Sandwich Plates*. Unpublished doctoral dissertation, Air Force Institute of Technology (AU), Wright–Patterson AFB, OH.
- Hojjo, M., Matsuda, S., Tanaka, M., Ochiai, S. & Murakami, A. (2006). Mode-I

Delamination Fatigue Properties of Interlayer-toughened CF/epoxy Laminates. *Composites Science and Technology*, 66(5), 665-675.

Howard, W. E., Gossard, T., & Jones, R. M. (1989). Composite Laminate Free-Edge Reinforcement with U-Shaped Caps, Part II: Theoretical-Experimental Correlation. *AIAA Jl*, 27(5), 617-623.

Hwang, J., Kwon, O., Lee, C., & Hwang, W. (2000). Interlaminar Fracture and Low-velocity Impact of Carbon/epoxy Composite Materials. *Mechanics of Composite Materials*, 36(2), 117-130.

Instron Corp. Measuring Damage Resistance of Composite to Drop Weight Impact Event (ASTM D7136/D7136), Retrieved March 15, 2011, from www.instron.com

Jones, R.M. (1999). *Mechanics of Composite Materials* (2 ed.). Philadelphia, PA: Taylor & Francis.

Karas, K. (1339). Platten unter seitlichem stoss. *Ing.-Arch.*, 10, 237-250.

Kim, R. Y. (1983). *Prevention of Free-edge*. Materials and Processes-Continuing Innovations: 28th National SAMPE Symposium and Exhibition, 12-14 Apr. 1983, Anaheim, CA.

Kuboki, T., Jar, P. Y. B., & Forest, T. W. (2003). Influence of Interlaminar Fracture Toughness on Impact Resistance of Glass Fibre Reinforced Polymers. *Composites Science and Technology*, 63(7), 943-953.

Kwon, Y. S., & Sankar, B. V. (1993). Indentation-Flexure and Low-Velocity Impact Damage in Graphite Epoxy Laminates. *Journal of Composite Materials*, 15(2), 101-111.

Lee, E. H. (1941). Impact of a Mass Striking a Beam. *ASME Transaction Journal of Applied Mechanics*, 129-138.

Lifshitz, J. M., Gov, F., & Gandelman, M. (1995). Instrumented Low-velocity Impact of CFRP Beams. *International Journal of Impact Engineering*, 16(2), 201-215.

Lingaiah, S., Shivakumar, K. N., Sadler R., & Sharpe M. (2008). *Electrospinning of Nylon-66 Polymer Nanofabrics*. AIAA 2008-1787, Schaumburg, IL.

Lipson, C., & Sheth, J. N. (1973). *Statistical Design and Analysis of Engineering Experiments* (First ed.): McGraw-Hill.

Masters, J. E. (1989). Improved Impact and Delamination Resistance Through Interleafing. *Engineering Materials*, 37, 317-348.

Matsuda, S., Hojo, M., Ochiai, S., Murakami, A., Akimoto, H., & Ando, M. (1999).

- Effect of Ionomer thickness on Mode-I Interlaminar Fracture Toughness for Ionomer Toughened CFRP. *Composites Part A: Applied Science and Manufacturing*, 30(11), 1311-1319.
- Mouritz, A. P. (2003). Comment on the Impact Damage Tolerance of Stitched Composites. *Journal of Materials Science Letters*, 22(7), 519-521.
- Mouritz, A. P. (2007). Review of Z-pinned Composite Laminates. *Composites Part A: Applied Science and Manufacturing*, 38(12), 2383-2397.
- Munir, M. M., Iskandar, F., Khairurrijal, & Okuyama, K. (2009). High Performance Electrospinning System for Fabricating Highly Uniform Polymer Nanofibers. *Rev. Sci. Instrum*, 80, 026106-3.
- Munir, M. M., Iskandar, F., Khairurrijal, & Okuyama, K. (2008). A Constant-current Electrospinning System for Production of High Quality Nanofibers. *Rev. Sci. Instrum.*, 79, 093904-4.
- O'Brien, T. K. (1984). *Interlaminar Fracture of Composites*. Hampton, VA.
- O'Brien, T. K. (1990). Towards a Damage Tolerance Philosophy for Composite Materials and Structures. In S.P. Garbo (Ed.), *Composite Materials: Testing and Design* (9th ed., Vol. 1059, pp. 7-13). Philadelphia: ATSM STP.
- Odagiri, N., Muraki, T., & Tobukuro, K. (1988). *Toughness improved high-performance Torayca prepreg T800H/3900 Series*. 33rd Int SAMPE Symp., Society for the Advancement of Material and Process Engineering, Covina, CA.
- Olsson, R. (2000). Mass Criterion for Wave Controlled Impact Response of Composite Plates. *Composites Part A: Applied Science and Manufacturing*, 31(8), 879-887.
- Olsson, Robin. (2001). Analytical Prediction of Large Mass Impact Damage in Composite Laminates. *Composites Part A: Applied Science and Manufacturing*, 32(9), 1207-1215.
- Pagano, N. J (Ed.). (1989). *Interlaminar Response of Composite Materials* (Vol. 5). Amsterdam: Elsevier.
- Pagano, N. J., & Pipes, R. B. (1971). The Influence of Stacking Sequence on Laminate Strength. *Journal of Composite Materials*, 5(1), 50-57.
- Preston, J. L., & Cook, T. S. (1975). Foreign Object Impact Damage to Composites. *ASTM Special Technical Publication 568*, 49.
- Reneker, D. H., & Yarin, A. L. (2008). Electrospinning Jets and Polymer Nanofibers. *Polymer*, 49(10), 2387-2425.

- Salpekar, S. A., O'Brien, T. K., & Shivakumar, K. N. (1996). Analysis of Local Delaminations Caused by Angle Ply Matrix Cracks. *Journal of Composite Materials*, 30(4), 418-440.
- Samatham, R., & Kim, K. J. (2006). Electric Current as a Control Variable in the Electrospinning Process. *Polymer Engineering & Science*, 46(7), 954-959.
- Schoeppner, G. A., & Abrate, S. (2000). Delamination Threshold Loads for Low Velocity Impact on Composite Laminates. *Composites Part A: Applied Science and Manufacturing*, 31(9), 903-915.
- Sela, N., & Ishai, O. (1989). Interlaminar Fracture Toughness and Toughening of Laminated Composite Materials: A Review. *Composites*, 20(5), 423-435.
- Shin, M. Y. (2000). *Formation of Polymer Nanofibers from Electrified Fluid Jets*. Unpublished doctoral dissertation, MIT, Massachusetts.
- Shin, Y. M., Hohman, M. M., Brenner, M. P., & Rutledge, G. C. (2001). Experimental Characterization of Electrospinning: The Electrically Forced Jet and Instabilities. *Polymer*, 42(25), 09955-09967.
- Shivakumar, K., Lingaiah, S., Chen, H., Akangah, P., Swaminathan, G. & Russell, L. (2009). Polymer Nanofabric Interleaved Composite Laminates. *AIAA Jl*, 47(7), 1723-1729.
- Shivakumar, K., Lingaiah, S., Chen, H., Akangah, P., Swaminathan, G., & Sharpe, M. (2009). *Polymer Nanofabric Interleaved Composite Laminate*. 50th AIAA/ASMC/ASCS/AHS/ASC Structures, Structural Dynamic & Materials Conference, Palm Springs, CA.
- Shivakumar, K.N., Elber, W., & Illg, W. (1985a). Prediction of Impact Force and Duration Due to Low-Velocity Impact on Circular Composite Laminates. *Journal of Applied Mechanics*, 52(3), 674-680.
- Shivakumar, K. N., Elber, W., & Illg, W. (1985b). Prediction of Low-Velocity Impact in Thin Circular Laminates. *AIAA Jl*, 23(3), 442-449.
- Steeves, C. A., & Fleck, N. A. (2006). In-Plane Properties of Composite Laminates with Through-Thickness Pin Reinforcement. *International Journal of Solids and Structures*, 43(10), 3197-3212.
- Stevanovic, D. (2001). *Delamination Properties of a Vinyl-Ester/Glass Fibre Composite Toughened by Particulate-Modified Interlayers*. Unpublished doctoral dissertation, The Australian National University, Canberra.

- Suemasu, H., & Majima, O. (1996). Multiple Delaminations and their Severity in Circular Axisymmetric Plates Subjected to Transverse Loading. *Journal of Composite Materials*, 30(4), 441-453.
- Sun, C. T., & Chu, G. D. (1991). Reducing Free Edge Effect on Laminate Strength by Edge Modification. *Journal of Composite Materials*, 25(2), 142-161.
- Takeda, N., Kobayashi, S., Ogihara, S., & Kobayashi, A. (1999). Effects of Toughened Interlaminar Layers on Fatigue Damage Progress in Quasi-Isotropic CFRP Laminates. *International Journal of Fatigue*, 21(3), 235-242.
- Tan, T. M., & Sun, C.T. (1985). Use of Statical Indentation Laws in the Impact Analysis of Laminated Composite Plates. *Jl. Applied Mechanics*, 52, 6-12.
- Theron, S. A., Zussman, E., & Yarin, A. L. (2004). Experimental investigation of the governing parameters in the electrospinning of polymer solutions. *Polymer*, 45(6), 2017-2030.
- Timenshenko, S. (1913). Zur Frage nach der Wirkung eines Stosse auf einer Balken. *Z. Mathetical Physics*, 62, 198-209.
- Wang, H. S., Fu, G. D., & Li X. S. (2009). Functional Polymeric Nanofibers from Electrospinning. *Recent Patents on Nanotechnology*, 3, 21-31.
- Yamashitaa, Y., Miyakeb, H., Higashiyamab, A., & Tanakaa, A. .Practical use of Nanofibers Made By Electro-spinning Process. Retrieved August 25, 2010, from <http://elearning.lib.fcu.edu.tw/bitstream/2377/3895/1/ce05atc902007000024.pdf>
- Yan, X., & Gevelber, M. (2010). Investigation of Electrospun Fiber Diameter Distribution and Process Variations. *Journal of Electrostatics*, 68(5), 458-464.
- Yokozeki, T., Iwahori, Y., Ishibashi, M., Yanagisawa, T., Imai, K., Arai, M., Takahashi, T. (2009). Fracture Toughness Improvement Of CFRP Laminates by Dispersion of Cup-stacked Carbon Nanotubes. *Composites Science and Technology*, 69(14), 2268-2273.
- Zhang, J., Lin, T., & Wang, X. (2010). Electrospun Nanofibre Toughened Carbon/Epoxy Composites: Effects of Polyetherketone cardo (PEK-C) Nanofibre Diameter and Interlayer Thickness. *Composites Science and Technology*, 70(11), 1660-1666.
- Zhang, X., Hounslow, L., & Grassi, M. (2006). Improvement of Low-Velocity Impact and Compression-after-Impact Performance by Z-fibre Pinning. *Composites Science and Technology*, 66(15), 2785-2794.
- Zheng, D. (2007). *Low Velocity Analysis of Composite Laminated Plates*. Unpublished doctoral dissertation, University of Akron, Akron.

APPENDIX A

CHARACTERIZATION OF COMPRESSIVE PROPERTIES OF TEST LAMINATES

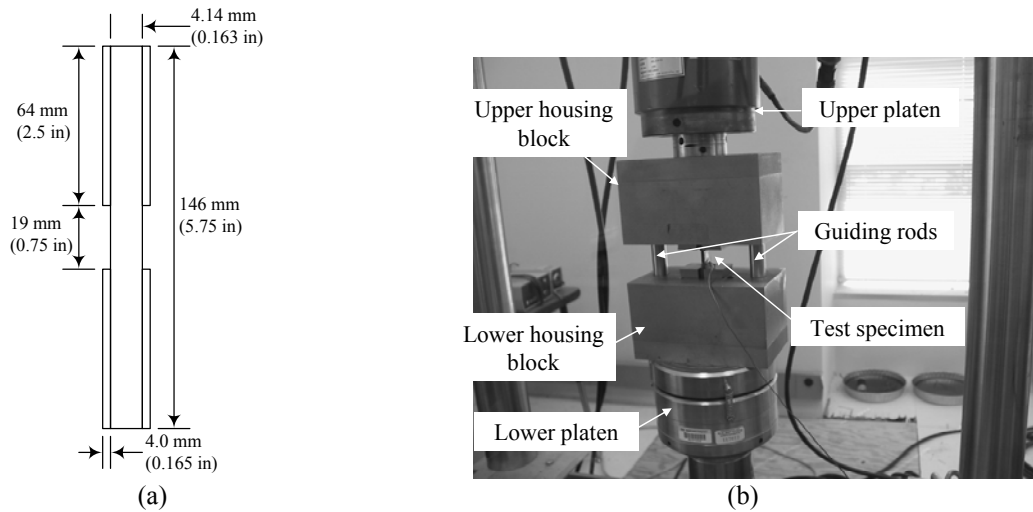


Figure A.1. Compression test specimen. (a) Schematic and (b) Compression testing of specimen

Table A.1. Summary of compressive strength of undamaged laminate

Test ID#	Base Compressive Strength, F_{1cs} MPa	Interleaved Compressive Strength, F_{1cs} MPa
1	646.9	581.2
2	637.0	615.7
3	649.0	603.9
4	690.7	628.0
5	642.1	665.4
	650 (22)*	620 (31)

*standard deviation

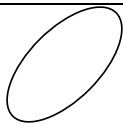
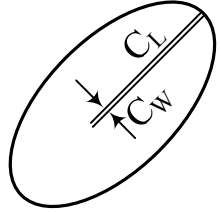
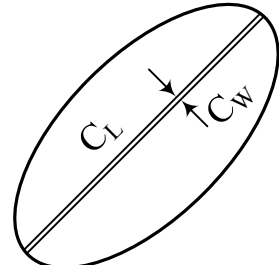
Since the results overlapped, there was no significant difference between the undamaged compressive strength of the base and interleaved laminates and the weighted average was calculated to be 635 MPa.

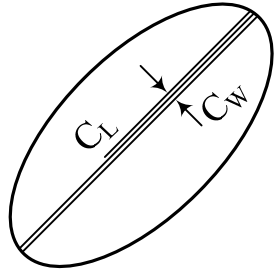
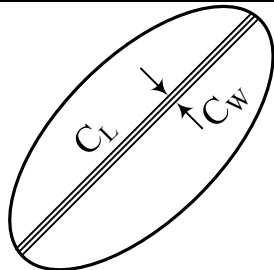
APPENDIX B

DAMAGE ASSESSMENT OF IMPACT TEST BASED ON VISUAL INSPECTION

Visual damage of the impacted laminates was seen clearly on the backside. The shape of the damage was approximated as elliptical with semi major and minor axes of length A and B , respectively. These details are listed under the “Comment” column. A strip of unidirectional delaminated ply was observed and its width and length were represented by C_L and C_W , respectively.

B.1 Base Specimens

Visual Impact Damage Assessment (Base Specimens)			
Impact		Front Surface	Back Surface Damage (mm)
Height, H , mm	Energy, E_0 , J	Indentation Depth, d , mm	Comments (Major axis $2A$; minor axis $2B$)
0-57	0-3.0	0.0	No Visible Damage
64-83	3.0-4.4	0.1	 No Visible Cracks; $2A = 18.5$; $2B = 14$
89	4.7-4.9	0.1	 Multiple Cracks, $C_L = 10$; $C_W = 5$ $2A = 23.5$; $2B = 14$
102	5.4-5.5	0.13	 Multiple Cracks, $C_L = 2A$; $C_W = 7$ $2A = 28$; $2B = 16$

152	7.9-8.1	0.15-0.18	 <p>Multiple Cracks, $C_L = 2A$, $C_W = 8$ $2A = 36$; $2B = 18$</p>
254	13.2-13.6	0.22	 <p>Elliptical Delamination, Multiple Cracks, $C_L = 2A$, $C_W = 11$ $2A = 40$; $2B = 23$</p>

B.2 Base Laminate Representative Photographs (back face damage)

Backface damage boundary and the length of fiber breakage were marked by white pen, and then the laminate was photographed. These images for different impact heights are shown below.



$H = 64$ mm (2.5 in)



$H = 76$ mm (3.0 in)



$H = 83$ mm (3.25 in)



$H = 89$ mm (3.5 in)



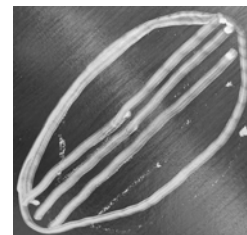
$H = 102$ mm (4.0 in)



$H = 102$ mm (4.0 in)

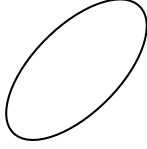
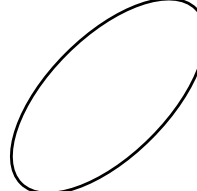
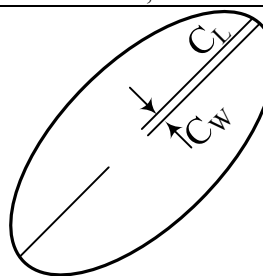
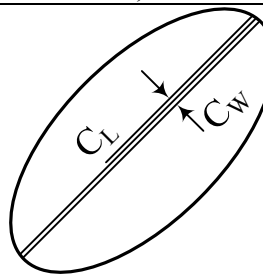


$H = 152$ mm (6.0 in)



$H = 152$ mm (10.0 in)

B.3 Interleaved Specimens

Visual Impact Damage Assessment (Interleaved Specimens)			
Impact		Front Surface	Back Surface Damage (mm)
Height, H , mm	Energy, E_0 , J	Indentation Depth, d , mm	Comments (Major axis $2A$; minor axis $2B$)
0-76	2.9-3.9	0.0	No Visible Damage
83	4.1-4.4	0.0-0.08	No Visible Damage
89	4.5—4.6	0.08—0.1	 No Visible Cracks $2A = 20$; $2B = 14$
102	5.4—5.6	0.13	 No Visible Cracks $2A = 17.5$; $2B = 15$
152	7.9—8.1	0.15	 Multiple Cracks, $C_L = 15$; $C_W = 5$ $2A = 22$; $2B = 20$
254	13.2—13.3	0.22	 Multiple Cracks, $C_L = 2A$, $C_W = 8$ $2A = 42$; $2B = 18.5$

B.4 Interleaved Laminate Representative Photographs (back face damage)



$H = 89 \text{ mm (3.5 in)}$



$H = 89 \text{ mm (3.5 in)}$



$H = 102 \text{ mm (4.0 in)}$



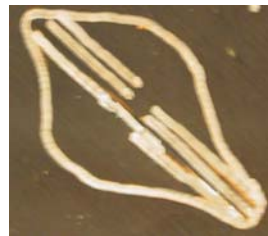
$H = 102 \text{ mm (4.0 in)}$



$H = 152 \text{ mm (6.0 in)}$



$H = 152 \text{ mm (6.0 in)}$



$H = 254 \text{ mm (10.0 in)}$

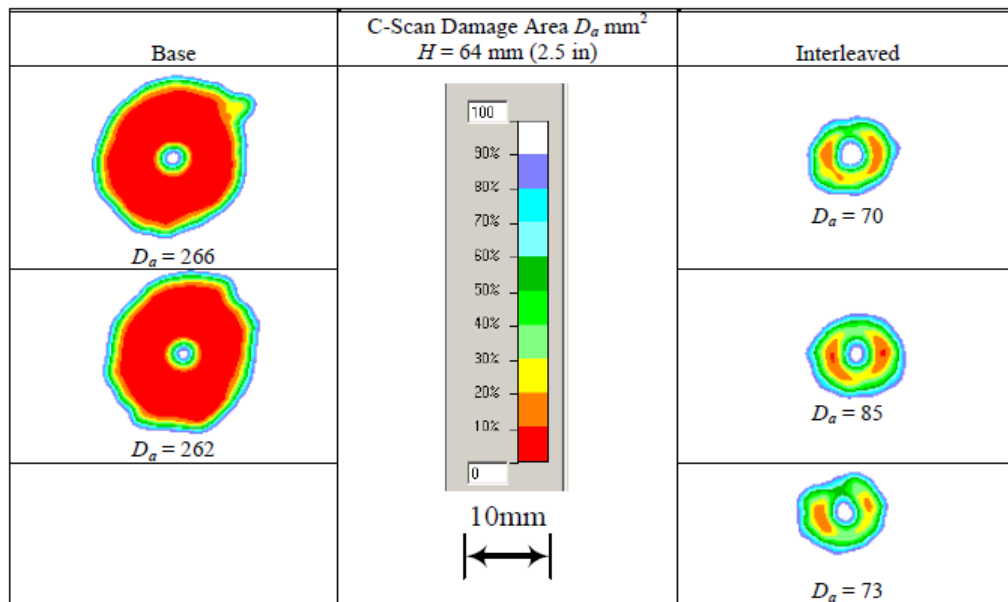
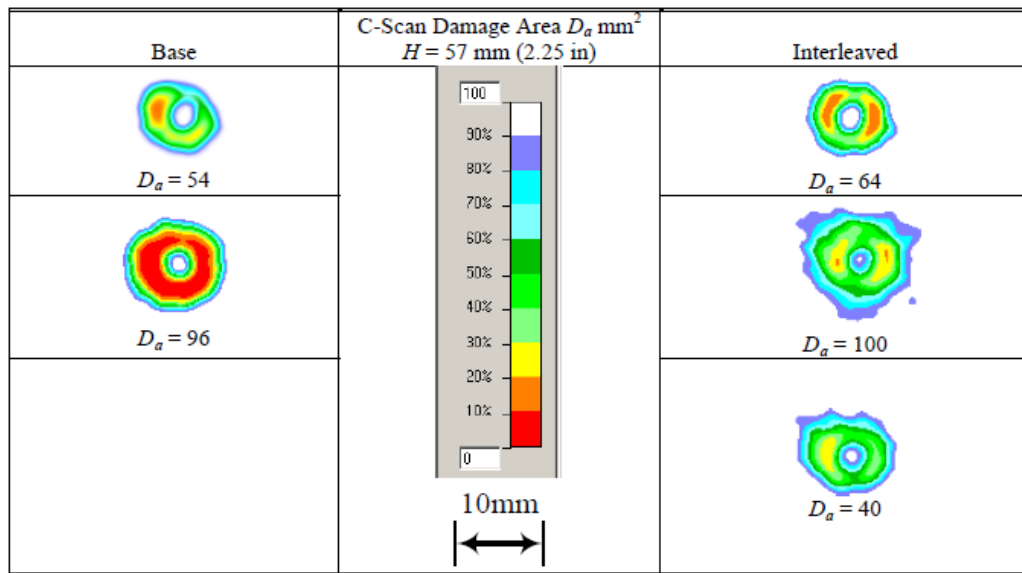


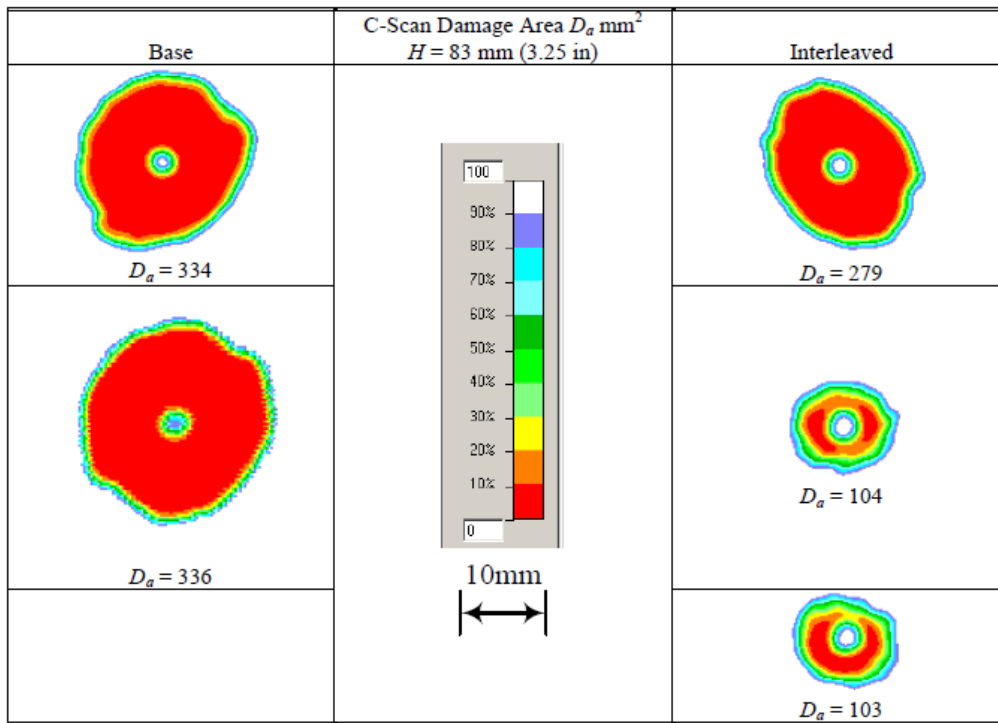
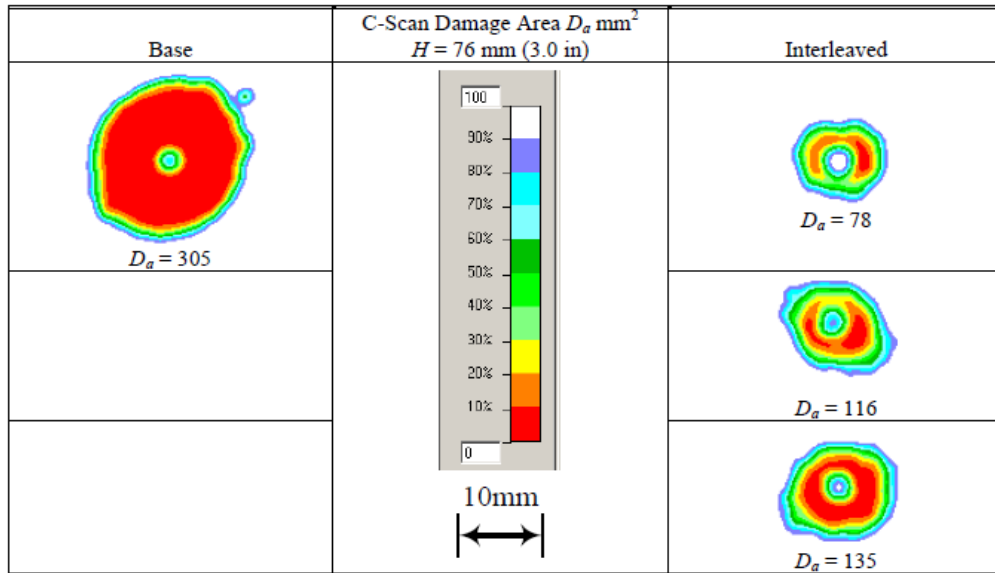
$H = 254 \text{ mm (10.0 in)}$

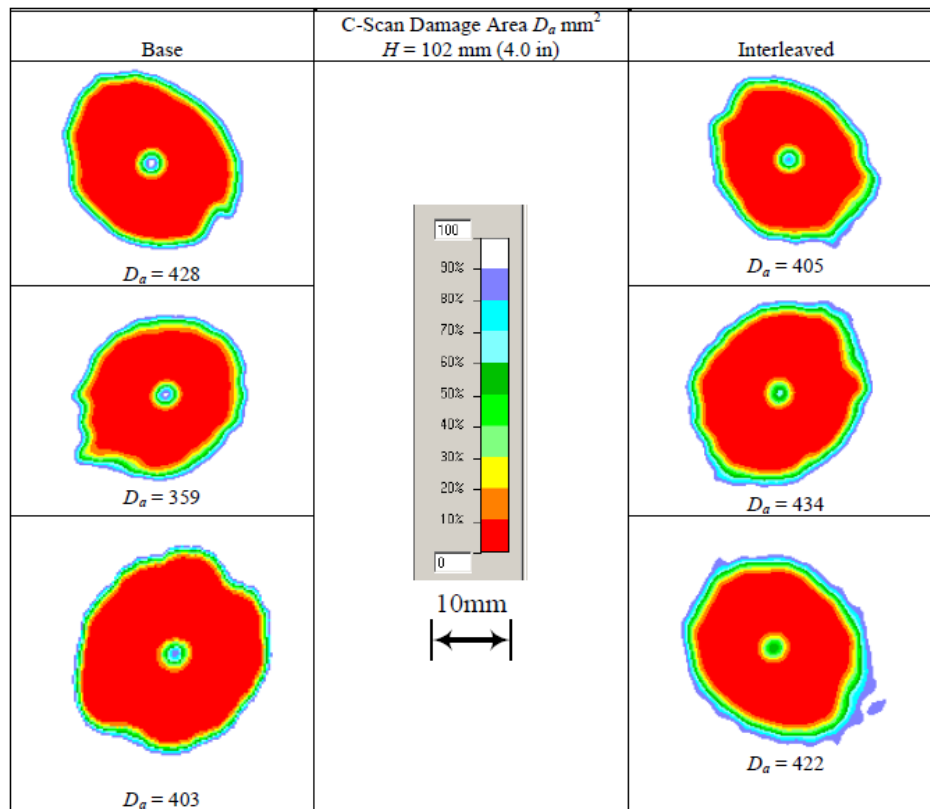
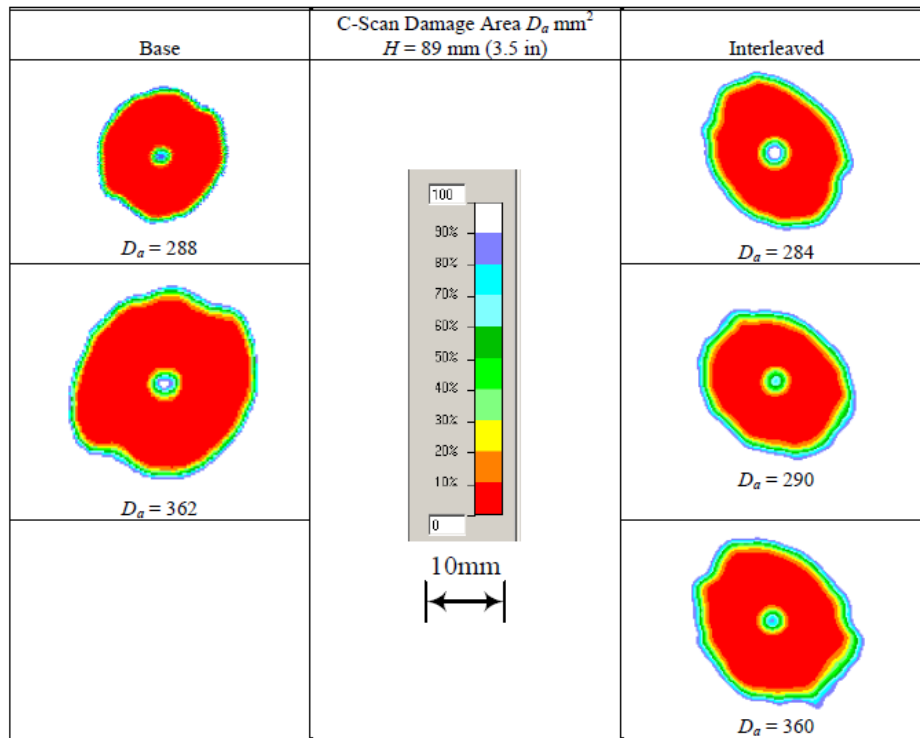
APPENDIX C

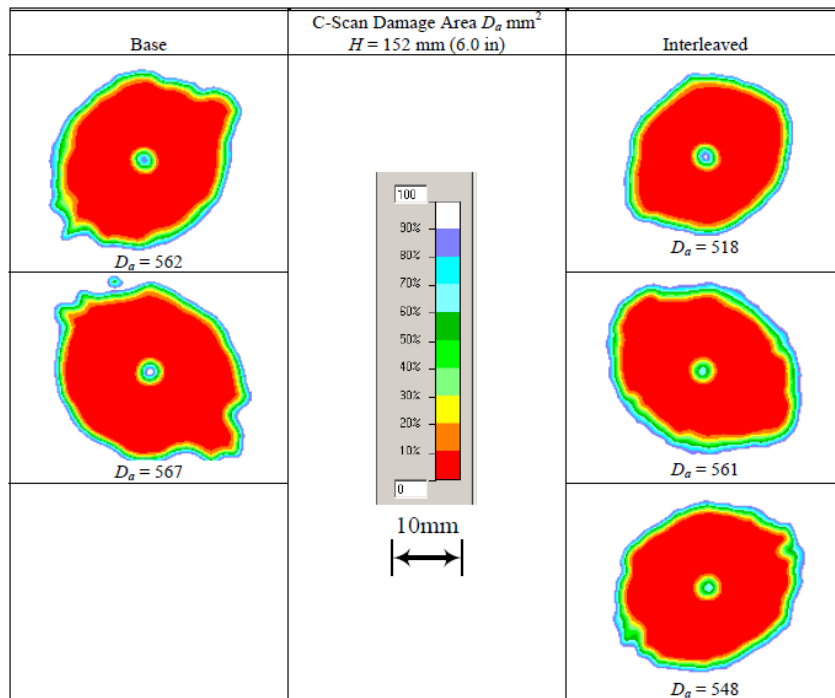
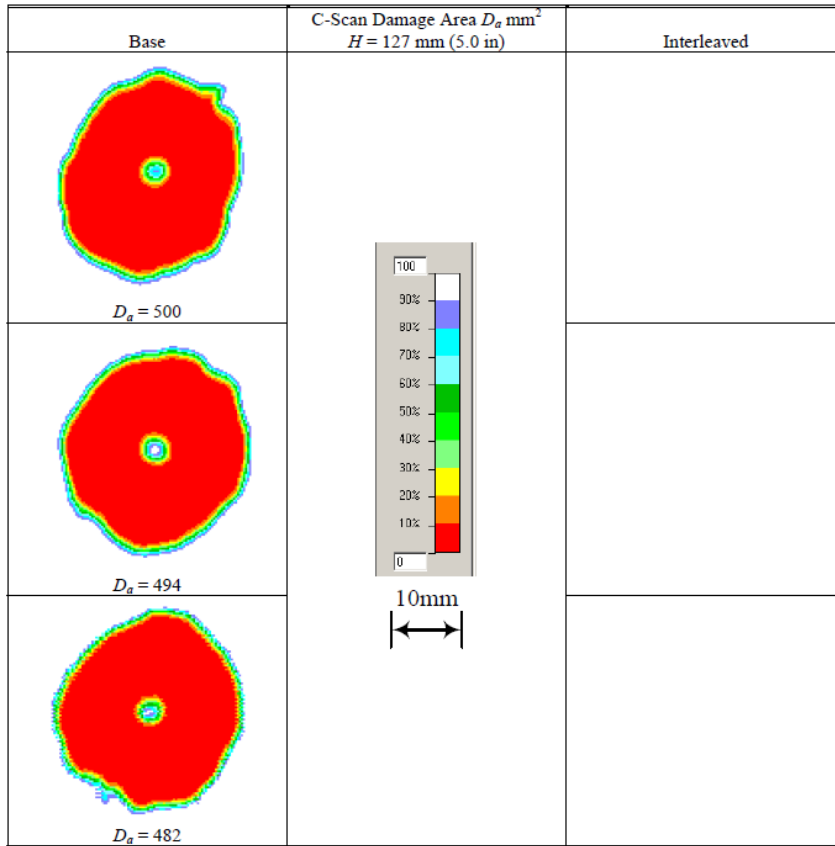
C-SCAN RESULTS

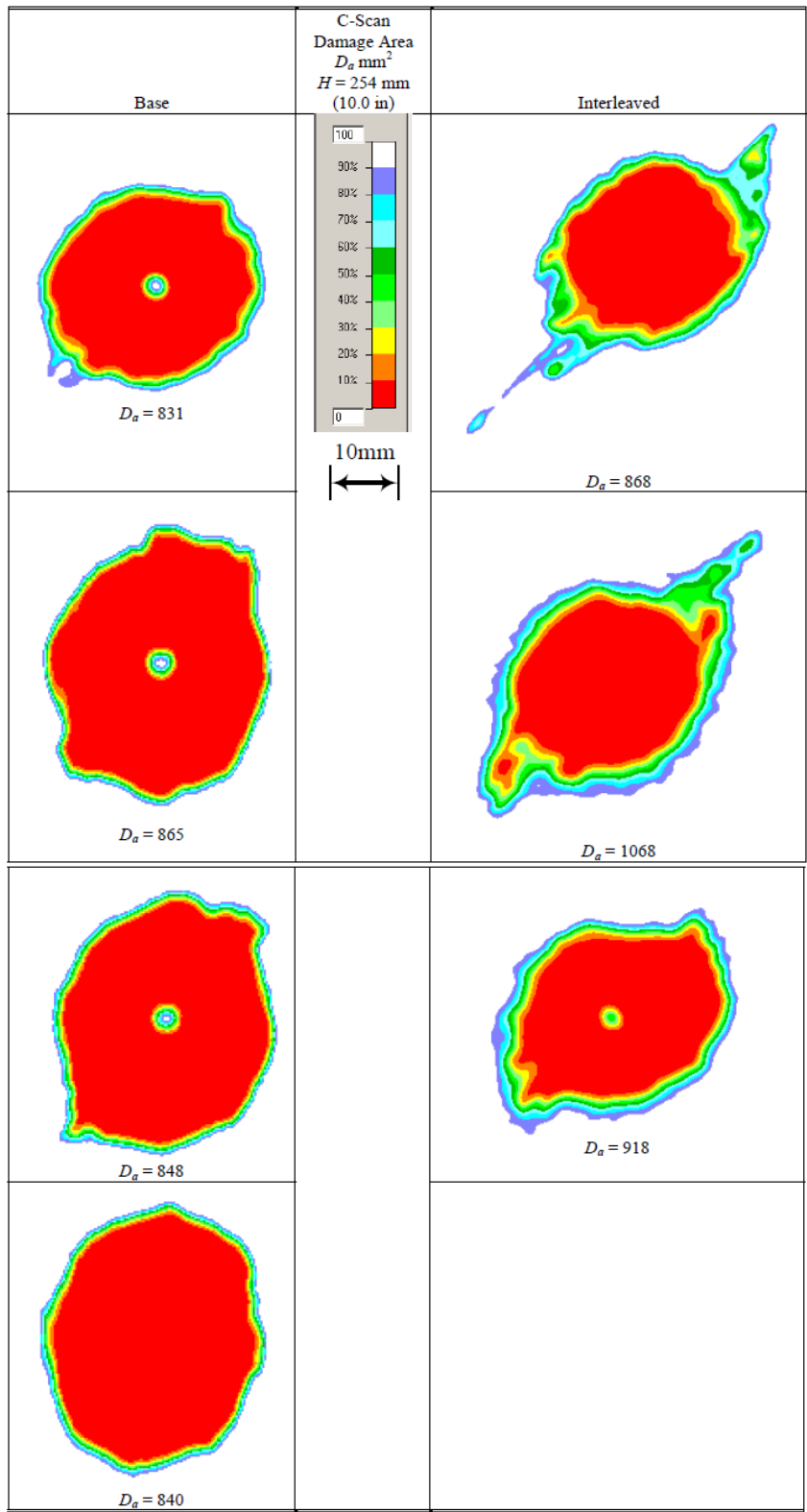
C-scanned damaged images of base and interleaved laminates at different impact heights are shown below.











APPENDIX D

SUMMARY OF IMPACT TEST DATA

D.1 Base Specimen

Test Specimen ID#	Impact Height, H , mm	Indentation Depth, d , mm	C-Scan Damage Area, D_a , mm ²	Impact Force, kN	
				Critical, P_c	Maximum, P_{max}
3_3	57	0.000	54	--	3.980
3_12		0.025	96	--	3.945
3_4	64	0.102	266	--	4.091
3_10		0.102	262	--	4.251
3_8	76	0.102	305	4.344	4.344
3_14		0.102	334	4.231	4.231
1_3	83	--	356	4.428	4.428
3_11		0.102	288	4.179	4.179
1_14	89	--	362	4.638	4.638
3_6		0.127	428	4.508	4.508
3_7	102	0.127	359	4.214	4.214
2_7		--	403	4.498	4.498
1_10	127	--	500	4.909	4.958
2_10		--	494	4.533	4.697
2_12	152	--	482	4.570	4.676
3_13		0.178	537	4.416	5.189
3_5	152	0.152	567	4.572	5.161
2_9		--	--	4.934	5.048
3_9	254	0.216	831	4.235	7.329
1_6		--	865	4.882	7.214
1_7		--	848	4.840	7.292
1_9		--	840	4.580	6.788
				4.5 (0.4)*	

*experimental error

Test Specimen ID#	Impact		Energy, J		
	Height, H , mm	Duration, T_e , ms	Impact, E_θ	Critical, E_c	Dissipated, E_d
3_3	57	4.79	3.22	--	0.05
3_12		4.74	2.93	--	0.00
3_4	64	5.17	3.46	--	1.32
3_10		5.08	3.41	--	1.17
3_8	76	5.32	4.10	3.57	1.43
3_14		5.37	4.43	3.60	1.35
1_3	83	5.29	4.36	4.06	1.66
3_11		5.43	4.65	3.50	1.46
1_14	89	5.36	4.85	4.23	1.64
3_6		5.43	5.54	3.96	1.70
3_7	102	5.40	5.38	3.46	1.28
2_7		5.35	5.49	4.08	1.67
1_10	127	5.40	6.80	4.61	2.11
2_10		5.39	6.84	4.04	1.97
2_12	152	5.37	6.72	4.07	1.83
3_13		5.45	8.07	3.76	1.84
3_5	152	5.47	8.08	3.97	1.92
2_9		5.38	7.92	4.62	2.40
3_9	254	5.35	13.22	3.58	2.47
1_6		5.28	13.45	4.67	3.29
1_7		5.26	13.55	4.64	3.32
1_9		5.48	13.50	4.30	3.95
				4.0 (0.7)*	

*experimental error

D.2 Interleaved Specimen

Test Specimen ID #	Impact Height, H , mm	Indentation Depth, d , mm	C-Scan Damage Area, D_a , mm ²	Impact Force, kN	
				Critical, P_c	Maximum, P_{max}
P2_10	57	0.000	64	--	3.930
P1_1		0.000	100	--	3.858
P1_7		0.000	40	--	3.980
P1_14	64	0.000	70	--	4.138
P2_9		0.000	85	--	4.047
P2_14		0.000	73	--	4.074
P1_2	76	0.000	78	--	4.369
P1_6		0.000	116	--	4.477
P2_1		0.000	135	--	4.315
P2_12	83	0.076	279	4.571	4.571
P1_10		0.000	104	4.582	4.582
P1_11		0.000	103	--	4.533
P1_5	89	0.102	284	4.678	4.678
P1_13		0.076	289	4.705	4.705
P2_3		0.076	357	4.589	4.589
P2_4	102	0.102	405	4.717	4.717
P2_7		0.127	434	4.777	4.777
P1_4		0.127	422	4.555	4.555
P2_6	152	0.152	571	4.631	5.204
P2_8		0.152	556	4.701	5.159
P2_5		0.152	529	4.672	5.188
P1_3	254	0.203	884	4.850	7.031
P1_8		0.203	1071	4.786	7.207
P1_9		0.178	926	4.831	7.056
				4.7 (0.2)*	

*experimental error

Test Specimen ID#	Impact		Energy, J		
	Height, H , mm	Duration, T_e , ms	Impact, E_0	Critical, E_c	Dissipated, E_d
P2_10	57	4.75	2.94	--	0
P1_1		4.82	2.98	--	0
P1_7		4.72	2.98	--	0
P1_14	64	4.76	3.35	--	0
P2_9		4.77	3.34	--	0.10
P2_14		4.79	3.32	--	0.06
P1_2	76	4.78	3.93	--	0.08
P1_6		4.72	3.87	--	0.00
P2_1		4.82	3.93	--	0.16
P2_12	83	5.03	4.39	4.35	1.53
P1_10		4.74	4.26	4.26	0.09
P1_11		4.79	4.15	-	0.00
P1_5	89	5.14	4.60	4.48	1.56
P1_13		5.09	4.61	4.43	1.52
P2_3		5.18	4.53	4.32	1.33
P2_4	102	5.28	5.46	4.58	1.70
P2_7		5.29	5.55	4.66	1.80
P1_4		5.34	5.39	4.23	1.79
P2_6	152	5.31	8.06	4.39	2.24
P2_8		5.33	7.90	4.43	2.02
P2_5		5.31	7.97	4.42	2.10
P1_3	254	5.50	13.26	4.80	5.02
P1_8		5.21	13.33	4.63	3.20
P1_9		5.47	13.24	4.72	4.49
				4.5 (0.3)*	

*experimental error

APPENDIX E

IMPACT RESPONSE PLOTS FOR BASE SPECIMENS

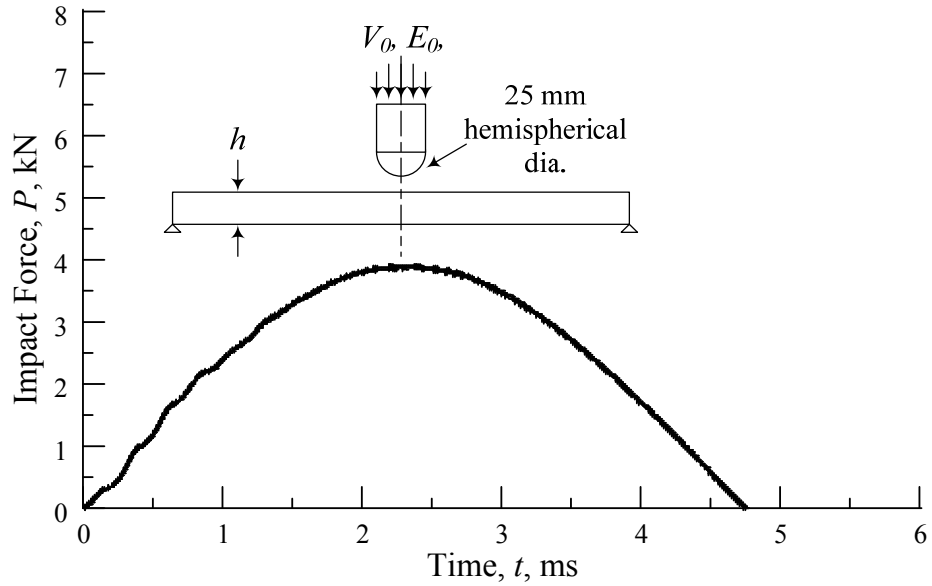


Figure E.1. Force versus time at $H = 57$ mm (2.25 in)

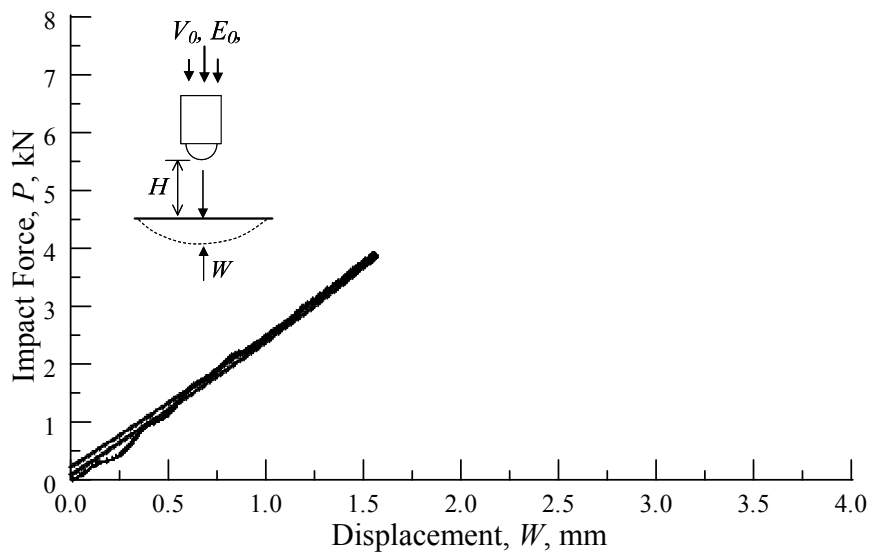


Figure E.2. Force versus displacement at $H = 57$ mm (2.25 in)

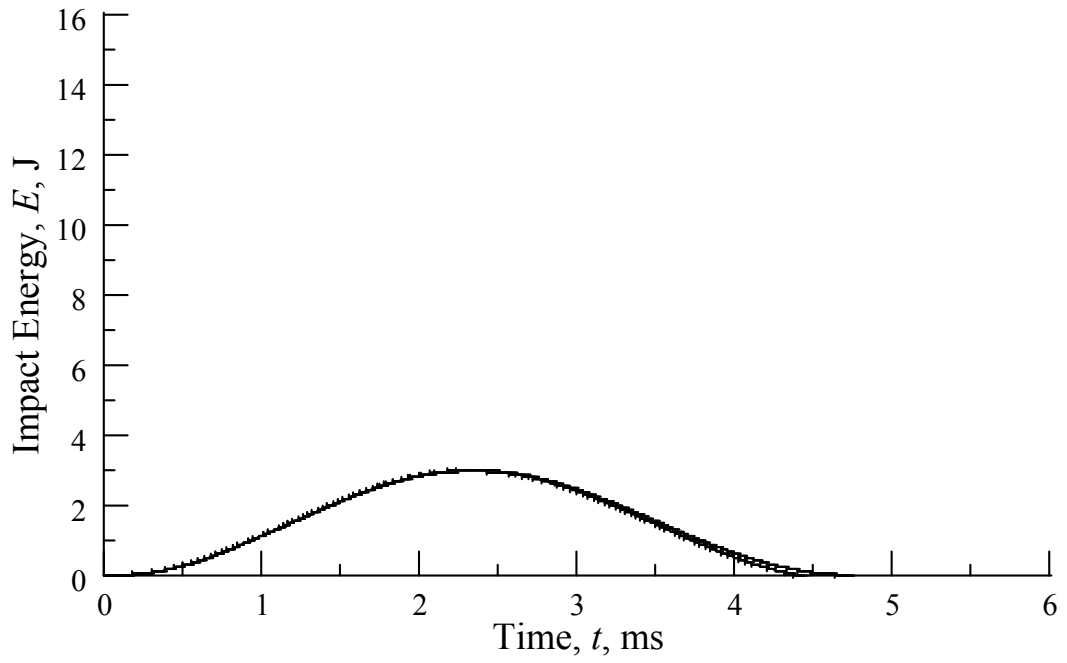


Figure E.3. Energy versus time at $H = 57$ mm (2.25 in)

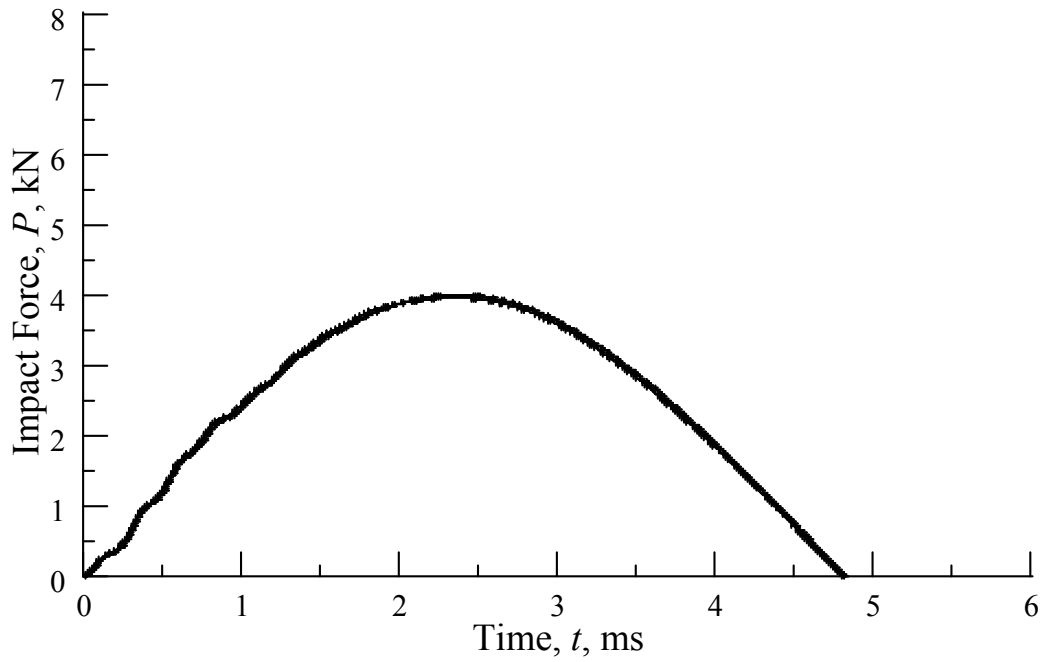


Figure E.4. Force versus time at $H = 64$ mm (2.5 in)

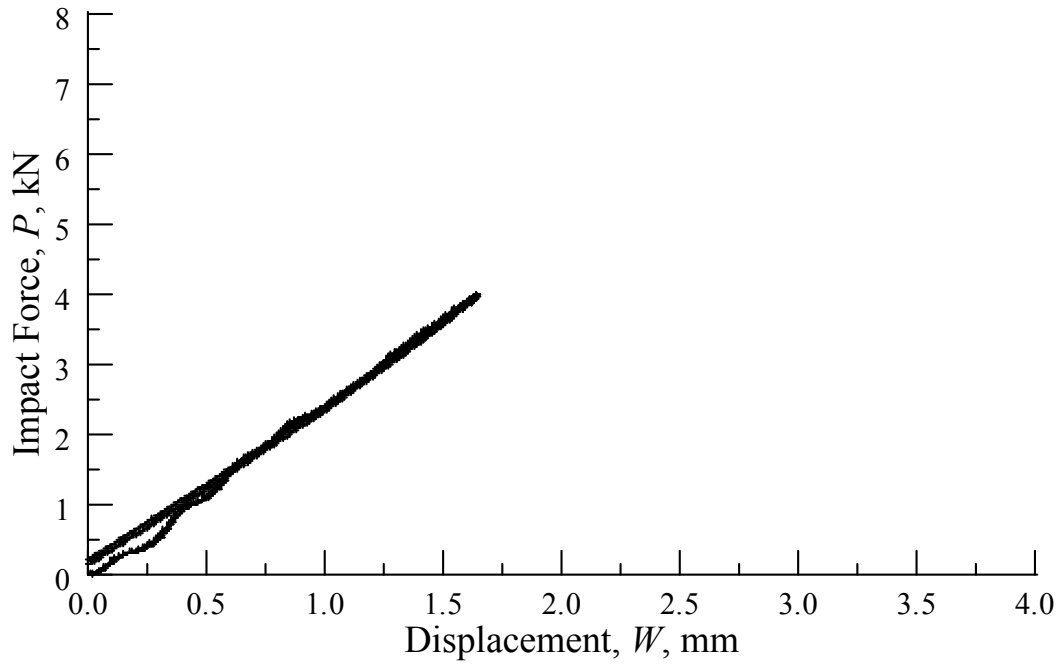


Figure E.5. Force versus displacement at $H = 64$ mm (2.5 in)

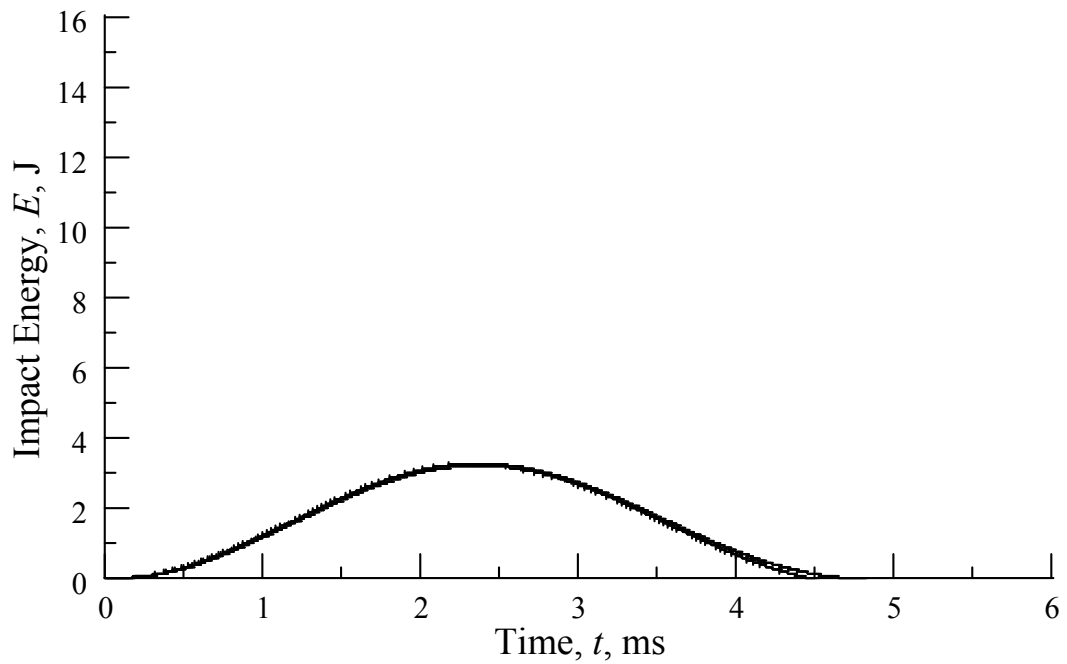


Figure E.6. Energy versus time at $H = 64$ mm (2.5 in)

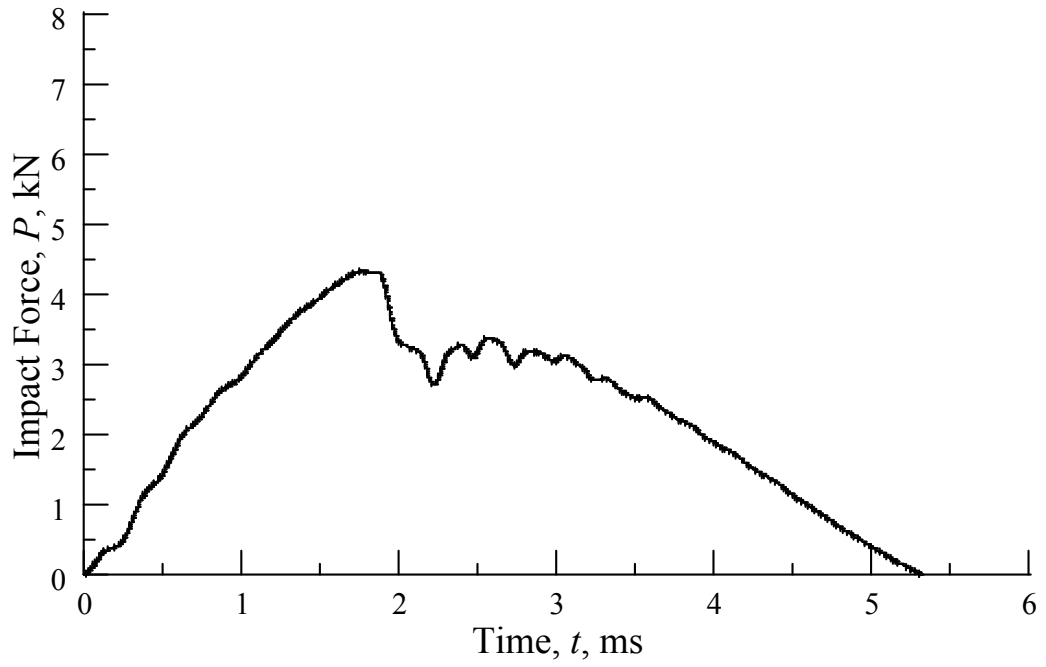


Figure E.7. Force versus time at $H = 76$ mm (3.0 in)

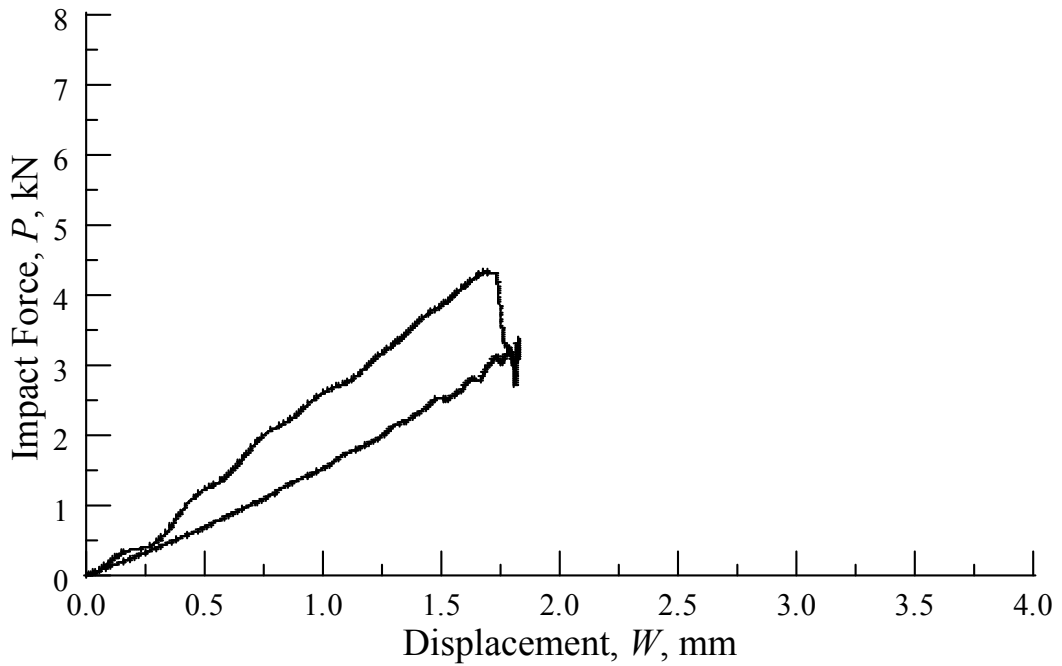


Figure E.8. Force versus displacement at $H = 76$ mm (3.0 in)

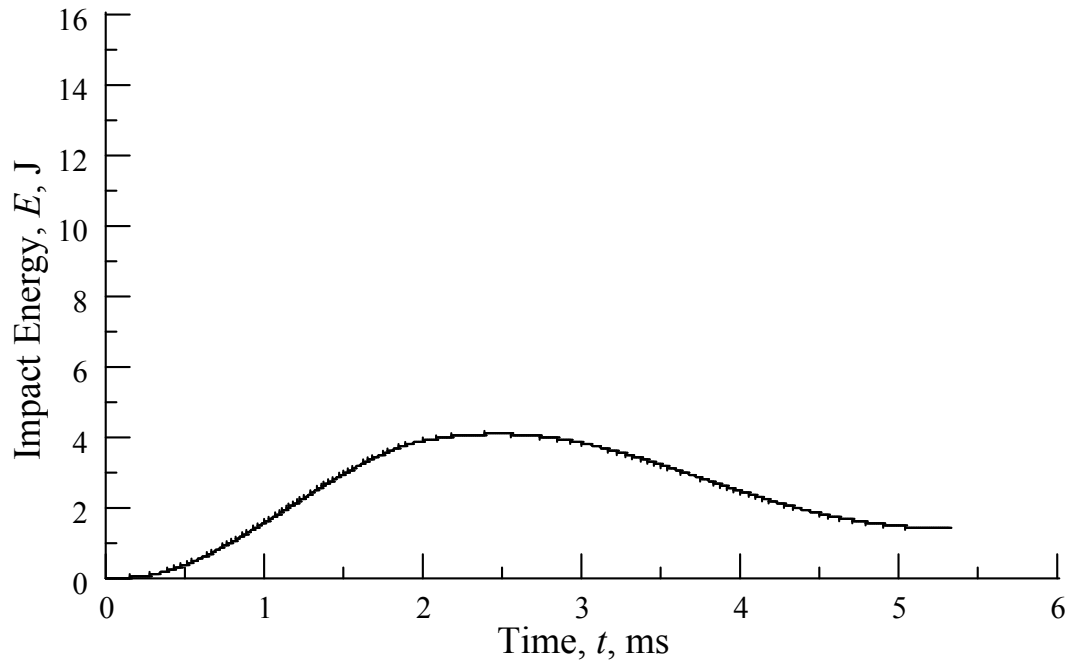


Figure E.9. Energy versus time at $H = 76$ mm (3.0 in)

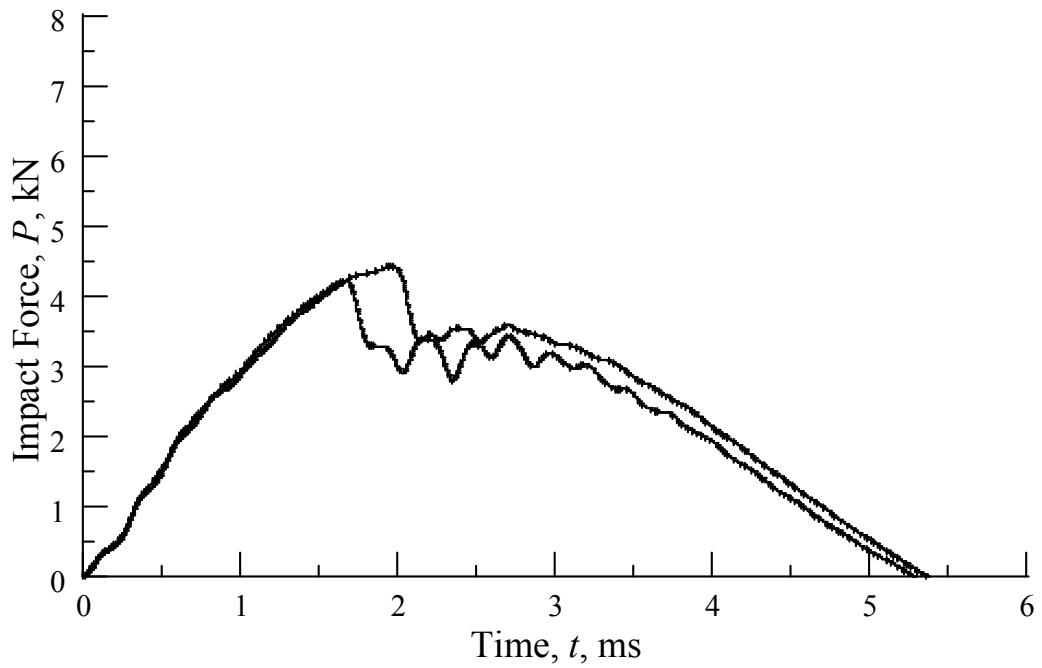


Figure E.10. Force versus time at $H = 83$ mm (3.25 in)

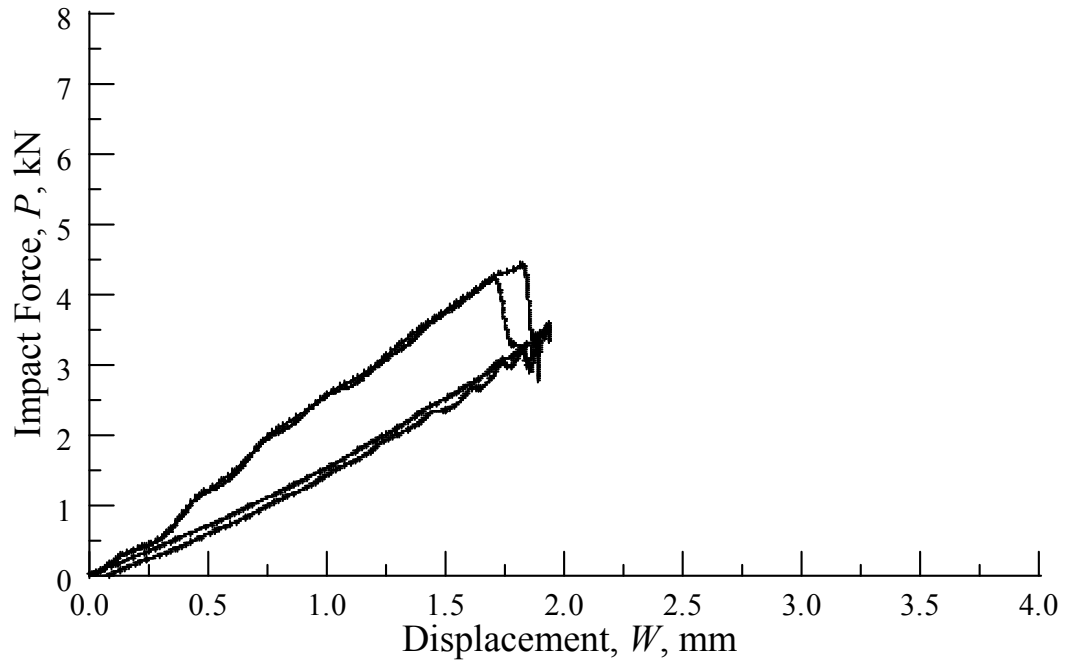


Figure E.11. Force versus displacement at $H = 83$ mm (3.25 in)

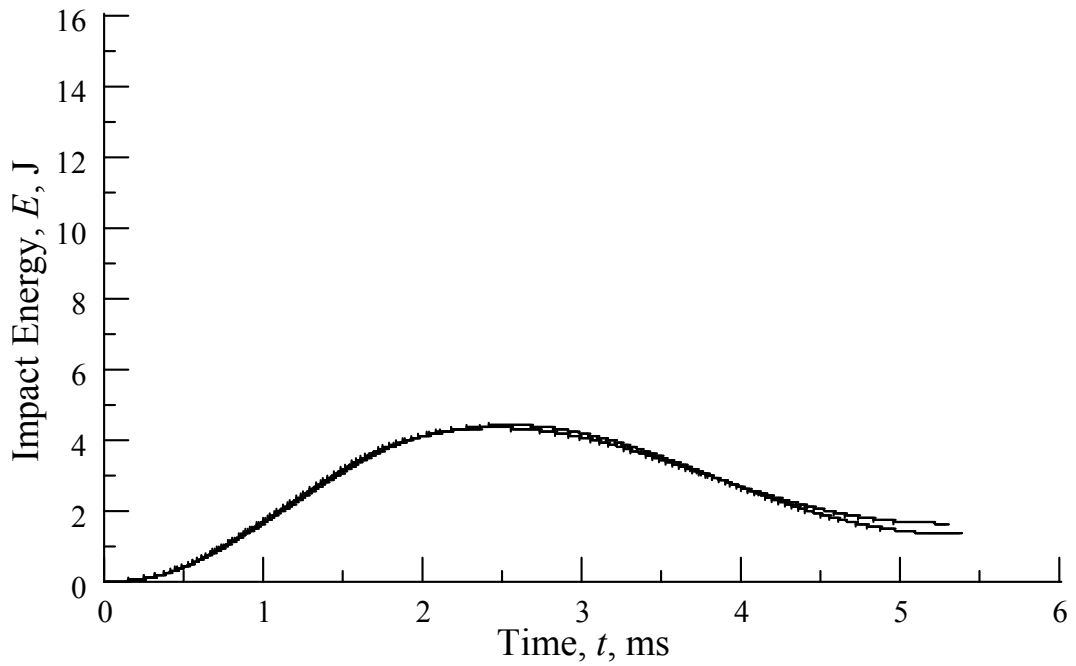


Figure E.12. Energy versus time at $H = 83$ mm (3.25 in)

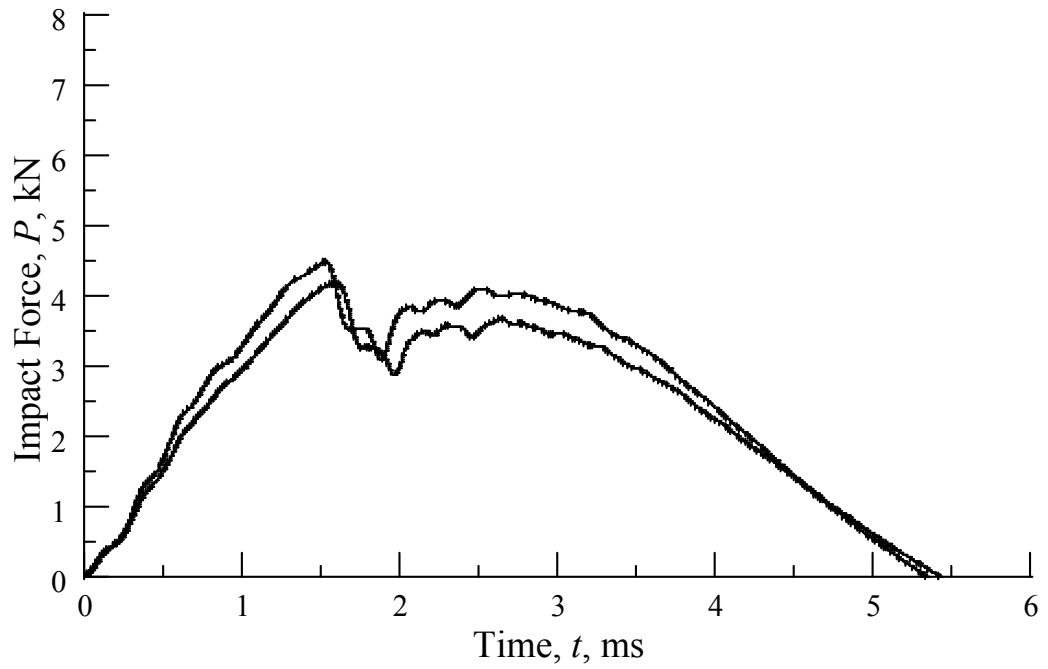


Figure E.13. Force versus time at $H = 89$ mm (3.5 in)

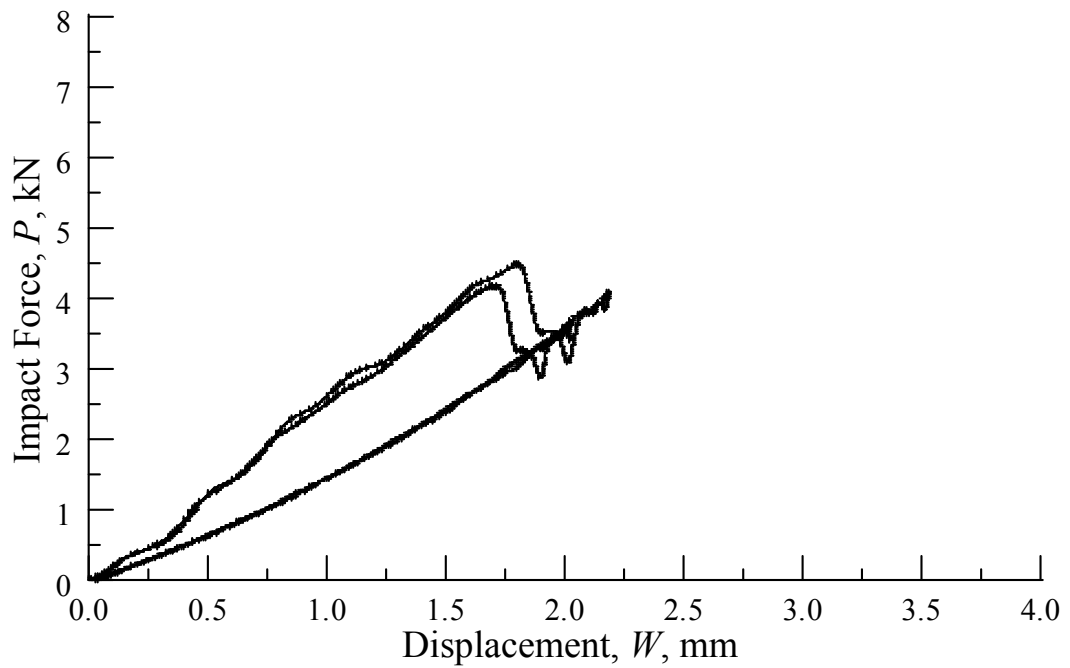


Figure E.14. Force versus displacement at $H = 89$ mm (3.5 in)

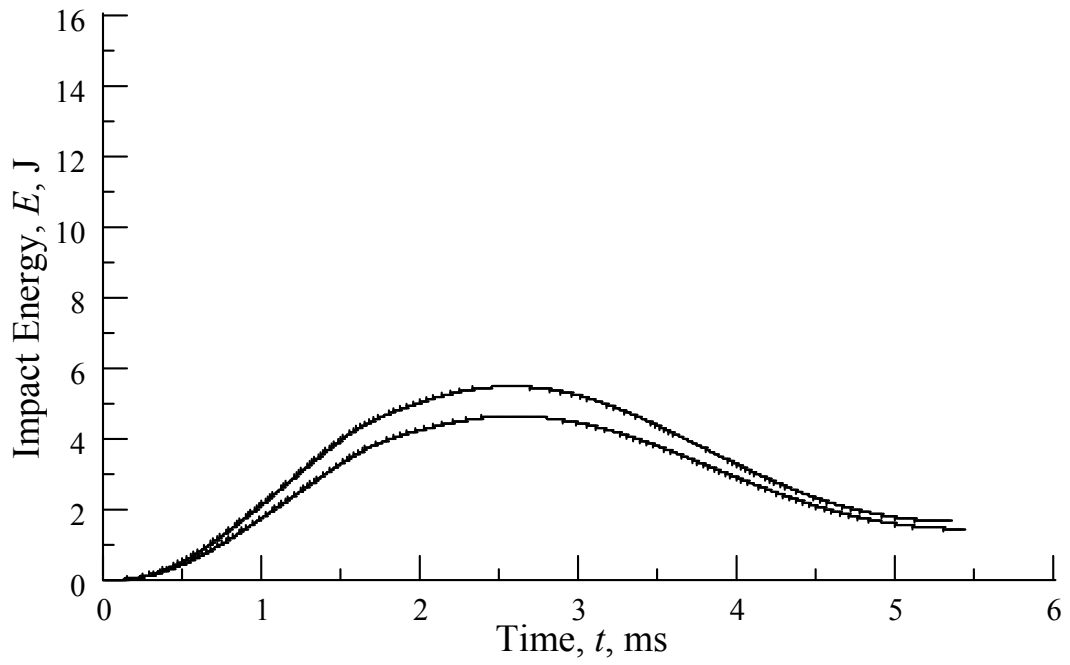


Figure E.15. Energy versus time at $H = 89$ mm (3.5 in)

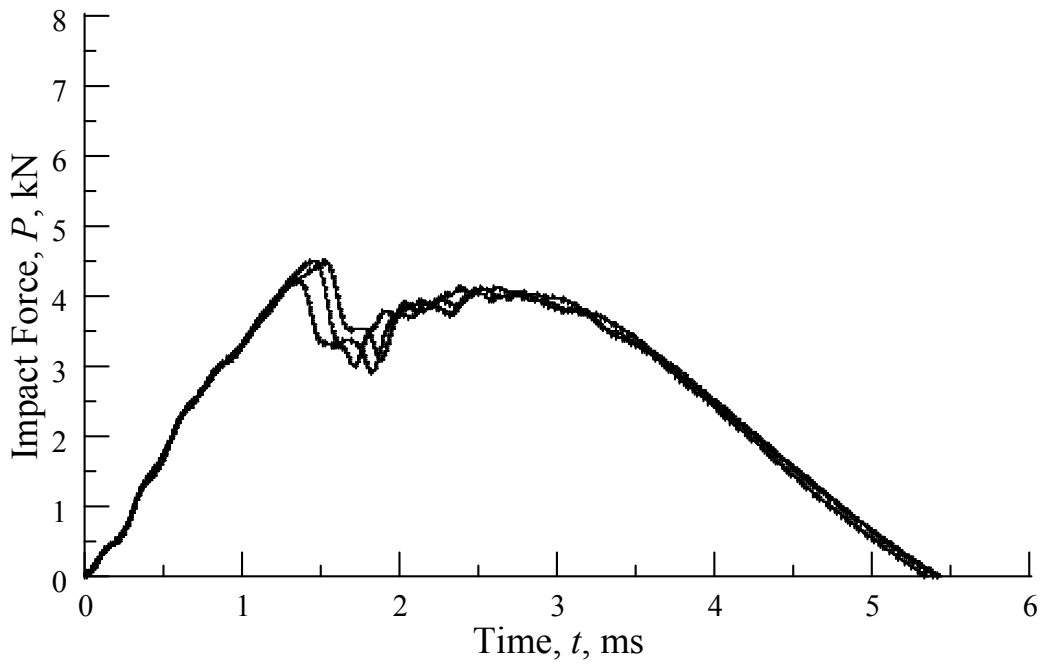


Figure E.16. Force versus time at $H = 102$ mm (4.0 in)

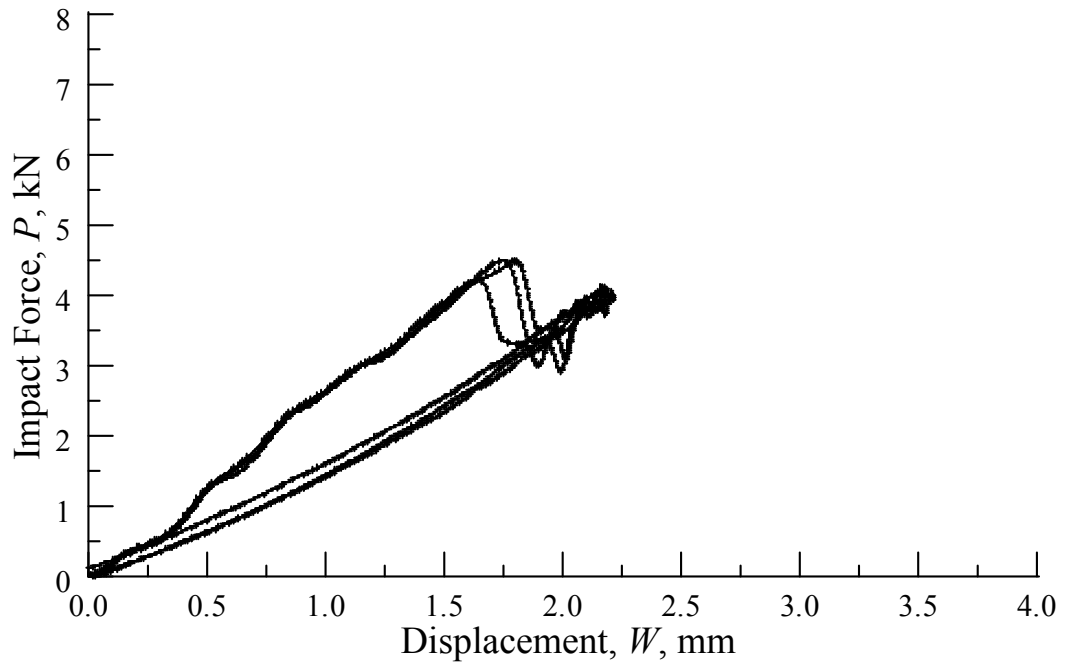


Figure E.17. Force versus displacement at $H = 102$ mm (4.0 in)

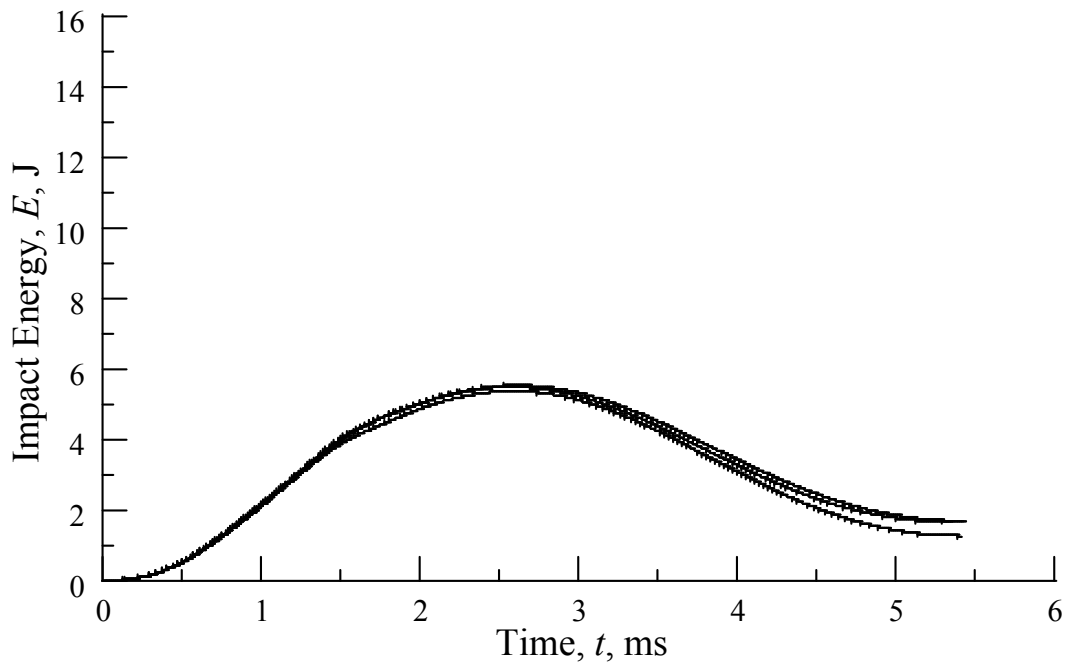


Figure E.18. Energy versus time at $H = 102$ mm (4.0 in)

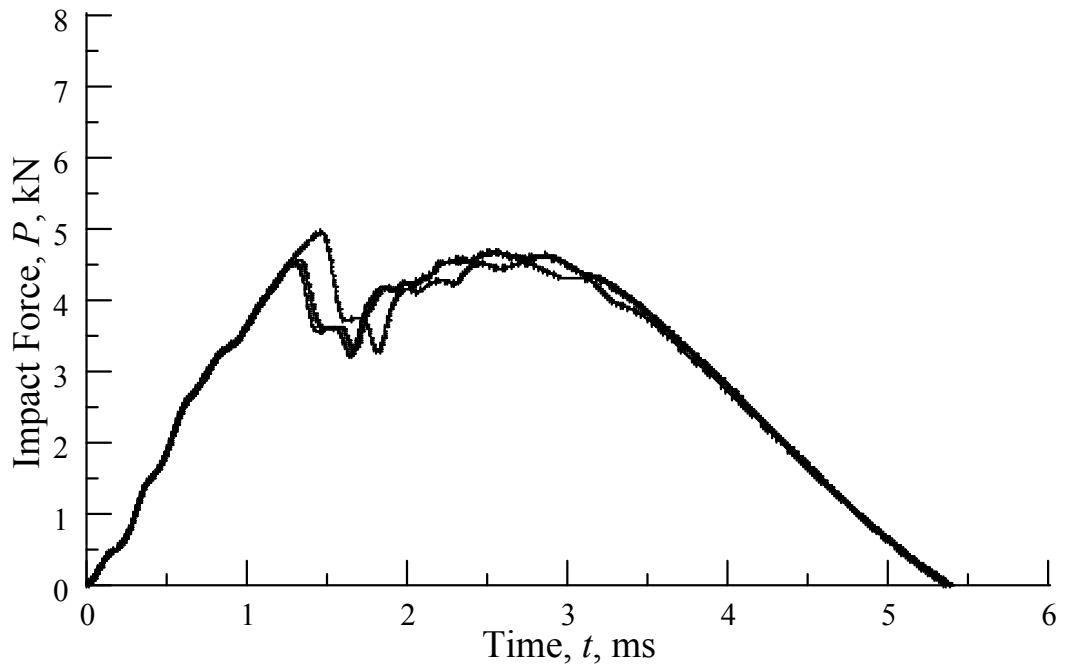


Figure E.19. Force versus time at $H = 127$ mm (5.0 in)

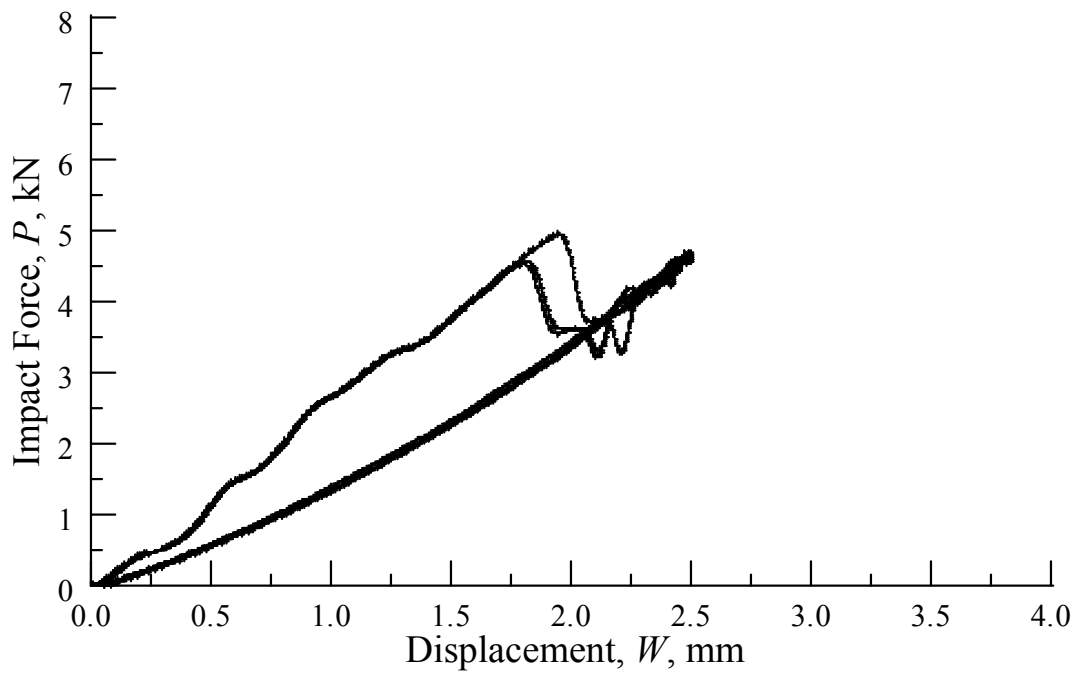


Figure E.20. Force versus displacement at $H = 127$ mm (5.0 in)

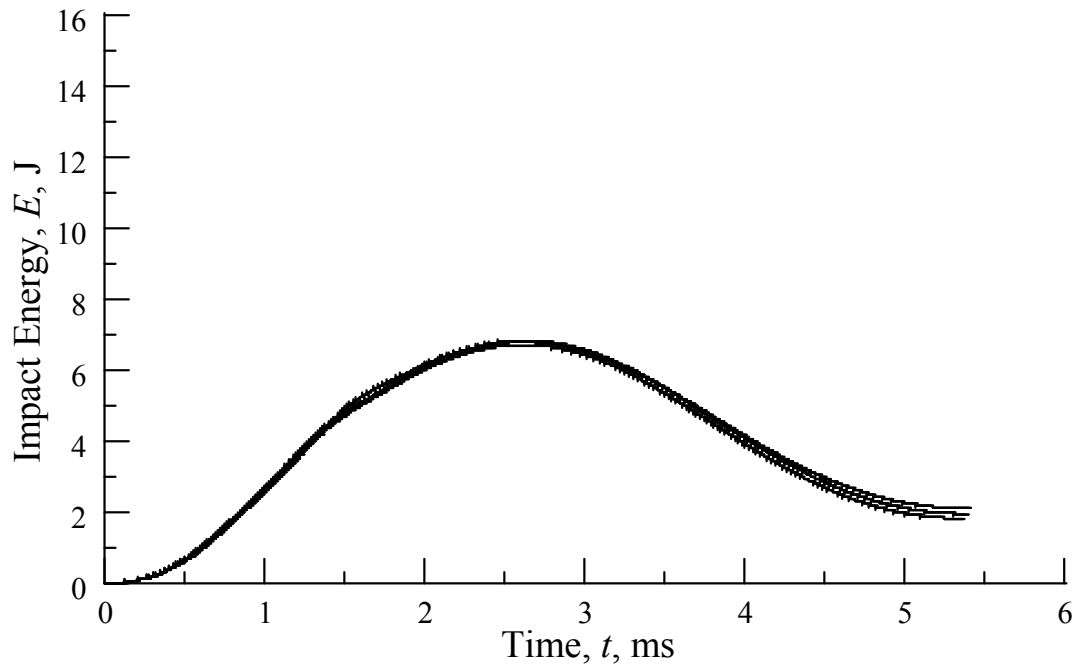


Figure E.21. Energy versus time at $H = 127$ mm (5.0 in)

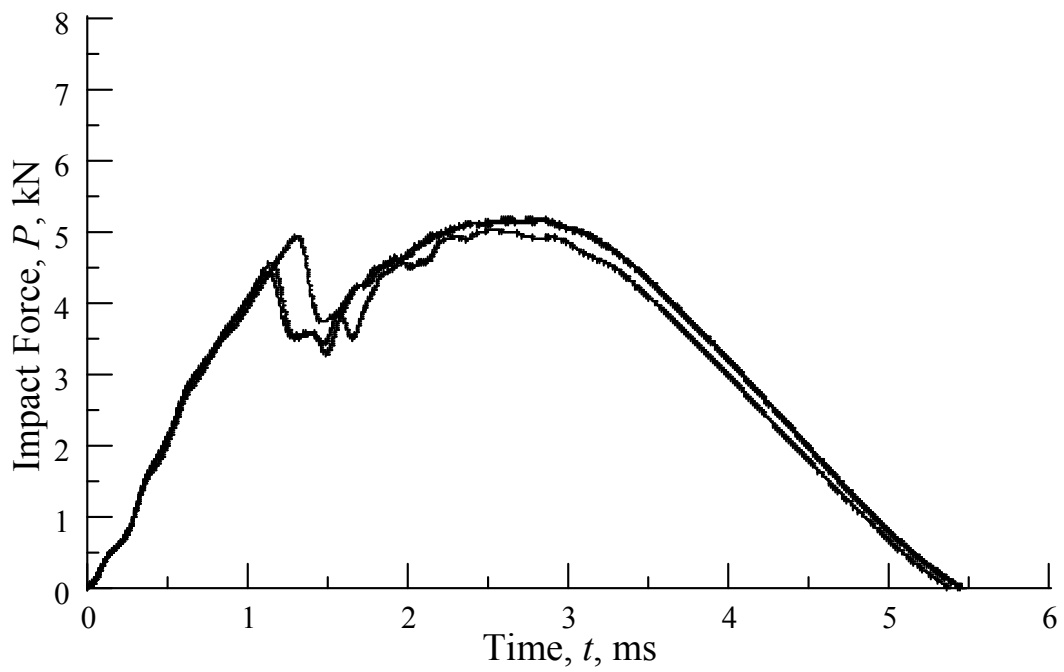


Figure E.22. Force versus time at $H = 152$ mm (6.0 in)

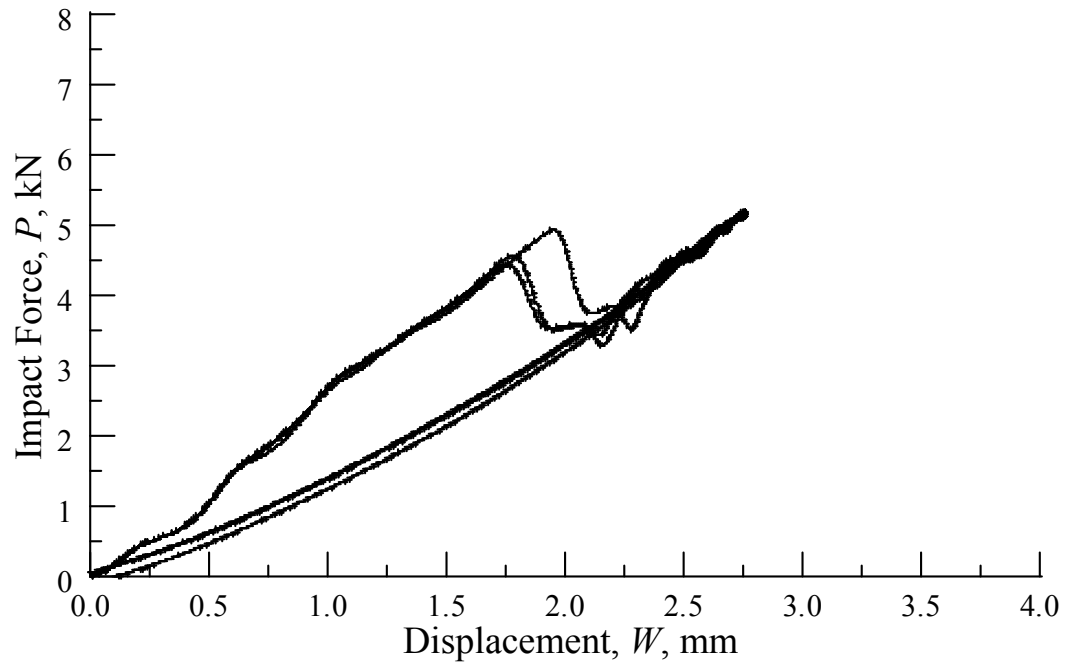


Figure E.23. Force versus displacement at $H = 152$ mm (6.0 in)

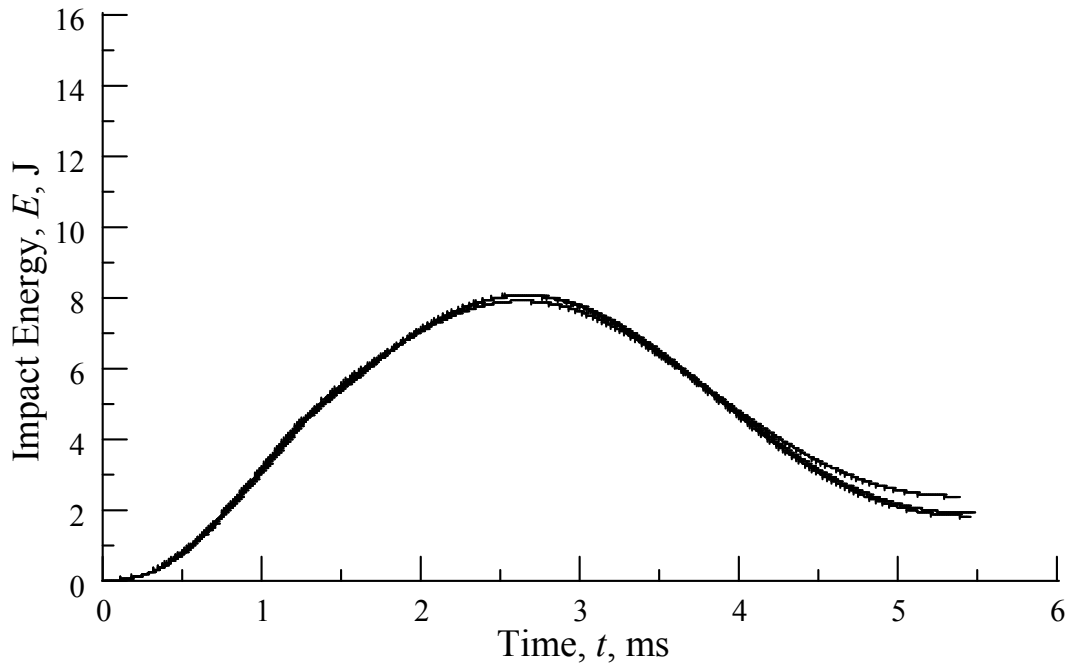


Figure E.24. Energy versus time at $H = 152$ mm (6.0 in)

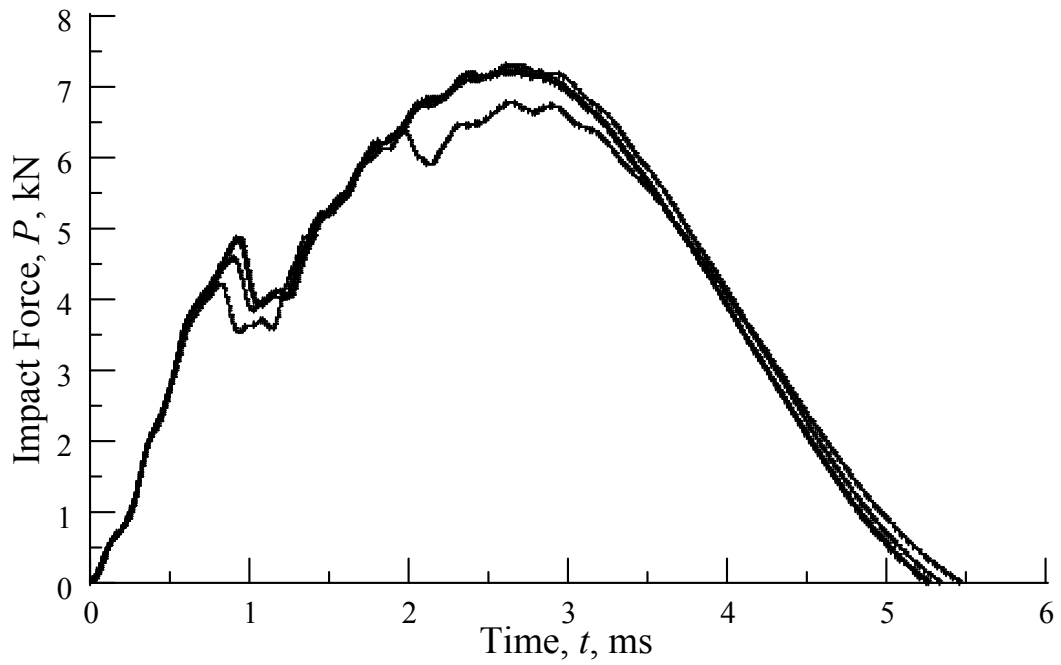


Figure E.25. Force versus time at $H = 254$ mm (10.0 in)

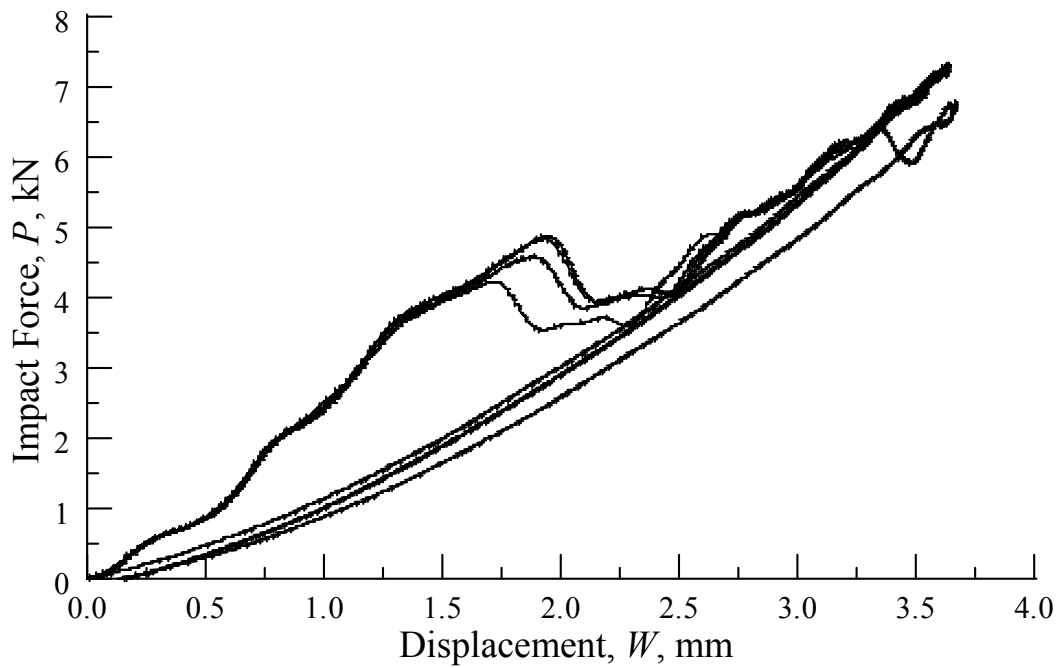


Figure E.26. Force versus displacement at $H = 254$ mm (10.0 in)

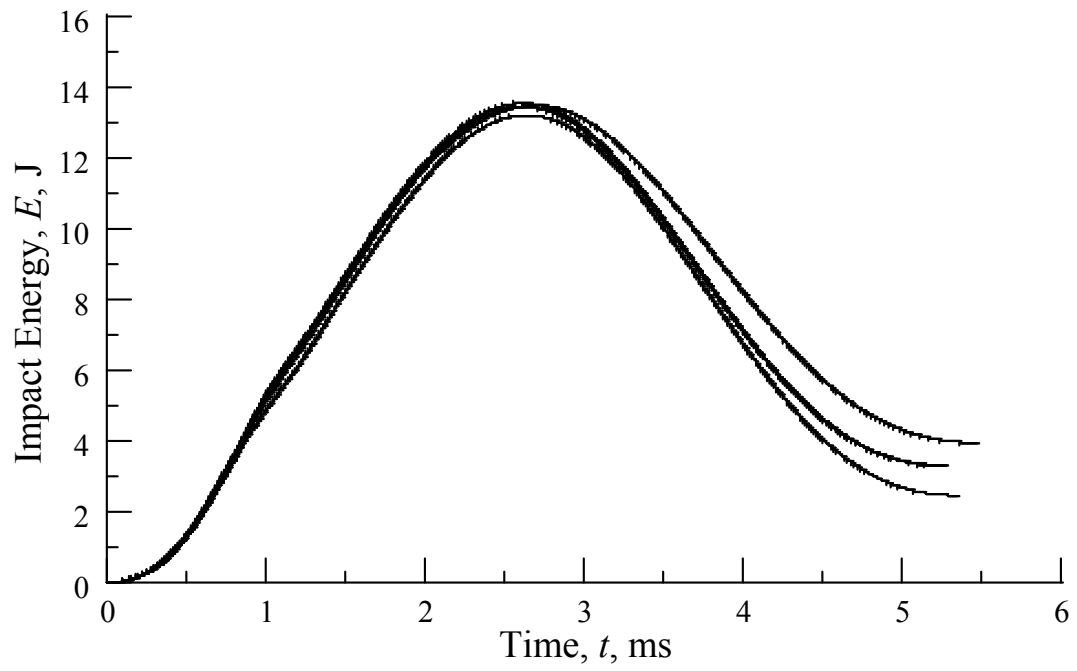


Figure E.27. Energy versus time at $H = 254$ mm (10.0 in)

APPENDIX F

IMPACT RESPONSE PLOTS FOR INTERLEAVED SPECIMENS

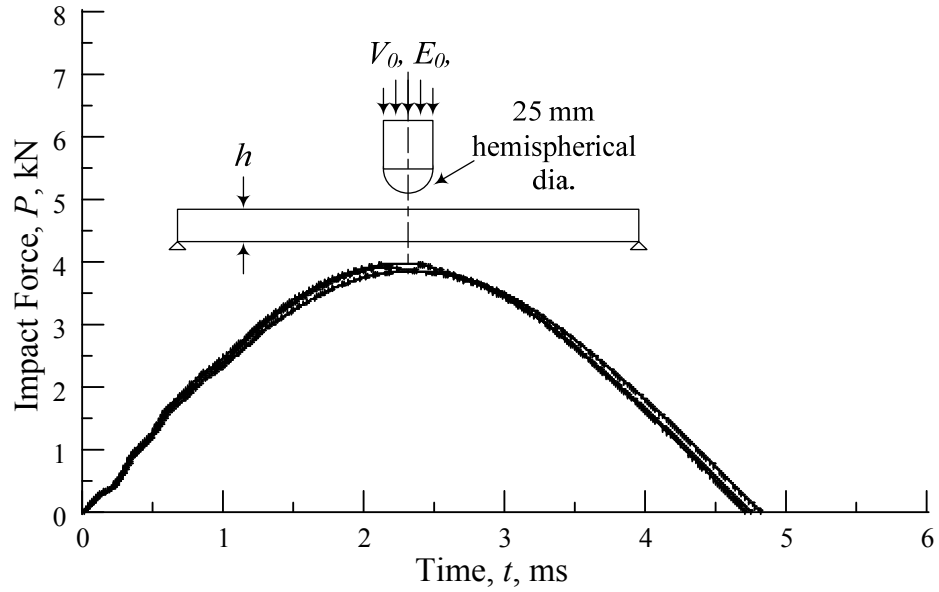


Figure F.1. Force versus time at $H = 57$ mm (2.25 in)

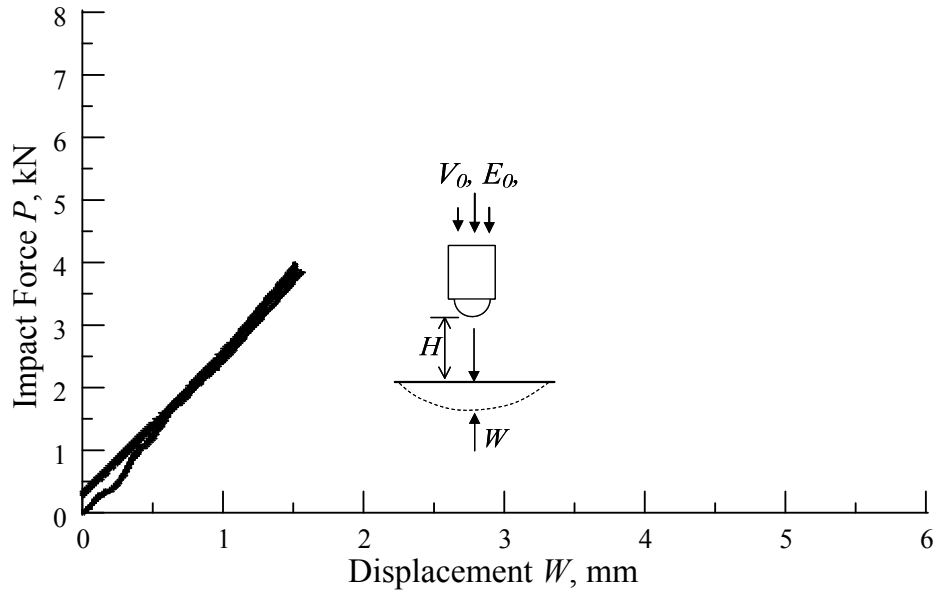


Figure F.2. Force versus displacement at $H = 57$ mm (2.25 in)

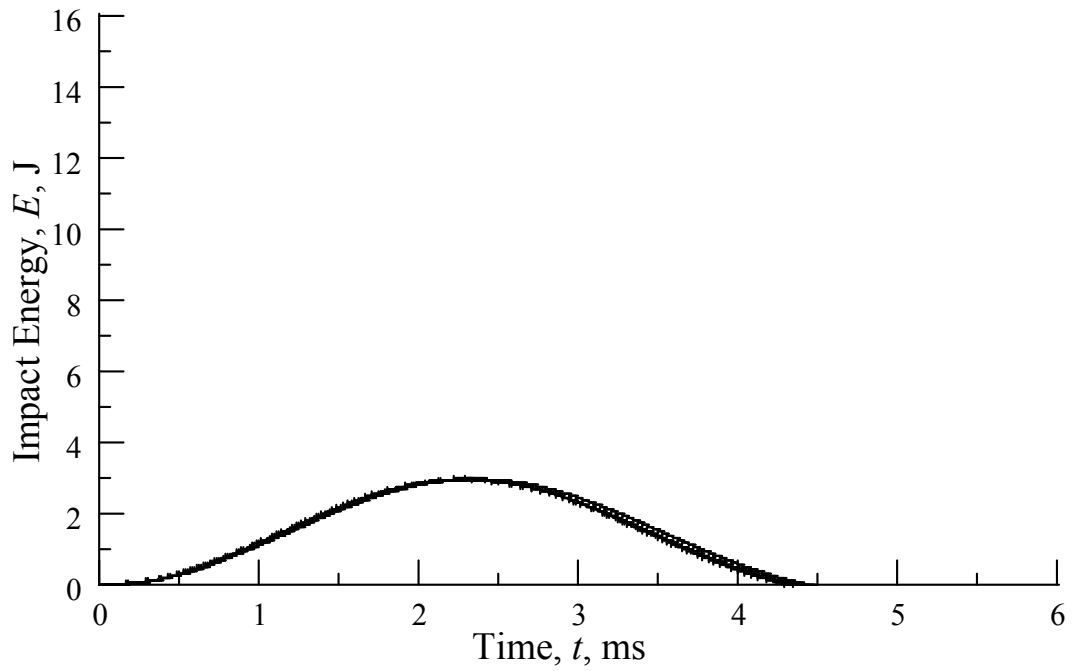


Figure F.3. Energy versus time at $H = 57$ mm (2.25 in)

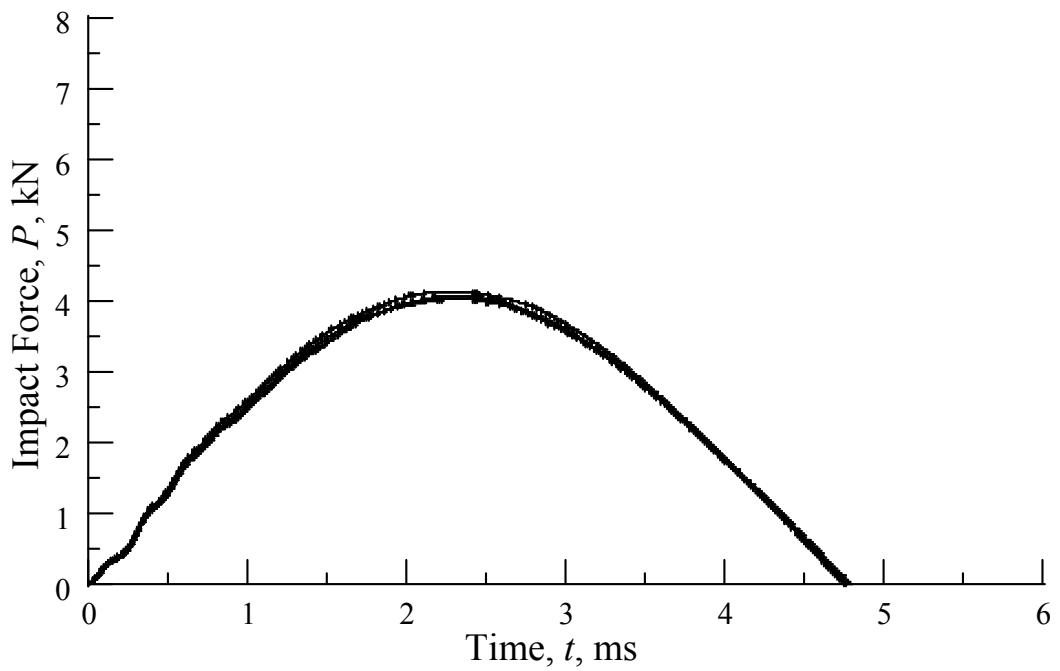


Figure F.4. Force versus time at $H = 64$ mm (2.5 in)

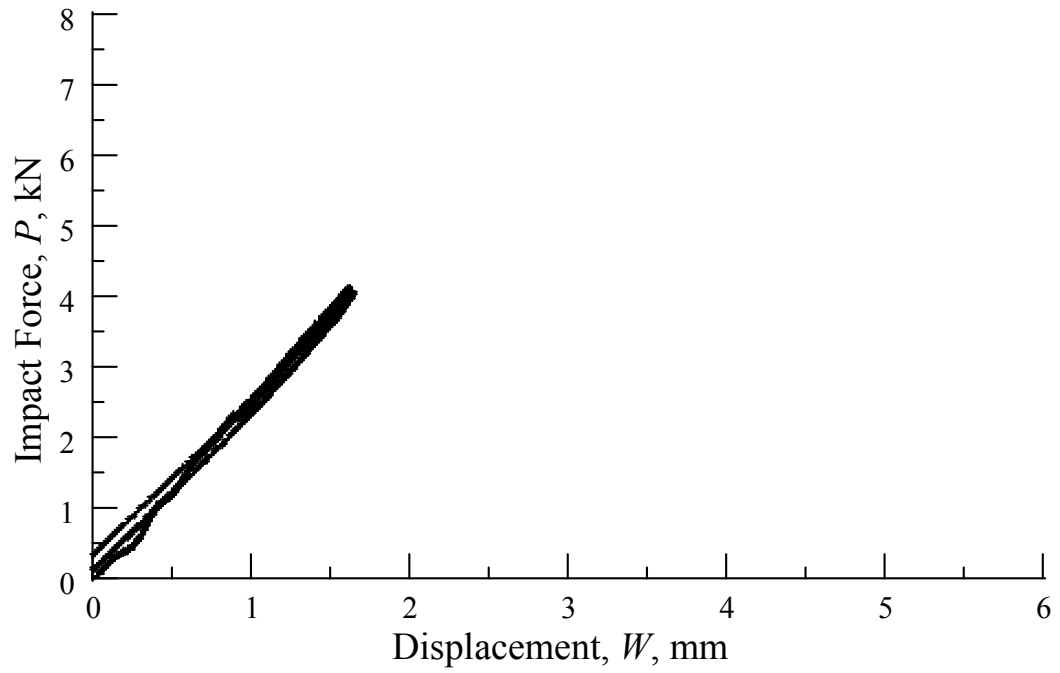


Figure F.5. Force versus displacement at $H = 64$ mm (2.5 in)

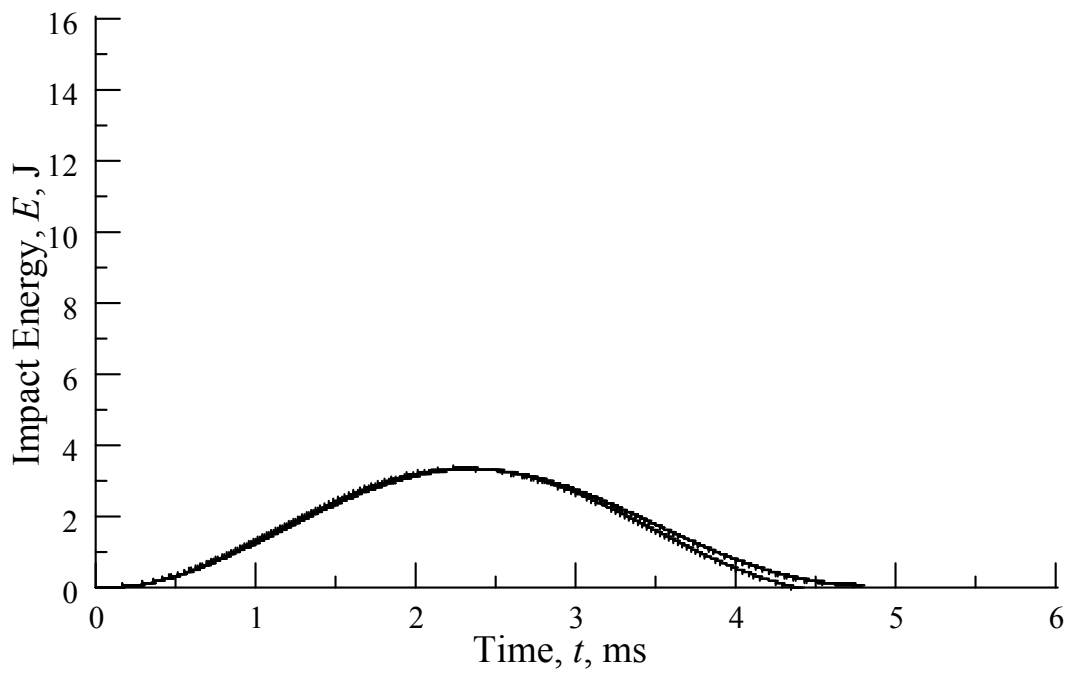


Figure F.6. Energy versus time at $H = 64$ mm (2.5 in)

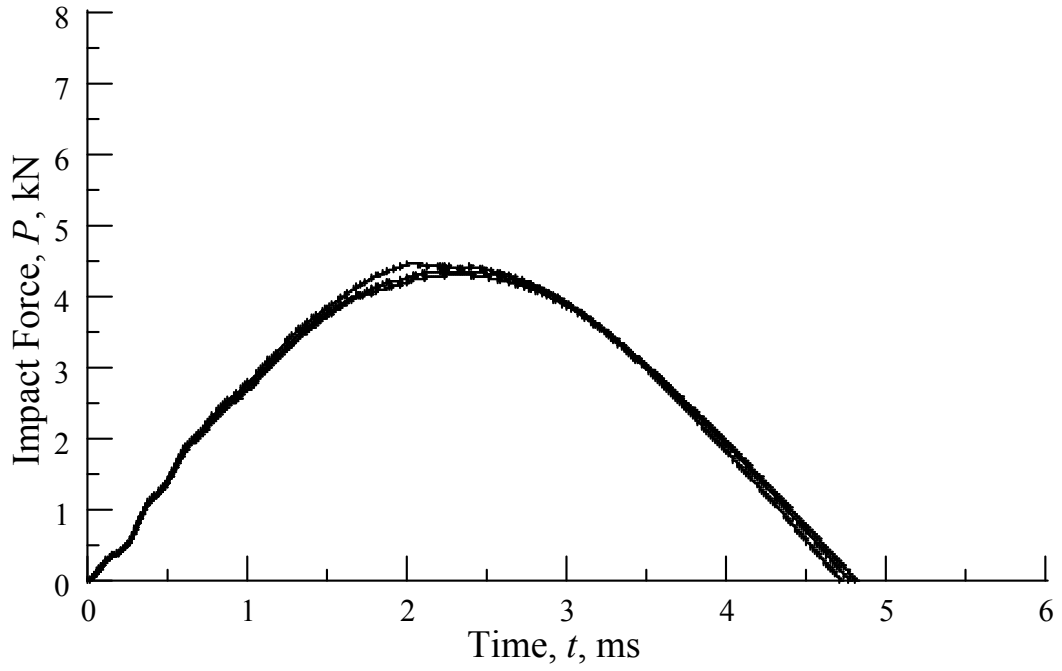


Figure F.7. Force versus time at $H = 76$ mm (3.0 in)

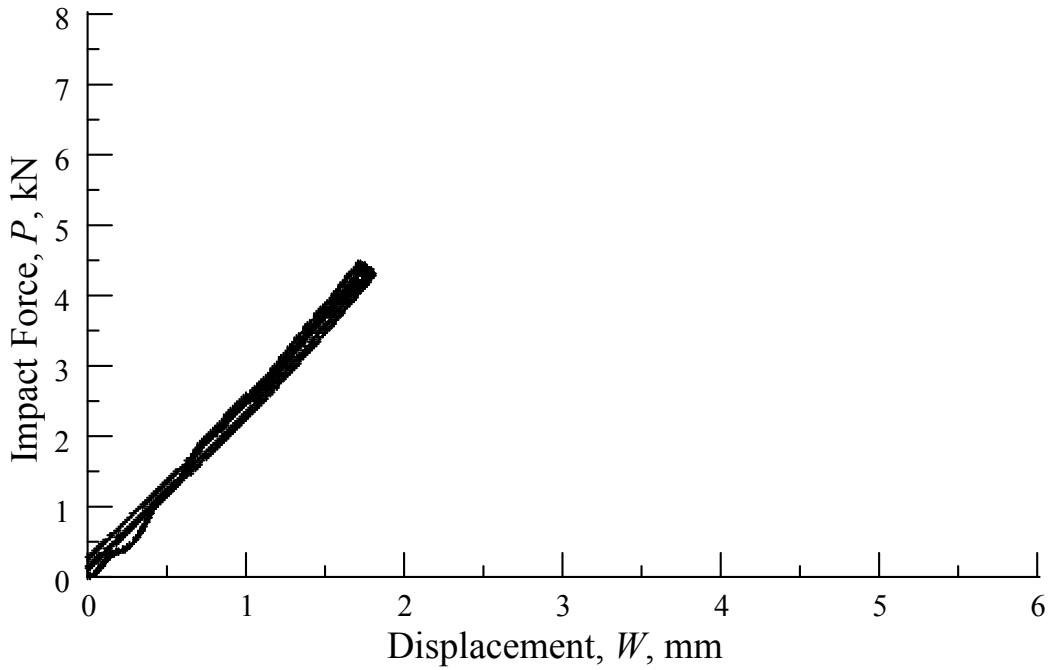


Figure F.8. Force versus displacement at $H = 76$ mm (3.0 in)

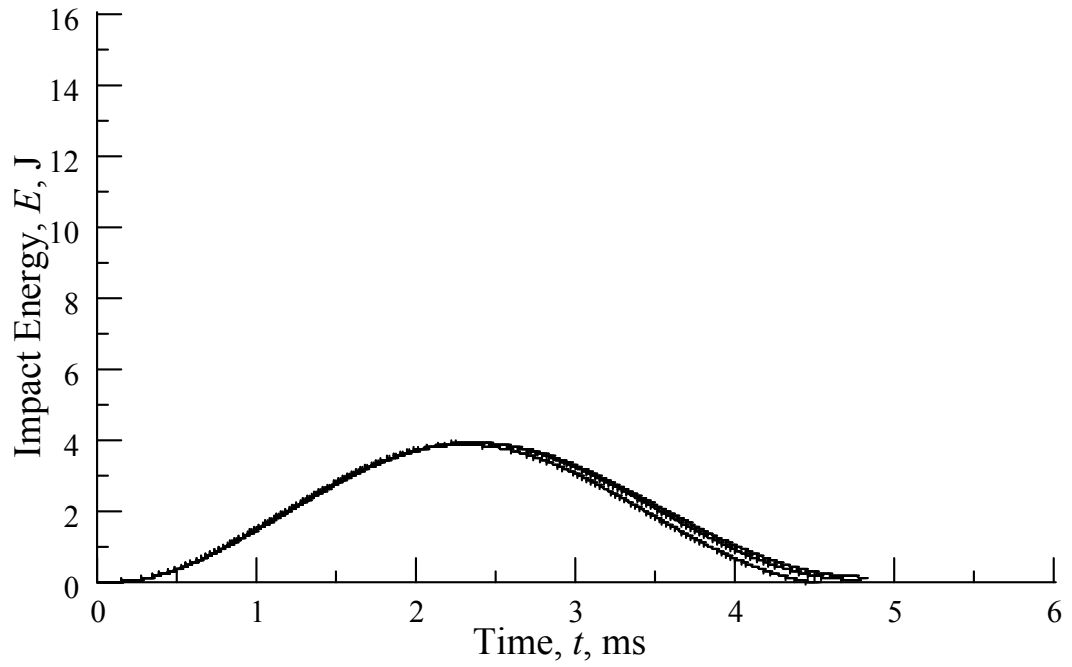


Figure F.9. Energy versus time at $H = 76$ mm (3.0 in)

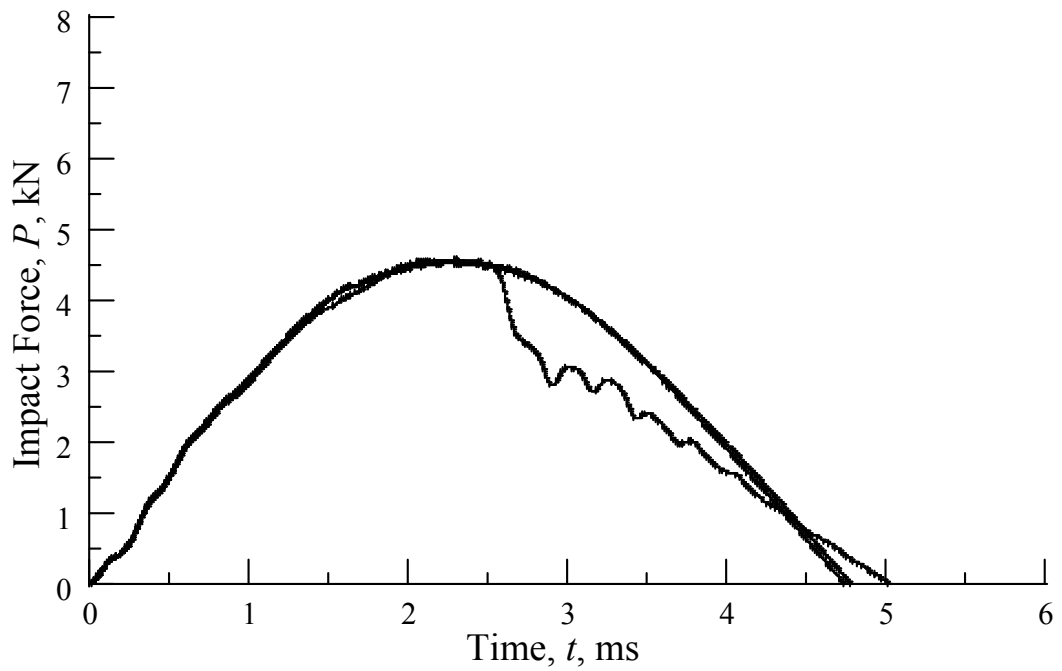


Figure F.10. Force versus time at $H = 83$ mm (3.25 in)

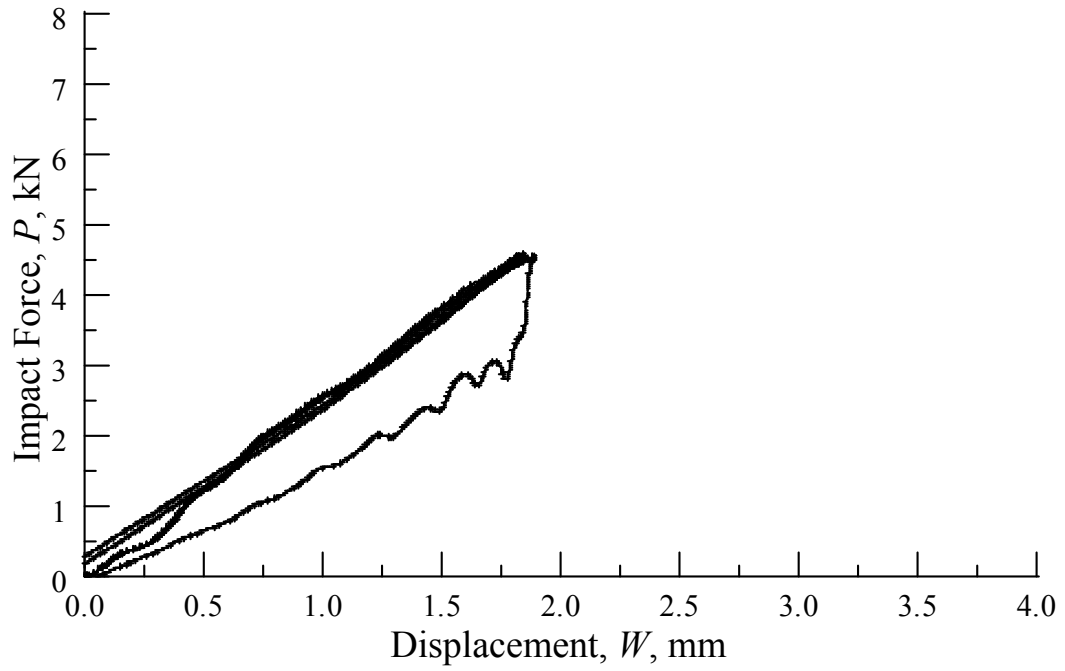


Figure F.11. Force versus displacement at $H = 83$ mm (3.25 in)

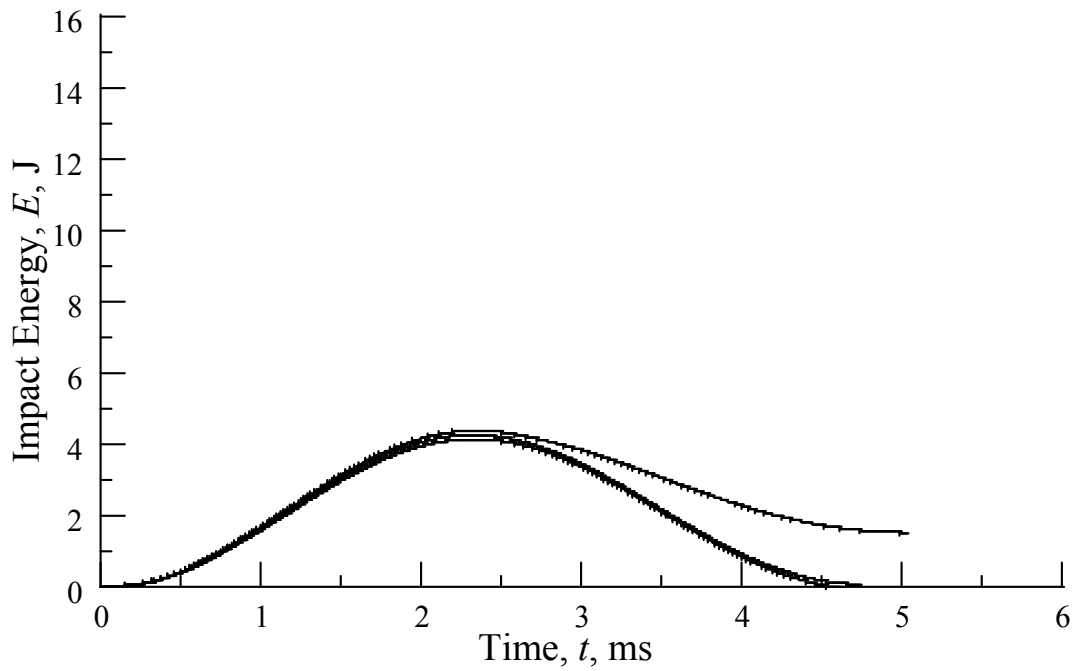


Figure F.12. Energy versus time at $H = 83$ mm (3.25 in)

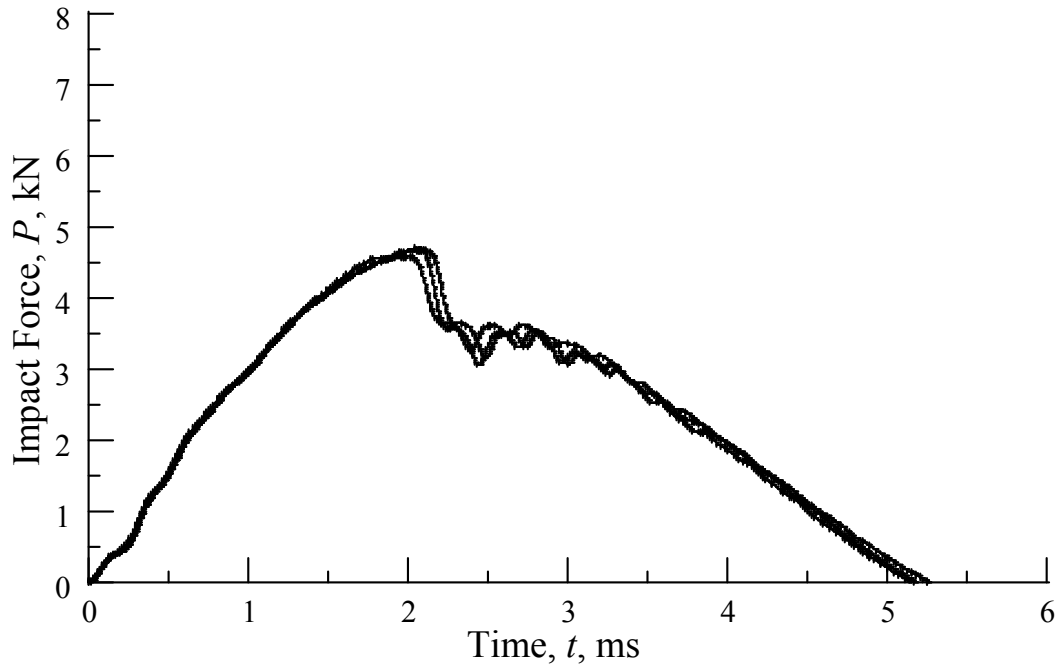


Figure H 13. Force versus time at $H = 89$ mm (3.5 in)

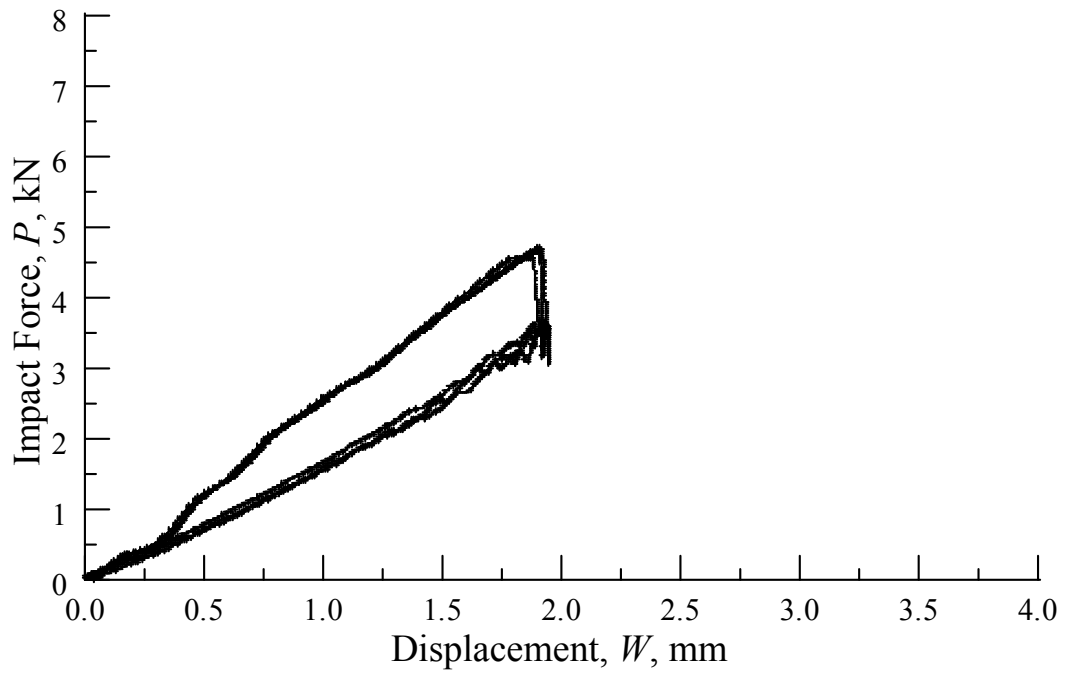


Figure F.14. Force versus displacement at $H = 89$ mm (3.5 in)

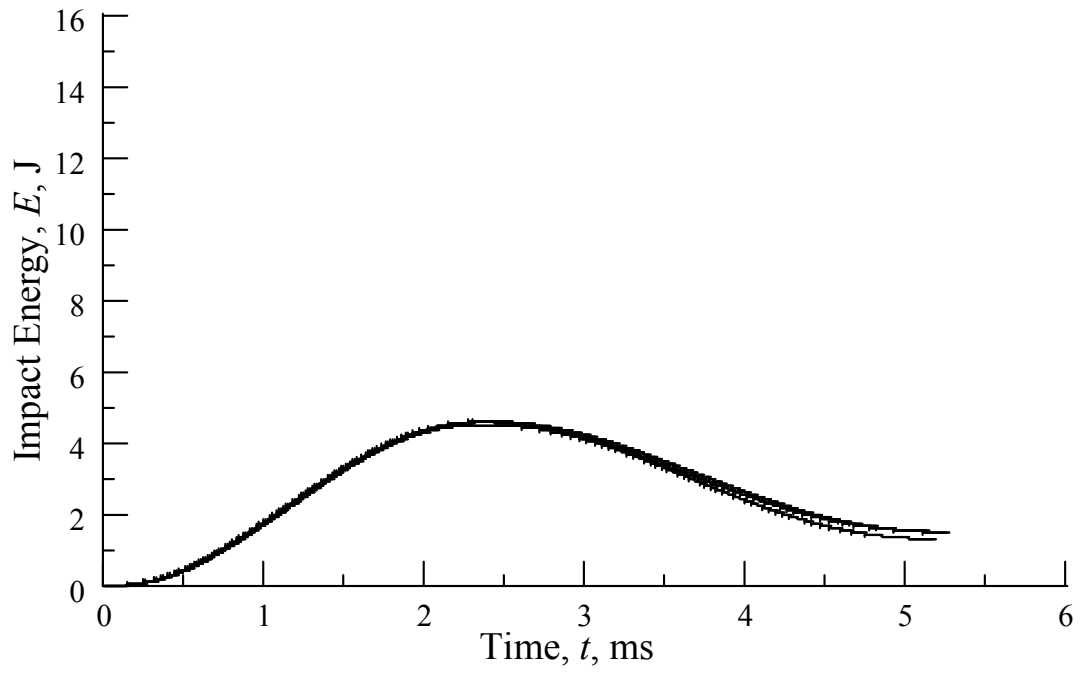


Figure F.15. Energy versus time at $H = 89$ mm (3.5 in)

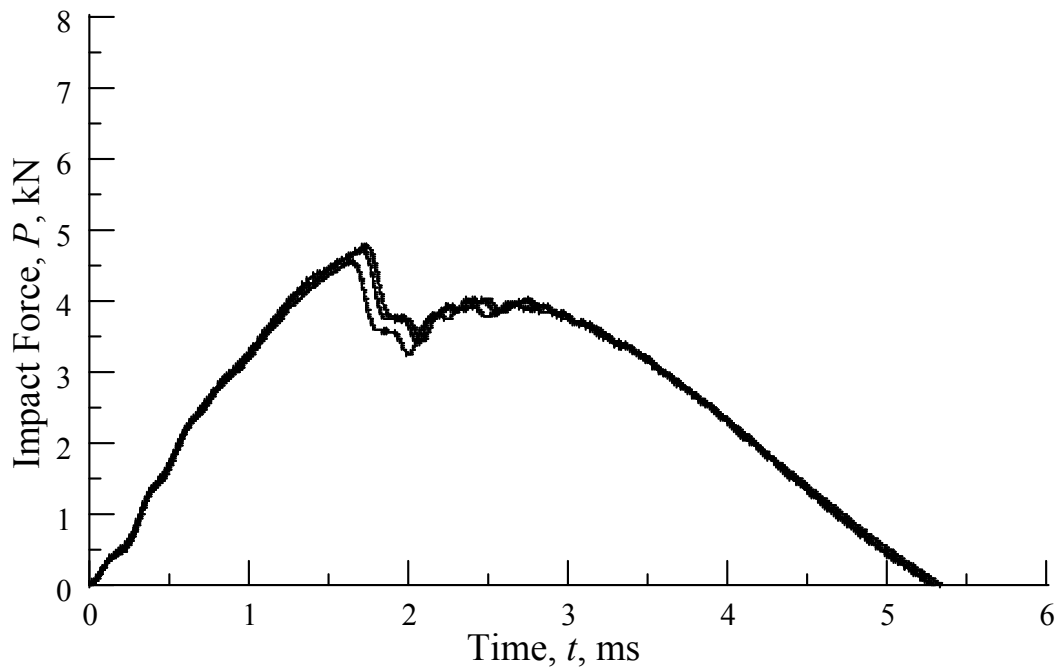


Figure F.16. Force versus time at $H = 102$ mm (4.0 in)

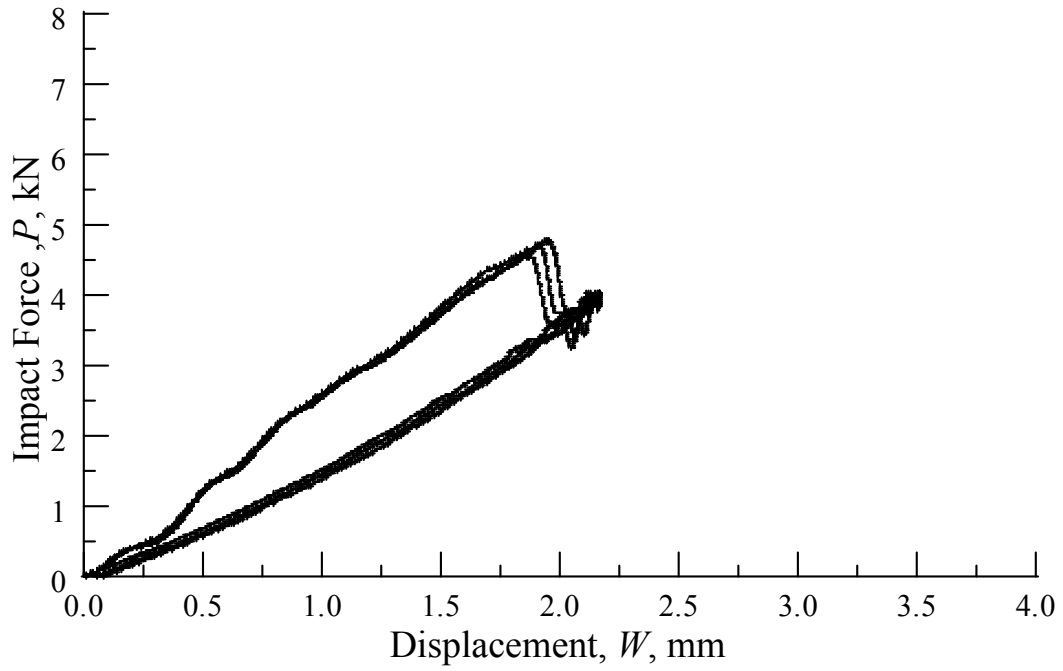


Figure F.17. Force versus displacement at $H = 102$ mm (4.0 in)

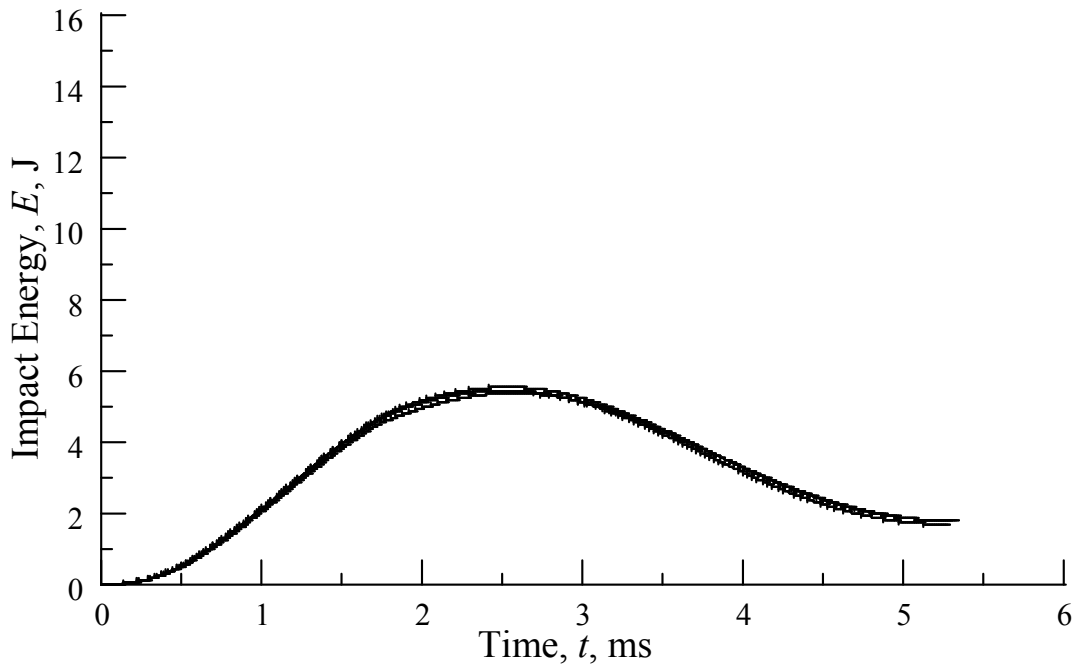


Figure F.18. Energy versus time at $H = 102$ mm (4.0 in)

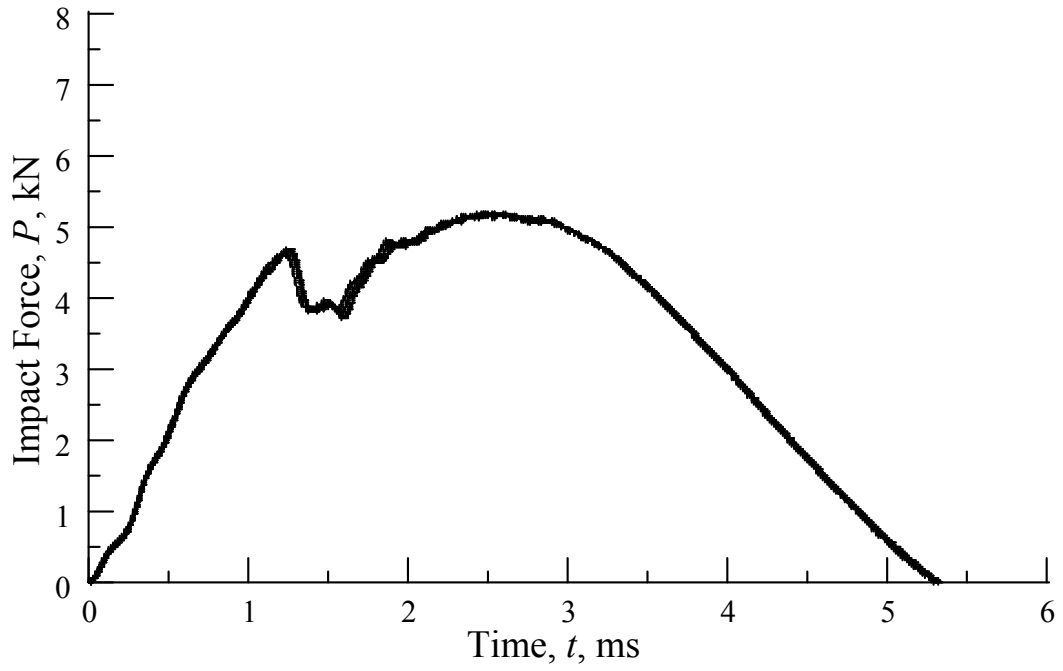


Figure F.19. Force versus time at $H = 152$ mm (6.0 in)

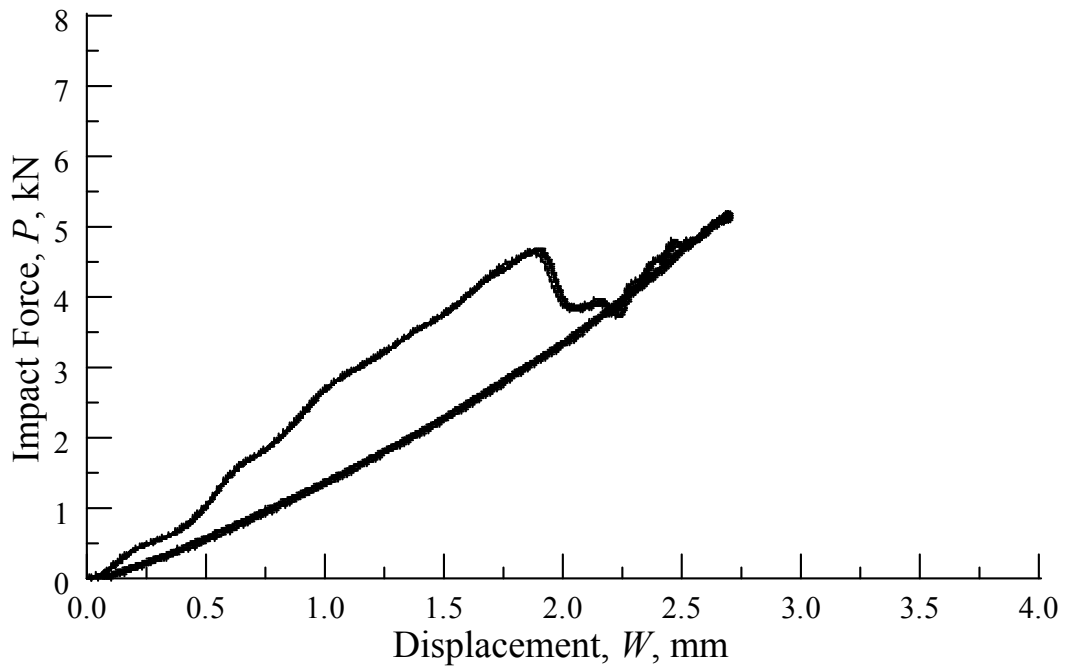


Figure F.20. Force versus displacement at $H = 152$ mm (6.0 in)

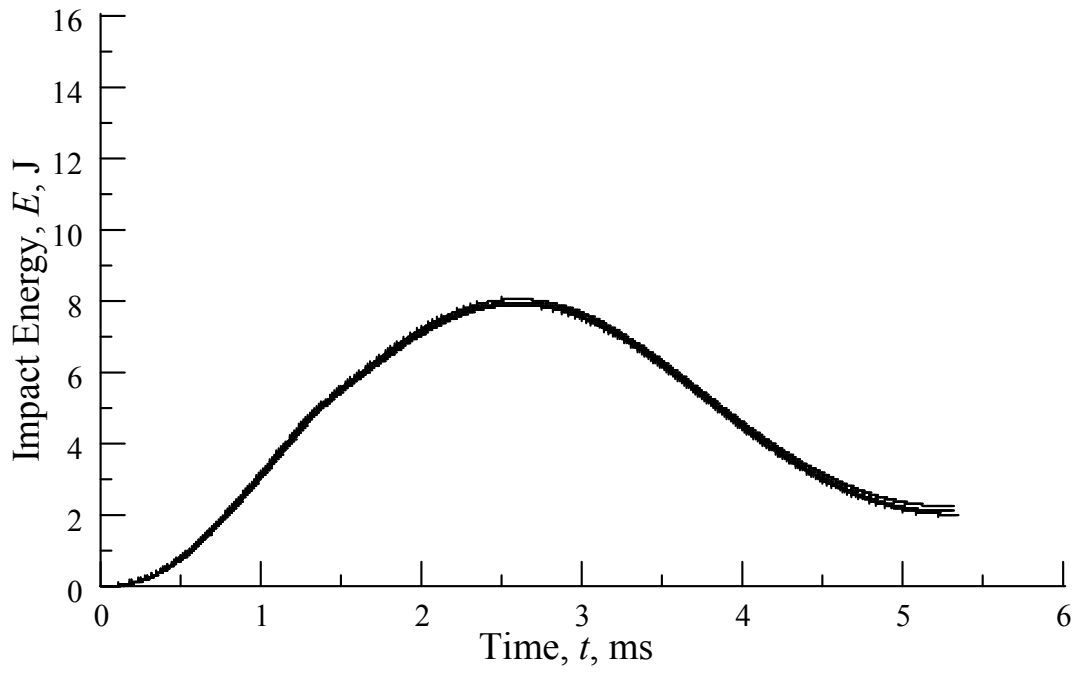


Figure F.21. Energy versus time at $H = 152$ mm (6.0 in)

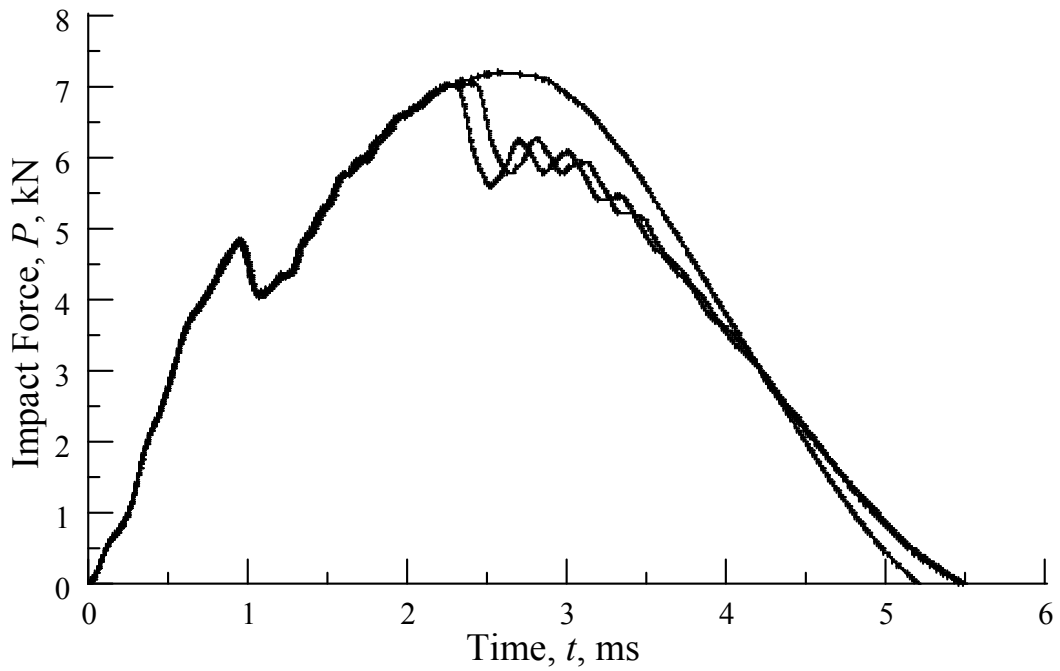


Figure F.22. Force versus time at $H = 254$ mm (10.0 in)

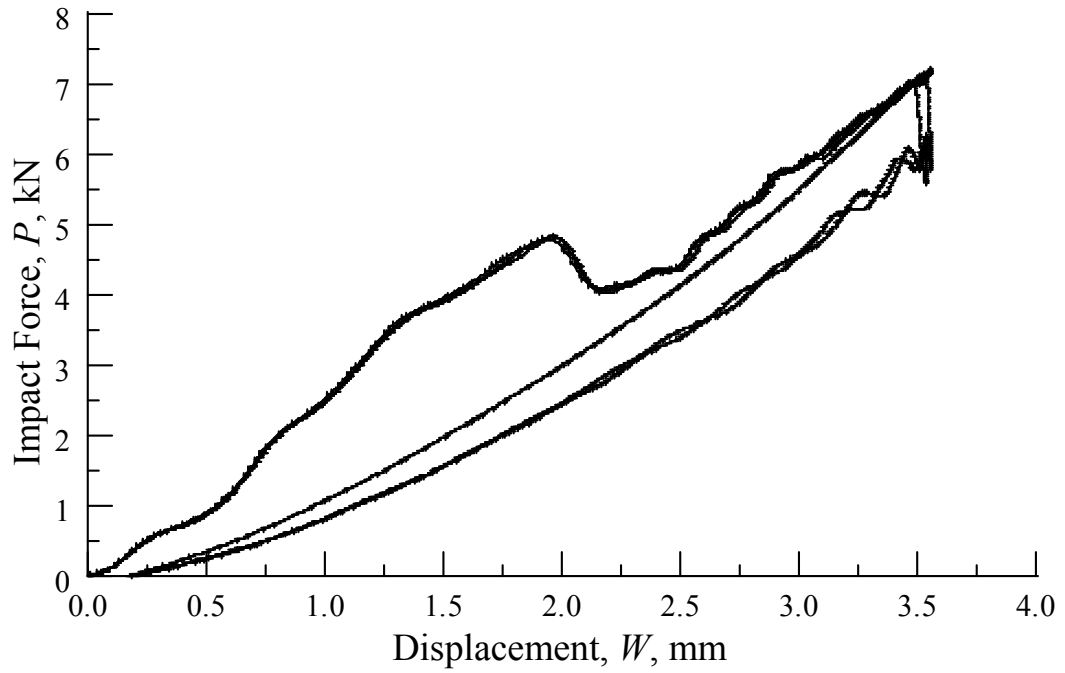


Figure F.23. Force versus displacement at $H = 254$ mm (10.0 in)

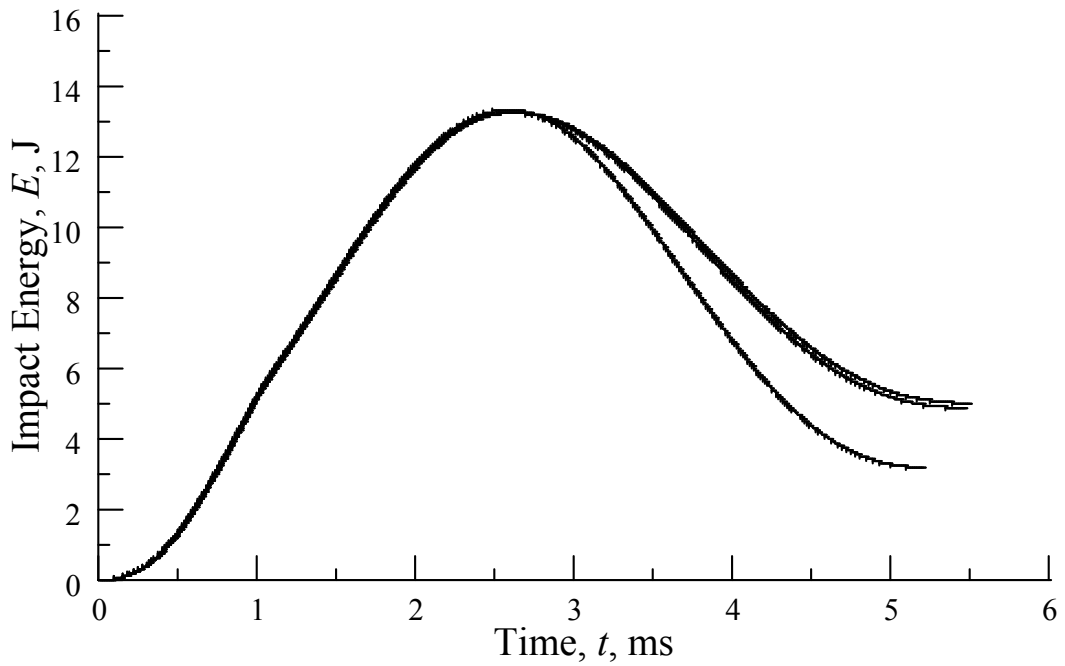


Figure F.24. Energy versus time at $H = 254$ mm (10.0 in)